CHARACTERISING LUNG TISSUE PATHOLOGY AND IMMUNITY IN VACCINATED AND UNVACCINATED RHESUS MACAQUES CHALLENGED WITH SARS-COV-2





CILLIAN GARTLAN

REUBEN COLLEGE

UNIVERSITY OF OXFORD

SUPERVISED BY PROFESSOR MILES CARROLL

DOCTOR OF PHILOSOPHY THESIS

© 2024 CILLIAN GARTLAN

Declaration

This thesis is the result of my own work and all contributions by others are outlined on page 8. No substantial part of my thesis has already been submitted or is being concurrently submitted for any qualification at the University of Oxford or any other institution. Parts of **Section 1.5** and **Section 1.6** have been adapted from a publication of which I am first author (Gartlan C, Tipton T, Salguero FJ, Sattentau Q, Gorringe A, Carroll MW. Vaccine-Associated Enhanced Disease and Pathogenic Human Coronaviruses. Front Immunol. 2022 Apr 4;13:882972. doi: 10.3389/fimmu.2022.882972.), as described in the text. This thesis does not exceed the word limit set by the Nuffield Department of Medicine for a doctoral thesis.

Table of contents

Declaration ii

Acknowledgements v

Contributions viii

Abbreviations x

Abstract xiii

Chapter 1: Introduction 15

1.1. The SARS-CoV-2 virus 15

1.2. Tissue immune responses to SARS-CoV-2 infection 16

1.2.1. Nasal cavity: the site of initial infection 17

1.2.2. Linking peripheral immunology with lung pathology 18

1.2.3. Lung tissue responses to SARS-CoV-2 20

1.3. Respiratory virus immunity and vaccination 28

1.4. The use of animal models to answer outstanding questions about the lung tissue response to COVID-19 32

1.5. Background on Vaccine-Associated Enhanced Disease 36

1.6. VAED and SARS-CoV-2 42

1.7. Preclinical vaccine studies at UKHSA Porton Down 45

1.8. Thesis aims 48

Chapter 2: Defining the cellular environments within post-challenge lung tissue 51

2.1. Histopathology, immunohistochemistry and in-situ hybridization 52

2.1.1. Methods 53

2.1.2. Results 54

2.2. Immunohistochemistry-based cell counting 58

2.2.1. Methods 58

2.2.2. Results 59

2.3. Multiplex immunofluorescence 60

2.3.1. Cell DIVE protocol 62

2.3.2. Initial analysis 65

2.4. Single-cell analysis of immunofluorescence data 67

2.5. Discussion 80

Chapter 3: Transcriptomic characterisation of lesioned and non-lesioned tissue regions 92

3.1. Spatial transcriptomics experiment 94

3.2. Filtering, quality control and dimensionality reduction 99

3.3. Differential gene expression analysis 109

3.4. Pathway enrichment analysis 122
3.5. Discussion 135
Chapter 4: Soluble factors in lung tissue pathology 145
4.1. Assessment of the impact of formalin inactivation on antibody binding to SARS-CoV-2 spike protein 147
4.1.1. Methods 147
4.1.2. Results 148
4.2. BAL cytokine analysis 149
4.2.1. Methods 152
4.2.2. Results 153
4.3. Discussion 160
Conclusions 163
Bibliography 170
Appendix 182
Supplementary tables and figures 182
Cell DIVE staining optimisation 255
Macrophage phagocytosis assays 257

Acknowledgements

The support from my supervisors Professor Miles Carroll, Professor Javier Salguero, Dr Tom Tipton, Professor Quentin Sattentau and Professor Andrew Gorringe has been essential to my progress and discussing ideas with them throughout my DPhil has been very helpful. As my primary supervisor, Miles could not have been any more supportive and has often gone above and beyond in his support for myself and the other DPhil students in the group, which I am extremely grateful for. I feel very fortunate to have had such a positive experience during my DPhil and to be inspired to continue to pursue research in the future.

The Carroll group, including the DPhil students, the postdoctoral scientists and research assistants have provided a friendly working environment which I greatly appreciate. Dr Tom Tipton was always there to answer my day-to-day queries and provide general feedback on the project on a regular basis. Dr Caolann Brady, another DPhil student in the group working on these NHP samples, has been particularly helpful during this project as we bounced ideas off one another regularly and shared samples and data according to our separate project interests.

The other DPhil students who were in the lab for most of my time in the Carroll group, Dr Hannah Klim, Dr Grace Hood and Dr Caolann Brady have all become close friends of mine and I'm thankful for their humour, regular discussions of our work that highlighted their continued passion for it and for all of the good times we've shared together – both inside and outside of the lab! They have helped to shape my DPhil experience into such a positive one and they have also each set a very high bar for DPhil research in the group, which I've done my best to reach.

The friends I've made in Oxford have helped me to really enjoy my life here for the last three years and make the best of this time. I've been fortunate enough to make many great friends here so I won't name everyone individually (they know who they are) but I'd like to give a particular shout-out to Julia Salafranca for her friendship, constant support and enthusiasm. To all the friends who also supported me from afar (not too far in the case of Ireland), thank you.

Reuben College has provided a great space for me not only to study but to meet friends, set up collaborations through academic dinners and provide funding and an outlet for my public engagement interests. I'd like to thank all of the fellows, students and staff of Reuben College who have also helped to make my Oxford experience special.

I would like to acknowledge those who have trained me to carry out the techniques mentioned throughout this DPhil. Sarah Hill, Dr Dylan Windell and Ananya Bhalla provided training for the Cell DIVE and were very helpful in helping me to troubleshoot problems. Dr James Bancroft and Dr Edward Drydale trained me to use the EVOS M5000 and the ARIVIS Vision4d software.

This project has been a collaboration with many research groups who I've enjoyed working with. Collaborators at UKHSA Porton Down, which include Prof Javier Salguero and members of his Pathology Team; Laura Hunter, Alison Bird and Chelsea Kennard were all very welcoming during my time at Porton Down for the histopathology work. Collaborators at the John Radcliffe Hospital, in the Transplantation Research and Immunology Group (TRIG) co-led by Professor Fadi Issa and Professor Joanna Hester, facilitated the spatial transcriptomics experiment. I'd like to particularly thank Megan Bradbury for assisting with the library preparation and Dr Amy Cross and Dr Joanna Hester for taking the time to work through this long experiment with me on the day (and late into the night!). Dr Stephen Taylor and Peter Todd put in a lot of work to get their MDV platform working for my Cell DIVE data, I'd like to thank them for their patience with this and their commitment to the project despite its difficulties. I would also like to thank Prof Helen Lockstone and Dr Jack Crook for providing advice on the transcriptomics analysis and giving me the confidence to move forward with my analysis pipeline.

To my previous mentors at Trinity College Dublin, namely Prof Lydia Lynch who initially encouraged me to apply to Oxford for a DPhil and Prof Luke O'Neill who was also very encouraging in my application to Oxford, I am very glad I took your advice!

This work would not have been possible without funding from the UK Health Security Agency for my PhD studentship and some consumable funds, as well as the Coalition for Epidemic

Preparedness Innovations (CEPI), who also provided funds for this work. Together, both of these organisations also provided the NHP samples that all of this work is based on.

Finally, I would like to thank my family. Particularly my parents, who have always been so supportive of what I want to do and have always gone out of their way to help me as much as they can. None of my achievements would have been possible without you.

Contributions

This project involved collaborations across the Centre for Human Genetics, the Kennedy Institute of Rheumatology and the John Radcliffe hospital (all at the University of Oxford), as well as a collaboration with UKHSA Porton Down.

The following individuals contributed to the work presented in this thesis and their contributions are listed alongside their names:

- Prof Miles Carroll – overall supervision, regular discussions on project direction, reading thesis drafts and macaque sample acquisition
- Prof Javier Salguero – pathology annotations, region selection for spatial transcriptomics, RNAscope protocol, immunohistochemistry protocol, sample preparation and regular discussions about the project
- Dr Tom Tipton – supervision and discussions on project and reading thesis drafts. Tom also helped with flow cytometry, the growth/differentiation protocol and the PBMC isolation protocol (all in supplemental)
- Dr Laura Hunter, Chelsea Kennard & Alison Bird (and other members of Pathology at UKHSA Porton Down): lung tissue sample prep, RNAScope and immunohistochemistry
- Dr Stephen Laidlaw – running the cytokine analysis experiment at CL3 conditions
- Megan Bradbury – library prep for and initial QC for the spatial transcriptomics work
- Dr Amy Cross – advice on the GeoMx and help running the GeoMx experiment
- Dr Joanna Hester – advice on the GeoMx, help running the GeoMx experiment and allowing us to use their lab's machine
- Dr Fadi Issa – advice on the GeoMx and allowing us to use their lab's machine
- Dr Oliver McCann – converting the files from sequencing into a usable format for analysis
- Prof Mark Coles – allowing us to use the Cell DIVE, providing macaque bone marrow and lymph node samples for imaging validation

- Dr Joannah Fergusson – providing macaque bone marrow and lymph node samples for imaging validation and sharing knowledge on antibodies for macaque tissue imaging
- Prof Stephen Taylor – modification of the SpOOx pipeline and MDV for Cell DIVE data, helping with analysis of Cell DIVE data using MDV software. Running segmentation and z-score normalisation on the Cell DIVE images
- Peter Todd – modification of the SpOOx pipeline and MDV for Cell DIVE data, helping with analysis of Cell DIVE data using MDV software

Abbreviations

ACE2 = angiotensin-converting enzyme 2

ACN = adjacency cell network

ADCC = antibody-dependent cellular cytotoxicity

ADCP = antibody-dependent cellular phagocytosis

ADE = antibody-dependent enhancement

AED = antibody-enhanced disease

APC = Antigen-presenting cell

BAL = Bronchoalveolar lavage

BALT = bronchial-associated lymphoid tissue

CDC = complement-dependent cytotoxicity

CPM = counts per million

cross-PCFs = cross-pair correlation functions

DAD = Diffuse alveolar damage

DGE = differential gene expression

ELISA = enzyme-linked immunosorbent assay

ELISpot = enzyme-linked immunosorbent spot

EMT = epithelial to mesenchymal transition

FDR = false-discovery rate

FFPE = formalin-fixed paraffin-embedded

FIV = formalin-inactivated vaccine

FcγR = Fc gamma receptor

GLM = generalised linear model

GO-BP = gene ontology biological processes

GSEA = gene set enrichment analysis

H&E = haematoxylin and eosin

iBALT = induced-bronchial-associated lymphoid tissue

IBEX = iterative bleaching extends multiplexity

IF = immunofluorescence

IHC = immunohistochemistry

IMC = imaging mass cytometry

ISH = in-situ hybridisation

ITAM = immunoreceptor tyrosine-based activation motif

LSM = light-sheet microscopy

MDM = monocyte-derived macrophage

MDSC = myeloid-derived suppressor cell

MPO = myeloperoxidase

MSigDB = Molecular Signatures Database

NES = normalised enrichment score

NGS = next-generation sequencing

NHP = non-human primate

PBS = Phosphate-buffered saline

PCA = principle component analysis

PFU = plaque-forming units

PanCk = Pan-Cytokeratin

QC = quality control

QCM = quadrat correlation matrix

RBD = receptor-binding domain

RLE = relative log expression

SARS-CoV-2 = Severe acute respiratory syndrome coronavirus 2

smFISH = single-molecule fluorescence in situ hybridization

TCM = central memory T cells

TEM = effector memory T cells

TLR = toll-like receptor

TMM = trimmed mean of M-values

TRM = Tissue-resident memory

Treg = regulatory T cell

UKHSA = UK Health Security Agency

VAED = vaccine-associated enhanced disease

VST = variance-stabilising transformation

Abstract

Much has been learned about how SARS-CoV-2 drives lung immunopathology. However, studies of post-mortem human lung tissue have confounding factors including different viral loads, infection timepoints and treatments. Animal studies allow us to standardise these factors, examine a wider range of pathological states and study the impact of vaccination on protection against or enhancement of lung pathology. As human studies can only collect tissue samples post-mortem, the impact of vaccination on the in-situ tissue response to infection has not been studied.

Using spatial transcriptomics and multiplex immunofluorescence, we characterise the immune mechanisms driving pathology and protection in the lung across vaccine and challenge scenarios in rhesus macaques challenged with SARS-CoV-2. Lung tissue from vaccinated (DNA, mRNA, viral vector and formalin-inactivated vaccines), unvaccinated, and re-challenged macaques were studied. Lesioned and non-lesioned regions of lung tissue were selected for analysis in order to link results with the pathological context in-situ.

Rhesus macaques had a spectrum of pathology outcomes depending on the level of immunity conferred by prior infection or vaccination. Rhesus macaques recapitulated several mechanisms of severe human COVID-19 disease, particularly when lesioned areas were focused on. In contrast, non-lesioned regions could not be used to effectively separate high and low pathology animals, demonstrating the importance of pathology-guided spatial analysis. We did not find any evidence of vaccine-associated enhanced disease (VAED) in vaccinated animals with high pathology.

$CD4^+$ T cells were found in greater numbers in the lung tissue of vaccinated or previously-challenged NHPs and activated $CD4^+$ T cells were more prevalent in the most

protected group, vaccinated with the viral vector vaccine. $CD8^+$ T cells and APCs were found to correlate with histopathology scores in lesioned areas and may co-localise spatially, suggesting ongoing antigen presentation to $CD8^+$ T cells in more severe disease. These associations warrant further investigation for mechanistic insights.

Chapter 1: Introduction

1.1. The SARS-CoV-2 virus

The Severe acute respiratory syndrome coronavirus 2 (SARS-CoV-2) virus is the causative agent of the COVID-19 pandemic. The virus is thought to have first infected humans at a live animal market in Wuhan, China following multiple spillover events [1–4]. The SARS-CoV-2 virion is made up of the spike, nucleocapsid, membrane and envelope structural proteins, as well as non-structural proteins, such as the RNA-dependent RNA polymerase which are important for viral replication. The spike protein mediates cell entry by binding to angiotensin converting enzyme 2 (ACE2) through the spike protein's receptor binding domain (RBD), although other viral and proteins also play a part in cell entry mechanisms, as reviewed elsewhere [5]. In the context of immunity against SARS-CoV-2, the spike protein is therefore an important target and neutralising antibodies typically bind to the RBD in its RBD-up conformation to directly block its interaction with ACE2 or bind elsewhere on the spike to sterically hinder its ability to engage with ACE2 [6]. As part of lineage B of the betacoronavirus genus, SARS-CoV-2 is closely related to SARS-CoV (SARS) and Middle East respiratory syndrome coronavirus (MERS-CoV). A comparative pathology study in cynomolgus macaques found similarities in lung pathology between these three viruses, with SARS pathology being the most severe [7]. Given these similarities, the approach to handling the SARS-CoV-2 pandemic was informed by what was known of its close relatives, although this also led to some concerns about vaccine-associated enhanced disease (VAED) which had been reported for other betacoronaviruses (discussed in **Section 1.6**).

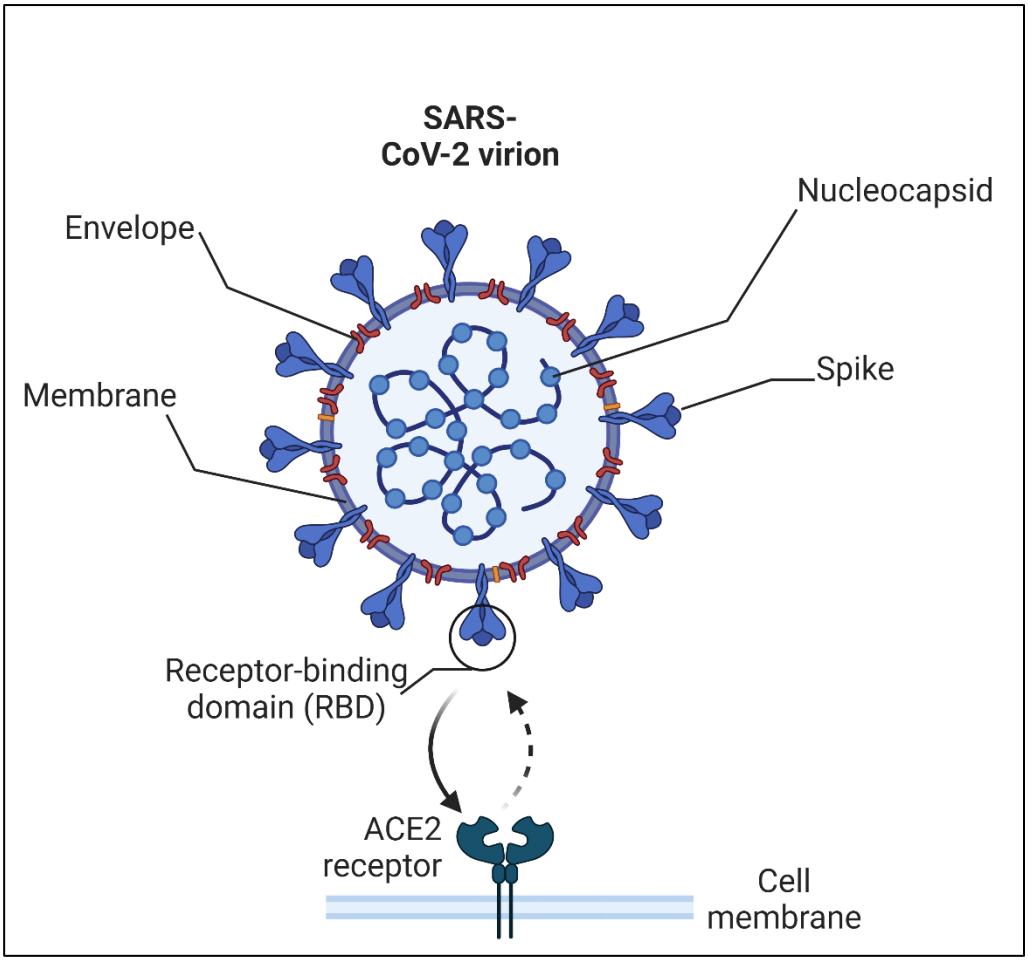

Figure 1: The basic structure of the SARS-CoV-2 virion. Showing the spike, nucleocapsid, membrane and envelope structural proteins. Created with Biorender.com.

1.2. Tissue immune responses to SARS-CoV-2 infection

SARS-CoV-2 is a respiratory virus that can cause severe disease and mortality through mediating damage to lung tissue. Since the beginning of the SARS-CoV-2 pandemic, post-mortem examinations of lung tissue from patients who succumb to COVID-19 have demonstrated diffuse alveolar damage (DAD) as the primary histological feature [8,9]. However, there is heterogeneity in lung pathology even within these fatal cases and several other pathological features have been observed in the lung, including tissue thrombosis and bronchopneumonia, the latter of which being particularly evident when secondary bacterial infections are found [9]. Different stages of disease progression can also be observed within the same tissue and these stages each have their

own associated histopathological features [9,10]. While COVID-19 can also manifest in disease phenotypes outside of the lung [11], these are not within the scope of this thesis.

1.2.1. Nasal cavity: the site of initial infection

As a respiratory virus, SARS-CoV-2 initially establishes infection in the upper respiratory tract, particularly in nasal epithelium [12,13]. A human challenge study has demonstrated that during infection the nose has much higher viral titres than the throat [14]. However, this may be at least partially due to challenge doses being administered intranasally. Previous infection with closely-related SARS-CoV-2 variants appear to confer strong protection against both re-infection and symptomatic disease, compared to previous exposure with more distant variants [15]. While neutralising antibodies are highly correlated with protection against both infection [16] and severe disease [17], levels of neutralisation fall due to both antibody waning and virus evolution. T cells may have a role in providing broader protection against SARS-CoV-2 [18,19]. In individuals vaccinated against SARS-CoV-2, broadly-specific tissue-resident memory (TRM) T cells are only found in the nasal mucosa of those who have experienced breakthrough infection and not those who are only vaccinated [18]. This highlights the ability of live virus to stimulate TRM cells at the site of infection. Conversely, circulating T cells have also been found in frontline healthcare workers of the COVID-19 pandemic who, despite presumably being exposed to high viral loads, have not seroconverted and are therefore thought to have experienced abortive infections due to T cell-mediated sterilising immunity [19]. In these individuals, the T cells were specific to a viral polymerase and were thought to exist prior to SARS-CoV-2 and potentially expand upon subsequent exposure and abortive infection. Apart from this unique case of T cell responses providing rapid protection, T cells are mostly thought to protect against severe pathology rather than infection in memory contexts. Overall, both antibodies and T cells play important roles in protecting against infection and severe disease, although T cell responses have been largely assessed in the periphery rather than in their native tissue context. Even in the absence of damage to nasal epithelium, loss of olfactory sensory function has been noted in response to nasal infections, mediated by IFN-γ signalling [20]. Anosmia is a common symptom of COVID-19 and

the downregulation of olfactory receptor expression in response to inflammation has been suggested as a potential mechanism [21]. The effects of COVID-19 on the olfactory system have been reviewed comprehensively elsewhere [22], as has the effect of COVID-19 on chemosensory receptors more broadly [23].

In-depth single-cell analysis of nasopharyngeal swabs and blood has been carried out on samples from a SARS-CoV-2 human challenge study and provided new insights into the gene expression profiles of T cells based on their clonotype in relation to SARS-CoV-2 antigens [24]. Interferon responses in the blood were found before they were detected in the nasopharynges. Individuals with sustained infections had delayed nasopharyngeal immune infiltration while those with transient upper airway infections had more rapid infiltration [24]. High expression of *HLA-DQA2* particularly in upper airway cells such as macrophages, dendritic cells, monocytes, B cells and Langerhans cells were associated with abortive and transient infections, while low *HLA-DQA2* expression in these cells was associated with sustained infections in the participants. Another study that examined upper airway immunity through nasopharyngeal swabs found diverse adaptive immune cell populations including many long-lived TRM T and B cells [25]. In individuals with breakthrough SARS-CoV-2 infections, virus-specific populations of these resident cells were found, with an enrichment of IgA^+ B cells in the upper airway.

1.2.2. Linking peripheral immunology with lung pathology

The peripheral blood response to COVID-19 has been well characterised, particularly by the COvid Multi-Omics Blood Atlas (COMBAT) consortium and the Cambridge Institute of Therapeutic Immunology and Infectious Disease-National Institute of Health Research (CITIID-NIHR) COVID-19 BioResource collaboration [26,27]. The relative ease of access to blood means studies such as this can have much higher sample sizes than studies that require tissue. Human vaccine immunology studies also rely on peripheral blood to study serum antibody and circulating cellular responses. However, in reality the battleground of respiratory infections takes place in upper and lower respiratory tract tissues, not in blood [28]. The study of lung tissue has provided insights into how in-situ immune responses may exacerbate [10,29,30] or prevent [31] respiratory virus

pathology. The latter case, where lung responses protect against pathology, is particularly difficult to study in humans given the requirement for lung tissue samples that capture these protective responses in action, as lung tissue samples can only be obtained post-mortem [28]. While studies of peripheral blood provide insights into the immune response to infection, their relation to the tissue environment has been highlighted in a follow-up to the COMBAT study, the COVID-19 Lung Single Cell Mass Cytometry Imaging Consortium (COSMIC) study [10]. The COSMIC study carried out spatial analysis on post-mortem lung tissue from patients who succumbed to COVID-19. In comparison to studies on blood from severe patients that highlight an increase in immature cycling monocytes [26,32] , these immature monocytes were not found in the lung, which the authors suggest may be due to rapid differentiation into mature monocytes and macrophages in the lung [10]. The study also outlined the importance of phenotyping using protein staining over reliance on transcriptomics only. While $CD4^+$ and $CD8^+$ T cells were hypothesised to be depleted in fatal COVID-19 lungs from gene expression levels in a single-nucleus RNA sequencing study from post-mortem COVID-19 lung cells [33], this imaging study demonstrated that they were in fact found at high levels in post-mortem samples, as noted by the authors [10]. However, in line with studies on peripheral blood, an increase in the number of MAIT cells in the lung was noted [10]. Another study that compared respiratory samples (acquired by saline wash of endotracheal tubes in patients) and blood samples found associations between blood factors and airway responses [34]. This study found that $CD163^+$ monocytes were found in higher numbers than conventional monocytes in the blood and these $CD163^+$ monocytes were also found in airway samples and damaged alveoli from the same patients [34]. Activated T cells in severe COVID-19 were localised to the airways and were not found at high levels in peripheral blood. The authors demonstrated a correlation between these airway T cells and improved outcome, while this association is not seen with T cells from peripheral blood. By looking at airways, a mechanism of monocyte recruitment to the lung in COVID-19 was uncovered, as the myeloid chemoattractant CCL2 was found at high levels [34]. As with other respiratory virus infections, the initial response to infection tends to involve alveolar macrophages, granulocytes, stromal cells and infiltrating monocytes which produce proinflammatory cytokines and chemokines, contributing to inflammation and recruiting

both innate and adaptive immune cells to the infected site [35]. During COVID-19 the macrophage composition of the lung changes and aberrantly-activated monocyte-derived macrophages (MDMs) begin to dominate and produce many pro-inflammatory mediators while resident alveolar macrophages are depleted [33,36–39]. Overall, recruitment of peripheral cells is very important in driving lung pathology but studying peripheral immunology alone cannot give mechanistic insights on the drivers of pathology at the site of infection. The role of peripheral immune infiltrates into lung tissue during protective outcomes (including following vaccination) however remains quite poorly understood, as airway and lung tissue samples (and matched blood) from less severe individuals during the time course of infection are not easily acquired and as these people will not present with COVID-19 at hospitals due to their milder symptoms.

1.2.3. Lung tissue responses to SARS-CoV-2

Much of the work characterising the antiviral immune responses of human lung tissue has been carried out by the Farber lab, which is able to acquire large numbers of post-mortem human tissues from organ donors. TRM T cells in human lungs were first characterised in the context of transplant recipients [40] but are now known to also play an important part in antiviral tissue immunity. In tissue from seropositive organ donors up to 6 months following infection, SARS-CoV-2-specific T cells, B cells and T_{FH} cells have been found mostly in lungs and lung-associated lymph nodes, with some also found in the spleen and bone marrow [41]. The majority of the SARS-CoV-2 specific B cells were tissue-resident and a proportion of the T cells were also tissue-resident [41]. While these cells appear to persist, their associations with protective responses in humans remain incompletely understood, as this study acquired tissues from individuals who died of causes other than COVID-19 and it is not possible to acquire such lung samples from healthy, 'protected' individuals. Therefore, there is no comparative pathology that can be used as a readout of efficacy in these human studies.

New technologies allow for single-cell and/or spatial omic studies of tissue samples [42]. Many studies have applied such approaches to study COVID-19 lung pathology in post-mortem human tissue, including the aforementioned COSMIC study and others [10,30,33,43–45]. Broadly, these studies

profile proteins, mRNA or both and depending on the techniques used, the output data may or may not be spatially resolved. Methods that do not allow for spatial resolution include bulk RNA-sequencing of digested tissue sections, single-cell RNA sequencing of cells from bronchoalveolar lavage (BAL) fluid or cells from digested lung tissue, mass spectrometry and flow cytometry. Studies that look at cells in BAL fluid give an insight into non-adherent airway cells, which are washed into the phosphate-buffered saline (PBS) fluid, but not cells located deeper in the lung tissue parenchyma [46]. Spatially-resolved methods (typically used on frozen or fixed tissues) include spatial transcriptomics / digital spatial profiling, imaging mass cytometry (IMC), immunohistochemistry (IHC) and immunofluorescence (IF). Spatial transcriptomics methods can involve in-situ sequencing or high-resolution in-situ hybridisation imaging. The GeoMx DSP platform from Nanostring uses in-situ hybridisation probes to detect mRNA transcripts in selected regions of interest (ROIs) within tissues, rather than measuring the transcripts directly [47]. This probe-based method is sometimes referred to as 'digital spatial profiling' rather than 'spatial transcriptomics', although the more common term 'spatial transcriptomics' will be used for the remainder of this thesis. The in-situ hybridisation approach has been reported to make the DSP platform more sensitive than other commercial sequencing-based spatial transcriptomics platforms like the Visium from 10X Genomics, although it is also more prone to non-specific detection [48]. More recently, new platforms such as the CosMx from Nanostring, Xenium from 10X genomics and MERFISH from Vizgen allow for spatially-resolved single-cell and even sub-cellular multiplex transcriptomics in intact tissue [49–51], initially with the trade-off of smaller gene panels and therefore an inability to look at the whole transcriptome, although this is rapidly changing and new spatial profiling methods with improved resolution and panel sizes are regularly being published.

Apart from post-mortem tissue samples, which are rare, insights into the lung response in COVID-19 typically come from BAL fluid. Similar to studies of peripheral blood, such studies can involve single-cell sequencing, antibody assays and/or cytokine analysis. A single-cell RNA sequencing study on BAL fluid identified abundant pro-inflammatory MDMs in severe COVID-

19 airways when compared to healthy controls and highly clonally-expanded $CD8^+$ T cells in moderate COVID-19 airways [39]. When comparing severe and moderate cases, it was evident that BAL fluid from severe patients had higher proportions of both neutrophils and macrophages and lower proportions of T cells, myeloid dendritic cells and plasmacytoid dendritic cells. The transcriptomic analyses confirmed the presence of several macrophage subpopulations which had upregulated transcription factor genes associated with pro-inflammatory responses in only the severe COVID-19 patients [39]. Patients with severe COVID-19 also had greater populations of proliferating T cells, lower $CD8^+$ T cell numbers and the $CD8^+$ T cells were found to have an upregulation of genes associated with cell homeostasis, initiation of translation and nucleoside metabolic pathways [39]. Patients with moderate disease instead had $CD8^+$ T cells with upregulated genes associated with migration, activation and cytokines [39]. The study also looked at cytokines in the BAL and found increased levels of pro-inflammatory cytokines, especially IL-8, IL-1β and IL-6 in severe patients. The single-cell analysis attributed IL-1β, IL-6 and TNF production, as well as the production of various chemokines (CCL2, CCL3, CCL4 and CCL7) to lung macrophages from severe patients [39]. While some chemokines (CXCL9, CXCL10 and CXCL11) were found much higher in both patient groups than in control samples, CXCL16 was only found to be elevated in moderate infection [39]. In summary, Liao *et al*. proposed, in agreement with other literature, that cytokine storms are associated with severe COVID-19 and also proposed that lung macrophages in severe COVID-19 recruit neutrophils and monocytes through the receptors CCR1 and CXCR2, while CXCR3 and CXCR6 are engaged in moderate disease for T cell recruitment [39]. Another study of BAL fluid found increased IL-6 in the BAL fluid of COVID-19 patients but could not identify the cells that produced the IL-6, unlike the study from Liao *et al*. and proposed that the IL-6 was produced by cells in the lung parenchyma that were not sampled in their BAL procedure [52]. This highlights that BAL sampling does not always capture all of the relevant cells for assessment of lung pathology or immunity and highlights advantages of studying the lung parenchyma itself when these samples are available.

Grant *et al*. studied BAL fluid from 88 patients that had respiratory failure owing to SARS-CoV-2 infections and 211 patients with suspected pneumonia from other pathogens, primarily using a combination of flow cytometry and bulk sequencing, with single-cell RNA sequencing carried out on a subset of 10 COVID-19 patients [53]. Like other single-cell BAL work, Grant *et al*. demonstrated that the alveolar spaces in COVID-19 were enriched in monocytes and both $CD4^+$ and $CD8^+$ T cells. Single-cell transcriptomics revealed alveolar macrophages were infected with SARS-CoV-2 and that these cells produced T cell chemoattractants. The infiltrating T cells produce IFN-γ which the authors hypothesise activated the macrophages to produce pro-inflammatory cytokines and promote a feedback loop that drives inflammatory alveolar responses [53]. Using single-molecule fluorescence in situ hybridization (smFISH), alveoli with relatively healthy morphology were found next to damaged alveoli, which contained macrophages infected with SARS-CoV-2, demonstrating the importance of spatial context when studying COVID-19 pathology [53]. A study that profiled T cell responses in the BAL fluid of patients with SARS-CoV-2-associated pneumonia found that early enrichment of T cells correlated with survival, particularly those with interferon-stimulated profiles and those that were specific for SARS-CoV-2 structural proteins such as the nucleocapsid and spike proteins [54]. In contrast, poor outcomes were associated with T cells that had activation of NF-κB-associated pathways later in disease and were specific for the ORF1ab complex.

Studies of BAL fluid from SARS-CoV-2-vaccinated people have shown that peripheral vaccination alone does not stimulate durable and tissue-resident mucosal immune responses, a breakthrough infection is required [55,56]. Even in the absence of prior vaccination, infection with SARS-CoV-2 has been shown to induce tissue-resident T cells with functionally protective profiles in airways (as measured in airway samples taken from washes of endotracheal tubes) [34]. The frequency of these cells was found to correlate both with survival and with younger age and $CD4^+$ and $CD8^+$ TRM dominated the airway T cell profile. The TRM and effector memory T cell (TEM) subsets expressed higher levels of the activation marker HLA-DR and the immune checkpoint PD-1 and lower levels of the IL-7 receptor CD127 [34]. Transcriptionally, airway T cells

also upregulated *GZMB*, perforin and *IFNG*, which are associated with antiviral protection. Airway T cells also upregulated the expression of genes associated with chemokines, including *CCL2* and *CCL4*, contributing to the previously-discussed monocyte recruitment. While the frequencies of TEM and central memory T cells (TCM) were increased in airways of COVID-19 patients compared to healthy controls, the frequency of regulatory T cells (Tregs) was lower. Overall, a mixture of tissue-resident and recruited T cell subsets were found in the airways of COVID-19 patients and T cells in the airways were associated with improved outcome [34].

The use of single-cell resolution spatially-resolved methods such as multiplex immunofluorescence and imaging mass cytometry (IMC) allow for the interrogation of cellular neighbourhoods, rather than just individual cells, as functional units [57,58]. Spatial methods are highly relevant to understanding pathological phenotypes in tissues, particularly when compared to isolated single-cells from tissue digestions without spatial context. For example, whether the cells (or cellular neighbourhoods) are found in a pathological lesion or in a relatively healthy part of tissue can help to ascertain their role in the observed histological landscape. On top of this, transcriptomics and/or analysis of phenotypic protein markers related to function can help to further deconvolute whether cells or neighbourhoods found within lesions are driving inflammation or fibrosis and whether cells in non-lesioned regions of tissue are mere bystanders that avoided the pathological consequences of infection, (if a virus has not made its way to this part of the tissue for instance) or are actively involved in suppressing inflammation in these regions.

Spatial transcriptomic techniques have been used to study post-mortem COVID-19 lung pathology and allow for the comparison of transcriptomic profiles within morphological features, such as those associated with particular anatomical compartments or more severe lesions vs milder lesions [29,30,45]. Rendeiro *et al*. used the GeoMx platform to examine lung injury in the context of early COVID-19 progression, late COVID-19 progression and bacterial pneumonia, comparing these data to healthy lung tissue [29]. Up to 24 ROIs per tissue were examined with a panel of 1,850 probes and ROIs included airway, vascular and alveolar areas. Rendeiro *et al*.

found that pathways associated with inflammatory responses were increased in COVID-19 patients compared to the other groups and particularly in the alveolar and airway compartments in samples from early COVID-19 [29]. Pathways associated with epithelial-to-mesenchymal transition (EMT), angiogenesis and myogenesis were also increased in COVID-19 compared to the other groups, but these pathways were associated with the later stage of the disease. Finally, complement activation and apoptosis were noted in blood vessels and alveolar regions in late COVID-19 in both their spatial transcriptomics and IMC data [29]. The authors therefore concluded that in fatal COVID-19, early responses are associated with inflammation and late responses are associated with fibrosis and aberrant resolution of this inflammation. Cross *et al*. similarly carried out a study on COVID-19 lung tissue using the GeoMx with a similarly-sized panel, although they compared areas of severe DAD to mild to moderate DAD [30]. The authors found that the histopathological severity was not always associated with higher SARS-CoV-2 RNA and identified upregulation of TNF superfamily member genes *BAFF* (*TNFSF13B*) and *TRAIL* (*TNFSF10*) in severe ROIs. With their spatial transcriptomic data and comparisons to single-cell RNA sequencing data, they hypothesised that *IFNG* expression on T cells and NK cells was associated with induction of the chemokines *CXCL9*, *CXCL10*, and *CXCL11* by myeloid cells which recruits $CXCR3^+$ leukocytes, which include T cells and NK cells, driving a positive feedback loop [30]. Severe DAD was also associated with cytotoxic genes, complement factor *C1QB* and pathways related to T cell activation and differentiation, cytokine production, antigen presentation, response to IFN-γ and cytotoxicity. Mild to moderate areas were associated with pathways related to haemostasis, wound healing and regeneration [30]. Another study using the GeoMx on COVID-19 lung tissue found heterogeneity in viral infection levels in different compartments of the lung and across patients, and compared virus-positive ROIs and virus-negative ROIs [45]. Clustering of the top 500 variable genes detected by bulk RNAseq from patient samples demonstrated clustering of the samples according to high vs low virus levels, and this clustering was recapitulated when interferon-stimulated genes from the smaller GeoMx dataset were analysed, showing high-virus ROIs were enriched for IFN responses. The mixed virus cluster and high virus cluster from the bulk data was associated with EMT and myogenesis

pathways, with the high virus samples also associated with upregulated JAK-STAT signalling [45]. In the protein GeoMx analysis Desai *et al*. found that two patients had elevated expression of the immune checkpoints CTLA4 and PD-L1 in high virus ROIs compared to their low virus ROIs, although these patients did not stand out for immune checkpoint expression by whole-slide IHC, highlighting once again the importance of separating heterogenous tissue data into relevant ROIs to tease out important differences relating to pathological features [45]. The authors also caution the use of BAL fluid from one part of the lung to measure viral loads in patients, given the heterogeneity of viral RNA levels observed in different lung lobes from the same patients.

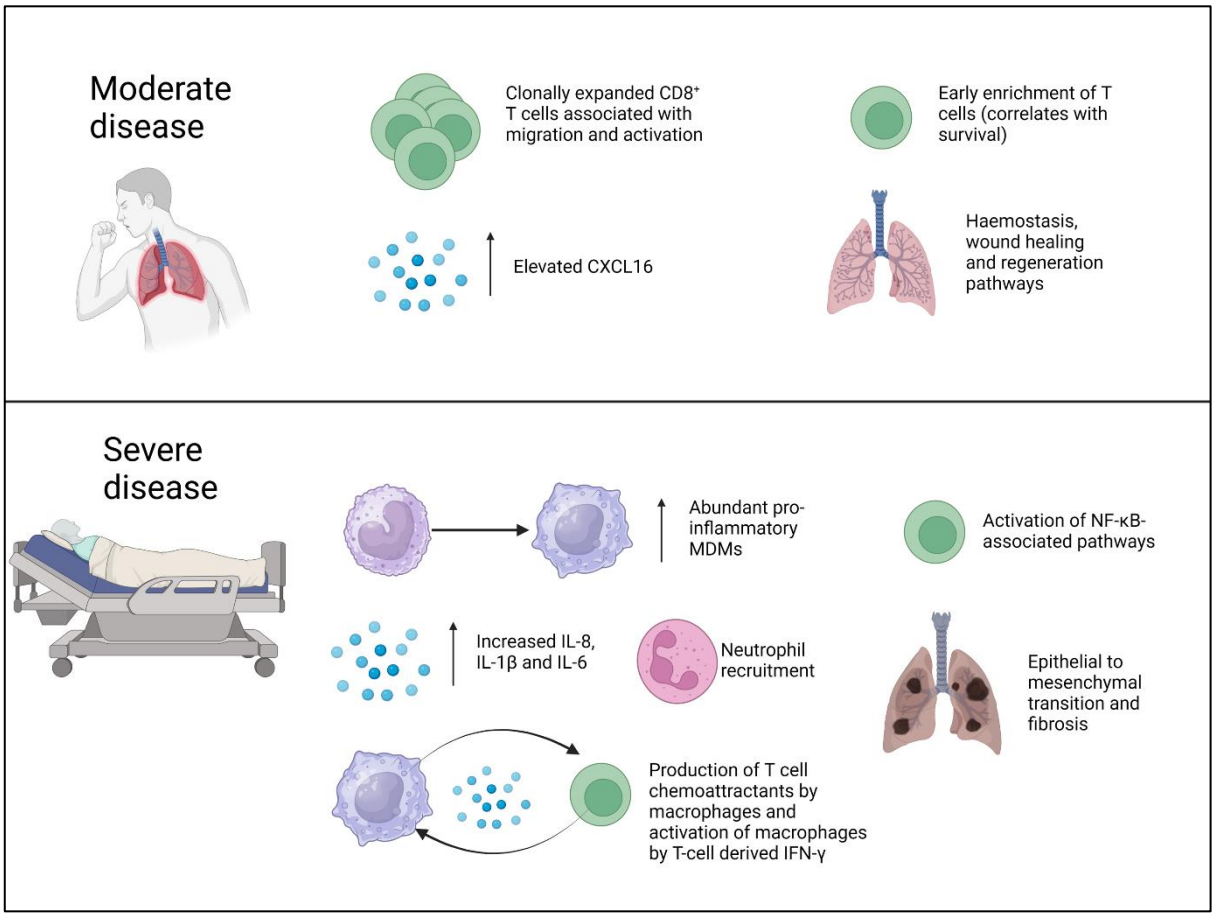

Figure 2: The lung tissue response to SARS-CoV-2 in moderate disease and severe disease. Created with Biorender.com

IMC studies of SARS-CoV-2 post-mortem lung tissue have used high-plex antibody panels to examine a wide range of cell types at single-cell resolution and to draw associations with pathological states [10,29]. Rendeiro *et al*. carried out IMC analysis with a 36-marker panel as well

as their previously-discussed GeoMx analysis [29]. Outside of the phenotypic markers, the authors first noted a significant reduction in the lacunar space of infected lungs, which reduced from 41.1% in healthy lungs to 15.3% in late stage COVID-19, highlighting the vast inflammation and fibrosis associated with COVID-19. Using immune markers Rendeiro *et al*. observed a strong increase in myeloid cell infiltration in COVID-19 patient lungs and the greatest increase was seen in $CD14^{+}CD16^{+}CD206^{+}CD163^{+}CD123^{+}$ interstitial macrophages, particularly in samples from late COVID-19 and these were hypothesised to have been recruited from the periphery [29]. The study also used a larger panel on a subset of patients and found that the alarmin calprotectin (S100A9) was increased in COVID-19 lungs and particularly within neutrophils and macrophages, while alveolar epithelial cells had a more modest increase in calprotectin and increased expression of HLA-DR. Alveolar epithelial cells that were positive for SARS-CoV-2 spike protein demonstrated high levels of the assembled complement membrane attack complex (C5b-C9) and of cleaved caspase 3, particularly in late COVID-19 [29]. The COSMIC study [10], discussed briefly earlier in this chapter, also used IMC to investigate COVID-19 lung pathology, although this study had a greater emphasis on spatial neighbourhood analysis rather than relying exclusively on cell number and phenotype associations. The COSMIC study also looked at the progression of disease by grouping patient samples by histopathology features of alveolitis (ALV), DAD and organising pneumonia (OP) which are consistent with the progression of disease from injury to repair, before carrying out analysis on multiple ROIs per patient [10]. The authors noted an increase in fibroblasts, proliferating endothelial cells, bronchial epithelium and macrophage subsets from the transition from ALV to DAD to OP, consistent with transitions to repair states and differentiation of monocytes to macrophages over the course of the disease [10]. For spatial associations, the authors developed a suite of mathematical tools which included cross-pair correlation functions (cross-PCFs) which consider whether particular cell types are co-located above what would be expected from random spatial association, within a radius of 20μm around each cell. Apart from this, quadrat correlation matrices (QCMs) and an adjacency cell network (ACN) was generated to look at broader spatial associations and to look at cell-cell contact, respectively [10]. With these spatial tools, the authors found that neutrophils adjacent to

$CD8^+$ T cells were increased in all histopathology states and that proliferating alveolar epithelium was most in contact with monocyte-$CD31^+$ clusters and neutrophil-$CD8^+$ T cell clusters in DAD. Immature neutrophils in particular were associated with the neutrophil-$CD8^+$ T cell clusters and these were also often co-localised with the monocyte-$CD31^+$ clusters and proliferating alveolar epithelium, forming a pro-inflammatory network in DAD [10].

Mothes *et al*. combined spatial transcriptomics (with the Visium platform) with electron microscopy, single-nucleus RNA-sequencing and three-dimensional light sheet microscopy (LSM) to examine adventitial niches in COVID-19 lung, with a particular focus on chemokine interactions with their receptors [59]. The authors describe dysregulated crosstalk between immune cells and stromal cells in severe COVID-19 which drives non-resolving inflammation that persists beyond viral clearance. In particular, Mothes *et al*. found that endothelial dysfunction triggers fibrosis and that adventitial microenvironments contain $CCR7^+$ T cells that have phenotypes associated with exhaustion [59]. CCL21 expression was linked with these exhausted T cell subsets and along with CCL18, these chemokines also associated with tissue fibrosis and EMT. The single-nuclear RNA-sequencing data demonstrated that $CD163^+$ macrophages were the source of CCLL18 and LSM data confirmed that tissue density was increased particularly in samples with prolonged COVID-19 (7-15 weeks) [59]. It was also noted in the transcriptomic data that transcriptional signatures of ectopic lymphoid structures were present in a subset of the prolonged COVID-19 lung samples, which was correlated with fibrosis score and activated adventitial niches. Mothes *et al*. hypothesise that these adventitial niches may facilitate the formation of ectopic lymphoid structures [59].

1.3. Respiratory virus immunity and vaccination

Immune cells in tissues can come from peripheral circulation where they are temporarily drawn into the tissue, particularly in the case of an inflammatory stimulus, or they can become tissue-resident, remaining in the tissue long-term. These tissue-resident cells are thought to be important in protection against viruses due to their ability to mount rapid responses at the site of infection, particularly in the case of TRM T cells [60]. Lung-resident $CD4^+$ TRM cells in mice have been

found to provide protection against respiratory viruses [61]. Intranasally-administered live-attenuated influenza vaccine (in clinical use under the name FluMist) in mice has been found to generate protective virus-specific lung $CD4^+$ and $CD8^+$ TRM cells [31], which is interesting considering that this vaccine is cold-adapted to replicate in the nasal mucosa but not in the lung [62] . This study also looked at different routes of administration across vaccine types and found that injection of the live-attenuated vaccine did not generate protective responses and neither did intranasal administration of an inactivated influenza virus, while injection of this inactivated virus did mediate protective responses. The protection mediated by the injected inactivated virus appeared to be mediated by a superior antibody response, although only the intranasal live-attenuated vaccine was cross-protective against multiple influenza strains [31]. This study demonstrates that in order to stimulate virus-specific TRM in the lung, live viruses and intranasal administration may be required. It also highlights the important role of TRM cells in mediating cross-protective responses [31], which has also been highlighted elsewhere [63]. While not looking specifically at tissue-resident populations, evidence has shown that T cell cross-reactivity even to highly-mutated SARS-CoV-2 variants remain as high as 80% when compared with the original strain [64], although their role in protection is difficult to ascertain in human studies and some individuals have poorer cross-reactive T cell responses than others [65]. The proposed mechanism of protection provided by TRM cells, particularly the $CD8^+$ subset, is rapid production of IFN-γ upon infection [66]. TRM cells are thought to be long-lived following their establishment, as these cells have been found to have reduced turnover when compared to circulating memory T cells [67] and their tissue-adapted phenotypes can also be found in human lungs from early childhood [68]. These advantages make TRM induction an attractive vaccine target, particularly against rapidly-evolving respiratory pathogens, which include influenza and SARS-CoV-2. In addition, while intramuscular vaccines against respiratory pathogens such as SARS-CoV-2 have been shown to be effective at protecting against infections in the short term and against severe disease longer-term [69], intramuscular vaccines are thought to confer immunity largely through serum neutralising antibodies [17]. This has also been shown in a study by Caolann Brady *et al.* from our group (manuscript in review). However, recent mucosal booster vaccine studies in non-human primates

(NHPs) have demonstrated that different correlates of protection may exist in airway mucosa compared to the periphery in the context of mucosal immunisation [70–72]. These correlates include nasal IgA, mucosal IgG, T cell responses in BAL and BAL antibody-dependent cellular phagocytosis (ADCP). For intramuscular SARS-CoV-2 vaccines, neutralising antibodies demonstrate waning over time [73] particularly in older populations, even following three doses [74]. Coupled with the emergence of new variants which can blunt the protective efficacy of vaccine-induced antibodies, mucosal TRM-inducing vaccines could become important in preventing severe disease or even infection establishment with respiratory viruses, although they require further development for clinical use. The early activation and retention marker CD69 and αE integrin CD103 are the markers commonly used to differentiate TRM cells from circulating T cells [75]. In mucosal sites such as the lung, both $CD4^+$ and $CD8^+$ TRM cells are enriched for CD103 expression [75]. As CD69 can also be expressed as an early activation marker for T cells, some studies looking at TRM cells in mucosal sites only use CD103 as a TRM marker, although looking at other early activation markers can confirm whether CD69 is acting in response to residency or activation [67]. In the lung, most $CD8^+$ TRM cells express both CD69 and CD103 and a minority express CD69 and not CD103, while the opposite is true for $CD4^+$ TRM cells [67].

Viral vector vaccines induce strong broadly-reactive spike-specific T cell responses as well as neutralising antibodies [76] but it remains to be seen how these T cells function in the lung following challenge and whether any TRM T cells are induced post-infection in this context. Vaccine-induced T cells have recently been demonstrated to respond much more rapidly upon breakthrough infection with SARS-CoV-2 compared to memory B cells [77], which may be particularly important for preventing severe disease when neutralising antibodies wane. As has been reviewed elsewhere, $CD8^+$ T cells have a role in protection from SARS-CoV-2 [78] and T cell depletion studies in rhesus macaques suggest that rapid T cell responses speed up the recovery process and in the context of re-infection, can contribute to protection, in particular when antibody responses are suboptimal [79,80]. For viruses with different circulating strains and variants that can evade neutralising antibody responses, T cells may therefore be very important for broad

protection against these variants. However, these depletion studies could not examine the relative contributions of circulating vs resident T cell populations in mediating protective outcomes. Airway $CD4^+$ T cells have been found to confer cross-reactive protection against SARS-CoV-1 and MERS-CoV in an intranasal vaccine study in humanised mice, mediated by IFN-γ, highlighting the role of T cells in broader protection against respiratory coronaviruses [81].

While intranasal vaccines have been successful in preclinical models for preventing severe disease and reducing nasal and lung viral loads [82,83], there remains a lack of evidence demonstrating their efficacy in humans, despite approvals for vaccines based on intranasal or nebuliser-based delivery in some countries. One of the few examples of published work on this disparity demonstrated a failure to induce consistent mucosal or systemic antibody responses by an intranasal viral vector vaccine [84], despite success in preclinical models [82]. The authors hypothesised several reasons for the failure in humans compared to animal models, including poor infectivity of the vector for human respiratory epithelium, lower dose and variable biodistribution of the vaccine between animal models and humans owing to differences in airway structures. Other mucosal viral vectors, which were highly successful in NHPs [71,72], may have better airway tropism. However, another potential explanation is the effect of previous antigen exposure at mucosal surfaces through infection, which may lead to the generation of a non-sterilising tissue-resident response which cannot be overcome by subsequent vaccination. As previously discussed, infection or vaccination with live virus generates TRM responses [18,31]. Given the widespread nature of SARS-CoV-2 spread, previous exposure is a confounding variable that is very difficult to control for in human studies and may explain the high efficacy of mucosal vaccines demonstrated in animal models, as animals in these experiments have not typically been exposed to the virus previously. Until mucosal vaccine studies are carried out in previously-exposed animal models, the hypothesis that previous exposure blunts mucosal vaccine efficacy cannot be tested. TRM cells have been found in the nasal mucosa of individuals vaccinated with an intramuscular SARS-CoV-2 vaccine and subsequently exposed to infection [18] and a study of BAL fluid demonstrates that antigen-specific T cells can persist in the lung mucosa

after vaccination and infection, although their numbers begin to decline over time [55]. The ability for lung TRM induced in the lung parenchyma by a combination of intramuscular vaccination and virus exposure to protect against pathology upon infection or re-infection cannot be easily determined in humans and may require animal tissue studies. It is known that exposure to the virus induces TRM in human lung tissue (among other tissues) as discussed previously [41] but the impact of vaccination on this population and the roles of TRM cells in protection or exacerbation of respiratory pathology remain unknown.

1.4. The use of animal models to answer outstanding questions about the lung tissue response to COVID-19

While much has been learned about human COVID-19 pathology from the various approaches described above, there are many confounding factors that make human studies very difficult to standardise. These include (but are not limited to) different initial viral loads, unknown timepoints of infection and different treatment strategies for patients, which themselves are administered at different timepoints post-infection and may impact resulting lung pathology. While human challenge studies have recently been able to overcome some of these confounding factors [14], they are limited to studying immune responses in the periphery and cannot extensively examine lung tissue responses. Despite all of the confounding factors, studies of post-mortem human lung tissue have provided credible mechanistic insights into the immune mechanisms driving the most severe lung pathology, which ultimately results in death. By examining less inflamed regions of the lungs of these patients, other groups have hypothesised mechanisms driving the evolution of pathology from early stages of infection to later stages, which involve resolution of inflammation, fibrosis and repair [10,29,59]. These single ‘snapshots’ of post-mortem lung tissue allow us to infer what processes may be involved in driving the most severe infections. However, asymptomatic mild to moderate infections make up the vast majority of human infections [85], with the most severe cases being associated with factors such as greater age [86]. Macaque models of SARS-CoV-2 reflect this mild to moderate pathology [87] while aged baboons demonstrate a more severe pathology [88], as older humans do and aged macaques demonstrate poorer immune responses and

prolonged viral shedding when compared to younger macaques [88,89]. However, the use of aged animals remains an uncommon practice. Due to all the confounding factors associated with human studies, animal models are required for in-depth, standardised tissue studies of respiratory virus infections and in particular for studying how vaccination alters the lung response. This is because animals in a study can all be vaccinated (in the case of vaccine studies) and challenged at the same timepoints with equal doses of virus and different endpoints can be investigated depending on the study. Some animal studies have different endpoints, particularly when infection is not lethal, so different stages of tissue pathology post-infection may be interrogated depending on the endpoints chosen. Comparative pathology studies are therefore most robust when animal models are used. As previously mentioned, mucosal vaccine studies in previously-exposed animals could also help to evaluate the ability of previous exposure to prime mucosal responses and explain whether this hampers mucosal vaccine efficacy. Animal models can also be useful to determine correlates of protection for SARS-CoV-2 [90]. Many human studies rely primarily on peripheral sampling and therefore miss out on the immune responses of important mucosal sites such as the lung [91]. Currently, in the absence of deep, standardised tissue profiling in both humans and animal models, binding and neutralising antibodies consistently emerge as the best candidates for these correlates of protection [91], apart from in the context of mucosal vaccination with sampling carried out in BAL and nasal washes [70–72].

Vaccination has had a massive impact on global mortality from COVID-19 [92] and yet the impact of vaccination on the lung tissue immune environment remains poorly understood. It is well-known that vaccines are highly protective but what we know about the changes in lung immunity following vaccination (and subsequent infection) stem primarily from studies in peripheral blood, which likely correlate with tissue responses but are unlikely to capture the whole picture (see **Section 1.1**). Studies of BAL fluid from vaccinated people can give some insights into the lung response, as previously discussed [55,56] but will only retrieve cells from the surface of the airways rather than the deeper tissue. As well as this, peripheral blood and BAL studies lack the aforementioned spatial context which may be important for understanding pathology and

protection in the lung. Prior to clinical trials, SARS-CoV-2 vaccines were tested in both small and large animal models and were evaluated for safety and efficacy. In terms of efficacy, these studies typically investigate lung histopathology (primarily through haematoxylin and eosin (H&E) staining for annotation of pathological features and viral antigen staining), antibody responses (by enzyme-linked immunosorbent assay (ELISA) and neutralisation assays) and T cell responses (by enzyme-linked immunosorbent spot (ELISpot)). The information garnered from these studies is enough to evaluate safety and sheds light on potential mechanisms of protective efficacy, paving the way for human trials. However, multi-omic tissue studies are very rarely carried out on tissue samples from animal studies, despite their highly-standardised nature meaning that they often have fewer confounding variables. This may be due in part to the expense associated with these technologies. Large animal models, such as NHPs are much more comparable to humans and so mechanistic insights from tissue investigations could be applicable to human disease. However, differences in the immune markers between NHPs and humans must be considered, particularly when characterising cell types and subsets, as characteristic marker expression can vary between species [93]. Other models, such as the Syrian hamster model, are better at recapitulating the severity of pathology seen in more severe human cases, although this comes with the caveat of being much less similar to humans in many other ways when compared to the rhesus macaque model [94,95]. Mild disease in rhesus macaque SARS-CoV-2 infections have demonstrated that virus-specific T cells become detectable in BAL from day 7 to 10 after the decline of IFN-activated myeloid cells and lung inflammation [96]. At this time, virus-specific T cells could not be detected in the upper airways. Nelson *et al*. suggested therefore that the mild disease in the rhesus macaque model is associated with restriction of viral replication by innate immune mechanisms, before antigen-specific T cells arrive in the lung and begin to upregulate tissue residency markers [96]. It remains unknown whether adaptive immune cells have more of a role to play in resolution of mild disease in this model in the context of previous vaccination, or whether the added protection from vaccination is conferred primarily through circulating antibodies from the periphery.

Animal models allow us to control for most of the factors that are variables in human studies, which means we can look at the impact of vaccination and challenge on tissue, examine how mild to moderate disease manifests, as well as how multiple challenges impact tissue responses, all with defined timepoints and doses of virus. Re-challenge SARS-CoV-2 studies in macaques demonstrated that previous challenge provided at least short-term protection against re-infection with the same variant, which was important information early in the pandemic [97,98]. Many methods that can be carried out on intact tissue samples also work when the tissue is formalin-fixed paraffin-embedded (FFPE), although for imaging in particular, the modification of antigens by formalin fixation can cause difficulties when it comes to targeted staining with antibodies. As FFPE samples are stable for long periods of time, older studies for which there is no fresh or frozen material available can still provide valuable insights into understanding tissue immunology. Tissues from infection studies must be formalin-fixed for safety. As well as the many standardised factors, animal studies may also allow for higher sample numbers than human studies that look at tissue, as retrieving human tissue can be very difficult. These low sample numbers from human studies therefore result in poorer statistical power in their analyses. For instance, two spatial transcriptomic studies of post-mortem human lungs have n = 10 and n = 3 COVID-19 samples respectively (these studies also had additional control tissues) [29,30] and the COSMIC study had n =12 post-mortem COVID-19 lung samples for tissue imaging (n =4 from each pathology grouping), as well as n = 2 control tissues [10]. By combining standardised animal studies, many more tissues could be analysed and therefore much higher sample numbers could be achieved. Carrying out spatial-omic lung tissue parenchyma studies on SARS-CoV-2 preclinical samples may also have the added benefit of providing insights into how well particular animal models, such as the rhesus macaque, recapitulate the severe pathology found in the various human tissue studies, how mild to moderate pathology compares and how vaccination changes this response locally. This could be very useful particularly in the context of vaccine and therapeutic evaluation for SARS-CoV-2 and other coronaviruses. As macaque models are normally a final-stage animal model before clinical testing, characterising the immune responses

and pathology in this animal should be prioritised, particularly with the wealth of sample material generated from the worldwide efforts against SARS-CoV-2.

1.5. Background on Vaccine-Associated Enhanced Disease

This section of the thesis is adapted from a published review article entitled 'Vaccine-Associated Enhanced Disease and Pathogenic Human Coronaviruses' of which I am the first author [99].

Vaccine-associated enhanced disease (VAED) occurs when vaccination promotes responses that worsen disease when the subject is subsequently infected with the pathogen being vaccinated against [100]. VAED has been observed in humans following vaccination against dengue virus, respiratory syncytial virus (RSV) and measles virus [101–103]. At the beginning of the SARS-CoV-2 pandemic there were concerns that vaccines developed against this virus could promote VAED [104,105], based on preclinical SARS-CoV-1 and MERS-CoV vaccine studies in mice and NHPs that appeared to demonstrate VAED. We have published a review article which describes known and theoretical mechanisms of VAED (**Figure 3**), with a focus on pathogenic coronaviruses and in particular how these mechanisms may or may not apply to SARS-CoV-2 [99]. In this review we also discussed problems with previous preclinical VAED studies, including poor interpretation of histopathological data and how contaminants in preclinical vaccine and challenge material may explain some supposed VAED observations, as described by Shaw *et al*. in the context of RSV [106].

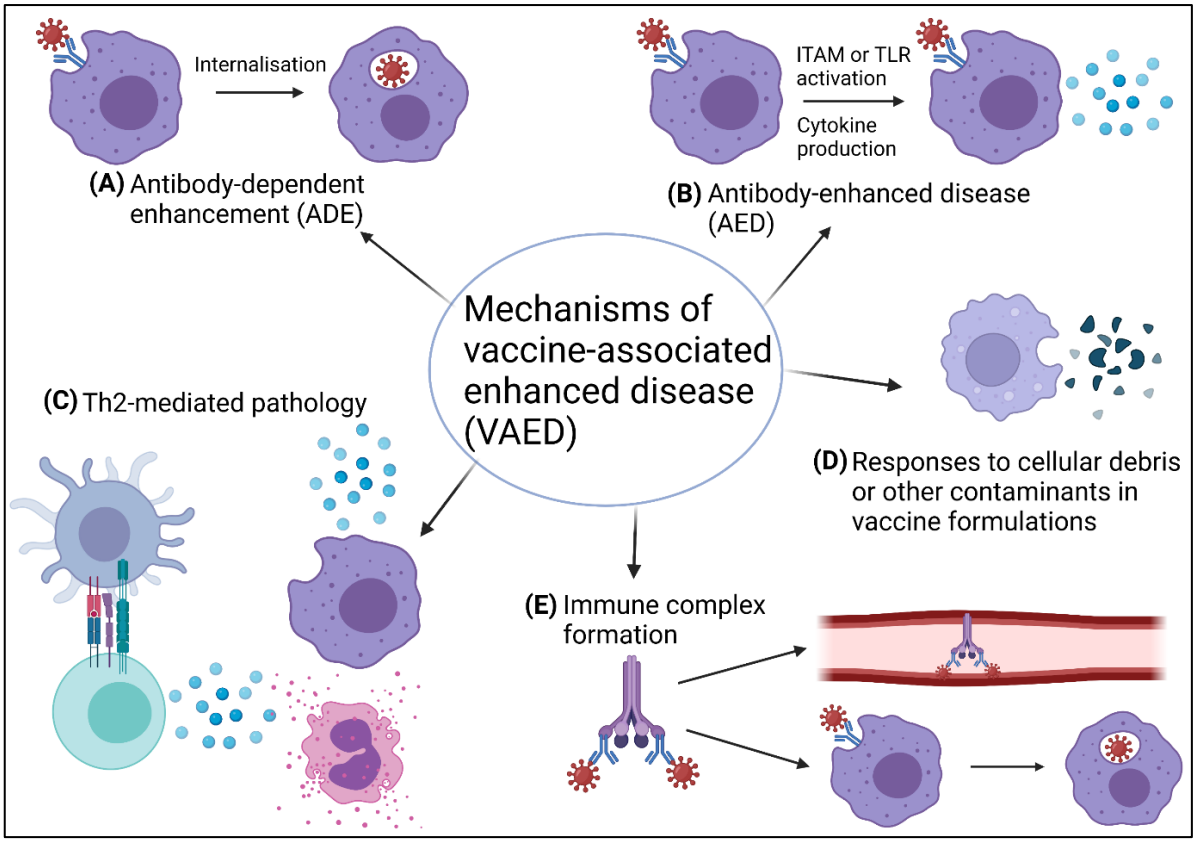

Figure 3: Mechanisms of vaccine-associated enhanced disease. (A) Antibody-dependent enhancement (ADE) occurs when antibodies increase the ability of a virus to infect cells (also see **Figure 4**). (B) Antibody-enhanced disease (AED) occurs when antibodies exacerbate inflammation, resulting in pathology (also see **Figure 4**). (C) Th2-skewed responses can be pathogenic for some infections and so vaccines that induce Th2 responses in this case can cause pathology. Usually Th2 pathology is associated with eosinophil infiltration. (D) Components of vaccine formulations such as bovine serum albumin (BSA) and cellular debris can mediate pathogenic cellular responses to these components when encountered again as contaminants in the challenge material. While these components are normally removed during vaccine preparation, some preclinical studies have not included appropriate washing and centrifugation steps to facilitate this. (E) Immune complexes between viral proteins, antibodies and/or complement can lead to a build-up of deposits in blood vessels and organs or facilitate enhanced uptake of virus through myeloid cells, causing ADE. Both of these outcomes can enhance pathology. Created with BioRender.com. Taken from review [99].

Defining VAED can be quite difficult, as VAED must be distinguished from vaccine failure. VAED means that vaccination induces immune responses that are later detrimental upon infection

with the pathogen in question. Vaccine failure means that the vaccine failed to induce an immune response or did not induce an immune response of a high enough magnitude to make a difference to the course of infection. Therefore, in order to distinguish VAED from vaccine failure, one must understand the pathogenesis of the virus in question in unvaccinated cases and be able to compare vaccine + challenge pathogenesis to this, to see if there is an observable difference. Much research has been done on the pathogenesis of SARS-CoV-2 both in humans and in animal models such as rhesus macaques, in both vaccinated and unvaccinated contexts. However, while the mechanisms of protection provided by approved vaccines are relatively well understood [107], the reasons for the lack of protection (or potential disease enhancement) by unsuccessful vaccine candidates is not. This may be because candidates that are protective in preclinical studies are often studied in much further detail (both preclinically and clinically) so that these candidates can be approved for clinical use. The associated costs involved mean that vaccine manufacturers may opt for another vaccine platform or drop out of a vaccine race rather than invest in deconvoluting the immune responses induced by an unsuccessful candidate. Therefore, it is unknown whether pathological outcomes in animals that received some of the vaccine candidates can be attributed to vaccine failure or to VAED. This is an important question to answer for SARS-CoV-2 vaccines, particularly in the context of; emerging variants that partially evade humoral immunity induced by approved vaccine candidates, understanding the risk of VAED for vaccines against other coronaviruses (including those that may spill over to humans in the future) and to understand VAED in a broader context so that concerns can be investigated appropriately and delays to vaccine development can be avoided [105].

Antibody dependent enhancement (ADE) occurs when the rate of viral infection increases in the presence of antibody against the virus, usually through enhanced uptake of virus into myeloid cells through Fc gamma receptors (FcγRs) followed by productive infection and viral dissemination after the death of the host cell. Observations of increased uptake of virus into myeloid cells alone is therefore not grounds for ADE. Antibody-enhanced disease (AED) on the other hand occurs when antibodies bound to a virus also bind to FcγRs of myeloid cells and

increase inflammation, through cytokine production, to such an extent as to cause immunopathology. AED can occur following activation of immunoreceptor tyrosine-based activation motifs (ITAMs) through FcγRs [108], or activation of endosomal toll-like receptors (TLRs) following antibody-mediated uptake of virus. In my review article, I defined ADE and AED separately in this way (**Figure 4**) [99], to distinguish the antibody-dependent phenomenon that increases infectious virus titres (seen in dengue virus) from another antibody-dependent phenomenon hypothesised to mediate inflammation during infection with viruses such as SARS-CoV-2 [109,110].

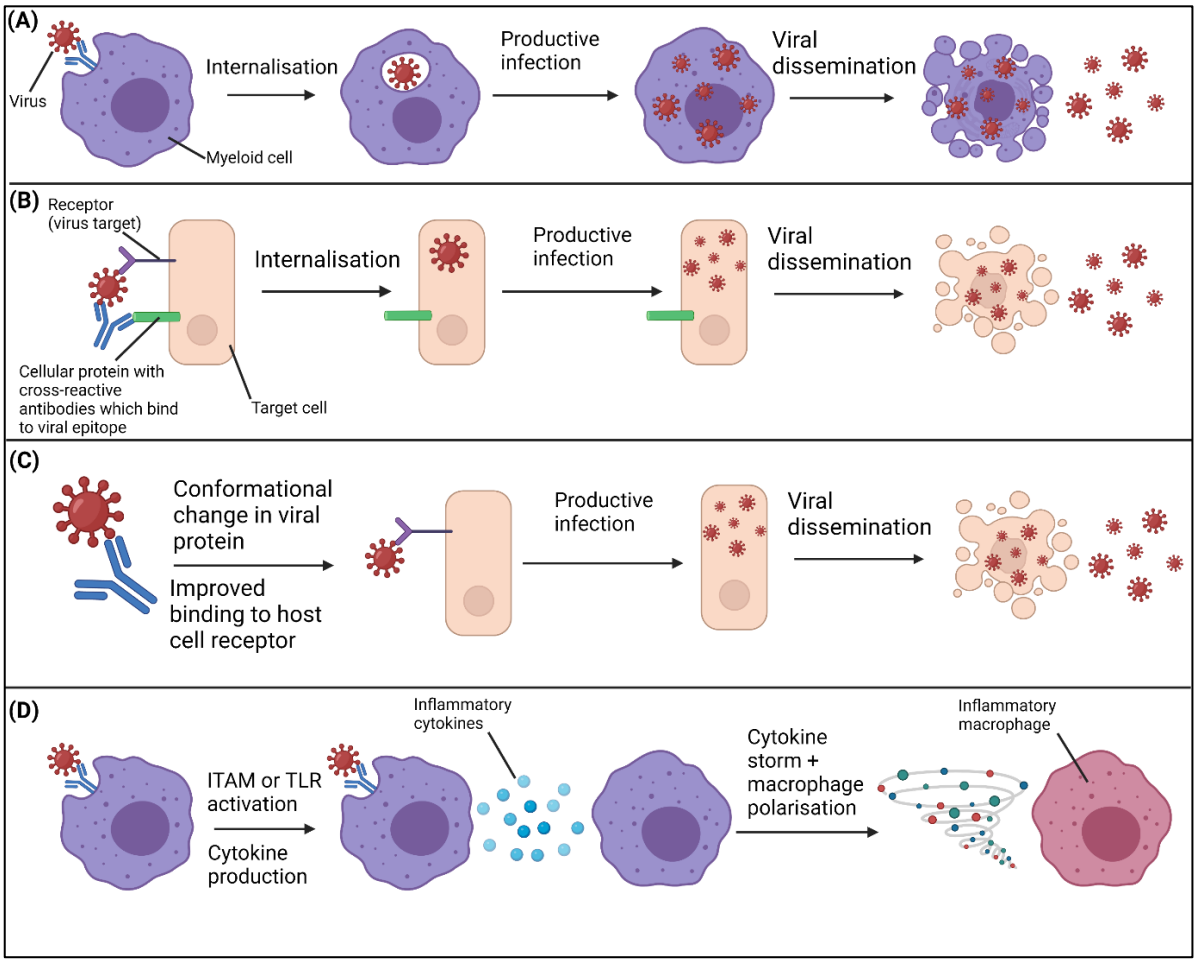

Figure 4: Overview of antibody-dependent enhancement (ADE) and antibody-enhanced disease (AED). (A) Non-neutralising antibodies or sub-neutralising antibody concentrations bind to viruses and interact with Fc receptors on myeloid cells. This facilitates the internalisation of viruses. Viruses that can productively infect myeloid cells can proliferate and spread following their uptake, enhancing infection. This is a form of ADE. **(B)** Cross-reactive antibodies bind to both virus and host cell components,

bringing viruses in close contact with their receptor. Receptor-mediated uptake and enhanced infection follows. This is another form of ADE. **(C)** Antibodies against a particular epitope drive a conformational change in a viral protein which enhances infection through improved binding to the host cell receptor. This is another form of ADE. **(D)** Antibodies bound to virus interact with Fc receptors on myeloid cells and either activate immunoreceptor tyrosine-based activation motifs (ITAMs) associated with these receptors, or facilitate viral uptake and subsequent activation of endosomal toll-like receptors (TLRs). Through either of these mechanisms, inflammatory cytokines and chemokines are produced, exacerbating inflammation to a pathogenic extent and polarising myeloid cells towards more inflammatory phenotypes. These are forms of AED. Productive infection of myeloid cells is not required for this mechanism. Created with BioRender.com. Taken from review [99].

In order to prevent the induction of poorly-neutralising antibodies, vaccines must express neutralising epitopes in their appropriate conformations. Poorly-neutralising antibodies can bind virus but may not neutralise the virus, meaning only the Fc-mediated effector functions of antibodies remain. Fc-mediated effector functions can be protective through ADCP, complement-dependent cytotoxicity (CDC) or antibody-dependent cellular cytotoxicity (ADCC) [111]. However, Fc-mediated effector functions of antibodies can also cause enhanced pathology through ADE or AED [99]. The tropism of the virus in question along with the balance between the engagement of different types of FcγRs, both activating and inhibitory, is what determines the protective or pathogenic outcome. The strength of antibody binding to different FcγRs therefore also has an impact and antibody fucosylation can influence this, with afucosylation of antibodies associating with pathology in dengue virus and SARS-CoV-2 infection [112,113].

ADE in dengue virus infection is thought to be mediated by sub-neutralising antibodies, and this phenomenon is dependent both on antibody titre and neutralisation capacity [114,115]. This means that at a particular range of poorly-neutralising antibody titres, antibodies become pathogenic due to ADE outweighing protective mechanisms conferred by higher titres and the lack of any effect from low titres [114]. However, dengue virus is a rare case among viruses that leads to this mechanism, as it can productively infect myeloid cells (which can be enhanced by antibodies through ADE) and has multiple serotypes, meaning protective antibodies generated against one

serotype may be sub-neutralising for another [116]. ADE is thought to have contributed to VAED observed in the clinical use of a dengue virus vaccine, which is now only approved for use in seropositive individuals [101]. However, while dengue virus is a rare case, the lessons learned around ADE in dengue virus infection and vaccination can be applied to other viruses, including those that do not infect myeloid cells. In other viruses, sub-neutralising antibodies may be pathogenic due to AED rather than ADE. Formalin inactivation has been hypothesised to potentially induce suboptimal antibody responses by altering antigen structure through cross-linking [117], which could theoretically cause VAED through ADE or AED. Additionally, formalin inactivation has also been hypothesised to sometimes cause VAED by creating carbonyl groups on vaccine antigens, which can later stimulate Th2-biased responses in response to challenge, as demonstrated in RSV [118]. Non-neutralising or sub-neutralising antibodies can also promote immune complex formation, which contributes to VAED in RSV [119].

Re-challenge studies can be important for dissecting potential mechanisms for VAED. If more enhanced pathology is observed upon re-challenge than initial challenge, then something about the immune response upon re-exposure is to blame. This implies that the pathogen in question naturally induces a response that is later detrimental upon recall. Where this is the case, such as in exposure to different serotypes of dengue virus, VAED can often be explained by the vaccine inducing a response that is similar to that induced naturally upon first exposure to the pathogen. This means that the enhanced pathology observed upon re-challenge is instead seen upon first exposure to the pathogen in previously seronegative individuals that are vaccinated with a vaccine that has the potential to induce VAED, and this is indeed the case in dengue virus [101]. In most cases however, re-exposure to a pathogen does not confer enhanced pathology, as immune memory tends to be more protective than detrimental. Therefore, for most pathogens, any enhanced pathology (over what would be expected from seronegative exposure) observed following vaccination and subsequent challenge can be attributed specifically to an immune response induced by the vaccine, implying that the vaccine response differs from that induced by natural infection.

Feline infectious peritonitis virus (FIPV) is a coronavirus that infects cats [120] and can productively infect macrophages through ADE [121], which is observed upon re-exposure [122]. Some vaccine candidates for FIPV have caused VAED [123], hypothesised to be through the same mechanism. However, FIPV is quite a unique case, as this severe pathogenesis mediated by ADE begins to arise following the mutation of the FIPV spike protein within the host, specifically a mutation that confers the ability to infect macrophages [124]. In human coronavirus infections, antibodies are thought to mostly have a protective role [107,125]. Some of the preclinical vaccine studies for MERS-CoV and SARS-CoV-1 demonstrated potential signs of VAED and study authors have hypothesised enhancement mechanisms such as ADE and AED through non-neutralising antibody responses, which I have reviewed [99]. Whether or not the pathology noted in these studies can be truly characterised as VAED is up for debate, as some of the histopathology data is quite poor [99].

1.6. VAED and SARS-CoV-2

This section of the thesis is also adapted from a published review article entitled 'Vaccine-Associated Enhanced Disease and Pathogenic Human Coronaviruses' of which I am the first author [99].

There are several licenced vaccine candidates against SARS-CoV-2 that provide robust protection from severe disease, despite the emergence of immune-evading variants. However, for some vaccine candidates that did not proceed beyond the preclinical stage, it is unclear whether they may have had the capacity to induce VAED. ADE does not apply to SARS-CoV-2, as the virus does not productively infect myeloid cells [126,127]. While SARS-CoV-2 can infect and replicate within monocytes and macrophages, these infections are abortive [109,126]. Immune complex formation has been implicated in COVID-19 pathogenesis [128], however this phenomenon has not been observed in a VAED context in preclinical or clinical vaccine settings upon challenge or infection respectively. In SARS-CoV-2, if VAED is to be observed, the most likely immune mechanisms governing disease enhancement are AED and Th2-biased responses [99], although

neither of these mechanisms have been observed in the context of re-challenge, which is instead protective [97,98].

Formalin inactivation of viruses can alter the structure of their antigens, as discussed previously. **Figure 5** demonstrates how altering antigens could theoretically impact neutralising activity. In SARS-CoV-2 it has been proposed that formaldehyde fixation secures about half of the spike trimers in an RBD-down conformation and the other half in an RBD-up conformation, which means that the neutralising epitopes of the RBD are only available on half of the spike trimers [117]. This has been proposed to explain reduced immunogenicity and could theoretically lead to ADE/AED [99], although a formalin-inactivated vaccine formulated with alhydrogel did not exhibit any clear signs of VAED in NHPs, it may have induced transient enhanced pathology in ferrets [117]. By looking in more detail at the NHP samples from this study, the risks of VAED from this vaccine will be investigated in more detail in this thesis. A study using the same vaccine preparation in Syrian hamsters, a model of severe COVID-19 [94,95], found no enhancement of disease and protective effects could even be noted if the vaccine was given sub-optimally – either just before or shortly after viral challenge [129]. At such timepoints, the hypothesised poorly-neutralising antibody responses generated by such a vaccine formulation would also be present at sub-neutralising concentrations. This would make VAED more likely in theory, although this was not observed [129]. In mouse models, VAED has been observed in an alum-adjuvanted inactivated SARS-CoV-2 vaccine upon heterologous challenge with a bat-derived coronavirus [130]. In this case, VAED was dependent on the alum adjuvant and was attributed mostly to Th2 responses from $CD4^+$ T cells, rather than an antibody-dependent mechanism, as serum transfer led to only modest changes in pathological outcome in the lung.

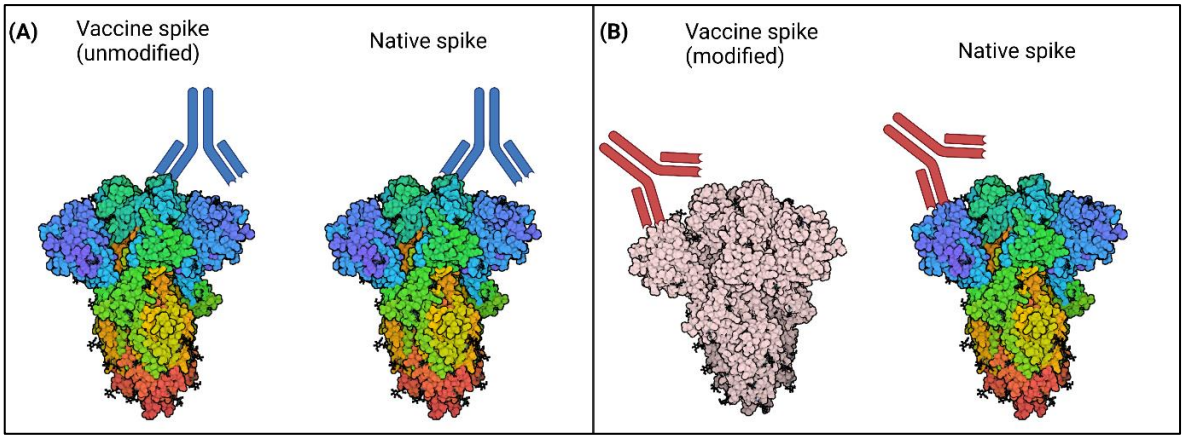

Figure 5: How modification of the spike protein could impact neutralising activity. **(A)** Native spike: Antibodies are generated against a neutralising epitope on the vaccine-derived spike protein, which closely represents the neutralising epitope found on circulating virus. As a result, neutralising activity against the vaccine-derived spike corresponds to neutralisation of circulating virus. **(B)** Modified spike: Antibody responses may be generated against a modified epitope, which no longer represents a neutralising epitope on circulating virus. As a result, antibodies produced in response to native spike may be sub-neutralising or non-neutralising and may contribute to VAED. Spike protein structure accessed through Protein Data Bank, PBD entry 6VXX [131]. Created with BioRender.com. Taken from review [99].

Antibodies from patients with more severe COVID-19 are observed having lower fucosylation in their Fc domains, conferring an increased affinity for an activatory Fc receptor CD16 (also known as FcγRIIIa) [113]. An AED mechanism has been described which may partially explain pathology in severe COVID-19 patients [109,110]. Together, these papers demonstrate that CD16 can mediate uptake of antibody-opsonised SARS-CoV-2 virus into monocytes and macrophages, which leads to activation of the NLRP3 and AIM2 inflammasomes, caspase-1 and gasdermin-D, followed by pyroptotic cell death. This is highly inflammatory, coinciding with release of IL-1 and IL-18 [109,110]. A humanised mouse model demonstrated that inhibition of the NLRP3 inflammasome could reverse chronic lung pathology mediated by AED but led to the release of infectious virus by infected macrophages [110]. This indicates that activated NLRP3 inflammasomes may prevent myeloid cells from being productively infected (and the ADE mechanism as seen in dengue virus), but the activated inflammasomes also cause the inflammatory pathology associated with COVID-19. However, only antibodies from severe COVID-19 patients could mediate enhanced

uptake of antibody-opsonised virus by monocytes and macrophages, contributing to this inflammatory cascade. Antibodies from individuals fully vaccinated with the Pfizer-BioNtech mRNA vaccine did not promote infection. However, the AED mechanism seen in severe patients demonstrates a theoretical AED mechanism of VAED for SARS-CoV-2, if a vaccine were to induce such antibodies. Evidence of VAED has been observed in a Th2-biased vaccine with de-folded spike delivered subcutaneously in the Syrian hamster model [132]. This VAED is associated with Th2 immune responses, exaggerated pneumonia, eosinophilic infiltration and reduced viral load. The reduced viral load is important to consider, since viral load reductions are often used as a marker of protective outcomes in preclinical vaccine studies, so this highlights the importance studying tissue to determine whether an intervention is protective or not, rather than assuming lower viral loads always correlate with reduced pathology. Interestingly, a role for antibodies was also hypothesised in this VAED, with single-cell sequencing data suggesting CCL-11 and IL-19 secretion by lung macrophages upon Fc-mediated viral uptake, which may have contributed to Th2 skewing [132]. Antibodies induced by this vaccine preparation bound spike protein but were present at low levels and were non-protective. It was previously found that this preparation also does not induce antigen-specific $CD8^+$ T cell killing activity [133]. The same group that demonstrated VAED in the Th2-biased vaccine with de-folded spike have recently shown that their outbred Syrian hamster model does not show any signs of VAED when vaccinated with licenced SARS-CoV-2 vaccines [134].

1.7. Preclinical vaccine studies at UKHSA Porton Down

For this project, we have access to samples from a variety of preclinical SARS-CoV-2 vaccine studies carried out at UK Health Security Agency (UKHSA, formerly Public Health England) Porton Down [117,135–137], as well as from a re-challenge study (manuscript in preparation). **Supplementary Table 1** contains information on the NHPs involved in these studies. The vaccine candidates include a variety of vaccine platforms such as a DNA vaccine (INO-4800) [135], RNA vaccine (CVnCoV) [136], viral vector vaccine (ChAdOx1) [137] and a formalin-inactivated vaccine (FIV) [117] formulated with alhydrogel. Of these candidates, only the viral vector was later

licenced for clinical use. It became the most widely-used vaccine against SARS-CoV-2 globally and has been highly effective in reducing disease burden, making this vaccine a useful control for a protective vaccine that does not induce VAED. The FIV vaccine on the other hand was designed to evaluate whether VAED would be a concern with SARS-CoV-2 [117], as some FIV candidates appeared to demonstrate the phenomenon in preclinical models for MERS-CoV and SARS-CoV-1 vaccines [99]. However, as previously discussed, this FIV candidate did not appear to induce VAED in NHPs [117]. The DNA, RNA and viral vector vaccines encode spike protein, which should be expressed in its native form given it is translated in mammalian cells upon vaccination. The FIV vaccine on the other hand is made up of whole inactivated virus and will therefore display a much wider variety of epitopes, many more of which will be non-neutralising. In the DNA vaccine study, vaccinated animals were given either one or two doses (booster dose given 28 days after the prime dose) and in the mRNA vaccine study, vaccinated animals were given either a high dose or low dose. Animals vaccinated with FIV or the viral vector were each given one dose. All of the animals across the vaccine studies were challenged with the same dose of virus (1 ml of Victoria/1/2020 SARS-CoV-2 at 5×10^6 plaque-forming units (PFU)) both intranasally (2ml) and intratracheally (1ml), 28 days after their final dose of vaccination, apart from the FIV-vaccinated animals, which were challenged 14 days post-vaccination. The re-challenged animals were administered their second dose of the virus 28 days after their first dose.

Histopathology scores were assigned to each animal based on a scoring system devised by veterinary pathologist Dr Javier Salguero at UKHSA and colleagues [87]. In this study, Fergus Gleeson, a clinical thoracic radiologist, also examined CT scans of two cynomolgus and two rhesus macaques 18 days post-challenge, where pulmonary abnormalities and ground glass opacity were noted in both cynomolgus and one rhesus macaque. These features were noted to be reminiscent of some of the pathological features of human COVID-19 disease.

Much work has already been carried out on these NHP samples [117,135–137], although there is much more to learn from the remaining material in order to determine whether any of the high-pathology animals experienced VAED, or if they simply failed to generate a sufficient immune

response following vaccination. Most of the analysis of the immune response has been confined to the periphery, the lung tissue responses have not been studied in-depth, which may give insights into potential VAED or how some vaccines induced better protective responses in the lung than others. All of the NHPs in the DNA vaccine, mRNA vaccine, FIV vaccine and re-challenge studies were culled at day 6-8 post challenge (day 62-64 overall), at which point only a low level of virus remains in the lung tissue [117,135,136]. In the viral vector vaccine study, four NHPs (17Z, 29Z, 22Z and 24Z) were culled at day 6 or 7 post-challenge, while 8 NHPs (13Z, 45Z, 26Z, 36Z, 31Z, 4Z, 18Z and 53Z) were culled at day 13, 14 or 15 post-challenge (**Supplementary Table 1**). The NHPs culled at a later timepoint exhibited lower levels of virus in the tissue and had resolved pathology to a greater extent [137]. For the purpose of our study, we will only focus on animals culled at day 6 or 7 post challenge, so that we have samples that are directly comparable.

Each of the NHPs across these studies have been assigned lung histopathology scores (**Figure 6**) according to the aforementioned scoring system developed by Salguero *et al*. which allows for the quantification of pathology owing to the presence of particular pathological features [87]. Unlike many other preclinical vaccine studies, this allows for a clearer distinction between degrees of disease severity without relying on interpretations of qualitative descriptions or the assumption that reduced viral loads correlate with reduced pathology (which, as discussed, is not always the case). Interestingly, one of the NHPs in the one-dose DNA vaccine group had a higher pathology score than any other NHPs across all of the studies at Porton Down, including unvaccinated controls [135]. Teasing out whether the vaccine failed or induced VAED in this animal could shed light on the use of this platform and its delivery mechanism (electroporation) in future vaccines. However, as discussed earlier, it is important to note that the rhesus macaque is an animal model that typically exhibits mild-moderate pathology rather than severe pathology [87], which is a potential limitation of this work. The macaques do not progress to organised pneumonia which is associated with a repair state in humans and has been observed in post-mortem lung tissue from patients who had longer hospital stays and were mechanically ventilated for longer [10]. The

previous data from all of these studies has been used by another DPhil student in the group to model post-vaccination correlates of protection in the serum (*Brady et al*, manuscript in review). In this paper, a cut-off histopathology score of 6.5 was used to classify animals into 'protected' (histopathology score below 6.5) or 'pathology' (histopathology score above or equal to 6.5). Similarly, virus level detected in the lower respiratory tract (measured in BAL) was classified into 'high' and 'low' categories. We use both of these categories in this thesis to stratify results.

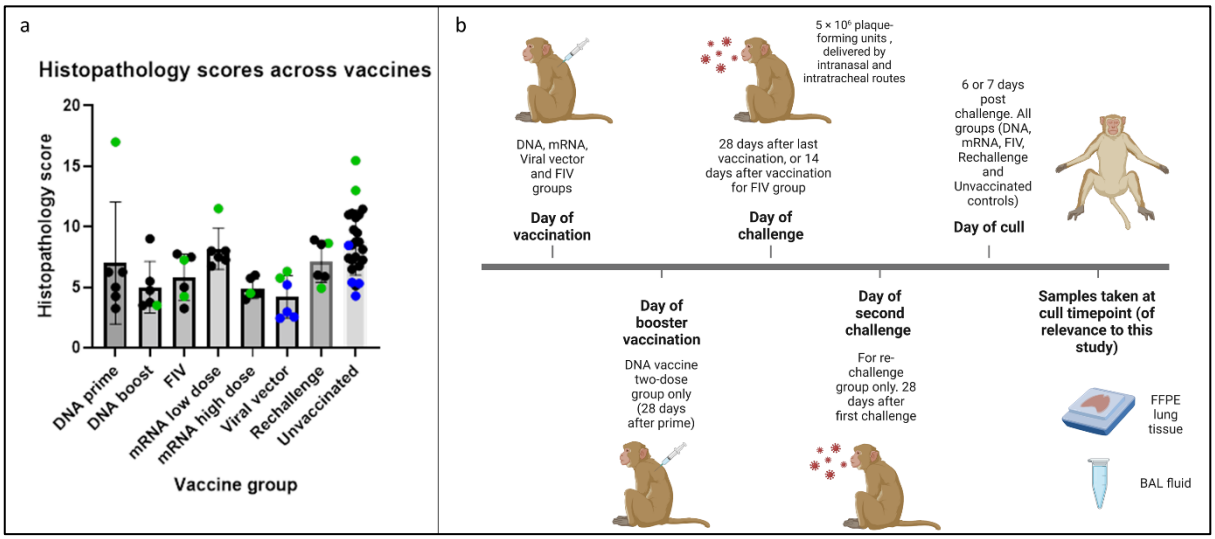

Figure 6: Overview of rhesus macaque vaccine studies conducted at Porton Down. a. Summary of histopathology scores across groups. Black dots: Animals culled at day 6-8. Blue dots: Animals culled at day 13/14. Green dots: Samples of interest. **b.** Timeline of rhesus macaque studies. Figure generated using data from studies conducted at Porton Down [117,135–137]. Created with Biorender.com.

1.8. Thesis aims

The central hypothesis of this thesis is that peripheral vaccination can alter the response of the lung tissue parenchyma upon SARS-CoV-2 challenge by inducing protective immune responses that make their way to the lung. The peripheral responses to vaccination have already been studied extensively in humans and in animal models, but for reasons outlined earlier in this chapter, the lung tissue response in humans has not been studied in its native spatial context post-challenge, as these samples cannot be retrieved. We use the rhesus macaque model to investigate this hypothesis. An alternative hypothesis is that vaccination may lead to enhanced pathology through

VAED [99], in cases where vaccinated animals had high histopathology scores (**Figure 6**). To study these questions, we use a combination of *ex vivo* techniques to study lung tissue and BAL fluid from rhesus macaques involved in SARS-CoV-2 preclinical studies carried out at UKHSA Porton Down. Apart from the central hypothesis, we also aim to carry out exploratory analysis to look for markers of mild to moderate COVID-19, correlates of protection in the lung and similarities between pathological pathways in the rhesus macaque model vs those found in human COVID-19 lung tissue studies. Each chapter will contribute to the hypothesis and exploratory questions using different techniques:

- **Chapter 2**: The cellular landscape of the lung tissue is investigated with basic histopathology techniques followed by multiplex immunofluorescence for single-cell resolution insights
- **Chapter 3**: Spatial transcriptomics of lung tissue is used to examine the cellular processes at play within lesioned and non-lesioned areas of the lung across vaccine groups and pathology classifications
- **Chapter 4**: BAL fluid supernatant is assayed to study the cytokine environment of the lung and antibody-dependent enhancement is investigated using serum antibodies

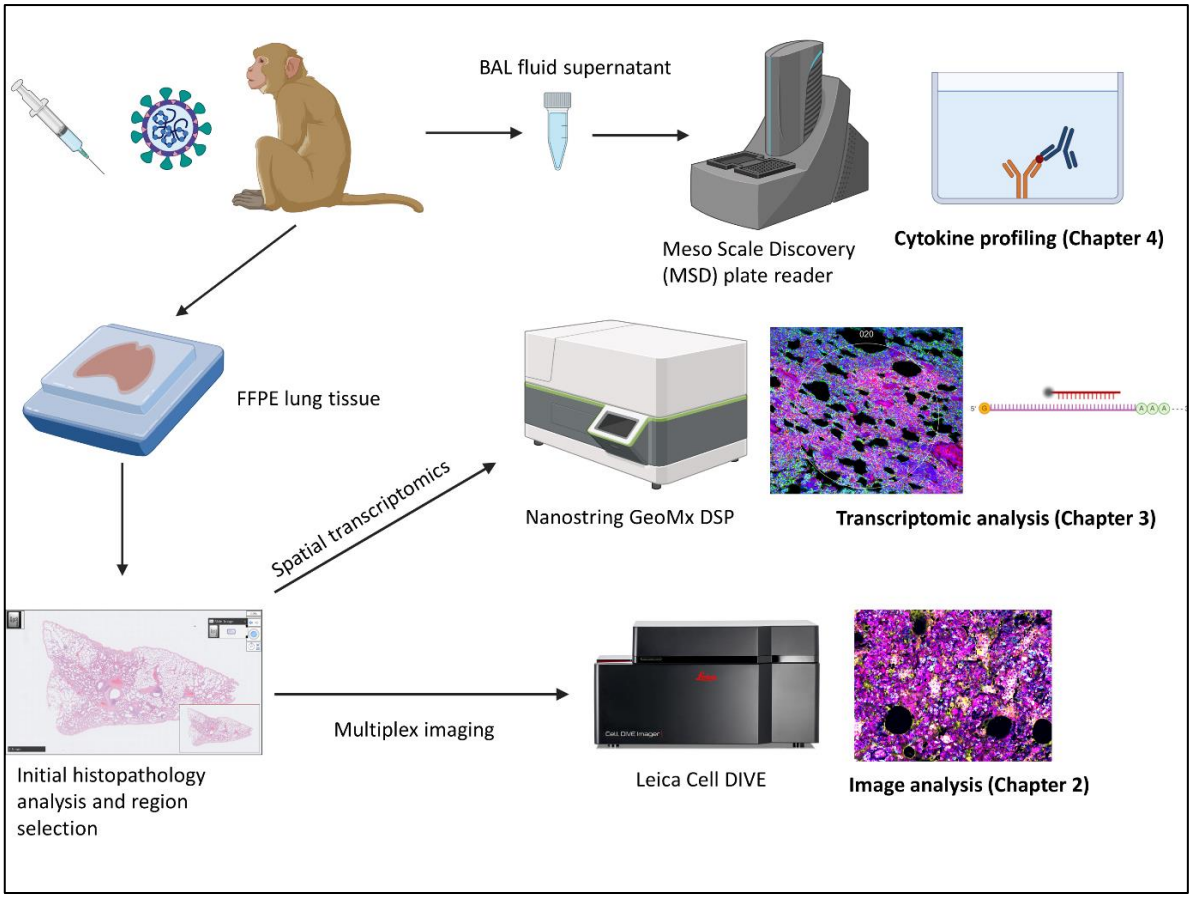

Figure 7: Thesis overview. Showing the primary techniques carried out and samples used in each chapter. Created with BioRender.com.

Chapter 2: Defining the cellular environments within post-challenge lung tissue

The cellular environments in the human lung that define severe COVID-19 have been well-characterised, as highlighted in **Chapter 1**. However, the cellular profiles associated with milder infections and with the context of previous vaccination have not been studied as extensively or not at all in the case of humans. Studies that have examined cellular profiles of the lower airway in SARS-CoV-2 vaccinated individuals have relied on BAL fluid sampling [55,56], which as described in **Chapter 1**, has its limitations as only cells that can be washed into the fluid can be sampled [46], and spatial context is not preserved. In the context of investigating VAED, for coronaviruses this may be associated with particular cell types and cytokine signatures in the lung, which would vary depending on the mechanism of VAED [99]. Macrophages are implicated in ADE and AED, while T cells and eosinophils are implicated in Th2-mediated VAED. Using FFPE lung blocks from NHPs, we characterised the lung histopathology and cellular profiles. We hypothesised that cellular environments in the lung, particularly adaptive immune infiltration, would vary depending on whether an animal was vaccinated and that these cellular environments may be linked to the varied histopathological outcomes. In the studies that the NHPs were originally involved in [117,135–137], their lung histopathology was characterised primarily through H&E staining and was assigned a lung histopathology score by veterinary pathologists according to a previously-described scoring system based on several histological features [87]. This allowed us to choose one high-pathology and one mid-low range pathology example within each study group to carry out initial IHC analysis (**Section 2.1**). The samples of interest (**Table 1 and Figure 6)** were chosen based on pathological profiles in consultation with Dr Javier Salguero, one of this project's supervisors and an experienced veterinary pathologist who leads the Pathology group at UKHSA Porton Down. These samples of interest also included unvaccinated unchallenged controls. Following initial histopathology and IHC work, samples across all the studies were examined in more detail using multiplex immunofluorescence, in order to gain deeper insights

into the lung tissue environment post-challenge in vaccinated, unvaccinated, unchallenged and re-challenged contexts at single-cell resolution.

Number	NHP ID	Study ID	Histo ref	Block Nr	Published?	Vaccine	Pathology	RNAscope
1	10A	6294	462/20	8	Vaccine	Single dose Inovio	17	0.012833
2	BLG	6312	582/20	14	Biorxiv	Low dose Curevac	11.5	0.00359
3	33A	6294	539/20	8	Vaccine	Two dose Inovio	3.5	0.0056
4	ZORA	6312	647/20	8	Biorxiv	High dose Curevac	4.5	0.00383
5	25A	6294	468/20	15	Vaccine	Naïve unvaccinated challenge	13	0.009333
6	22Z	6284	199/20	8	Communications Biology	Naïve unvaccinated challenge	15.6	0.032182
7		Archive	230/10/3b		n/a	Unvaccinated unchallenge	0	0
8		Archive	231/10/3b		n/a	Unvaccinated unchallenge	0	0
9	ALEX	6343	1/21	9	in preparation	Rechallenge	4.92	0.000951
10	BTW	6343	4/21	9	in preparation	Rechallenge	8.63	0.001142
11	31A	6294	472/20	8	Science Advances	FIV	4.25	0
12	54A	6294	541/20	8	Science Advances	FIV	7.25	0.002833
13	17Z	6284	193/20	9	Communications Biology	AZ	6.3	0
14	29Z	6284	196/20	9	Communications Biology	AZ	6	0.010667

Table 1: NHP samples of interest, which include a mixture of high and mid-low pathology lung samples across different vaccine studies. 'RNAscope' refers to the fraction of a whole-slide scan that was positive for SARS-CoV-2 spike mRNA by RNAscope.

In this chapter, we use imaging methods to determine whether any particular cell types in the lung tissue parenchyma are increased or decreased in frequency depending on histopathology, prior vaccination or prior challenge. We hypothesise that the relative frequency of some cell types will correlate with histopathology score, which could provide novel insights into correlates of protection in vaccinated lung tissue and the cell types driving lung pathology in the rhesus macaque model. In the latter case, we will compare our findings to human lung tissue studies of severe COVID-19 to determine the extent to which the rhesus macaque model, which exhibits mild to moderate pathology, recapitulates the cellular profile of human severe COVID-19.

2.1. Histopathology, immunohistochemistry and in-situ hybridization

By collaborating with the Pathology group at UKHSA Porton Down, we ensured that our pathological data is robust and we relate any of our findings back to pathology before any determinations about protection or disease enhancement in lung tissue can be made. H&E staining was carried out by the Pathology group for pathological evaluation (this was also previously done in the original studies). IHC was also carried out to examine a variety of immune cells of interest.

The IHC stains used were CD3, CD20, CD68 and myeloperoxidase (MPO) to quantify T cells, B cells, macrophages and neutrophils respectively. An ACE2 IHC stain was also used to look at expression of the receptor used by the SARS-CoV-2 spike protein. The same antibody clones and IHC staining techniques were used as previously reported by the Pathology group [138]. In-situ hybridisation (ISH, also known as RNAScope) was carried out for SARS-CoV-2 spike RNA using a probe from ACDBio (now Biotechne, Cat 848568).

By measuring the relative fraction of air pockets (also known as lacunar space) compared to the total area of the NHP lung tissue H&Es, we are able to examine the extent of inflammation in the tissue. Healthy, uninflamed tissue will have larger air pockets than inflamed tissue, in which the air pockets have reduced size due to infiltration of immune cells. With the H&E stain, we can also identify bronchial-associated lymphoid tissue (BALT) structures in the lung tissue. BALT is made up of immune cells, primarily T and B lymphocytes and has a role in initiating local lung immune responses and immune memory [139]. Induced-BALT (iBALT) is the term used for BALT that is produced in response to infection. As we can only look at tissues from NHPs post-cull, we cannot identify how much BALT was induced or previously present. Unlike in humans, many animals such as NHPs produce BALT more readily, not just in response to infection. Even in pathology, only about 8% of humans have been seen to have BALT, whereas BALT is much more commonly observed in both healthy and infected NHPs [140]. We noted at least one BALT site post-challenge in 10/12 of the NHPs of interest we chose for initial pathological assessment (**Figure 14**). BALT was not a major focus in our study. However, if comparing the amount of BALT across NHPs demonstrates major differences in particular groups, such as high vs low pathology score, this may give some insights into the role of iBALT in COVID-19 pathology.

2.1.1. Methods

H&E, IHC and RNAscope was carried out on 4µm sections from lung blocks from the samples of interest shown in **Table 1 and Figure 6** by the Pathology group at UKHSA Porton Down. The tissue sections were mounted on Superfrost slides prior to staining with the 'Leica Bond RXm' as described in a previous publication by the Histopathology group [138] for all of the H&E and

IHC stains. SARS-CoV-2 spike ISH was also carried out as described in another study [87]. Stained slides were scanned with the 'NanoZoomer S360' (Hamamatsu, Japan) and whole-slide images were examined using 'NDP.View 2' software (version 2.8.24, Hamamatsu Photonics K.K, Japan). Image analysis was performed using 'Nikon NIS elements AR' software (version 5.01.00, Nikon, Amsterdam, Netherlands), in which thresholds were separately selected for each stain such that the software could most accurately calculate the stained area while avoiding background staining where possible. The total area of the slide was obtained by drawing a border around the tissue section on the slide using 'Nikon NIS elements AR' software and the fraction of stained area per total area was calculated using the same software. Thresholds were also set in order to measure the fraction of 'air' in the air pockets within these tissues, which can also be referred to as the 'lacunar space' [29]. BALT structures were manually counted in the H&E-stained samples.

2.1.2. Results

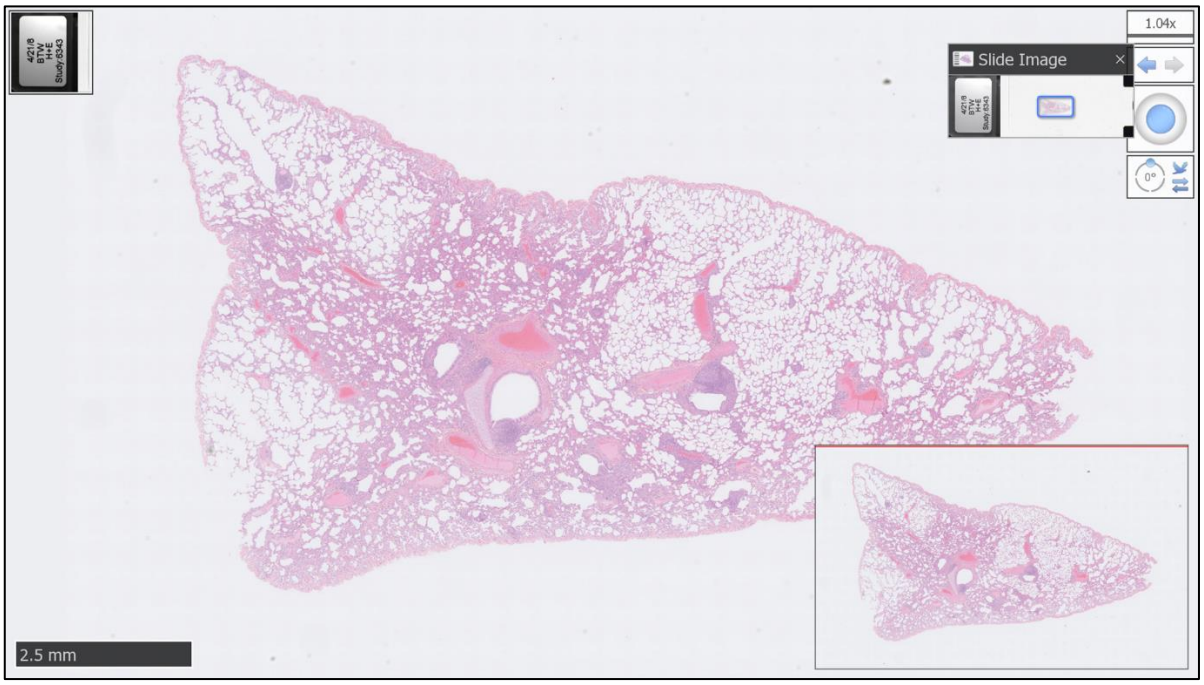

Figure 8: Representative image of a whole H+E-stained lung tissue section. Images taken with 'NanoZoomer S360' and examined with 'NDP.View 2' software.



Figure 9: Representative image of a H+E-stained lung tissue section showing a bronchial-associated lymphoid tissue (BALT) structure annotated with a red circle. Images taken with 'NanoZoomer S360' and examined with 'NDP.View 2' software.

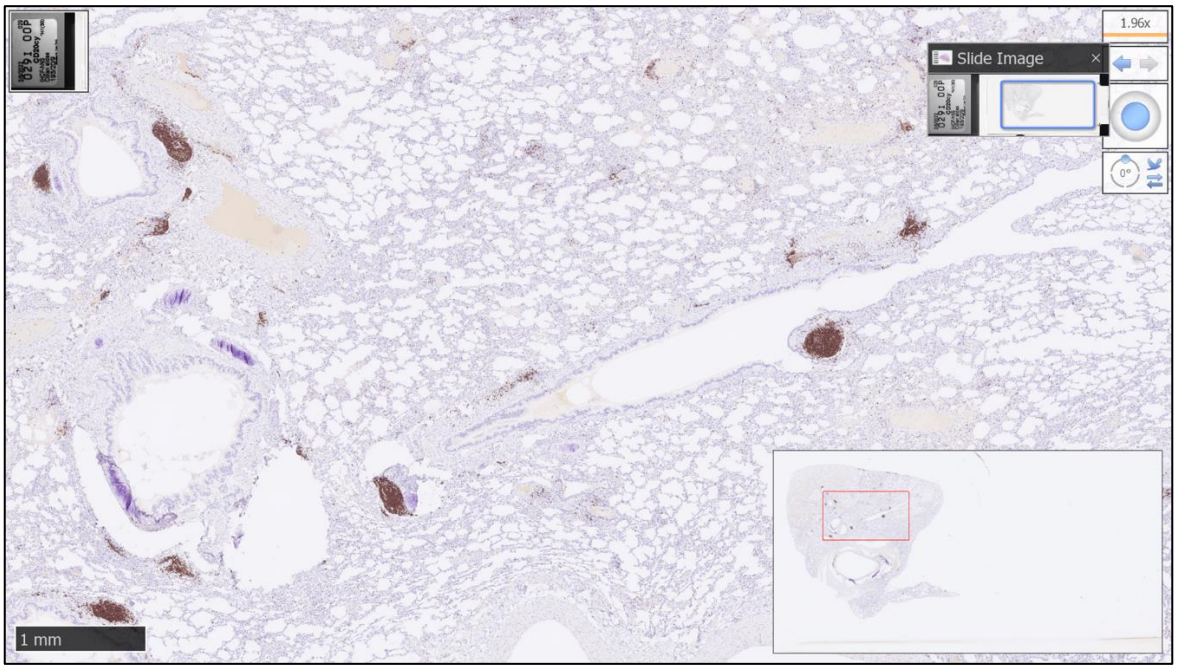

Figure 10: Representative image of a CD20-stained lung tissue section. Images taken with 'NanoZoomer S360' and examined with 'NDP.View 2' software.

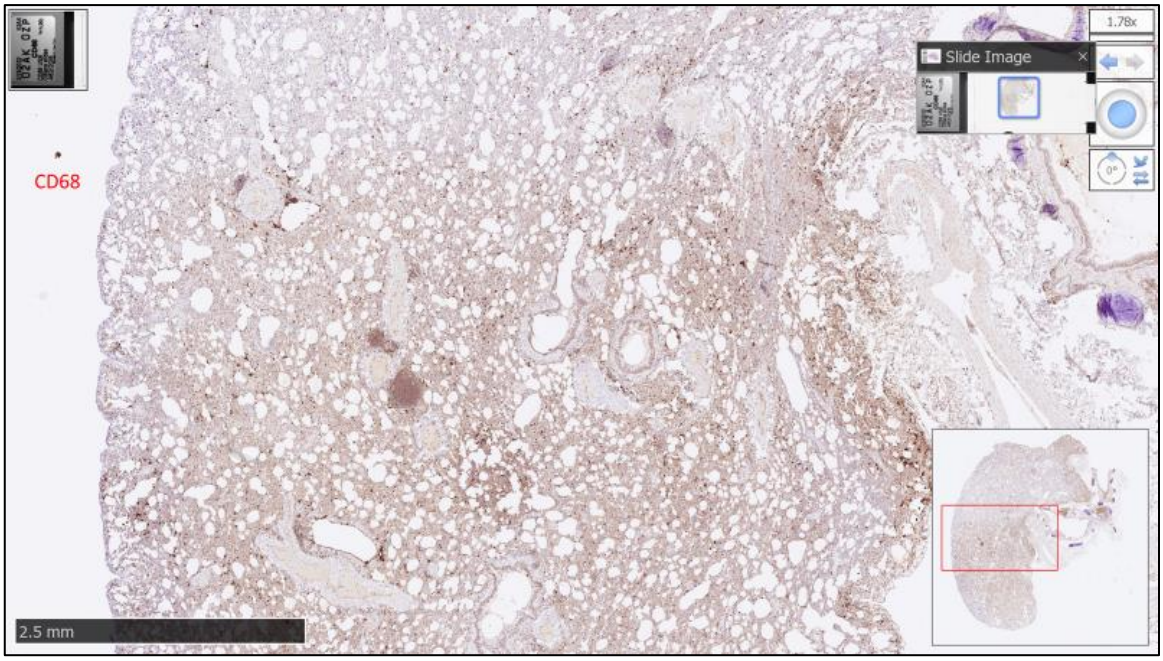

Figure 11: Representative image of a CD68-stained lung tissue section. Images taken with 'NanoZoomer S360' and examined with 'NDP.View 2' software.

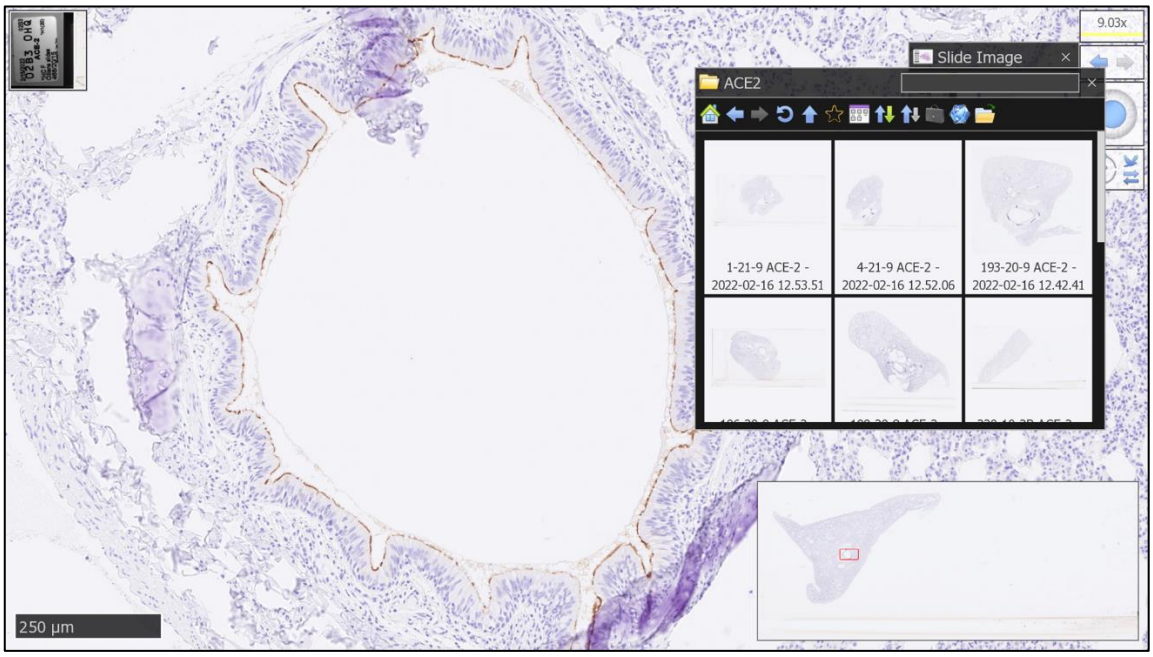

Figure 12: Representative image of an ACE2-stained lung tissue section. Images taken with 'NanoZoomer S360' and examined with 'NDP.View 2' software.

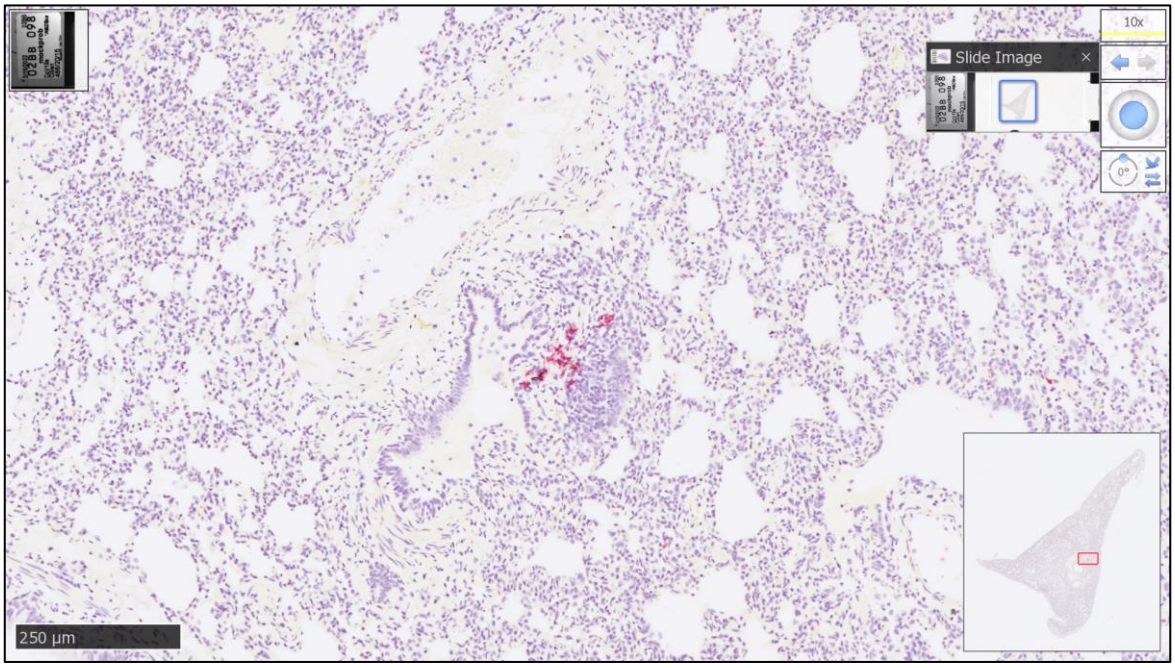

Figure 13: Representative image of a SARS-CoV-2 spike in-situ hybridisation (pink). Images taken with 'NanoZoomer S360' and examined with 'NDP.View 2' software.

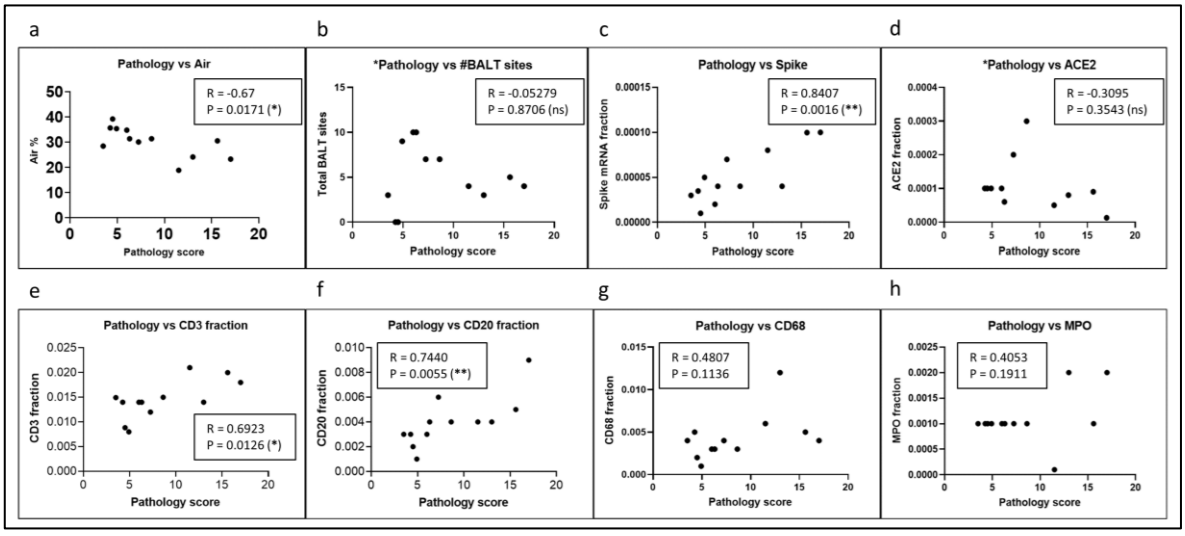

Figure 14: Correlations of H&E and IHC features with histopathology score. a. Fraction of air spaces (or lacunar space). **b.** Number of BALT sites. **c.** Fraction of spike mRNA staining by ISH. **d.** Fraction of ACE2 staining by IHC. **e.** Fraction of CD3 staining by IHC. **f.** Fraction of CD20 staining by IHC. **g.** Fraction of CD68 staining by IHC. **h.** Fraction of MPO staining by IHC. Quantifications for all graphs were carried out using 'Nikon NIS elements AR' software. The R value is Pearson's correlation coefficient and the p value is calculated using Pearson's correlation test.

2.2. Immunohistochemistry-based cell counting

In order to have a better idea of how immune cell infiltration might be associated with pathological outcomes in the NHPs, we created a machine learning pipeline in the software programme 'ARIVIS Vision4d' to quantify cell populations in the lung tissue. Background staining and other problems associated with colour thresholding alone led us to pursue this machine learning method for more quantitative results. However, we used this method only to quantify macrophages and neutrophils, not T cells and B cells. There are several reasons for this. Firstly, macrophages and neutrophils are already known to be strongly associated with COVID-19 pathology in the literature [110,141]. Secondly, the CD68 and MPO stains were the most troublesome for the Nikon NIS Elements AR software to handle due to high background and poor stain uptake respectively. Finally, T cells and B cells were largely associated with BALT, where they are densely packed and therefore could not be reliably counted with the machine learning software that we used. Two lung blocks per sample of interest were stained for CD68 and MPO and subsequently analysed. Analysis (**Figure 16**) is shown separately for the lung blocks with the lowest and highest cell counts.

2.2.1. Methods

A machine learning pipeline was created using ARIVIS Vision4d software. The 'machine learning segmenter' was trained using control images from an unchallenged animal in a tuberculosis study conducted at Porton Down, to ensure that the training data was distinct from the data to be analysed. Training consisted of highlighting cells of interest (macrophages or neutrophils) and separately highlighting background, until we were satisfied with the perceived accuracy and lower level of uncertainty in the resulting pipeline. The area of the slide containing the tissue was drawn around and the pipeline exported the number of macrophages or neutrophils in this area, and the area of the tissue slide (in voxels). For each NHP of interest, this process was repeated using stained (CD68 and MPO IHC) slices until two lung blocks from each NHP were analysed. Outputs were graphed and analysed using GraphPad Prism 9.3.1 (GraphPad Software, La Jolla, CA, USA).

2.2.2. Results

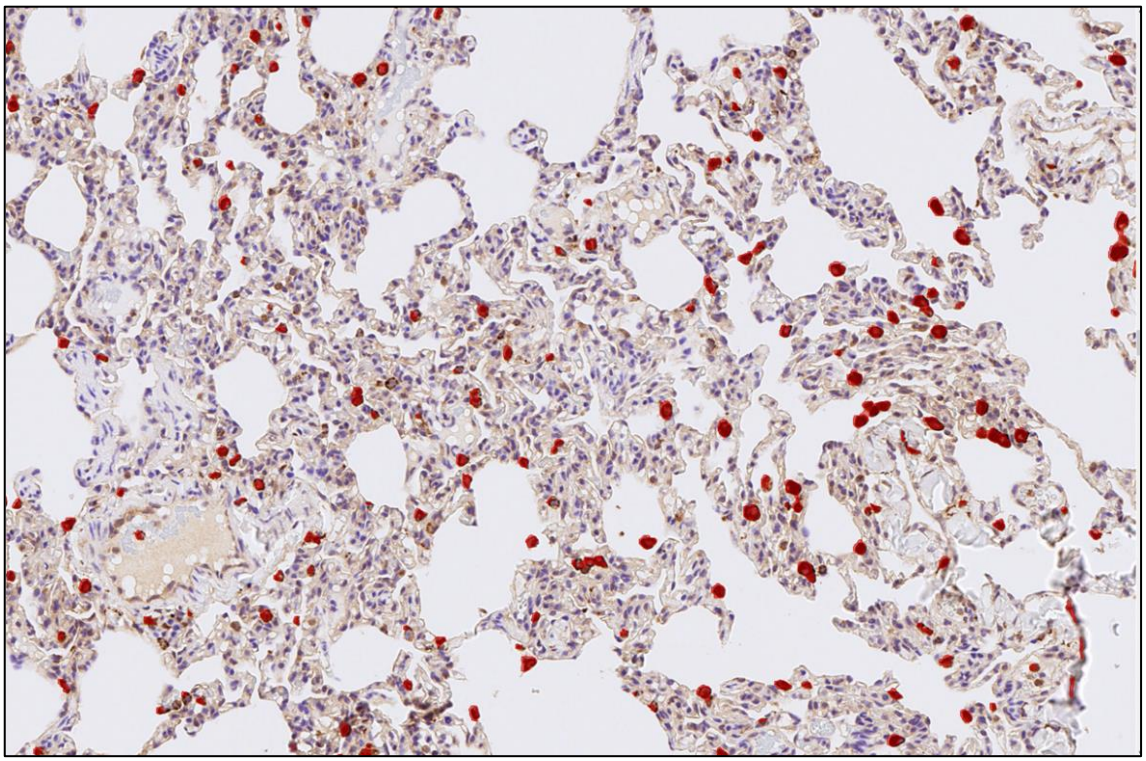

Figure 15: Representative image of macrophages (red) as identified by a machine learning pipeline in ARIVIS Vision4D. The pipeline was trained using control tissues stained for CD68.

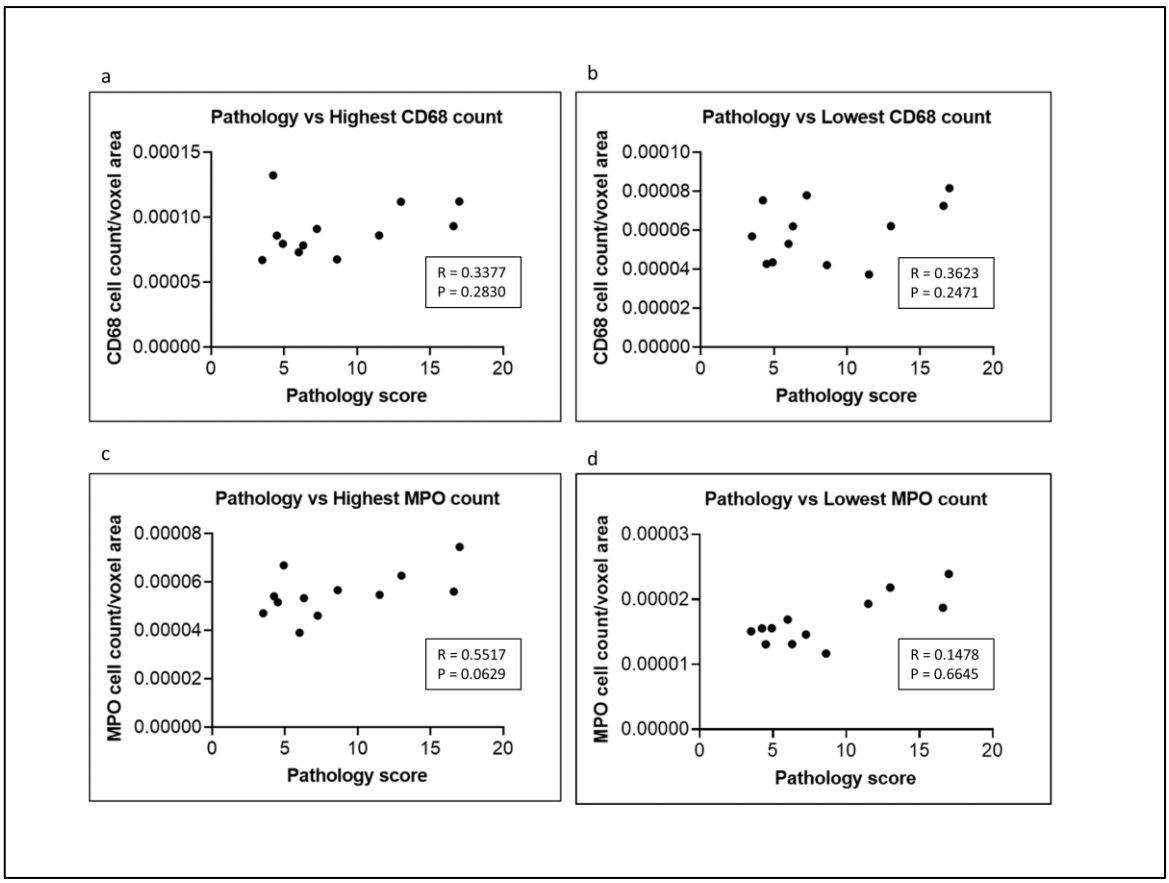

Figure 16: Associations of cell counts with histopathology scores. a. Lung area with the highest number of CD68-positive cells. **b.** Lung area with the lowest number of CD68-positive cells. **c.** Lung area with the highest number of MPO-positive cells. **d.** Lung area with the lowest number of MPO-positive cells.

2.3. Multiplex immunofluorescence

As mentioned in **Section 1.2.3**, single-cell spatial analyses of protein markers in lung tissue have shed light on immune populations and cellular neighbourhoods that are present in the lung during severe COVID-19 [10]. Interactions between $CD8^+$ T cells and neutrophils and between monocytes and endothelial cells were associated with severe pathology. This study, nor any other lung tissue study, has examined the cellular environment in-situ in the context of vaccination and challenge. In order to improve upon our previous IHC work (**Section 2.2**) we carried out multiplex immunofluorescence imaging using the Cell DIVE **(**GE Research, Niskayuna, NY, USA**)** with a panel of fluorescent antibodies which we optimised to study a variety of immune and structural cell types implicated in SARS-CoV-2-mediated lung pathology and immunity. The Cell DIVE

platform allows for whole-slide (or region-selected) multiplex imaging at single-cell resolution using 'off the shelf' fluorescent antibodies by incorporating a bleaching step between staining rounds (**Figure 17**), similarly to the iterative bleaching extends multiplexity (IBEX) workflow [142]. The Cell DIVE uses background images to remove autofluorescence and auto-aligns imaging rounds. Overall this results in image outputs that are similar to other multiplex imaging platforms that use DNA-barcoded antibodies [143]. However, due to the iterative staining and bleaching that involves many cover-slipping and de-cover-slipping steps, a disadvantage of the Cell DIVE platform is that tissue loss and tissue folding across different imaging rounds can become an issue. In these cases, images from the current imaging round must be manually aligned to the previous imaging round by the user and in some cases the tissue loss and tissue folding can lead to artefacts on the image, or can make lining up later rounds with earlier rounds impossible. We imaged lesioned and non-lesioned regions of lung tissue, as defined by Dr Javier Salguero, a veterinary pathologist at UKHSA Porton Down, from every in our previously-described cohort from previous studies [117,135–137]. By imaging lesioned and non-lesioned areas separately, we can compare whether the cells involved at damaged sites vs unaffected sites differ according to their vaccine/challenge group and gain insights into potentially pathogenic or protective cellular profiles in the NHP model of mild-moderate pathology and in a vaccine context.

There are several points that must be considered when designing the antibody panel for the Cell DIVE. Some antibody-fluorophore combinations did not bleach well following the bleaching step of the protocol, so these antibodies must be placed on the last round. For other markers, the epitopes bound by antibodies are particularly sensitive to the bleaching protocol, so the antibodies had to be placed early in the panel for staining to be successful. Primary-secondary antibody combinations must be added in the first round and the primary antibodies must be from different species. The CD31 antibody was not found to work well when conjugated, so was kept in the first round as a primary-secondary combination. Finally, some markers work better when conjugated to particular fluorophores. In our study, while all antibodies were initially tested at a concentration of 10µg/mL, some required further optimisation and were run at different concentrations in the

final staining runs (**Supplementary Table 2**). The following protocol was carried out twice (two separate 'imaging runs') in order to collect images from all of the NHP tissues.

2.3.1. Cell DIVE protocol

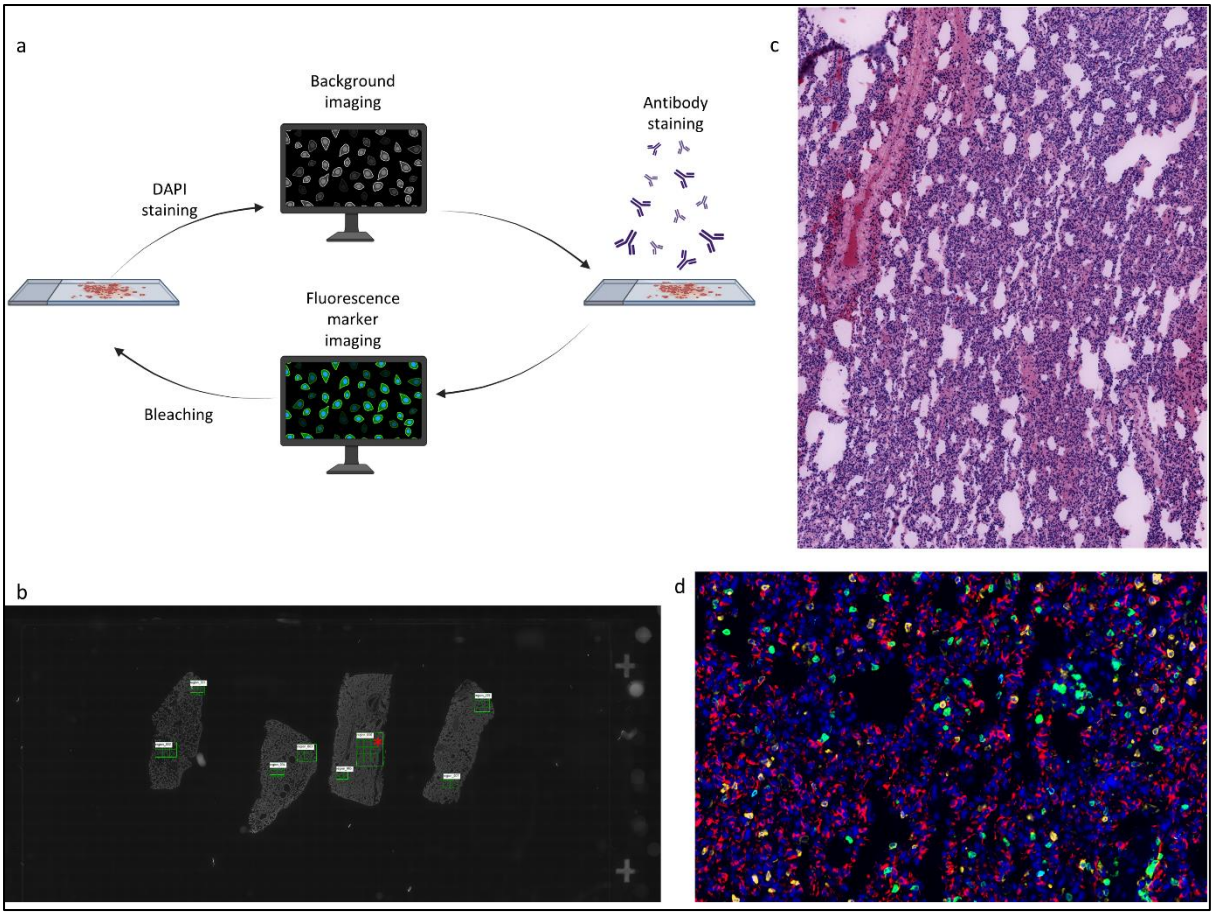

Figure 17: Cell DIVE imaging overview. **a.** Cell DIVE protocol, created with Biorender.com. **b.** Representative 'Scanplan' image taken at 10X magnification, from block 6. Region 6 marked with a red star. **c.** 'Virtual H&E' image of region 6 from block 6, taken at 40X magnification. **d.** Fluorescence image showing 5 markers: DAPI (dark blue), CD3 (green), PanCk (red), CD16 (yellow) and CD20 (light blue), taken at 40X magnification.

4µm sections of tissues were prepared and mounted on slides as described previously. For Cell DIVE imaging (and for spatial transcriptomics in **Chapter 3**), 'multiblocks' were created to combine tissue from 4-5 different animals onto one slide. The areas of tissue chosen for inclusion in the multiblocks were decided by a veterinary pathologist (Javier Salguero) based on his annotations of both lesioned and non-lesioned areas. 4µm-thick tissue slides from the multiblocks

were prepared at Porton Down before being shipped to Oxford for antigen retrieval, imaging and spatial transcriptomics (**Chapter 3**). The staining and imaging protocol followed the Cell DIVE Platform's instructions (GE Research, Niskayuna, NY, USA). On day 1, FFPE tissue sections were baked in an oven overnight at 60 °C. On day 2, the slides were cleared with a slide clearing protocol on the 'Leica Bond'. This clearing protocol first consisted of deparaffinisation in xylene, twice for 5 minutes, followed by rehydration twice for 5 minutes in each of 100%, 95%, 70%, 50% ethanol and PBS. Next, the tissues were permeabilised in a solution of 0.3% Triton X-100 in PBS for 10 minutes before washing with PBS for 5 minutes. Two antigen retrieval solutions were used for the next step, one Citrate-based solution at pH 6 and another Tris-based solution at pH 9. The Citrate-based solution was made up with 12.5mL citrate and 237.5mL deionised water, while the Trist-based solution was made up of 25mL of 10X Tris and 225mL deionised water. The antigen retrieval step was carried out using the NxGen decloaking chamber (Biocare Medical, Pacheco, CA, USA). The slides were first plated in the Citrate-based solution and a steam test strip was placed on the top of the staining dish before the decloaking chamber was locked. The pressure cooker turned on and when the temperature in the chamber reached 70 °C an external timer was started for 20 minutes. During this time, the pressure cooker reached 110 °C and remained at this temperature for 4 minutes before the temperature began to decrease. After the 20-minute timer, the slides were transferred to the Tris-based solution and the chamber was closed again, but not locked, to allow the temperature to continue to decrease. After another 20 minutes, the wire rack holding the staining dishes was removed from the chamber and placed on the benchtop. The pH of both antigen retrieval solutions was verified with pH strips. The slides remain in the Tris-based solution on the benchtop for 10 more minutes to cool before the slides were washed four times for 5 minutes each in PBS. Next, the slides were blocked overnight at 4°C in PBS with 3% BSA and 10% donkey serum (Bio-Rad). From this point, all wash and incubation steps were carried out in staining dishes at room temperature with gentle agitation unless stated otherwise. On day 3, slides were placed in a staining dish at 4 °C under an LED light for 24 hours to photo-bleach the tissue and minimise background fluorescence. On day 4, the slides were washed in PBS for 5 minutes followed by incubation in DAPI (ThermoFisher)

solution for 15 minutes and another PBS wash for 5 minutes. A cover slip was applied to the slides following addition of 75µL of mounting media, which consisted of 4% propyl gallate and 50% glycerol (Sigma-Aldrich). On the Cell DIVE imaging system, a 'scanplan' of the regions of interest (as selected by a veterinary pathologist) was acquired at 10X magnification (see **Figure 17**). The first imaging round was acquired at 20X magnification to calculate the background autofluorescence, subtracted from the first staining round, and to create 'virtual H&E' images. For generation of 'virtual H&E' images, autofluorescence of the cy3 channel is used to create a 'virtual' eosin stain and DAPI is used in place of haematoxylin as a nuclear stain. The coverslips were removed from the slides by placing them face-down at an angle in PBS. A mixture of one or more antibodies (depending on the round number, see **Supplementary Table 2**) was prepared and 200µL of the solution was added to each slide for overnight incubation at 4 °C. On day 5, the slides were first washed three times in PBS for 5 minutes. Only for this first staining round, a secondary antibody mixture was prepared and added to the slides for a 1-hour incubation at room temperature. Then the slides were washed three times in PBS for 5 minutes, coverslipped as previously described, and imaged. After this imaging round, the first bleaching round took place, starting by removing the coverslips as previously described, followed by incubating the tissue slides in 0.5M $NaHCO_3$ (pH 11.2) and 3% H_2O_2 with gentle agitation twice for 15 minutes, with a wash step of 1 minute in PBS in-between. The slides were then incubated in a DAPI solution for 15 minutes before one more 5-minute wash in PBS followed by coverslip addition and imaging. This imaging round is a 'bleach round', which is provides the new background fluorescence reading to be subtracted from the next imaging round. Staining and bleaching rounds were repeated as described above until all 6 staining rounds were completed. Each imaging step on the Cell DIVE was performed within 24 hours of the stain/bleach step. **Supplementary Table 2** details the antibodies used in each round. Antibodies that were not bought pre-conjugated were conjugated using either abcam conjugation kits (Cat ab236553 for AF488 and Cat ab269820 for AF555) or the ThermoFisher AF555 conjugation kit (Cat A20187) in the case of FOXP3. In cases where auto-alignment between rounds failed, the images were manually aligned on the Cell DIVE.

2.3.2. Initial analysis

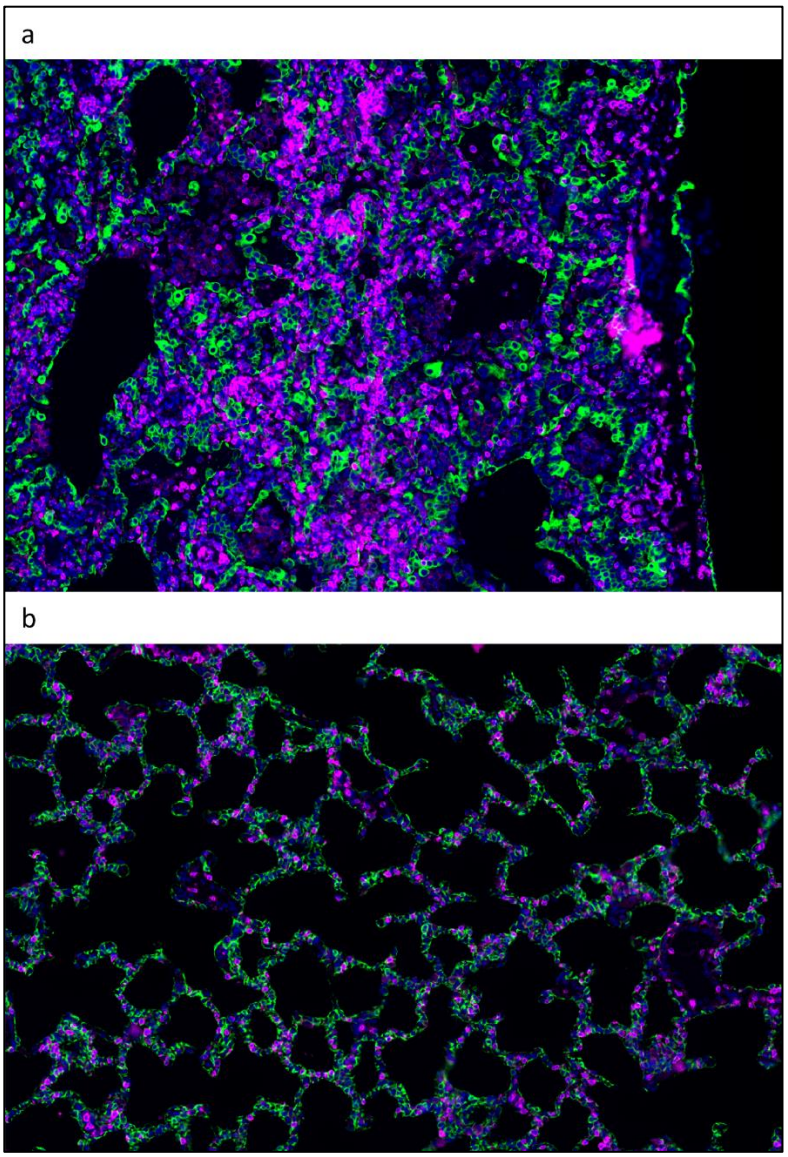

Figure 18: Representative Cell DIVE images from a lesioned area of lung tissue (a) and a non-lesioned area of lung tissue (b). DAPI (blue), PanCk (green), CD45 (pink).

Antibody staining was first validated in QuPath [144] version 0.5.0, using stained FFPE rhesus macaque tissue from lymph nodes and bone marrow (representative images **Supplementary Figure 43** to **Supplementary Figure 45**), before validating on lung tissue. Stains were compared with staining expected given previous literature and co-staining was examined to validate expected patterns. Antibody clones for staining were initially selected based on previous publications or supplier websites demonstrating efficacy in staining FFPE NHP tissues. For markers of interest that did not have proven efficacy in FFPE NHP tissues, clones were selected

based on listings of predicted reactivity in NHPs (according to suppliers) or in some cases anti-human antibodies without this prediction were tested. Markers that were tested but were deemed unsuitable due to poor or inconsistent staining following antigen retrieval and one round of bleaching include CD69, CD8 and CD14. Examples of tissue loss, tissue folding and poor staining were noted in many images due to the many coverslipping steps (see **Figure 19**). Some markers performed well in testing but were not included in the final analysis (**Section 2.4**) because of inconsistent staining between tissues or imaging runs. **Supplementary Table 2** shows all of the antibodies that were included in the final staining runs and the markers that were excluded from final analysis are annotated as such. Before further analysis, the sides of every image were trimmed by 10µm in order to remove edge effects, which caused cells at the borders of images to appear positive for particular markers due to non-specific fluorescence (see **Figure 19**). Images that had total tissue loss, very large amounts of tissue folding and/or large immunofluorescence artefacts were not included in the analysis (as well as images that failed completely by segmentation, see **Section 2.4**). This led to a total of 93 images being analysed. The breakdown of the images used in final analysis can be seen in **Table 2**.

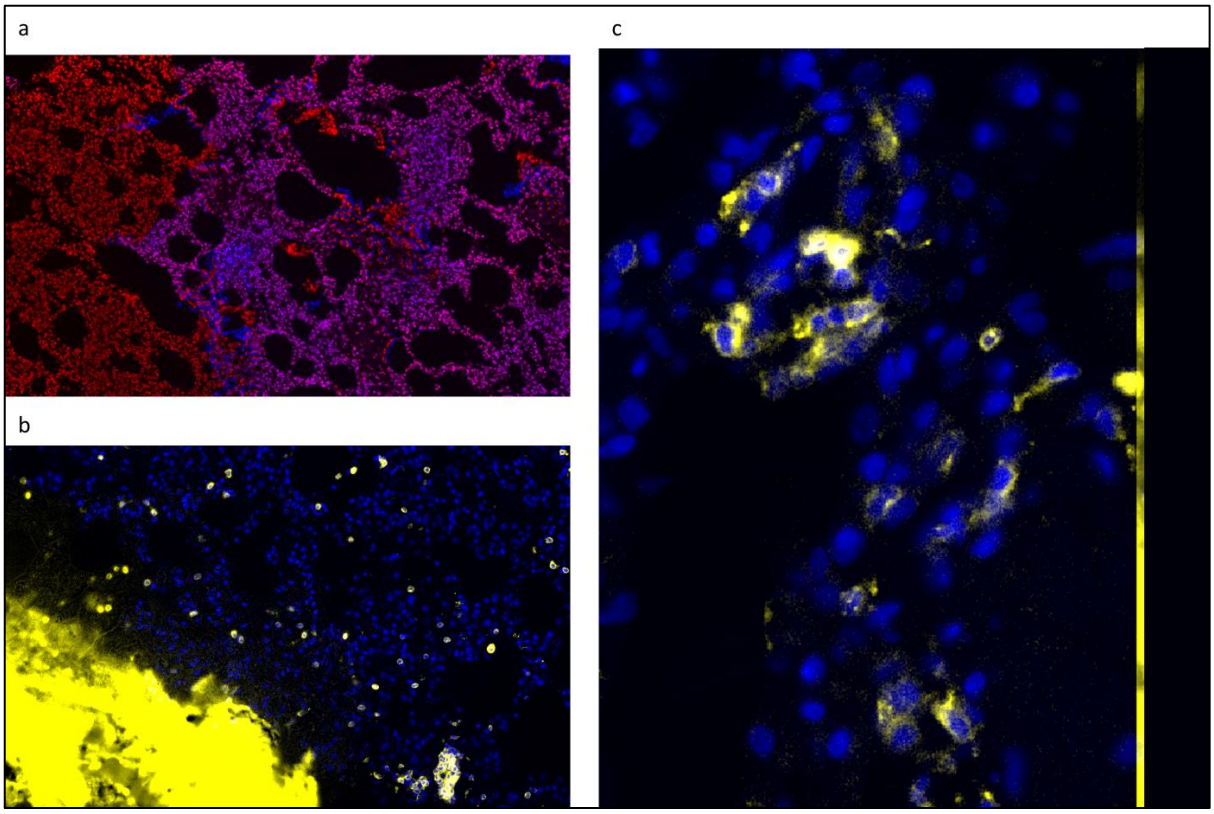

Figure 19: Issues with Cell DIVE images. a. Representative area with both tissue loss and tissue folding. **b.** Staining artefact in the bottom-left of the imaged region. **c.** Edge effect on the right border of the image. Images taken with the Cell DIVE. Final round DAPI (blue), first round DAPI (red) and CD3 (yellow).

2.4. Single-cell analysis of immunofluorescence data

Analysis of the multiplex immunofluorescence data was inspired by the aforementioned COSMIC publication and the SpOOx pipeline which was developed by the Byrne, Taylor and Ho groups at the University of Oxford [10]. Specifically, we used an updated version of the SpOOx pipeline (unpublished) in which filtering of channel thresholds can be passed to segmentation tools (in our case DeepCell/Mesmer). The images that were deemed appropriate for analysis were first put through DeepCell/Mesmer [145] (version 0.12.4) to carry out cell segmentation. As well as the nuclear stain DAPI, which was used to define the nuclei of individual cells, a variety of membrane protein markers from the panel were tested within DeepCell/Mesmer to inform cell boundaries for cell segmentation. We found that the epithelial cell marker Pan-Cytokeratin (PanCk) and the immune cell marker CD45 together had the best performance for cell segmentation, with intensity ranges of 1600-20000 in imaging run 1 and 1500-10000 in imaging run 2 for PanCk and 8000-22000 in imaging run 1 and 2000-7000 in imaging run 2 for CD45. DAPI segmentation ranges were 7000-60000 in imaging run 1 and 4000-54000 in imaging run 2. Cell segmentation with DeepCell/Mesmer was run by Professor Stephen Taylor on all of the images after we decided on the appropriate marker combination. Some images were not fully segmented (5 images) or in some cases, none of the image was segmented (10 images). An example of segmentation from one of the images can be seen in **Figure 20**.

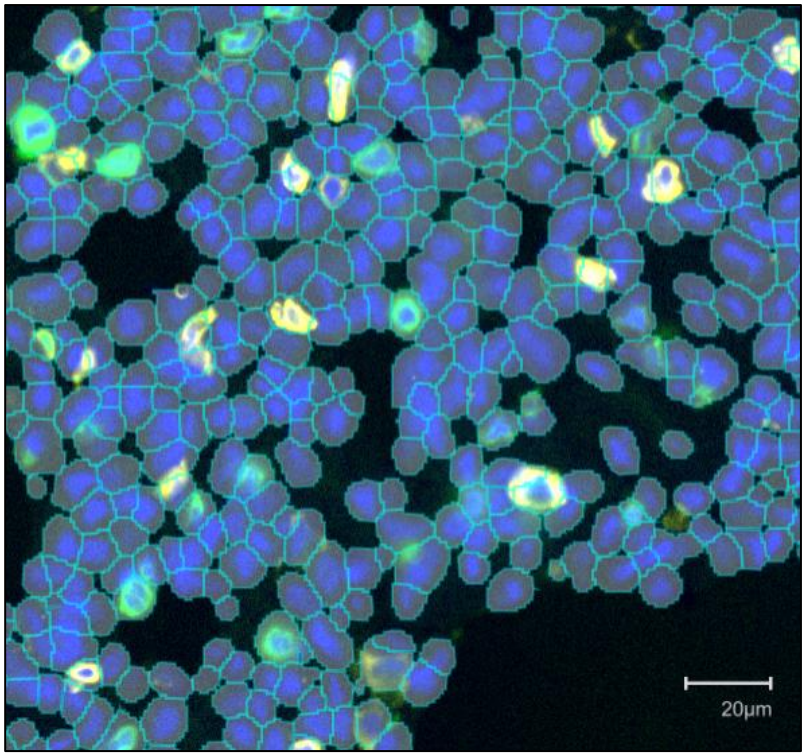

Figure 20: Repesentative example of DeepCell/Mesmer segmentation of an immunofluorescence image. Showing DAPI (blue), CD3 (green), CD16 (yellow) and segmentation borders (cyan).

Sample	NHP ID	Group	Histopathology score	Pathology class	Lesioned regions	Non-lesioned regions	Failed regions	Which regions failed?
1	31A	FIV	4.25	Protected	2	2	0	
2	29Z	Viral_Vector	5.76	Protected	2	2	1	One lesioned failed segmentation
3	22Z	Unvaccinated	15.46	Pathology	3	2	2	One lesioned and one non-lesioned
4	25A	Unvaccinated	13.00	Pathology	2	1	1	Nonlesioned failed segmentation
5	24Z	Unvaccinated	5.12	Protected	1	1	1	Nonlesioned failed
6	Archive230	Unchallenged	0.00	NA	0	2	2	All failed segmentation
7	Archive231	Unchallenged	0.00	NA	0	2	2	All failed segmentation
8	ALEX	Rechallenge	4.92	Protected	2	1	0	
9	54A	FIV	7.25	Pathology	2	2	0	
10	BLG	mRNA_Lowdose	11.50	Pathology	2	2	0	
11	ZORA	mRNA_Highdose	4.50	Protected	2	1	1	Nonlesioned failed segmentation
12	17Z	Viral_Vector	6.31	Protected	2	2	0	
13	BTW	Rechallenge	8.63	Pathology	3	2	0	
14	33A	DNA_Twodose	3.50	Protected	2	2	1	One nonlesioned failed
15	10A	DNA_Onedose	17.00	Pathology	4	3	2	Two lesioned failed segmentation
16	30A	DNA_Onedose	6.25	Protected	1	1	0	
17	24A	DNA_Onedose	6.25	Protected	1	2	0	
18	21A	DNA_Onedose	5.00	Protected	1	1	0	
19	5A	DNA_Onedose	3.25	Protected	1	1	1	Nonlesioned failed
20	38A	DNA_Onedose	4.25	Protected	2	1	0	
21	9A	DNA_Twodose	9.00	Pathology	1	1	1	Lesioned failed
22	12A	DNA_Twodose	4.75	Protected	1	1	1	Nonlesioned failed
23	45A	DNA_Twodose	5.50	Protected	2	1	0	
24	42A	DNA_Twodose	3.75	Protected	2	2	0	
25	13A	DNA_Twodose	3.50	Protected	1	1	1	Nonlesioned failed
26	29A	FIV	7.50	Pathology	1	1	1	Lesioned failed
27	3A	FIV	7.75	Pathology	2	1	1	Nonlesioned failed
28	2A	FIV	3.25	Protected	1	1	1	Nonlesioned failed
29	15A	FIV	7.25	Pathology	1	1	2	All regions failed
30	BBO	mRNA_Lowdose	8.00	Pathology	1	1	2	All regions failed
31	BRR	mRNA_Lowdose	7.25	Pathology	1	1	1	Nonlesioned failed segmentation
32	ARIL	mRNA_Lowdose	6.75	Pathology	2	1	1	One lesioned failed
33	BYC	mRNA_Lowdose	7.50	Pathology	1	1	0	
34	AAA	mRNA_Lowdose	8.00	Pathology	1	1	0	
35	ATM	mRNA_Highdose	5.75	Protected	1	1	2	All regions failed
36	AUU	mRNA_Highdose	4.00	Protected	1	1	1	Nonlesioned failed
37	ALBS	mRNA_Highdose	4.50	Protected	1	1	0	
38	ANAI	mRNA_Highdose	6.00	Protected	1	1	0	
39	AO	mRNA_Highdose	4.50	Protected	1	1	0	
40	BINKY	Rechallenge	6.00	Protected	1	1	1	Nonlesioned failed
41	BDC	Rechallenge	8.54	Pathology	1	1	0	
42	APOLL	Rechallenge	8.91	Pathology	1	1	0	
43	ANKI	Rechallenge	5.88	Protected	1	1	0	
44	AURO	Unvaccinated	7.25	Pathology	1	1	1	Nonlesioned failed
45	ART	Unvaccinated	6.50	Pathology	2	1	0	
46	ZIG	Unvaccinated	8.50	Pathology	1	1	2	All regions failed

			Lesioned	Non-lesioned	Failed (total)
	Totals		66	60	33
All regions	126				
Failed regions	33				
Final number	93				
NHPs	46				
Failed NHPs	6				
Total n number	40				

Table 2: Imaged regions. Showing the total number of regions imaged across the samples along with how many images were unsuitable for further analysis (annotated as 'failed images').

Following segmentation, Professor Stephen Taylor and Peter Todd imported the segmented images into their MDV platform for further analysis and carried out Leiden clustering, which was incorporated into the new 'MDV project'. As MDV was not initially designed to handle multiplex immunofluorescence (it was designed for IMC images), modifications were made my Professor

Stephen Taylor and Peter Todd over time so that MDV could be used to handle this data and filter the outputs in appropriate ways based on our feedback. An overview of the MDV workflow can be seen in **Supplementary Figure 1**. We found that Leiden clustering did not create satisfactory cell type clusters that we would expect based on prior knowledge of marker expression in the lung (**Supplementary Figure 2**) and the previous manual inspection with QuPath [144]. We hypothesised that, unlike for the COSMIC study which used IMC, our multiplex immunofluorescence images had more non-specific staining, tissue folding, tissue loss, imaging artefacts and inter-run and inter-sample staining variations, which caused clustering to perform poorly. Therefore, we used log2-transformation of intensity signals followed by z-score normalisation and clipping to manually define marker positivity and reduce between-sample and between-run variation across the images. The transformation and normalisation were carried out by Professor Stephen Taylor. Z-score normalization converts the marker expression values to a standard normal distribution within each image. Each segmented cell then has a z-score value for each marker calculated by averaging the intensity of that marker within all the pixels in the cell, transforming this intensity and applying z-score normalisation across all cells in the same image to see where each individual cell falls. We noticed that small peaks were being generated at the highest and lowest z-score values for most markers, so the z-scores were clipped so that while the score was centred around zero, the potential values were clipped at -3 and +3 standard deviation units. **Figure 21** shows the expression of each marker across the samples following z-score normalisation. Segmentation is never perfect, sometimes there is spill over of signal from neighbouring cells, so z-score values to define marker positivity were adjusted in MDV (**Supplementary Figure 1**) until the cells labelled as 'positive' were as close as possible to how positivity would be defined by manual annotation. These z-score values we used to define marker positivity can be seen in **Table 3**.

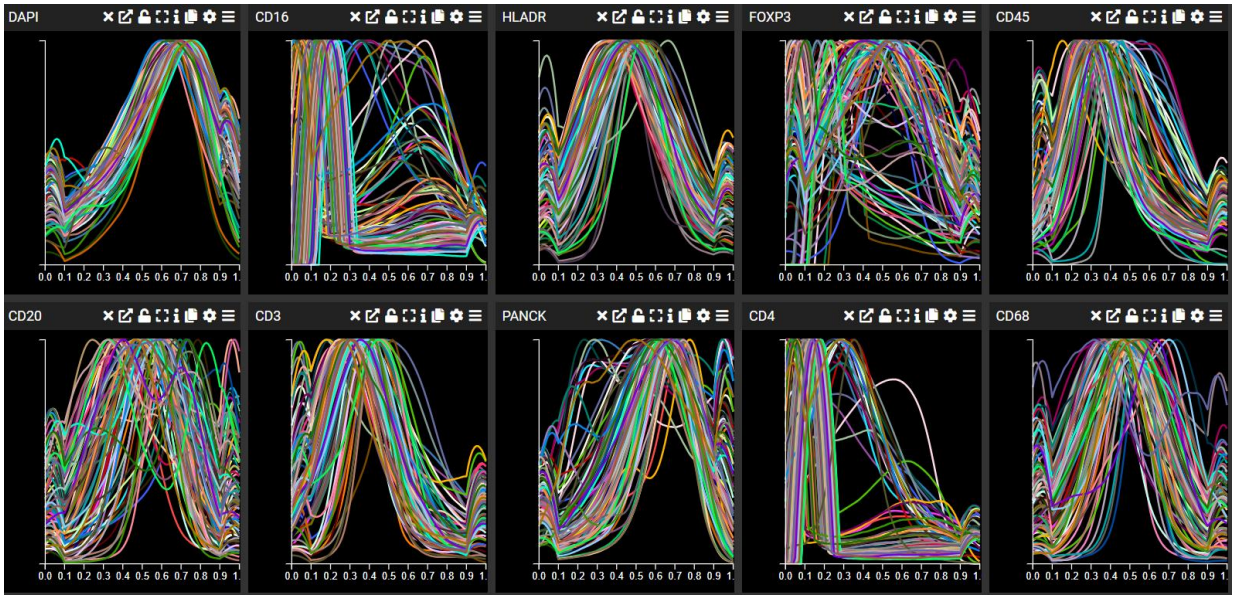

Figure 21: Marker expression across the samples. Expression values following z-score normalisation and clipping are shown on an intensity scale from 0 to 1 on the x axis. The y axis indicates the relative frequency of cells expressing different levels of the marker. Each individual sample is shown with a different colour line. Screenshot taken from MDV.

Marker	Z-score min
CD3	1.5
CD4	2
CD20	1.3
CD16	1.4
CD45-high	0.5
FOXP3	2.9
HLA-DR	1.3
PanCk	0

Table 3: Z-score minimum values for markers to be defined as 'positive' in a Cell DIVE image in MDV. Possible Z-scores range from -3 to +3.

The marker positivity thresholds were used to populate columns in an annotation table created within MDV. For every marker a cell is positive for, the value 'Pos' would be entered into the corresponding marker column, except in the case of CD45, where the value 'High' would be entered. This is because CD45 staining was very high across all images, even at low z-score thresholds, so we instead set a z-score threshold to mark cells that were highly positive for CD45,

to avoid capturing cells that potentially only have background levels of CD45. Cell size thresholds were also set and this information was added to the annotation table so that segmented 'cells' that were too small (area under 315 pixels) or too large (area over 1,700 pixels) to be actual cells could be filtered out. Visual inspection in MDV (**Supplementary Figure 1**) was used to define the marker thresholds and cell size thresholds. It was evident that small parts of debris, or rare cases where multiple cells were joined together, were successfully filtered out in most cases by the size filter. Finally, areas within the images that were first identified in QuPath as being unsuitable for analysis (due to tissue folding, tissue loss or staining artefacts) were manually drawn around within MDV and these cells were labelled in the annotation table as unsuitable for analysis. This ensured that cells with incomplete information (due to tissue loss or folding) were not included in analysis and that cells were not incorrectly annotated (in the case of staining artefacts). In the end, there were 1,173,808 cells that were suitable for analysis across all the images. The resulting annotation table which, as well as containing sample information, now contained information on marker positivity for each cell, cell size and whether a cell was unsuitable for analysis or not, was exported from MDV as a CSV and imported into R version 4.2.1 for filtering and further categorisation [146–151]. This R script is available upon request and its steps are summarised in the following paragraph. Images that failed in the QuPath checks were not analysed but images that only partially failed by segmentation could still be analysed, focusing on the areas that were correctly segmented.

Cell Type	CD45	CD3	CD4	FOXP3	HLADR	CD16	CD20	PanCk
Epithelial								Pos
Other Immune	High	Neg			Neg	Neg	Neg	Neg
T Cell		Pos			Neg			
CD4 T Cell		Pos	Pos		Neg			
HLA-DR CD4 T Cell		Pos	Pos		Pos			
CD8 T Cell		Pos	Neg		Neg			Neg
HLA-DR CD8 T Cell		Pos	Neg		Pos			
Treg		Pos	Pos	Pos				
B Cell							Pos	
APC innate immune		Neg			Pos	Pos		
APC		Neg			Pos			
CD16 Innate		Neg				Pos		
Uncharacterised	Neg	Neg	Neg	Neg	Neg	Neg	Neg	Neg

Table 4: How cell types are defined according to marker positivity and negativity.

In R, the annotation table was first filtered to remove columns that were not necessary for analysis, remove cells that were too small or too large and cells that were annotated as 'unsuitable'. Category columns were added based on whether an image was from a lesioned or non-lesioned area of tissue, whether the animal had high or low pathology and the histopathology score of the animal. Next, columns were created for separate cell types, such as 'Treg' which was defined as positive if CD3, CD4 and FOXP3 markers were all detected in a cell above the z-score annotation cut-offs (**Table 4**). Absence of markers was also used to define certain cell types or subtypes, for instance a $CD3^+$ cell that was not positive for CD4 was called a $CD8^+$ T cell (**Table 4**). Then a 'cell type' column was created, which was populated depending on which of the new columns were positive, unless there was a conflict or the cells were negative for all columns. Cells that were not positive for any of the 'cell type' annotations were labelled as 'uncharacterised' as our panel could not denote the cell type, or, if they were otherwise uncharacterised but were high for CD45, they were labelled 'Other immune'. In case of a conflict, for example where a cell is labelled as both a $CD4^+$ T cell and an epithelial cell, an appropriate name was given to the cell according to the markers it was positive for. So, a cell that appeared to be both a $CD4^+$ T cell and an epithelial cell would be labelled 'CD4_T_cell_PanCk'. This allows for cases where signal spill over from neighbouring cells leads to annotations that do not make biological sense, so that they can be analysed rather than simply excluded from analysis. As we also wanted to see whether counts differed between major cell categories that encompassed multiple subtypes such as 'All T cells', 'All innate immune cells', 'All adaptive immune cells' etc, we also duplicated rows in the table to denoted which 'major' cell type each cell would belong to (if it did belong to one of our defined categories). Otherwise we would only be able to count cell subtypes. To avoid cells being counted multiple times due to row duplication, we counted using the distinct 'Object IDs' of each cell rather than the number of rows in the table. **Table 4** shows all of the conditions for cell type annotations (before combinations of cell types are added, as well as the 'major' cell type categories).

Once the cells had all been appropriately annotated, cell type abundances were calculated as a fraction of the total cells in each image, to account for variations in imaging area size and different images having different numbers of cells, even if they were the same size. Next, cell type abundances per sample were calculated by averaging the cell type abundances in each image associated with a particular sample. This was done to ensure that all statistical comparisons and associations were carried out at a sample-level rather than an image-level, as each image should not be treated as a distinct sample considering there are often several images per NHP. In comparisons where only lesioned samples or only non-lesioned samples were used for analysis, the region subtype was averaged per sample. These data were used to generate bar plots showing how cell abundances varied by region type, pathology class, a combination of these or vaccine/challenge groups (also split into lesioned and non-lesioned regions). Finally, the data were also used to generate correlation graphs showing whether any particular cell types correlated positively or negatively with histopathology score. The R script used to carry out this analysis is available upon request. For the bar plots, all data is shown below (**Figure 22** to **Figure 27**) and for the correlation graphs, only the significant correlations are shown (**Figure 28** to **Figure 30**). Depending on the region type the other correlation graphs can be found in **Supplementary Figure 3**, **Supplementary Figure 4** or **Supplementary Figure 5**, in which all non-significant plots are joined together.

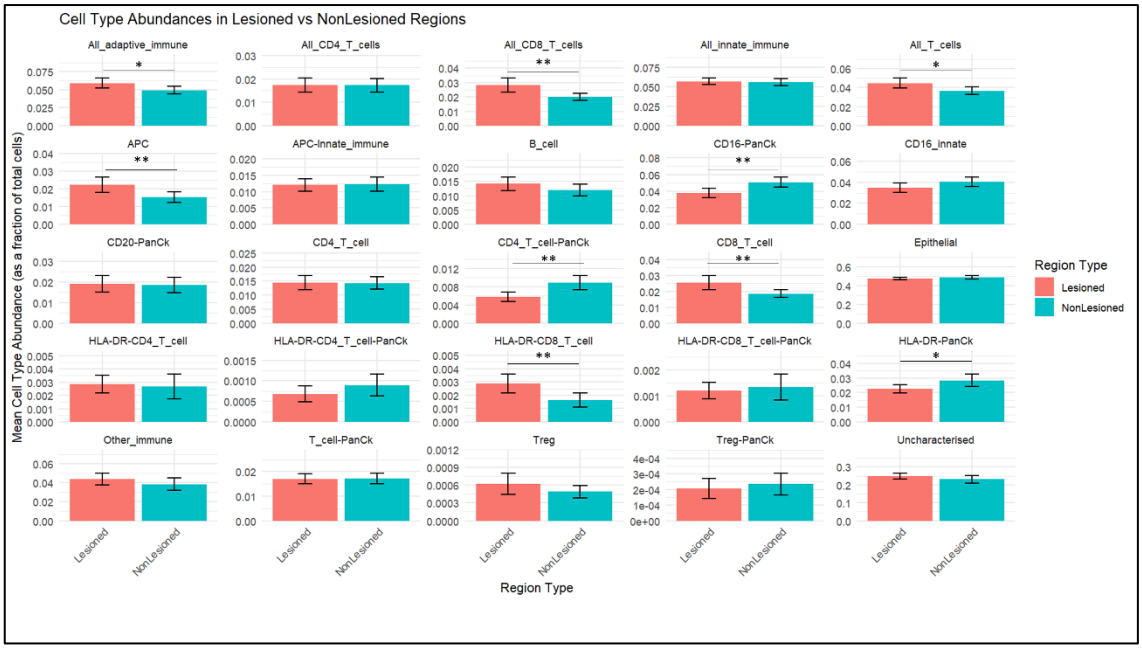

Figure 22: Cell type abundances by region type. Cell type abundances are compared using student's T test. Only significant p values are shown.

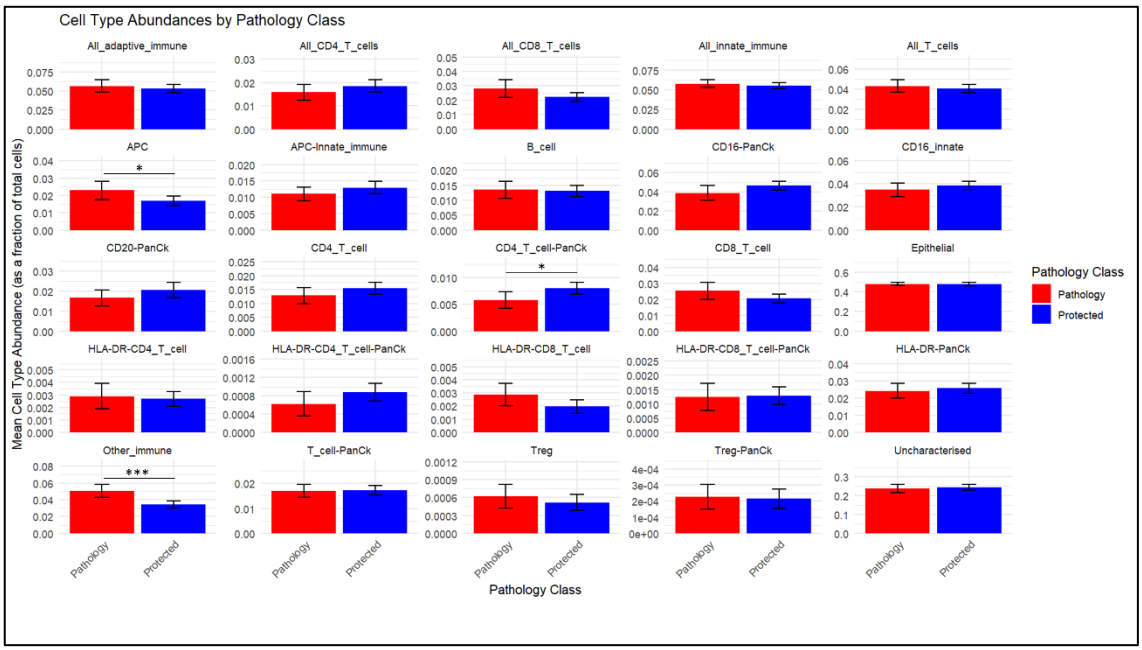

Figure 23: Cell type abundances by pathology class. Cell type abundances are compared using student's T test. Only significant p values are shown.

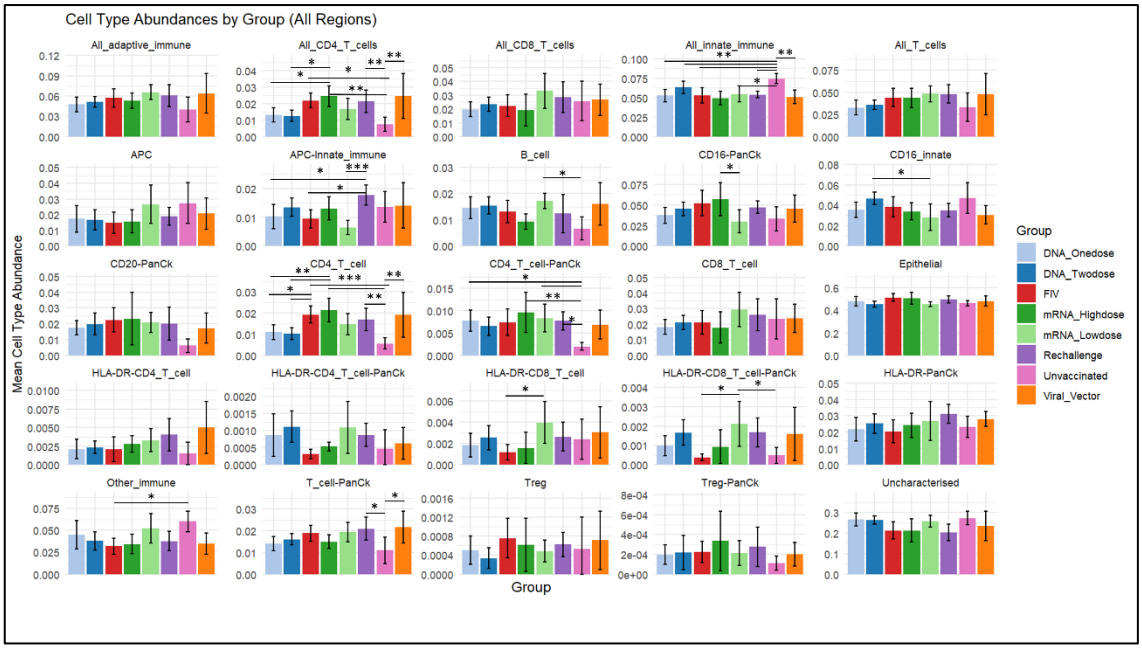

Figure 24: Cell type abundances by group, including both lesioned and non-lesioned regions. Cell type abundances across different groups compared using one-way ANOVA. Tukey's HSD is applied after a significant ANOVA to determine which pairs are significantly different. P values from Tukey's HSD are adjusted for multiple comparison testing based on the familywise error rate adjustment. Only significant p values are shown.

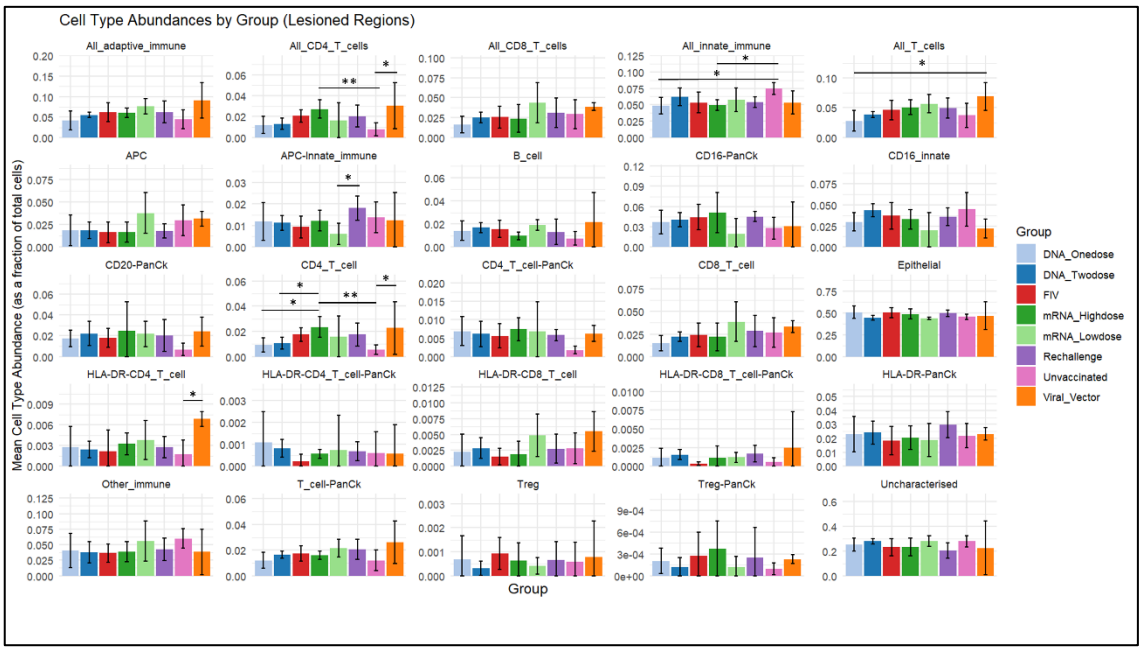

Figure 25: Cell type abundances by group, with lesioned regions only. Cell type abundances across different groups compared using one-way ANOVA. Tukey's HSD is applied after a significant ANOVA

to determine which pairs are significantly different. P values from Tukey's HSD are adjusted for multiple comparison testing based on the familywise error rate adjustment. Only significant p values are shown.

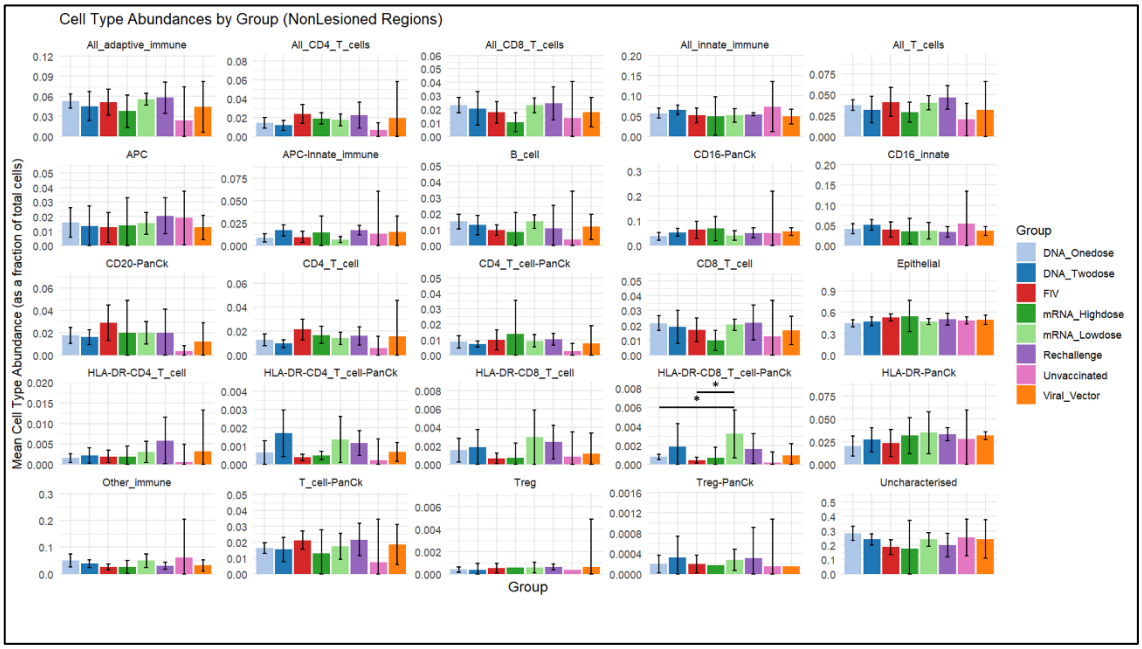

Figure 26: Cell type abundances by group, with non-lesioned regions only. Cell type abundances across different groups compared using one-way ANOVA. Tukey's HSD is applied after a significant ANOVA to determine which pairs are significantly different. P values from Tukey's HSD are adjusted for multiple comparison testing based on the familywise error rate adjustment. Only significant p values are shown.

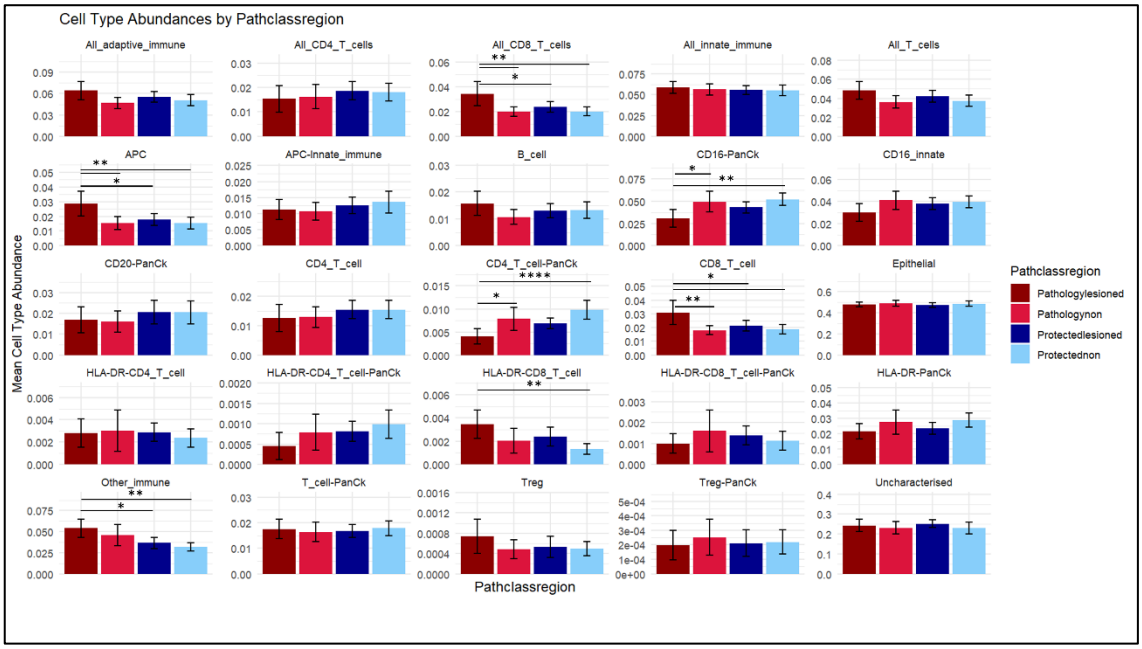

Figure 27: Cell type abundances by a combination of pathology class and region type. Cell type abundances across different groups compared using one-way ANOVA. Tukey's HSD is applied after a significant ANOVA to determine which pairs are significantly different. P values from Tukey's HSD are adjusted for multiple comparison testing based on the familywise error rate adjustment. Only significant p values are shown.

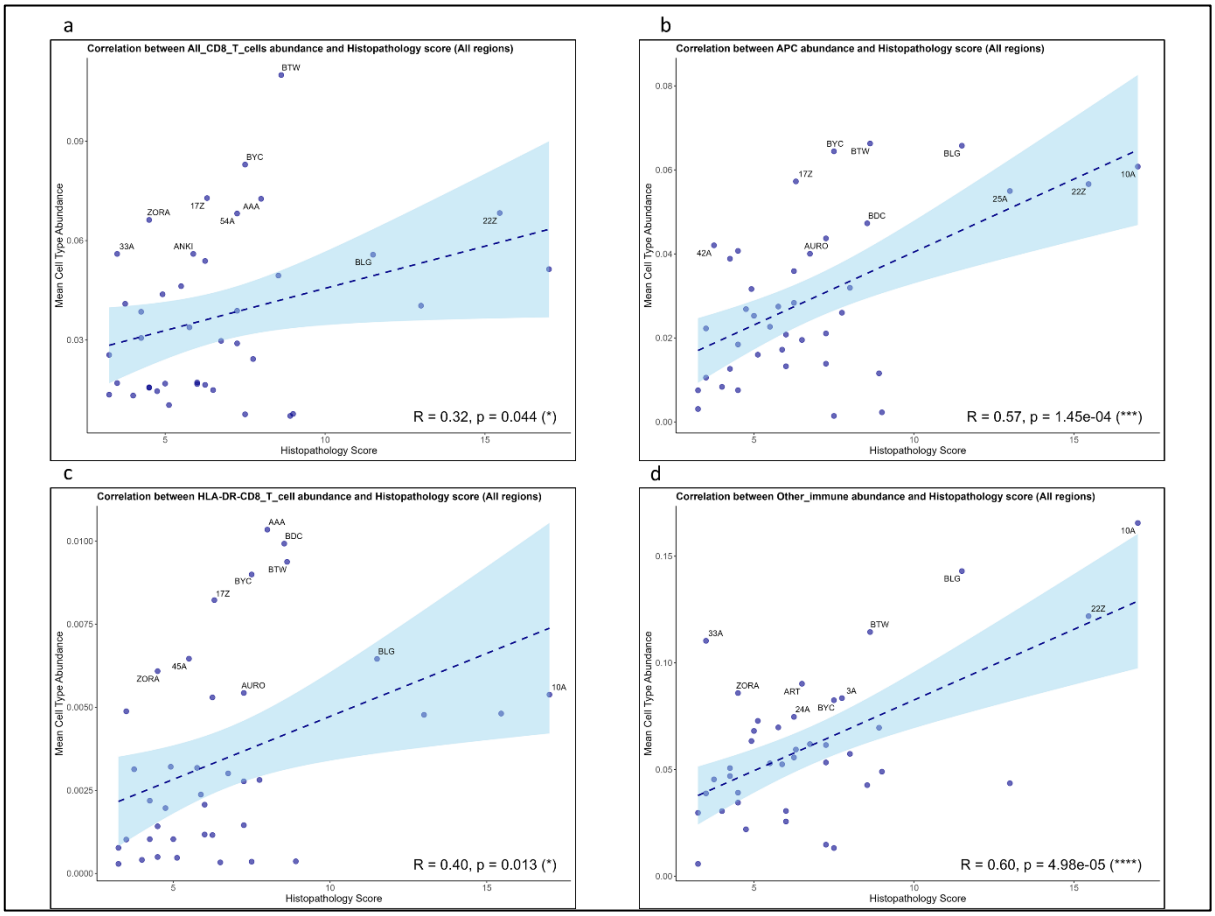

Figure 28: Correlations between cell type abundance and histopathology score across all region types. The dark blue dashed line is the regression line of the correlation between the cell type abundance and histopathology score, while the light blue colour represents the range of the associated confidence interval. Individual samples are overlaid as blue dots, with samples in the upper quartile of cell type abundance annotated according to NHP ID. The R value is Pearson's correlation coefficient and the p value is calculated using Pearson's correlation test. Only cell types that had significant correlations are shown. The cell type abundances with significant correlations are as follows: **a.** All CD8 T cell types. **b.** Antigen-presenting cells (APCs). **c.** HLA-DR$^+$ CD8 T cells. **d.** Other immune cells.

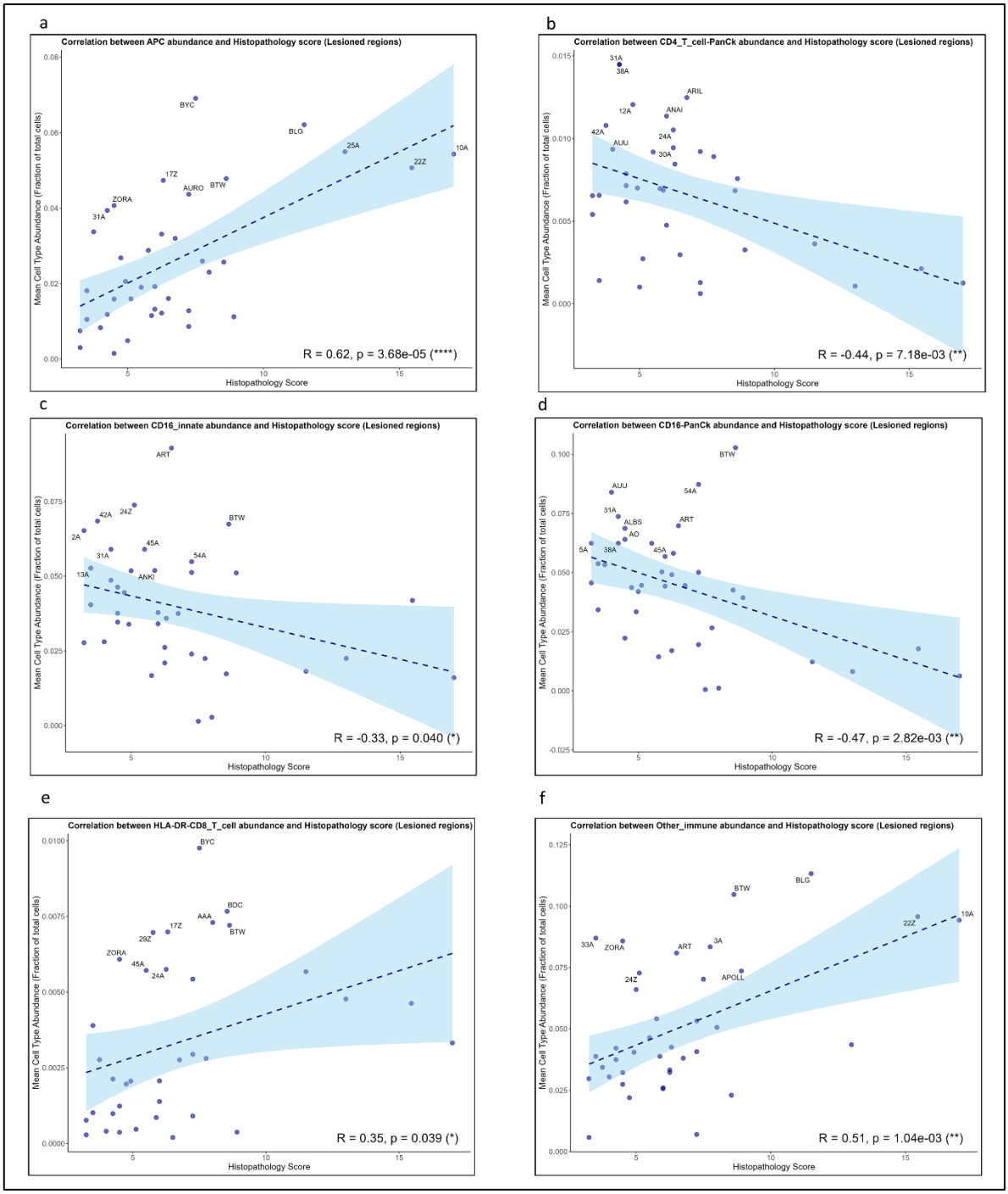

Figure 29: Correlations between cell type abundance and histopathology score across lesioned regions. The dark blue dashed line is the regression line of the correlation between the cell type abundance and histopathology score, while the light blue colour represents the range of the associated confidence interval. Individual samples are overlaid as blue dots, with samples in the upper quartile of cell type abundance annotated according to NHP ID. The R value is Pearson's correlation coefficient and the p value is calculated using Pearson's correlation test. Only cell types that had significant correlations are shown. The cell type abundances with significant correlations are as follows: **a.** Antigen-presenting

cells (APCs). **b.** CD4+ T cell- PanCk^{+} cell combination. **c.** CD16^{+} innate immune cells. **d.** CD16^{+}-PanCk^{+} cell combination. **e.** HLA-DR^{+} CD8 T cells. **f.** Other immune cells.

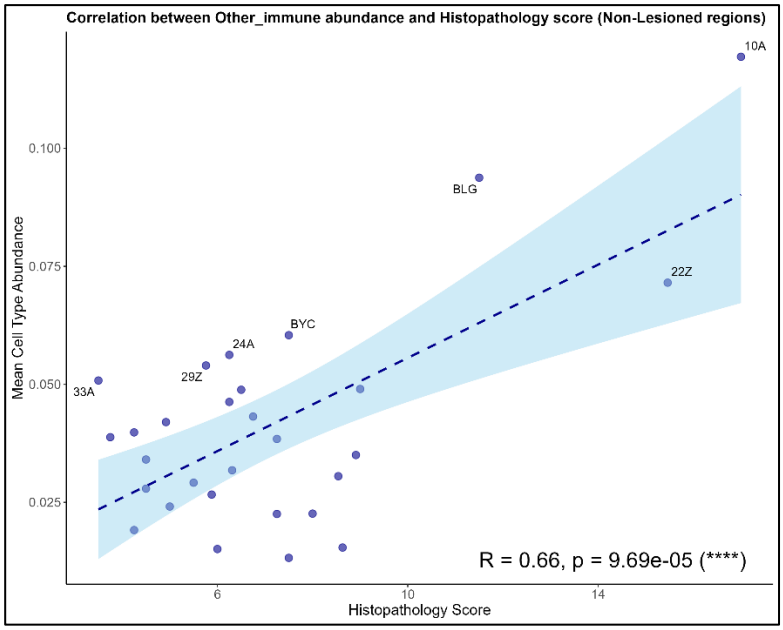

Figure 30: Correlation between 'Other immune cell' cell type abundance and histopathology score in non-lesioned regions. The dark blue dashed line is the regression line of the correlation between the cell type abundance and histopathology score, while the light blue colour represents the range of the associated confidence interval. Individual samples are overlaid as blue dots, with samples in the upper quartile of cell type abundance annotated according to NHP ID. The R value is Pearson's correlation coefficient and the p value is calculated using Pearson's correlation test. Only this cell type had a significant correlation with pathology score across non-lesioned regions.

2.5. Discussion

Whole-slide quantification of IHC staining demonstrated that, at least in a subset of samples, T and B cells correlated more strongly with pathology scores (**Figure 14**) than macrophages and neutrophils, even when machine learning segmentation was used to more accurately quantify macrophages and neutrophils (**Figure 16**). The MPO staining for neutrophils was quite poor and in the original thresholding approach, the staining was present in such low fractions of total area that the software did not differentiate between MPO staining levels in some tissues and instead rounded the values. The cell counting improved the CD68 analysis, which had much more

background than other stains, which would often be picked up by the original thresholding approach. Low sample size (n=12 samples of interest) likely contributes to the low statistical significance of the associations observed in our IHC work. We found the ACE2 staining to be quite poor across most of the samples and by counting BALT sites in H&E-stained whole-slide images we found no association between BALT and pathology, which may be due to the fact that NHPs have background levels of BALT even in the absence of infection [140]. In whole-slide RNAscope analysis we saw an association with spike mRNA and histopathology despite the very small amount of spike mRNA that could be detected in each slide (**Figure 14**). This suggests that a failure to control viral replication results in greater pathology. The increased immune cell (particularly T and B cell) infiltration may be attributed to this failure to clear the virus, as they may continue to be recruited to lung tissue in response to the remaining virus, driving immunopathology. Further work is needed to dissect potential mechanisms of immunopathology that may be at play, and whether or not different mechanisms associate with any of the vaccination regimens. Our whole-slide IHC staining and H&E analysis was limited, considering that we could not look at more than one marker at a time and we did not therefore have co-staining information which could help identify more cell types and subtypes. For instance, while we observed a correlation between the CD3 stain across the slide and histopathology score, we do not know if this was due to a particular T cell subset being more prevalent or whether all T cell subsets were more prevalent in pathology. As we started to see trends emerge with our limited samples of interest and our IHC staining, we then pursued more in-depth multiplex analysis with a more robust cell segmentation workflow. The ARIVIS Vision4D software is not open-source and our segmentation pipeline was trained on a limited set of samples. While visually the machine learning training appeared successful for identifying cells of interest, we need to be careful in drawing major conclusions from such a programme that has not been widely validated.

SARS-CoV-2 infection and its associated pathology is known to vary spatially, with some parts of the lung having greater pathology than others [45]. Therefore, we decided to focus our analysis from this point on lesioned and non-lesioned areas of the lung. We hypothesised that this

pathology-informed approach could provide better mechanistic insights as we can compare whether particular cell types are more or less prevalent in lesioned or non-lesioned areas in NHPs that fall into different categories (vaccine group, pathology vs protected etc). Considering the macaque model typically has mild-moderate infection, it also allows us to focus on the most severe damage in the lung tissue, which may be more likely to recapitulate human severe COVID-19. As we noted that most of the lung tissue appears to be relatively non-lesioned even in high-pathology animals, this also means that any findings related to pathology can be 'diluted' by the relatively healthy areas of the lung when whole-slide analysis is carried out rather than pathology-informed analysis.

With the Cell DIVE we set up a multiplex imaging panel that allowed for many stains to be observed on the same slide. While much time was spent optimising the panel and testing markers, many of the markers were unsuitable for analysis at the end. Most optimisation of antibody staining has been carried out on human and mouse data and this is also true for the Cell DIVE, of which there is much more information available for tissues from humans and mice as to which markers are suitable up to particular bleaching steps etc. However, while our panel was relatively small compared to what is theoretically possible with the Cell DIVE platform, we were able to gain insights into several important cell types and subtypes in the lung parenchyma in the context of vaccination and subsequent challenge. To our knowledge this has not been done before in the NHP model or in human lung tissue. The between-run variations we observed in staining could be due to fluorophore degradation between the staining runs and/or the weakening of the lasers in the Cell DIVE microscope. We also noted some samples had higher background staining for particular markers than others. Given this variation, z-score normalisation per-image was important to control for this and ensure that marker positivity was defined in the context of the other cells in a particular image. By visual inspection in MDV this appeared to work very well to ensure that background staining was not creating false-positive marker signals on cells. The tissue folding and tissue loss between staining rounds was a problem which we had to get around by manually annotating cells in these areas and we also did this for cells in areas with staining

artefacts. This manual approach was time-consuming but ensured that false positive cells or cells with incomplete staining information (staining on some rounds but not others owing to tissue movement etc) were not included in analysis. The exclusion of these cells from analysis means that while they do not bias the dataset with false positives, there are less cells to be analysed, so areas that were particularly high or low in certain cell types may have been removed. However, across all images we do not expect a particular cell type to be excluded to a greater extent than others, so other than smaller cell counts, we do not expect this to introduce bias in our results. For segmentation, we used DeepCell/Mesmer [145] which is a widely used cell segmentation algorithm that is trained on over 1 million manually labelled cells. The fluorescence intensity values were not always consistent across samples (**Figure 21**), so sample-level z-score normalisation was important to ensure that for markers with high variability across samples, cells were correctly annotated within samples. CD68 is shown in **Figure 21** but while the fluorescence intensity was consistent across samples, the actual staining was very grainy and had high background, so there was no z-score value that could consistently annotate $CD68^+$ cells (macrophages) to a satisfactory level. This was similar to the high background we saw in our IHC, despite the fact that a different clone was used. In future, more staining optimisation for this marker may need to be carried out or another clone may need to be tested.

When relating these findings to human COVID-19 it is important to note that rhesus macaques and humans have some immunological differences, including in how cell types are defined by marker positivity [93]. While these differences have been well characterised in peripheral blood [93], there is limited data on characterising these differences in tissues and even less on which antibodies work in FFPE tissue for immunofluorescent staining. Our multiplex marker panel allowed us to define particular cell types and subsets with confidence thanks to positive or negative co-staining between markers, however broader categories were needed in some cases to account for gaps in our panel and may encompass multiple cell types. For example, the cell category ‘APC’ (for antigen-presenting cell) was used to characterise cells that expressed HLA-DR but were not T cells and ‘Other immune’ was used to categorise cells that could not be

classified in detail due to the limitations of our panel size, but still had high enough CD45 staining to broadly characterise the cells as immune cells. In rhesus macaques the majority of NK cells in the lung express CD16, although there is also a sizable CD16-negative NK cell population and overall NKG2 is a good NK cell marker in macaques, but was not included in our panel [152]. Therefore, in the context of our annotations, most NK cells will fall into the 'Innate immune' category, while dendritic cells, monocytes and macrophages will fall into the 'APC-Innate immune' category due to their co-expression of CD16 and HLA-DR. Macaque granulocytes (including neutrophils) do not express CD16 [153,154], so cells categorised as 'Other immune' could include granulocytes such as neutrophils, eosinophils and mast cells, or the pathogenically-activated neutrophils and monocytes that are termed myeloid-derived suppressor cells (MDSCs) and have been implicated in COVID-19 [155]. Cells we characterised as $CD4^+$ T cells may also include some double-positive ($CD4^+$ and $CD8^+$) T cells, which are more frequent in rhesus macaques when compared to humans. In peripheral blood from rhesus macaques double-positive T cells have been found at a median frequency of 5.3% of singlet cells [93]. As HLA-DR expression on T cells is known to associate with T cell activation, particularly in COVID-19 [156] we included HLA-DR^+ $CD4^+$ T cells and HLA-DR^+ $CD8^+$ T cells as categories, although there may be some cases where signal spill over of APCs next to T cells results in this phenotype being classified. As our panel focused primarily on immune cells, we were not able to image fibroblasts and could not image endothelial cells in the end as the CD31 stain we optimised had high background.

Across all of the comparisons we made, there were many significant correlations between cell type abundances and histopathology or vaccine group. Firstly, in lesioned vs non-lesioned regions (**Figure 22**), we observed that the 'all adaptive immune' cell category was up, along with some of its subsets, namely the T cells ('All T cells') and all of the cytotoxic T cell associated categories 'all $CD8^+$ T cells', '$CD8^+$ T cells', 'HLA-DR^+ $CD8^+$ T cells'. Given that APCs were also significantly higher in lesioned vs non-lesioned regions, this could point to antigen presentation to $CD8^+$ T cells taking place to a much greater extent in lesioned regions. Given the heterogeneity of viral infection and distribution to the lung, this could be expected [45]. These data also suggest

that $CD8^+$ T cells rather than $CD4^+$ T cells dominate the adaptive immune response in lesioned areas of the lung, although as a whole adaptive immune infiltration is increased. In contrast, non-lesioned regions were significantly higher in cell types that are doubly positive as epithelial cells and immune cells, specifically the categories $CD4^+$ T cell-PanCk, HLA-DR-PanCk and CD16-PanCk. This suggests that in non-lesioned areas of the tissue, where pathology has not manifested, innate cells are closely associated with the epithelium, as are $CD4^+$ T cells. Mechanistic studies would be required to determine whether there is a causative effect of these cells in mediating protection in these parts of the lung compared to the lesioned parts, or if these cell associations merely indicate an absence of immunopathology rather than active protection from it. When animals are broadly categorised as high-pathology or low-pathology, agnostic of region type (**Figure 23**), APCs and 'Other immune' cells are higher in high-pathology while $CD4^+$ T cell-PanCk cells are significantly higher in protected tissues, as they were in non-lesioned tissues. The APC finding may again speak to the role of ongoing antigen presentation in areas of viral spread, while the highly significant increase in the 'Other immune' cell category may relate to the known increase in neutrophils in the lung of severe COVID-19 cases in human disease (as seen in BAL fluid [39]), demonstrating that this model recapitulates that aspect of pathology. If this 'Other immune' cell category consists primarily of neutrophils, as would be expected from the vast literature on human COVID-19 lung pathology (summarised in **Section 1.2.3**) and even in the periphery [157,158]**,** then the human lung studies that do not take spatial information into account would be recapitulated here, as this category is seen to be highly correlated with quantitative histopathology scores in our NHP cohort, regardless of region type (**Figure 28** to **Figure 30**). This demonstrates that neutrophil infiltration is not spatially restricted to lesioned areas of the lung and in fact our data suggests that the association is even stronger in non-lesioned regions of the lung (**Figure 30**), where we've shown adaptive immune cells to be less prevalent (**Figure 22**). This 'Other immune' cell category was the only cell type associated with histopathology score in non-lesioned regions (**Figure 30**).

When cell type associations were grouped by a combination of pathology class and region type (termed 'pathclassregion'), $CD8^+$ T cells (and their activated and non-activated subsets) and APCs are significantly increased in 'pathology lesioned' in particular, demonstrating again that ongoing antigen presentation to $CD8^+$ T cells may be associated with lesions in the lung, particularly in animals with higher histopathology scores. However, without spatial statistics to back up this hypothesis, it could also be the case that APCs and $CD8^+$ T cells are both increased in these areas but do not interact. Returning to these images and looking at T cell markers along with HLA-DR, we anecdotally noted some co-localisation in lesioned areas of high-pathology animals such as 10A (**Figure 31**). Both CD16-PanCk cell and $CD4^+$ T cell-PanCk cell abundances were particularly higher in 'protected non-lesioned' areas and particularly lower in 'pathology lesioned' areas. Correlations between cell type abundances and histopathology scores revealed several cell type associations, beyond the strongest associations which were with the 'Other immune' cell category as described previously. Most of the significant correlations were restricted to when only lesioned regions were analysed (**Figure 29**) but others, including 'All $CD8^+$ T cells', 'APCs' and 'HLADR$^+$ $CD8^+$ T cells' were present in region-agnostic histopathology score correlations (**Figure 28**). The APC association was particularly strong. However, the relative significance of these correlations may be skewed by the fact that we had more images of lesioned regions than non-lesioned regions (**Table 2**) and the $CD8^+$ T cell types were associated with lesioned vs non-lesioned in the pathology-agnostic comparison (**Figure 22**), but not in the pathology vs protected region-agnostic comparison (**Figure 23**). In correlations restricted to lesioned regions (**Figure 29**), HLADR$^+$ $CD8^+$ T cells were positively associated again, as were APCs and the aforementioned 'Other immune' population. The quantitative associations between $CD8^+$ T cells and histopathology score demonstrate another feature of human severe COVID-19 pathology, as $CD8^+$ T cells were found to be increased in post-mortem samples from COVID-19 patients [10]. Negative correlations with histopathology score were also found in lesioned regions, which may be linked to protection from severe disease considering the spatial context. These protection-associated cell types included '$CD4^+$ T cell-PanCk', 'CD16-PanCk' and 'CD16-innate'. '$CD4^+$ T cell-PanCk' and 'CD16-T cell-PanCk' are likely linked to

$CD4^+$ T cells and innate immune cells such as alveolar macrophages or monocytes (respectively) being closely associated with epithelial cells. However, rather than being associated with protection, it is possible that these cell types are associated with an absence of pathology, owing perhaps to peripheral control of viral infection by neutralising antibodies for example, in the case of vaccinated animals. This may be the case here, as alveolar macrophages (which are spatially close to epithelial cells, so may contribute to both our 'CD16-PanCk' and 'CD16-innate'populations) are depleted in severe COVID-19 [159]. However, the '$CD4^+$ T cell-PanCk' association with protection may warrant further investigation as a protective neighbourhood, particularly considering the association between $CD4^+$ T cell abundances in many of the vaccine groups when compared to unvaccinated animals (**Figure 24** and **Figure 25**).

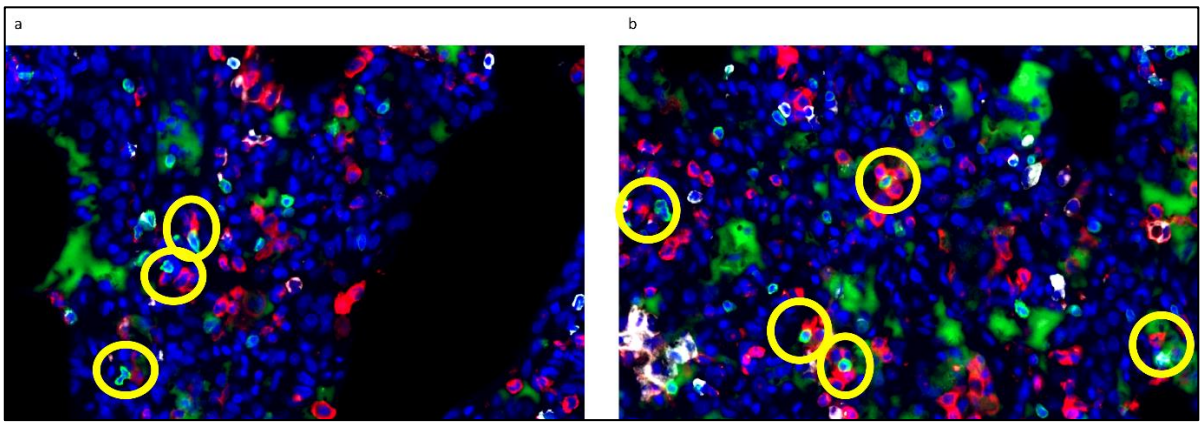

Figure 31: Example of $CD8^+$ T cell and APC cell co-localisation. Selected screenshots from multiplex immunofluorescence images in the highest-pathology NHP (10A). Yellow circles indicate areas where $CD8^+$ T cells are in contact with (or close proximity to) HLA-DR^+ cells. Stains are CD3 (green), CD4 (white) and HLA-DR (red).

In the between-group comparisons (vaccine groups, re-challenge, unvaccinated), there was only one significant association in non-lesioned regions, which was that 'HLA-DR^+ $CD8^+$ T cell-PanCk' cells were higher in low dose mRNA NHPs compared to NHPs that received one dose of the DNA vaccine or received the FIV vaccine. Across all regions and in lesioned regions (**Figure 24** and **Figure 25**), $CD4^+$ T cells were generally higher in vaccinated NHPs when compared to unvaccinated NHPs, apart from in DNA-vaccinated animals. Interestingly, this was not true of

the activated $CD4^+$ T cell subset (expressing HLA-DR), apart from in the viral vector vaccine group compared to unvaccinated, in lesioned regions (**Figure 25**). The $CD4^+$ T cell associations with vaccination (and in all regions, also with re-challenge) is an interesting finding considering that these vaccines were all delivered by intramuscular routes and not through mucosal delivery. This suggests that $CD4^+$ T cells induced by vaccination in the periphery may be able to make their way to the lung upon infection, where they are present by this timepoint, day 6/7 post-challenge. While it is not currently possible to profile antigen-specificity in tissue to know if this is the case for these cells, the association between vaccination and this cell type being more abundant in the lung post-challenge suggests this may be the case. Further to this point, the viral vector vaccine (ChAdOx1) [137], which was the most widely used vaccine against SARS-CoV-2 during the pandemic and was highly successful in preventing severe disease, was the only vaccine group that induced more activated ($HLA\text{-}DR^+$) $CD4^+$ T cells in the lung compared to abundances in unvaccinated animals. The fact that they are showing activation markers in these animals provides further evidence that they may be antigen-specific, although further work would be required to prove this. Typically, HLA-DR expression on T cells is associated with more severe outcomes [54,156,160,161] in COVID-19. However, despite being associated with severe disease, HLA-DR expression on T cells has been found to associate with survival from this severe disease [156]. In particular, survivors tended to have more $HLADR^+$ and $CCR5^+$ $CD4^+$ T cells. Broadly, T cells in the airways of COVID-19 patients have been found to associate with improved outcomes [34]. The protective lung profiles in a vaccination context have not been studied in this way. Studies that looked at the BAL fluid of vaccinated individuals found that adaptive immune responses to SARS-CoV-2 could only be found in convalescent individuals, not those who were only vaccinated [55,56]. Here, we provide some evidence that upon challenge, $CD4^+$ T cell abundances in the lung parenchyma are increased in vaccinated animals to a greater extent than in unvaccinated animals, which is similar to what is seen in T cell subsets in BAL fluid in humans who are vaccinated and infected vs just infected [55]. In the case of re-challenged animals, the increased $CD4^+$ T cells may be due to local tissue-resident immune memory, although we were not successful in using tissue-residency markers in our panel as the staining was not consistent. In

comparison to vaccinated animals, unvaccinated animals tended to have higher abundances of 'All innate immune' cells (**Figure 24**) and given the role of innate immune cells in driving COVID-19 lung pathology in human studies (which have largely not looked at vaccinated people, **Section 1.2.3**), this lines up with expectations. 'CD4$^+$ T cell-PanCk' cells appeared particularly low in unvaccinated animals and high in animals that received high-dose mRNA (**Figure 23**), which aligns with these groups being associated with high and low pathology, respectively.

Uncharacterised cells did not differ across any of our comparisons, which likely means that any non-immune and non-epithelial cells, which would not be captured in our panel, are not contributing to the cell type variation across our comparisons. In humans, an increase in fibroblasts (which we cannot detect in our panel) was associated with fatal COVID-19 [33]. Given the mild to moderate range of pathology seen in rhesus macaques [87], we would not expect fibrosis (also associated with late-stage repair [10]) to play a major role in pathology in our NHP lung samples. There were no signs of Th2-associated VAED (**Section 1.6**), as we would expect granulocytes such as eosinophils (which would come under 'Other immune') to be elevated in high-pathology vaccinated animals compared to unvaccinated in this case. Instead, this category is only associated with significant increase against another group in the case of unvaccinated animals (**Figure 24**).

The COSMIC study [10] showed that in severe COVID-19 airways, there was an increased presence of cellular neighbourhoods that consisted of immature neutrophils next to CD8$^+$ T cells. Given that we may have both increased neutrophils and CD8$^+$ T cells in high pathology there could be a similar mechanism at play at the more severe end of rhesus macaque COVID-19 lung pathology. However, we cannot carry out spatial analysis because the tissue loss means that there are 'holes' in our images which are difficult to account for in calculation of spatial statistics. The researchers that developed the spatial statistics for the COSMIC study are working on an updated tool to account for these 'holes' which we hope to use in the future to look at spatial neighbourhood associations across all our cell types and comparisons.

There are some limitations to consider from our cell type abundance analysis related to the Cell DIVE imaging. Firstly, that many of the abundance values on the graphs have large confidence intervals owing to intra-group variability. Secondly, the viral vector vaccine group had fewer samples, owing to the fact that we only used samples with the same cull timepoint as all other NHPs (see **Supplementary Table 1** and **Section 1.7**). Thirdly, some of the images contained BALT. This has been annotated and could be removed in future analysis but has been kept for now, considering that BALT may have a role to play in protection or pathology.

As we hypothesised, particular cell type abundances correlated with histopathology scores (**Figure 28** to **Figure 30**), shedding light on potential cell type correlates of protection and pathology in the lung parenchyma. The $CD4^+$ T cell-PanCk cell subset was found to be associated with lower histopathology scores in in lesioned areas although as a whole these were generally higher in non-lesioned areas, suggesting that $CD4^+$ T cells closely associated with epithelium may be protective against the development of pathological lesions and their more severe forms. We also hypothesised that rhesus macaque model may recapitulate some aspects of human severe COVID-19. The 'CD16-PanCk' and 'CD16-innate' populations, which may be analogous to alveolar macrophages, are depleted in human severe COVID-19 [159] as discussed and this may be why we found their cell abundances to be associated with protection, with the rhesus macaque model recapitulating this feature of human pathology. Other features that were recapitulated in this model include the association of $CD8^+$ T cells and neutrophils with severe COVID-19 lung tissue [10,39]. Another hypothesis we had was that prior vaccination or challenge would associate with cell type abundance in lung parenchyma. $CD4^+$ T cells were found to be more abundant in most vaccine groups (and the prior challenge group), when compared to unvaccinated animals while the opposite was true of innate immune cells (**Figure 24** and **Figure 25**). This demonstrates that prior immunity (conferred by prior vaccination or challenge) does impact cell type abundances in the lung parenchyma and suggests that antigen-specific $CD4^+$ T cells may make their way to the site of infection after previous immune priming. Apart from activated $CD4^+$ T cells being associated with viral vector vaccination in lesioned regions,

we did not note any other significant associations between different vaccinations and cellular profiles, with trends being generally associated with vaccine efficacy, as less effective vaccine regimens did not induce 'protective' immune cell profiles that were significantly different to unvaccinated NHPs in many instances.

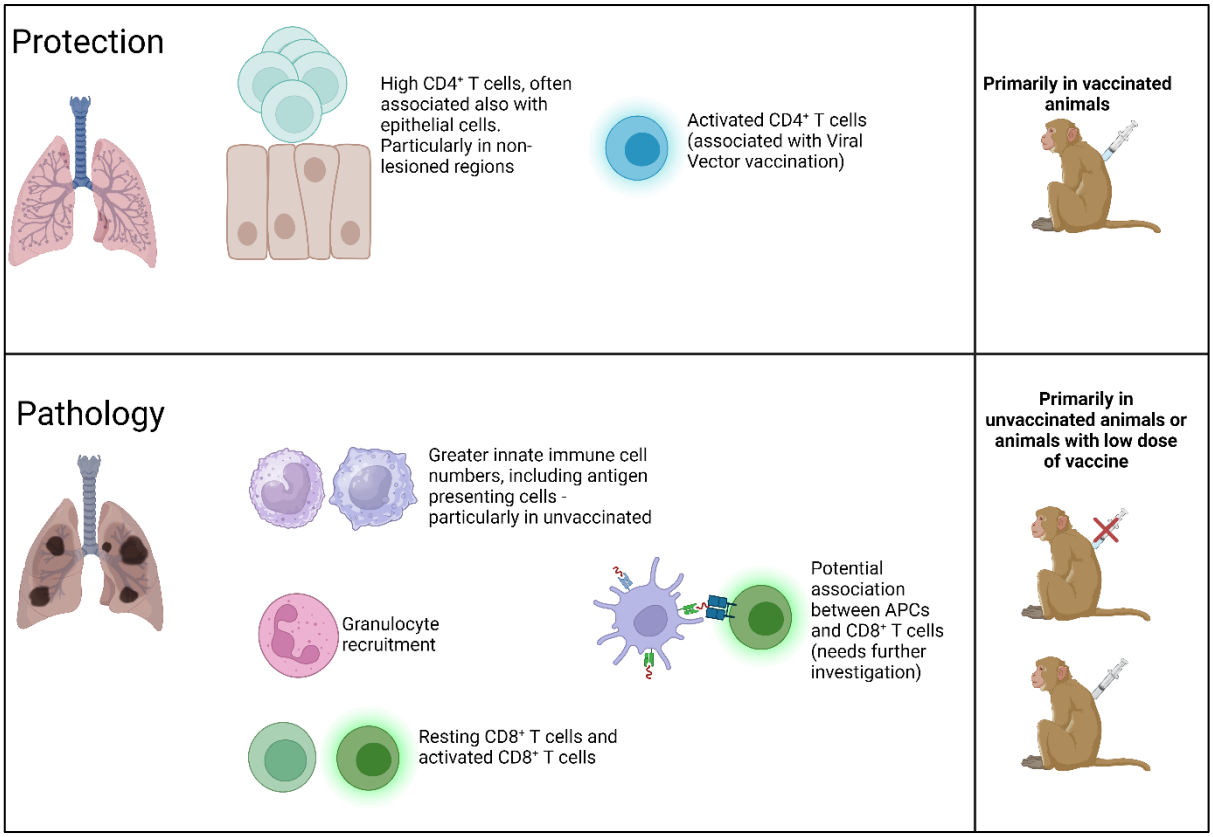

Figure 32: Graphical summary of Chapter 2 findings.

Chapter 3: Transcriptomic characterisation of lesioned and non-lesioned tissue regions

Spatial transcriptomics allow for analysis of gene expression in specific regions of interest (ROIs) within tissues [162]. Our collaborators based in the John Radcliffe hospital have demonstrated that spatial transcriptomics can be used to characterise mild and severe pathology in lung tissue of recently deceased COVID-19 patients, giving insights into immune-mediated mechanisms of pathology [30]. Transcriptomic analysis of Syrian hamster lung tissue revealed potential signatures of VAED in a Th2-biased alum-adjuvanted SARS-CoV-2 vaccine preparation [132]. We hypothesised that by comparing transcriptomic signatures in pathological areas of lung tissue across our NHP samples, we will be able to determine whether pathology in vaccinated NHPs differed from that in unvaccinated NHPs. This could shed light on both protective mechanisms and/or mechanisms of immune enhancement of pathology. For the latter, it will be of particular interest to compare transcriptomic signatures in vaccinated high-pathology NHPs with the signatures observed in the Syrian Hamster model of VAED [132] and to see whether pathways associated with the cells found in **Chapter 2** are present. By using spatial transcriptomics, we will also be able to provide spatial context to our findings, which could lead to more detailed insights into the cell types and pathways involved in mediating pathology when compared to bulk approaches. For our spatial transcriptomics experiment, we chose to use the NanoString GeoMx DSP platform because of its widespread use with human FFPE tissue and its whole-transcriptome capabilities [163]. This platform allows for selection of ROIs across four slides, which we profile the RNA transcripts within. Immunofluorescent morphology markers are added prior to ROI selection, so that IF imaging of the tissue samples can inform ROI selection. We used three IF markers; CD68, Pancytokeratin (PanCk) and SYTO 13 (**Supplementary Table 3**). CD68 marks macrophages, PanCk marks epithelial cells and SYTO 13 is a nuclear stain. The spatial transcriptomics experiment was restricted to our samples of interest (**Table 1 and Figure 6).**

The human whole-transcriptome atlas (WTA) probe set from Nanostring was used on the NHP lung tissue samples of interest. RNA probes with photocleavable oligonucleotide tags bind short sequences of RNA associated with particular human genes. UV light decouples the oligonucleotide tags from the RNA in the selected ROIs. These are then retrieved from the surface of the tissue and the oligonucleotide tags from each ROI are then deposited in separate wells of a 96-well microtiter plate. The tags contain a DNA barcode which corresponds to the particular tag and therefore a particular RNA sequence, which allows for analysis of the transcripts in each ROI when the plate has undergone library prep and next-generation sequencing (NGS). Nanostring have provided a spreadsheet outlining the % sequence identity between human and NHP genes/probes in their WTA panel of over 18,500 genes. This states that 12,597 genes have >= 95% identity, 16,375 have >= 90% identity, 17,203 have >= 85% identity and 17,502 have >= 80% identity. 5084 genes have 100% identity. We had been in touch with a group at the Oregon Health and Science University led by Professor Jacob Estes. This group have carried out spatial transcriptomic studies (unpublished) on rhesus macaques with the same technology we are using and have reassured us that there is a high level of cross-reactivity between the human and NHP RNA with the Nanostring probes and they have found only a relatively small number of genes which do not cross-react. Therefore, we were happy to proceed with this spatial transcriptomic study.

We hypothesise that through spatial transcriptomics profiling, we can determine whether high-pathology vaccinated animals have experienced VAED. If VAED has occurred, we expect to find Th2-associated pathways in these animals and if VAED has not occurred, we expect to find similar pathways to those in unvaccinated pathology, in which case we can classify the high-pathology vaccinated animals as experiencing vaccine failure. For this hypothesis, we will focus particularly on 10A, which experienced a greater histopathology score than unvaccinated animals despite receiving one dose of a DNA vaccine (**Figure 6**). We also hypothesise that transcriptomic responses in the rhesus macaque model in response to SARS-CoV-2 challenge may mimic the

responses seen in human disease and that vaccination or previous challenge may induce different pathways upon challenge.

3.1. Spatial transcriptomics experiment

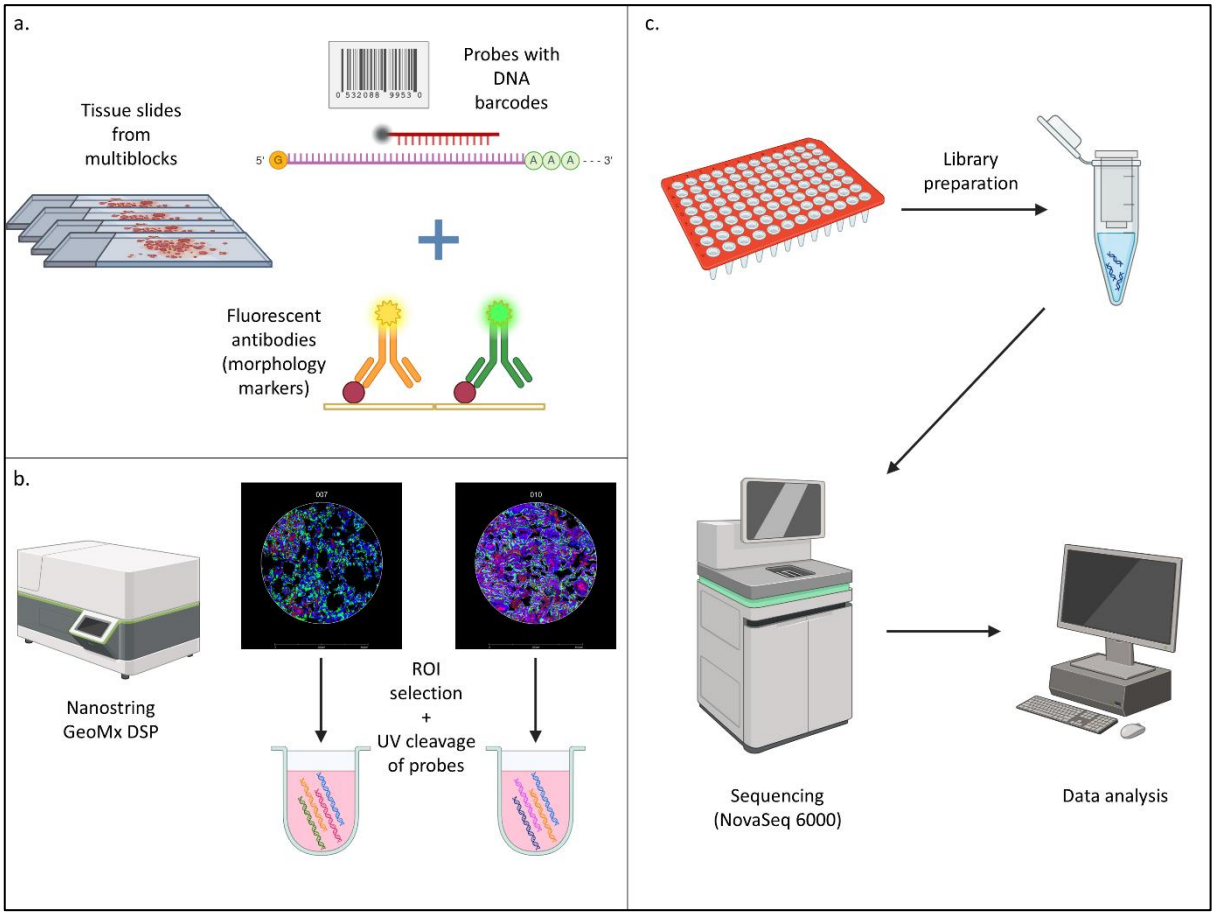

Figure 33: Spatial transcriptomics experiment overview. a. DNA-barcoded probes from Nanostring's whole-transcriptome atlas (WTA) panel were added to the four tissue slides for analysis, followed by a nuclear marker (Syto13) and fluorescent antibodies (CD68 and PancCk). **b.** ROI selection carried out on the GeoMx DSP (Nanostring), showing representative images of ROIs from the experiment. DNA probes within chosen ROIs are cleaved and added to separate wells of a 96-well plate. **c.** Library preparation and PCR are carried out on the plate from the GeoMx DSP experiment, followed by sequencing and data analysis. Created with Biorender.com.

In our experiment, we used 4µm lung sections from the NHPs of interest (**Table 1**). The Pathology group at UKHSA Porton Down used the previously-described multiblocks to mount 4 tissue sections of interest (**Table 1 and Figure 6)** onto each of the 4 slides used for the spatial

transcriptomics experiment. Manual slide preparation was carried out according to the manufacturer's instructions (Nanostring, MAN-10150-01). Briefly, 4μm tissue sections were mounted on Superfrost Plus slides and baked at 65 °C for two hours. The tissues were then deparaffinised and rehydrated before undergoing antigen retrieval in a 1X Tris-EDTA solution at pH 9. Next, proteinase K digestion was carried out to expose the RNA targets before the tissues were washed for 1 minute in neutral-buffered formalin to preserve tissue morphology. The RNA probes (GeoMx WTA panel, NanoString, 121401102) were added to the tissue and were incubated overnight at 37 °C for probe hybridisation. The next day, a set of washes were carried out to remove off-target probes before the addition of the morphology markers. CD68, PanCk and SYTO 13 IF markers (**Supplementary Table 3**) were used for visualisation and were added to the slide for 100 minutes before the slides were inserted into the GeoMx DSP. Dr Joanna Hester and Dr Amy Cross assisted with the running of the GeoMx experiment.

As previously described in **Chapter 2**, lesioned and non-lesioned areas were annotated by Dr Javier Salguero, an experienced veterinary pathologist, based on sequential sections from the same lung blocks used for the work described in **Chapter 2**. Within these areas of interest, we selected 4 lesioned and 3 non-lesioned 650μm-diameter circular ROIs on the GeoMx for the majority of tissue sections, guided by morphology staining of our slides on the Nanostring GeoMx DSP machine as well as the histopathological annotations (**Figure 34**). Representative images taken on the GeoMx DSP can be seen in **Figure 35** (whole-slide) and **Figure 36** (ROIs). Some extra ROIs were taken from some samples with larger annotated areas and only three were taken from archival tissues from unchallenged rhesus macaques. A summary of the ROIs taken can be seen in **Supplementary Table 4**. After the probes from each ROI were dispensed into the 96-well plate, the plate was kept at -20 °C until library preparation. RNAscope was carried out on sequential slides from the same blocks used for the GeoMx experiment (as described in **Section 2.1.1**) and the resulting images were overlaid onto the GeoMx using QuPath [144] version 0.5.0. There was no indication of viral RNA being present in any of the ROIs. As seen previously

(**Section 2.1.2**), the amount of observable viral RNA in the lung tissue at this timepoint is very low, even in animals with high histopathology scores.

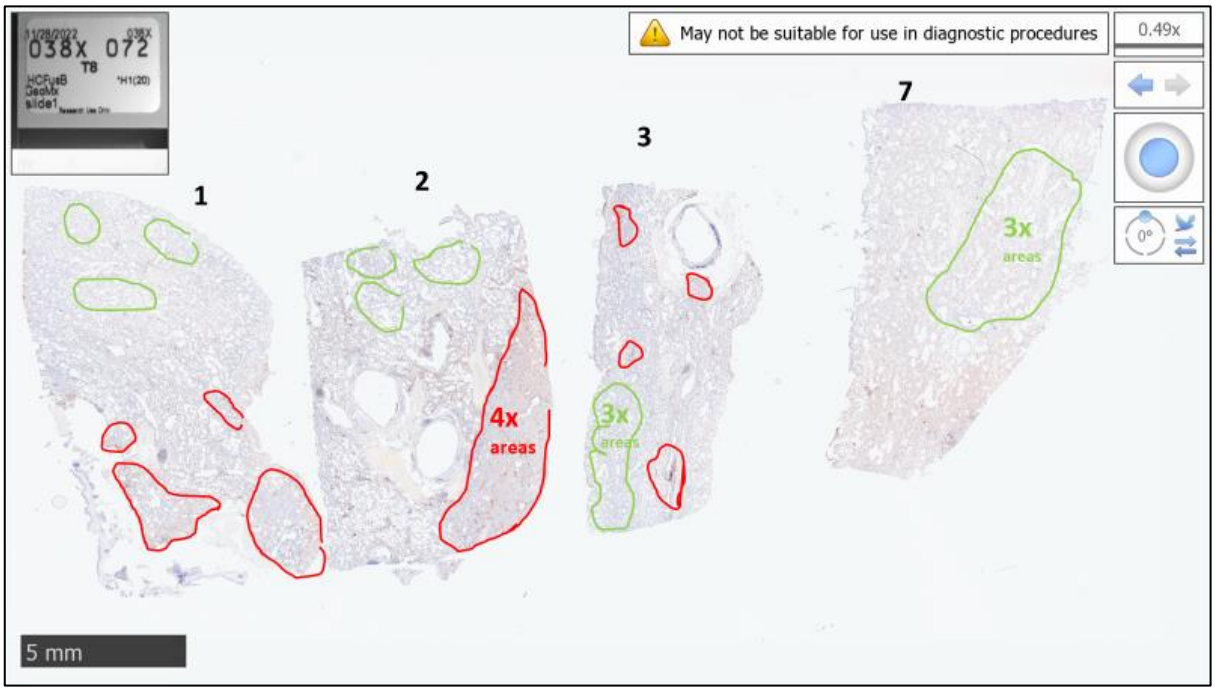

Figure 34: An example of some areas of interest (AOIs) in NHP lung tissues annotated for transcriptomic analysis. Lesioned areas (red) and non-lesioned areas (green) were selected by an experienced veterinary pathologist. The tissue sections shown above have been stained for CD68, which was the most important marker used for identification of lesioned areas and the sections used for Nanostring GeoMx DSP analysis were from a sequential slice shortly after this in the lung tissue block.

Library preparation was carried out according to the protocol supplied by the manufacturer (NanoString, MAN-10153-01). DPhil student Megan Bradbury assisted in the library preparation process. Initial quality control (QC) of the samples was carried out by Megan Bradbury using a Bioanalyzer to assess the quality of the DNA probes in our pooled library preparation and using a Nanodrop to quantify the DNA levels. The quality was found to be satisfactory. Subsequently, sequencing was performed on the NovaSeq 6000 platform by the Oxford Genomics Centre, who also carried out QC before sequencing and found the sample to be satisfactory. A second round of sequencing was required because of low probe counts for some of the ROIs, particularly those which had their transcripts in the edges of the 96-well plate used for PCR. We hypothesise that

the heating system did not evenly heat the plate and so the wells at the edges have minimal volume due to greater evaporation. To solve this, the material in these wells was re-suspended and prepared again. In the end, the probe count data from these 'failed' wells in the first sequencing round was replaced with the probe count data in the second round, which had much higher counts and was therefore much more suitable for analysis. The fastq files from sequencing were converted to DCC files, which were then uploaded to the GeoMx DSP to create a 'count file' of all the probe counts across the ROIs.

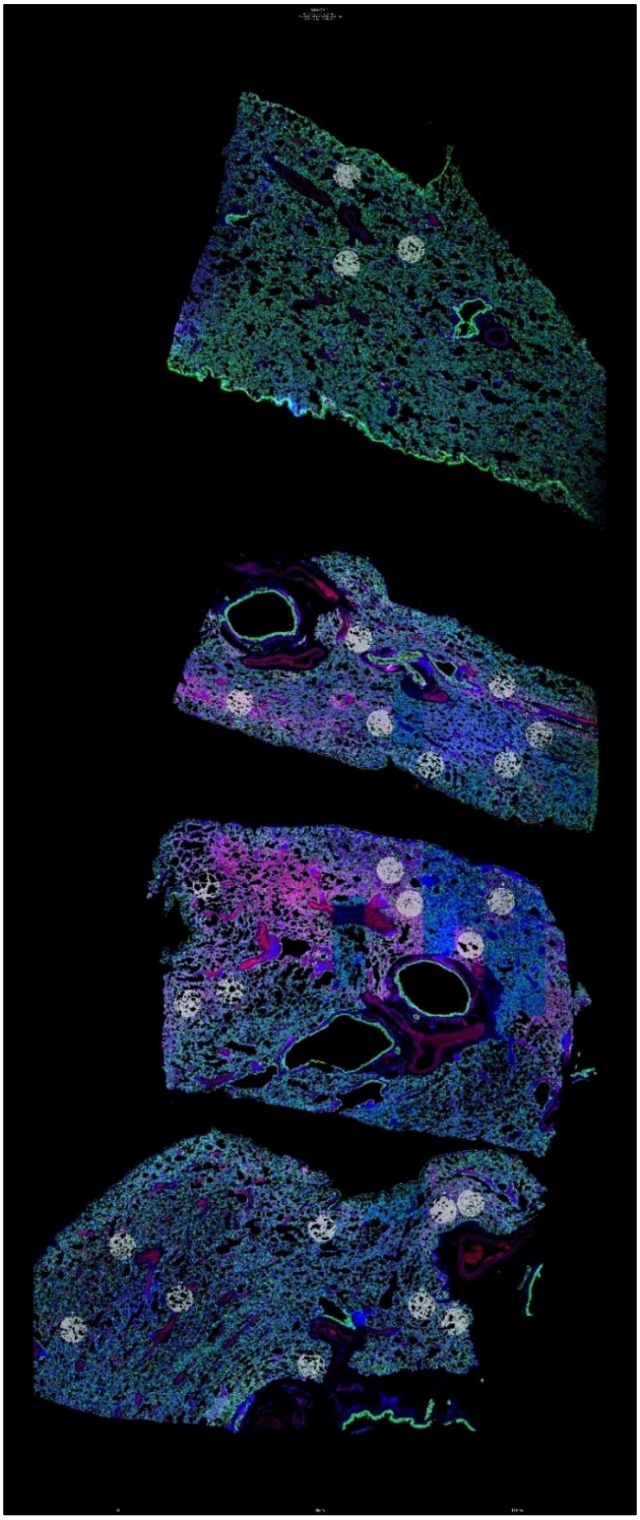

Figure 35: Overview of one slide on the GeoMx DSP. This slide contains 4 tissue sections from NHPs of interest. Blue = SYTO 13, Green = PanCk, Red = CD68. Circular ROIs selected for analysis (highlighted in white) are shown. Image taken using the GeoMx DSP from Nanostring.

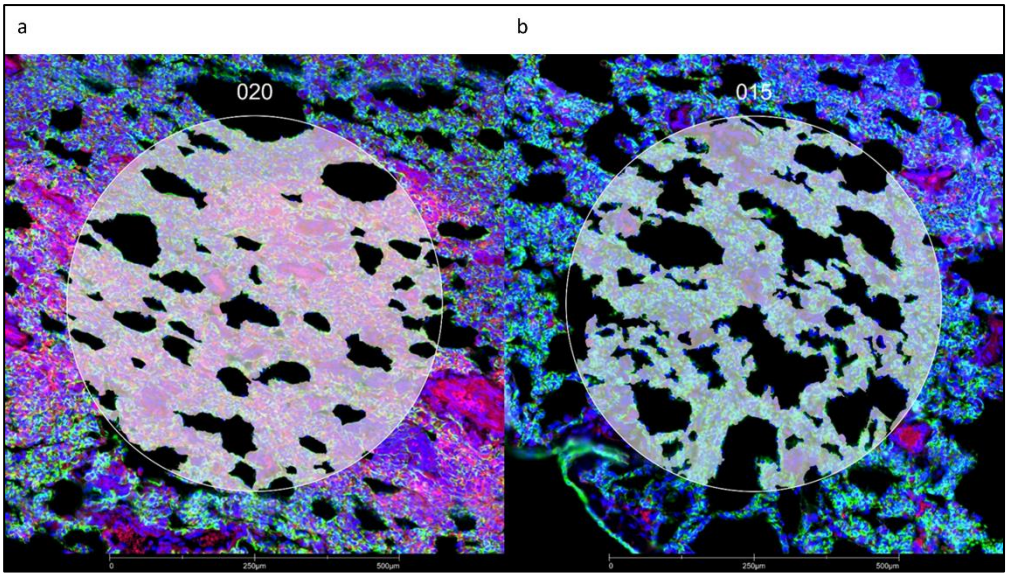

Figure 36: Representative images of one lesioned region of interest (ROI) (a) and one non-lesioned ROI (b), highlighting the areas to be taken for transcriptomic analysis (in white). Blue = SYTO 13, Green = PanCk, Red = CD68. Images taken using the GeoMx DSP from Nanostring.

The next sections in this chapter (**3.2** to **3.4**) detail the bioinformatic analyses of the resulting transcriptomic data from the GeoMx DSP. As multiple plots are often used together to interpret our findings, the results will be discussed in detail for all of these sections in **Section 3.5**.

3.2. Filtering, quality control and dimensionality reduction

Analysis of the data from the GeoMx DSP experiment was carried out using R version 4.2.1 [146,148,149,164–169]. The R script generated to analyse the GeoMx DSP data and the associated files needed to run this analysis are available upon request. Much of the initial steps for pre-processing the data before in-depth analysis involved using the standR package [168] and modifying its associated analysis vignette, which was developed by the Davis lab for robust QC, normalisation and analysis of spatial transcriptomics data from the GeoMx DSP. Three tab-delimited text files were imported into the R environment, a ‘count file’, a ‘sample annotation file’ and a ‘feature annotation file’. The ‘count file’ contains all the probe counts from the experiment, the ‘sample annotation file’ contains all the annotations we’ve assigned to each ROI such as the NHP name, vaccine group, ROI type etc and the ‘feature file’ contains the annotations of the genes in the dataset. Once imported, the data was first filtered to remove probes that had a low likelihood of

cross-reactivity with NHP RNA transcripts. Nanostring provided us with a list of all of the probes in the human WTA panel (which we used on our samples) and their estimated cross-reactivity with equivalent genes in NHP based on sequence alignment. They suggested a cut-off of 85% cross-reactivity, which removed 1473 genes from further analysis, before the next QC steps.

Next, the data was negative probe count data was analysed (**Figure 37**). Negative probes do not bind any specific sequences and should therefore be found in relatively equal amounts across the ROIs, however, in reality their counts can be quite variable. In order to find low-performing ROIs, a cut-off of 5 negative probes was used. Next, the QC flags from the GeoMx machine were checked and the same 15 low-performing ROIs by negative probe count were all found to have QC flags either just because of their negative probe count and/or because of low sequencing saturation and/or low raw reads. These ROIs were not initially removed from further analysis to see how the other gene QC tools applied to all ROIs. In the final run of the pipeline, these ROIs were removed before further analysis. Given that only one ROI from the 'unchallenged' tissues remained following the removal of low-performing ROIs, this ROI was also removed from analysis. This was also the case for the spare tissue from 10A, so this ROI was additionally removed. All of the ROIs removed because of the negative probe count cut-off were the same ROIs that would be removed by other QC metrics, so we were confident that these ROIs were inappropriate for further analysis and could be excluded. The list of ROIs used for analysis post-filtering can be seen in **Supplementary Table 5**.

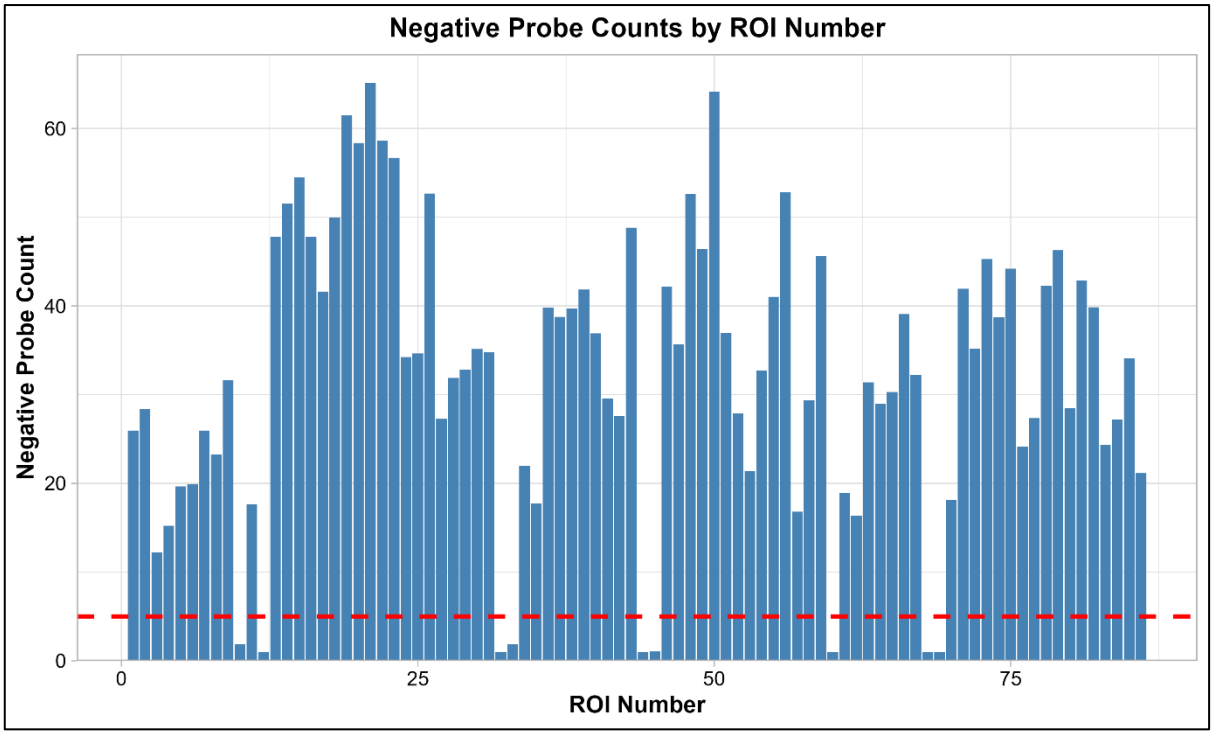

Figure 37: Negative probe counts across the ROIs. A cut-off of 5 negative probes (red line) was used to find low-performing ROIs.

Following this, we created an elbow plot (**Figure 38**) in order to determine a minimum probe count for inclusion of a gene in subsequent analysis. On the x axis we plotted different minimum count thresholds and on the y axis was the number of genes that would be kept in the analysis given the different minimum count thresholds. The number of genes kept was always in the context of a sample fraction of 0.06, meaning that number of genes must be expressed in at least 6 of our ROIs ($6/95 \approx 0.06$). Reading the plot, this means that if the minimum count threshold of a gene is 100 counts in 6 of the ROIs, there are about 10,000 genes that fit these criteria. In our analysis, 100 was the minimum count chosen based on the elbow plot, as this is the point where the increments of 5 counts begin to remove fewer genes (the slope is decreased). The removal of genes improves the statistical power of future analysis and lowly-expressed genes are thought to make minimal contributions to differential gene expression. In our case, this filtering step may also remove genes for which probes did not cross-react despite high predicted likelihood.

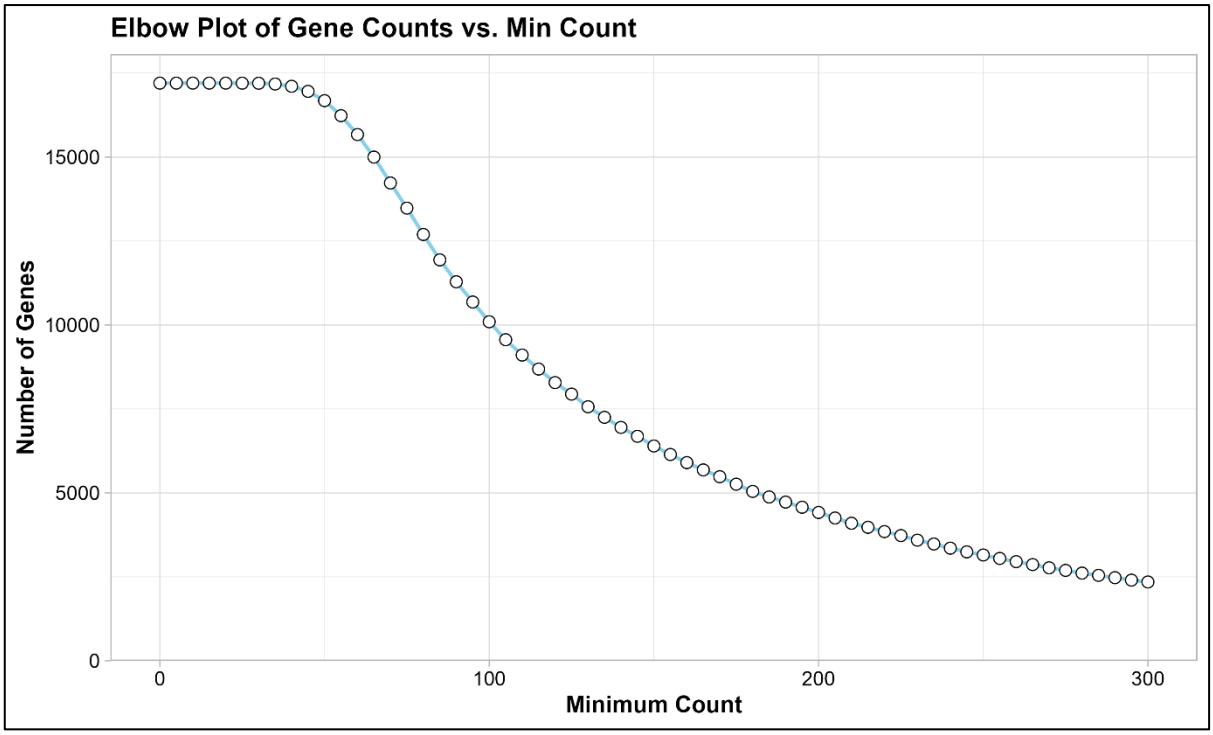

Figure 38: Elbow plot to decide on a minimum-count cut-off. A cut-off of 100 counts was chosen based on the above plot.

Next, density plots were generated (**Figure 39**) for a random sample of 10 genes that had low, medium or high counts (which is analogous to expression), to give an insight into their distribution. This will later provide the justification for the generalised linear model (GLM) used for differential gene expression (DGE) analysis. From these plots, we can see that the count data follows a negative binomial distribution, so we should use a GLM that takes this into account, rather than one that assumes normal distribution. For the next QC step, we generated plots that showed how the library size of each ROI varied according to the area of cells taken for analysis (**Figure 40**). For visualisation, we also coloured the points on this plot according to variables that might impact the association observed (namely the region type and which of our sequencing runs the ROI is from). Generally, we expect a linear correlation between the area of cells taken and the library size, as more cells should translate to more probe counts. This allows us to perform QC at a per-ROI level. As the ROIs we took for this study were very large, the library sizes were generally also large (once the poorly-performing ROIs by negative probe counts and QC flags etc were removed). In these plots we note a positive correlation as expected. As our ROIs were

circular and had a diameter of 650µm, the maximum area that could be taken if there were no gaps between cells or airway spaces would be 331,831 µm^2. In the plot coloured by region type (**Figure 40a**), it is clear that lesioned regions have higher area sizes that were taken for analysis, despite the ROI size being equal for all ROIs. We expected this difference because lesioned areas have much more immune infiltration and therefore fewer and smaller airway gaps than non-lesioned areas. In the plot coloured by sequencing run (**Figure 40b**), we can see that the ROIs that were re-run on a second sequencing run tend to have lower library sizes than those from the first run. This was also expected, given that we would have lost some material in the first sequencing run attempt. While there is still enough material for analysis, we need to ensure that the count data is appropriately normalised across the ROIs to take differences in library sizes into account.

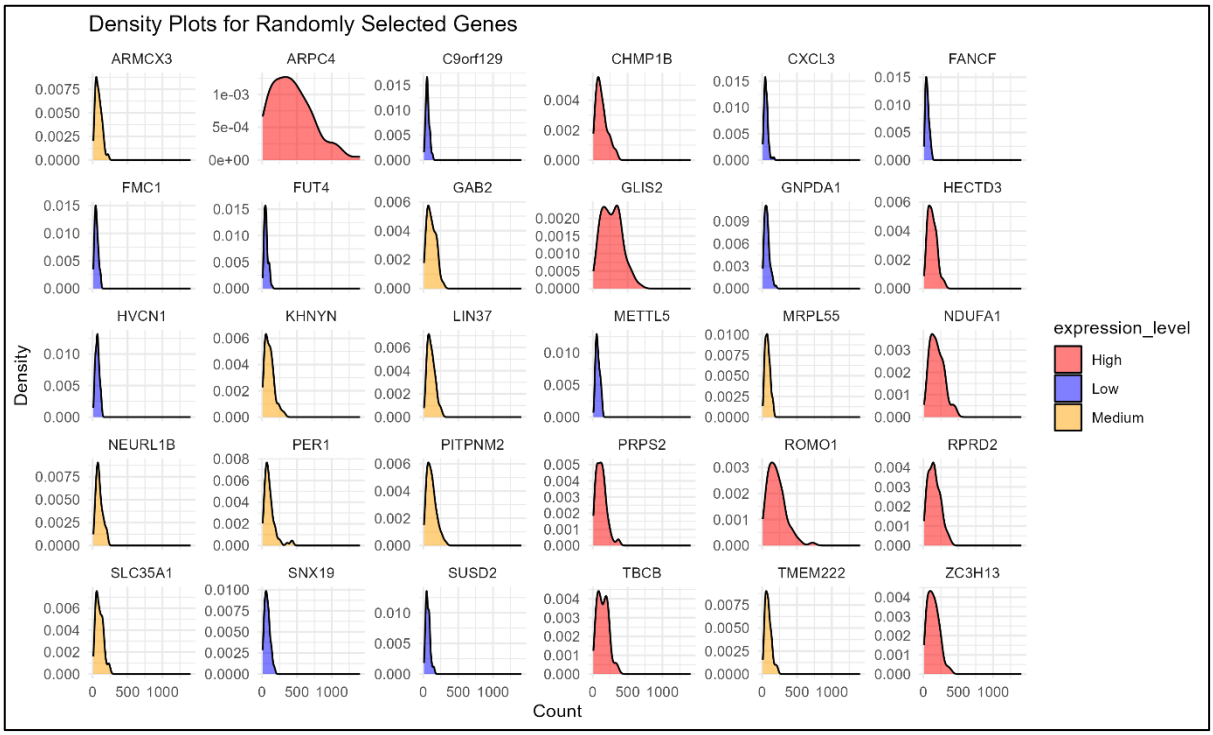

Figure 39: Density plots showing the distribution of counts for a randomly selected set of genes.

Density refers to the number of genes with the particular number of counts.

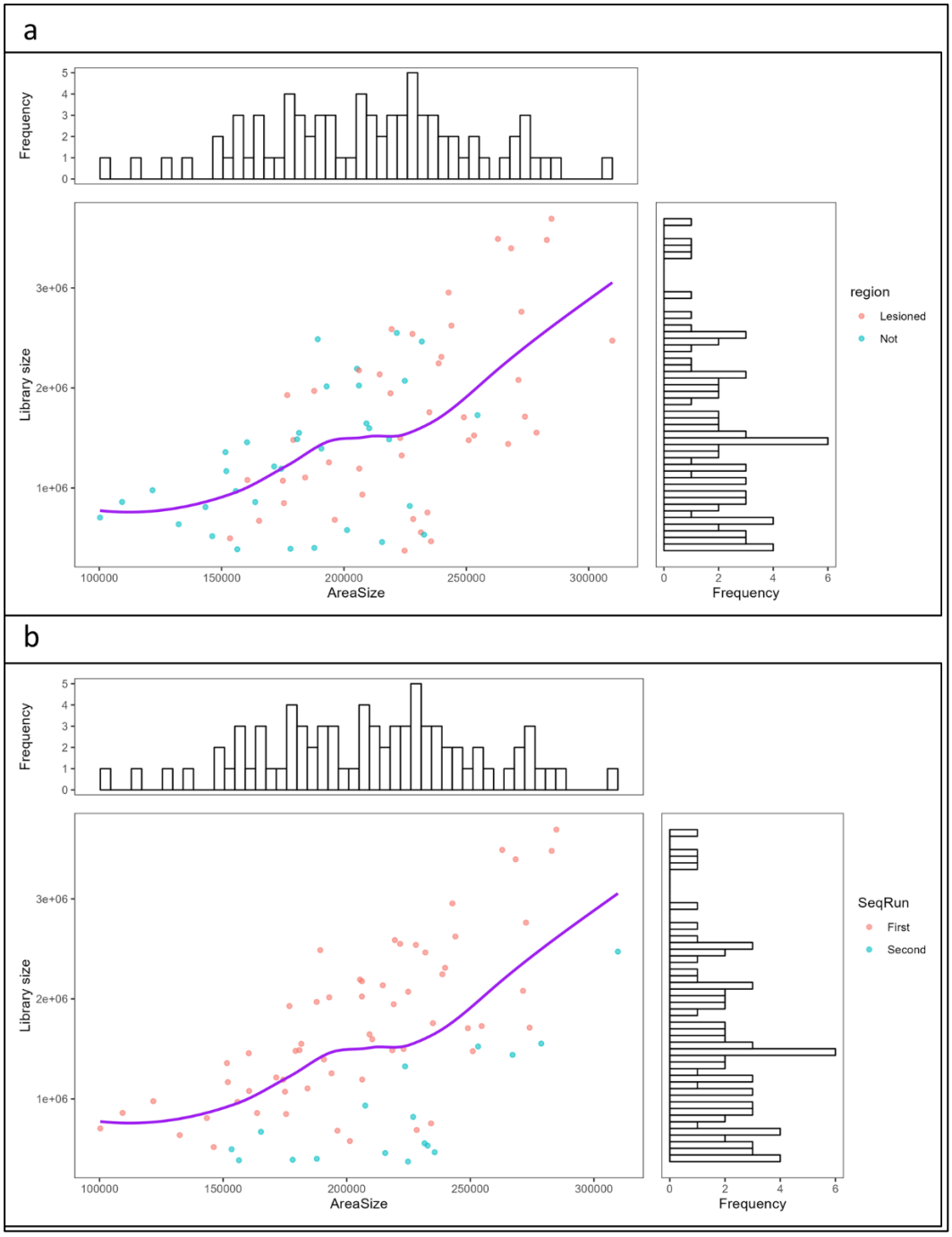

Figure 40: ROI-level QC, plotting library size vs the size of the ROI. The ROI points are coloured according to region type **(a)** or the sequencing run **(b)**. Library size refers to the total count number across all genes and area size is measured in μm^2.

Next, the relative log expression (RLE) distribution for the log counts per million (CPM) across all the ROIs were plotted in order to examine the relative distance between the median RLE in each ROI before normalisation (**Figure 41**). As described for the *standR* workflow [168], logCPM

simplifies visualisations of variance in gene expression. When this plot is coloured according to the sequencing run or the four GeoMx slides, they can be examined for differences according to these factors. From these plots, some of the greatest variation appears to be in some of the ROIs from the second sequencing run and slide 4 appears to be a potential outlier compared to the other slides. Variation between ROIs is expected due their different library sizes as shown earlier (**Figure 40**), so normalisation is carried out. The probe count data was normalised using trimmed mean of M-values (TMM) normalisation, which is commonly used for count data and removed most of the variation between ROIs when the RLE was plotted again (**Figure 42**). These plots demonstrated that normalisation worked very well across the ROIs and we do not need to carry out batch correction on a per-slide basis, as the pre-normalised data may have indicated.

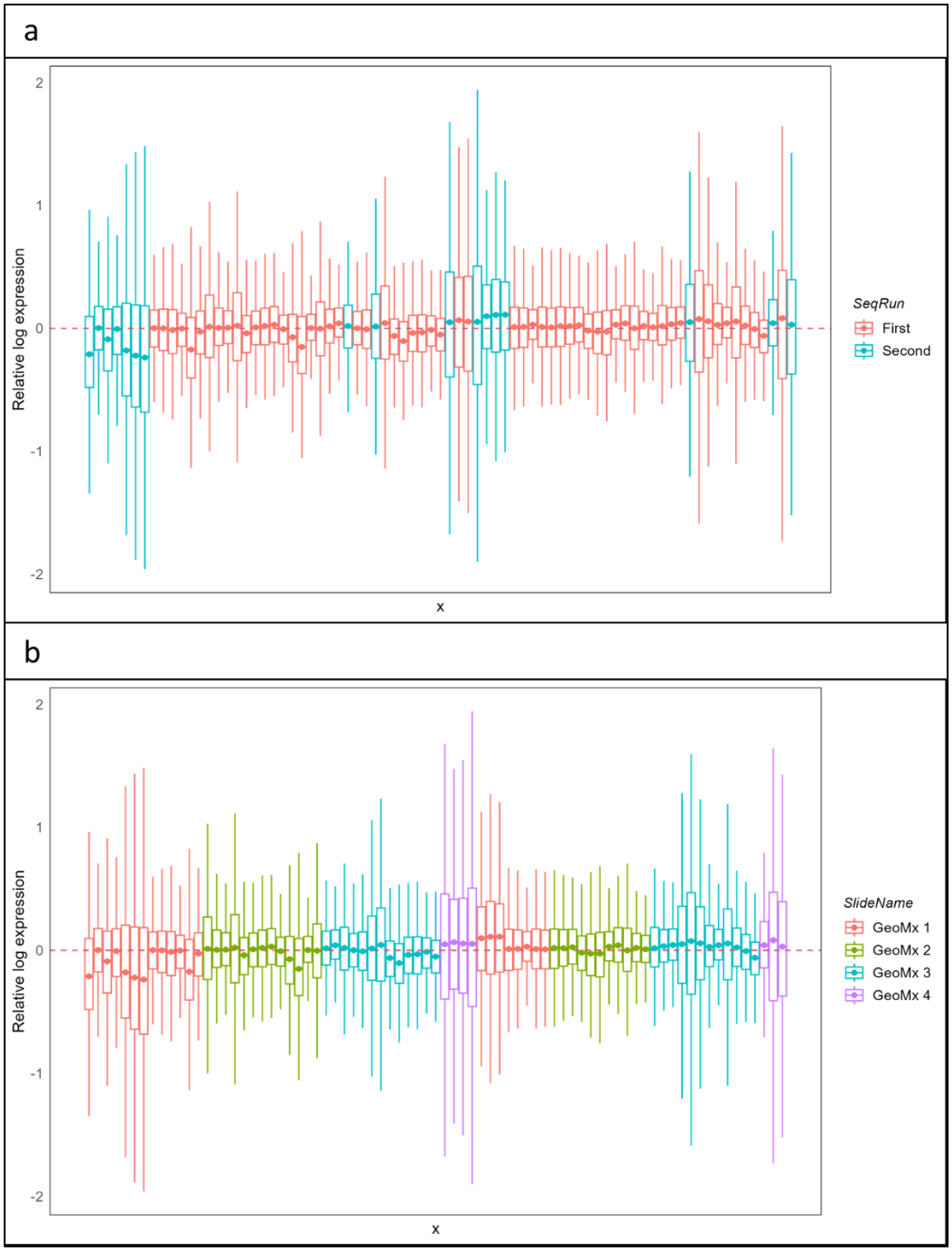

Figure 41: Relative log expression of counts per million for all of the ROIs. The x axis refers to different ROIs in our sample set. In **(a)** the ROIs are coloured according to the sequencing run and in **(b)** the ROIs are coloured according to the which of the four slides the ROI was taken from.

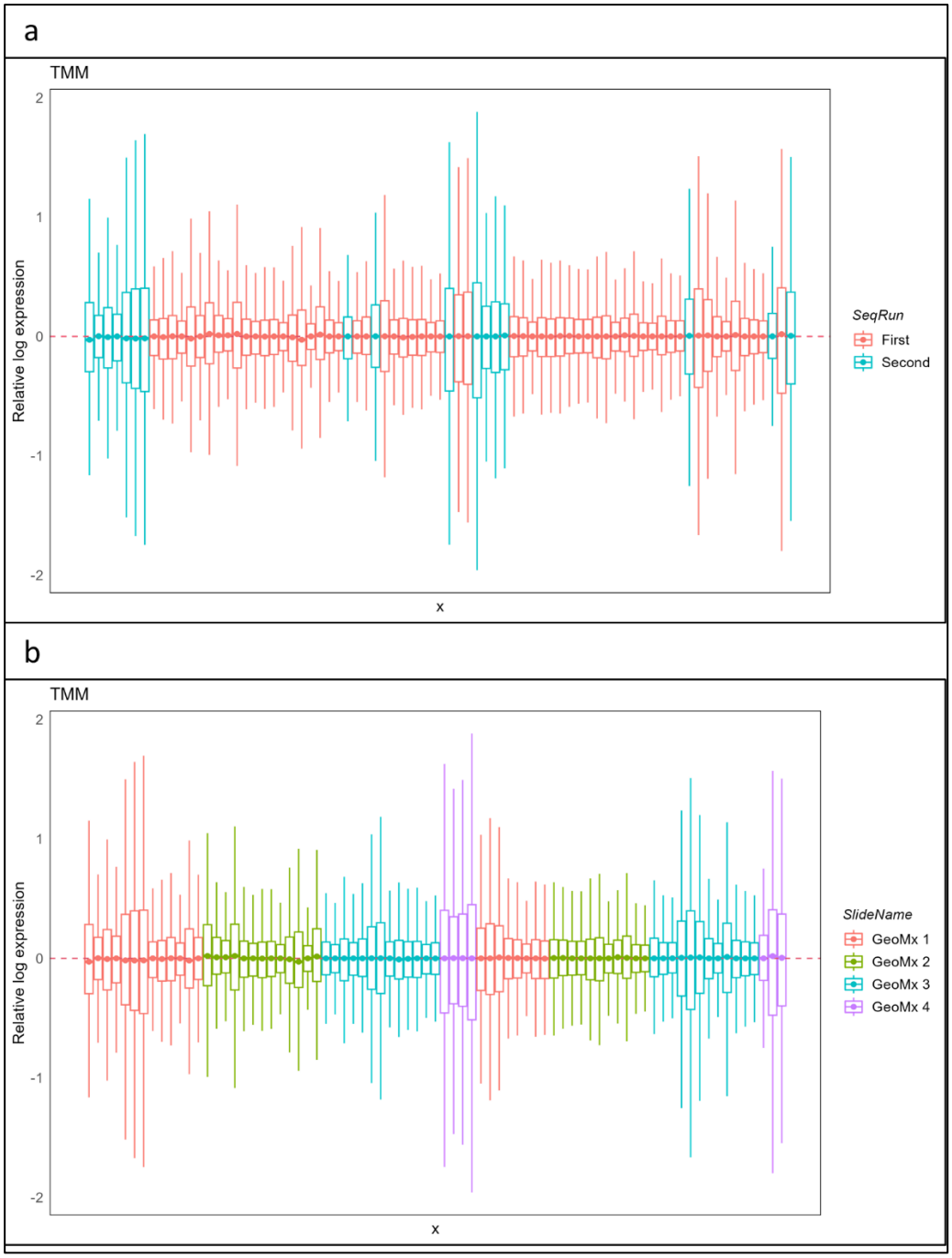

Figure 42: TMM-normalised relative log expression of counts per million for all of the ROIs. The x axis refers to different ROIs in our sample set. In **(a)** the ROIs are coloured according to the sequencing run and in **(b)** the ROIs are coloured according to the which of the four slides the ROI was taken from.

Principle component analysis (PCA) plots were then generated in order to visualise the potential factors contributing to variations in the transcriptomic profiles across the ROIs post-normalisation (**Figure 43**). From the PCA plots coloured by different factors, it appears that

together, the vaccine/challenge groups (termed 'vaccinedose') and the pathology class and region combination (termed 'pathregion') explain most of the variation as they appear to create distinct clusters. A PCA scree plot was also generated (**Figure 44**) to visualise the contribution of each of the principle components to the variation and demonstrated that the PC1 and PC2 axes (used in **Figure 43**) contributed to the majority of the variation.

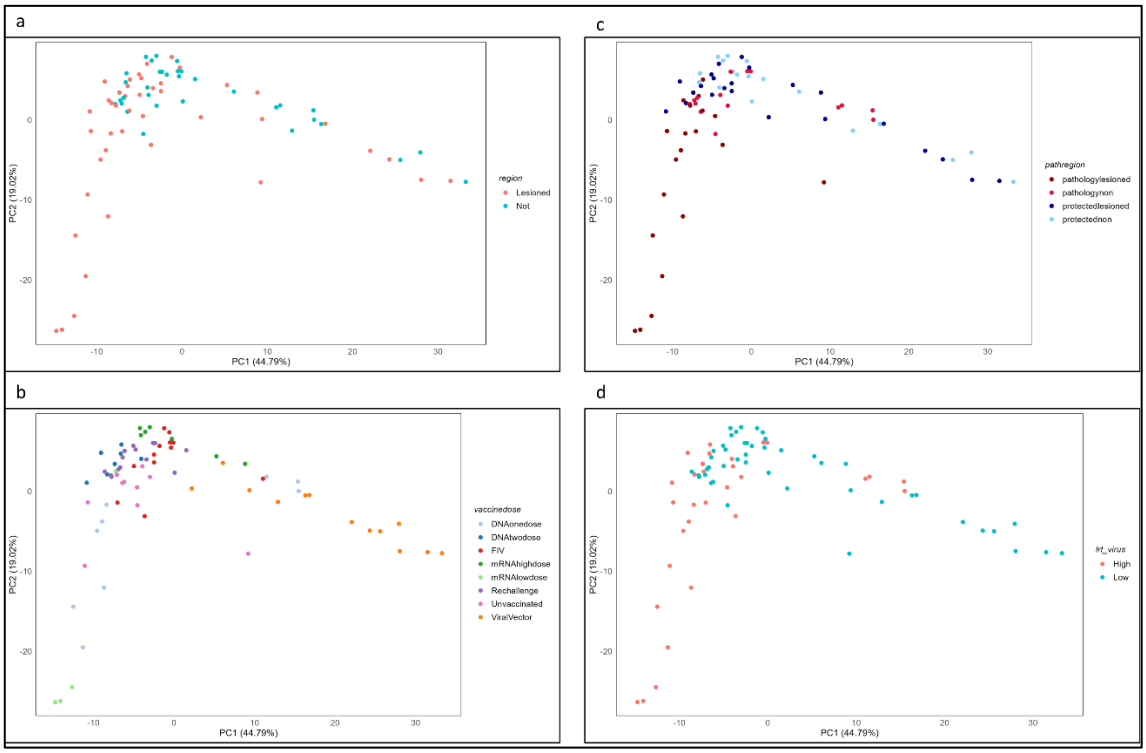

Figure 43: PCA plots. Each point on the PCA plots refers to a separate ROI and these are coloured by different classifications, such as **a.** region type, **b.** vaccine/challenge group, **c.** a combination of pathology class and region or **d.** the amount of virus measured in the lower respiratory tract. The percentage of the variation in the data accounted for by each principle component is shown.

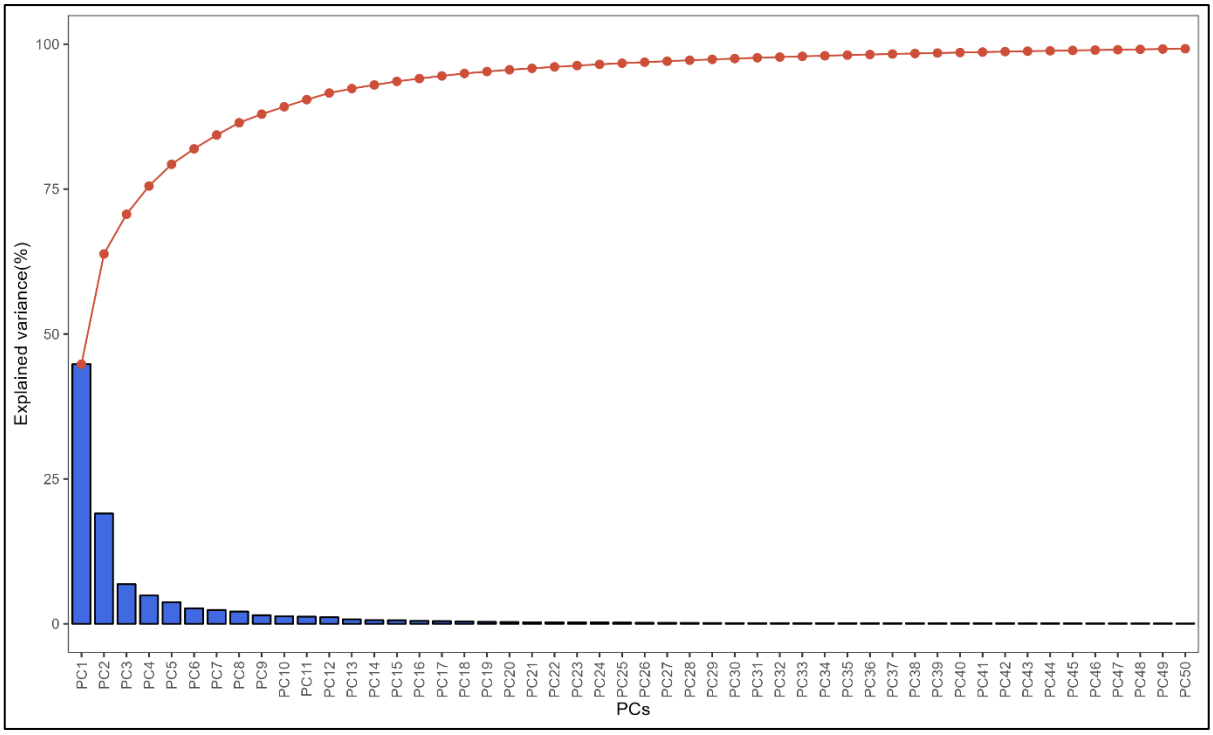

Figure 44: PCA scree plot post-normalisation.

3.3. Differential gene expression analysis

Differential gene expression (DGE) analysis was carried out for several different comparison types based on the following categories and subcategories involving one or more of these classifications: 'region' (Lesioned vs Not, across all NHPs of interest n = 12), 'vaccinedose' (every vaccine/challenge group is compared with one another in one-to-one comparisons, n=2 NHPs for all groups except DNAonedose, DNAtwodose, mRNAhighdose and mRNAlowdose where n=1), 'pathclass' (Pathology vs Protected, with n=6 for each group) and lrt_virus (high_virus vs low_virus, with n = 5 and n = 7, respectively). An example of a subcategory is 'PathRegion', where region (Lesioned vs Not) and pathclass (Pathology vs Protected) were combined to create four categories (pathologylesioned, pathologynon, protectedlesioned, protectednon), as seen in **Section 2.4**. Finally, subcategories for 'vaccinedose' and 'NHP' were created, where the comparisons were the same as described previously for these groups but focused only on comparing lesioned or non-lesioned areas like-for-like, for additional insights into teasing out differences between groups. The categories and subcategories used for analysis were as follows: **'region', 'VaccineDose', 'lesioned_VaccineDose',**

'nonlesioned_VaccineDose', 'NHP', 'lesioned_NHP', 'nonlesioned_NHP', 'PathRegion' and 'lrt_virus'. When comparisons within the 'NHP' groupings are shown, the NHP with higher pathology is always the first NHP shown.

To look at the variance in genes of interest across our ROIs with heatmaps, a variance-stabilising transformation from the DESeq2 package [167] was carried out before the count data for each gene was z-score normalised to aid in visualisation. Genes that were found to be associated with severe COVID-19 or with cell types implicated in severe disease in single-cell BAL fluid studies [34,39] and spatial transcriptomic studies on fatal COVID-19 human lung tissue [29,30] were focused on for these heatmaps. Only genes that passed our earlier QC and filtering steps were included. We created heatmaps to show variance in genes related to severe disease (**Figure 45**), monocytes and macrophages (**Figure 46**), myeloid chemotaxis (**Figure 47**) and other cell types along with associated processes and gene expression by these cell types that were linked to severe outcomes (**Figure 48**). Euclidean clustering was applied to both the x and y axis for each heatmap to group similar expression profiles together.

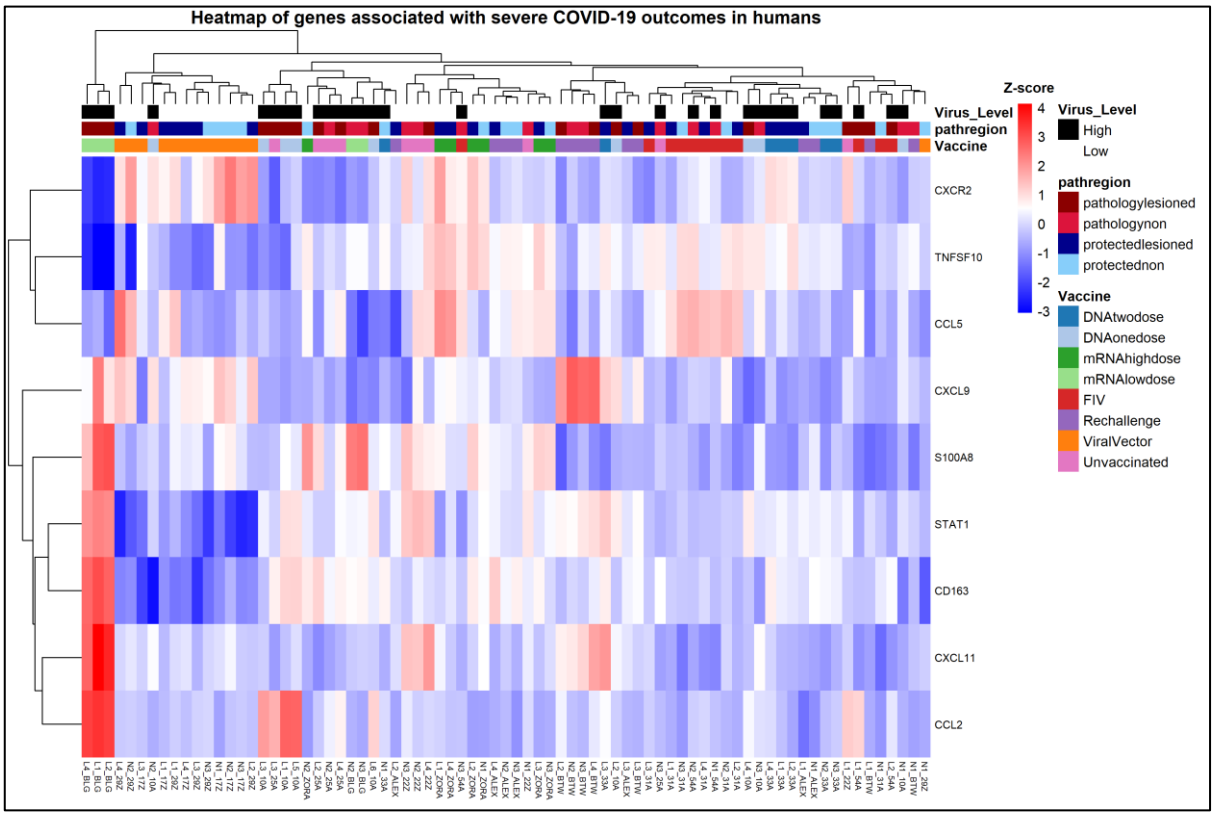

Figure 45: Heatmap of genes most associated with severe COVID-19 outcomes in humans. Only genes that passed earlier QC and filtration are shown. The x axis indicates the different ROIs from our dataset.

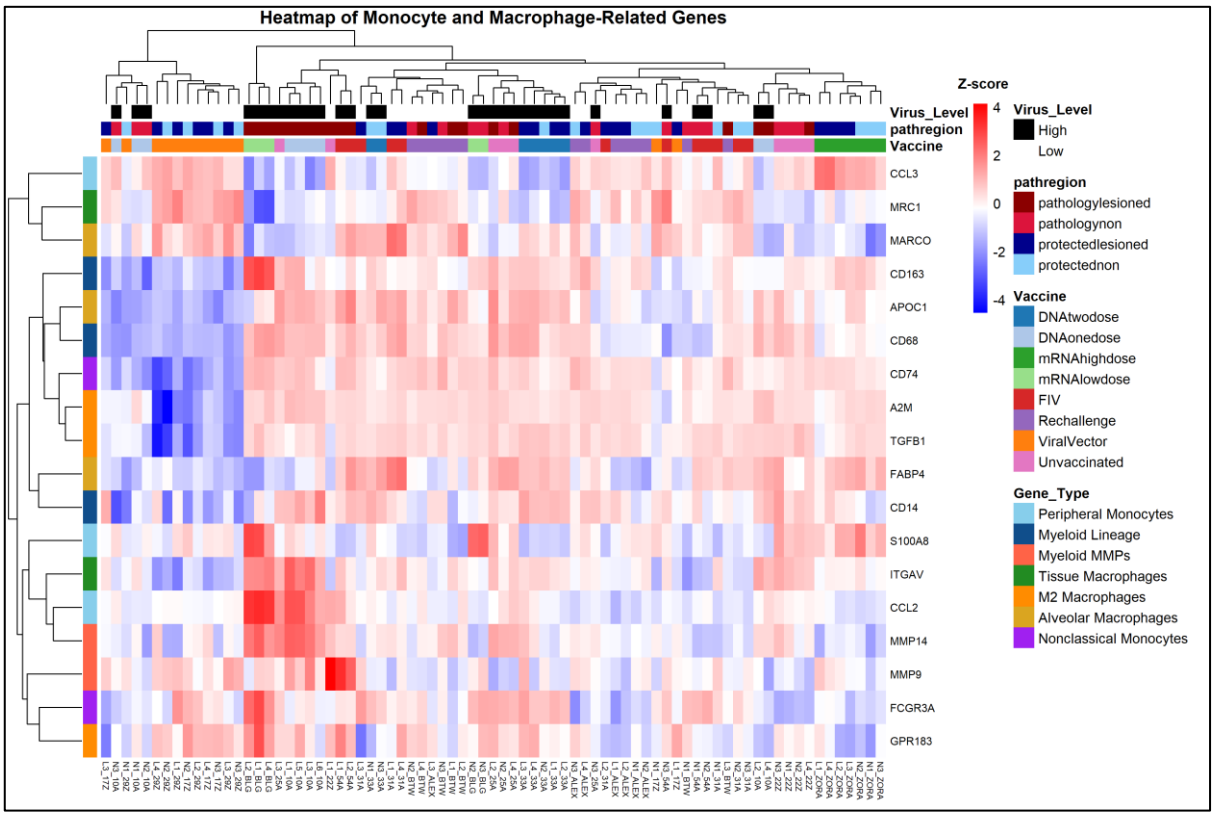

Figure 46: Heatmap of genes associated with monocyte and macrophage subsets in human COVID-19 datasets. Only genes that passed earlier QC and filtration are shown. The x axis indicates the different ROIs from our dataset.

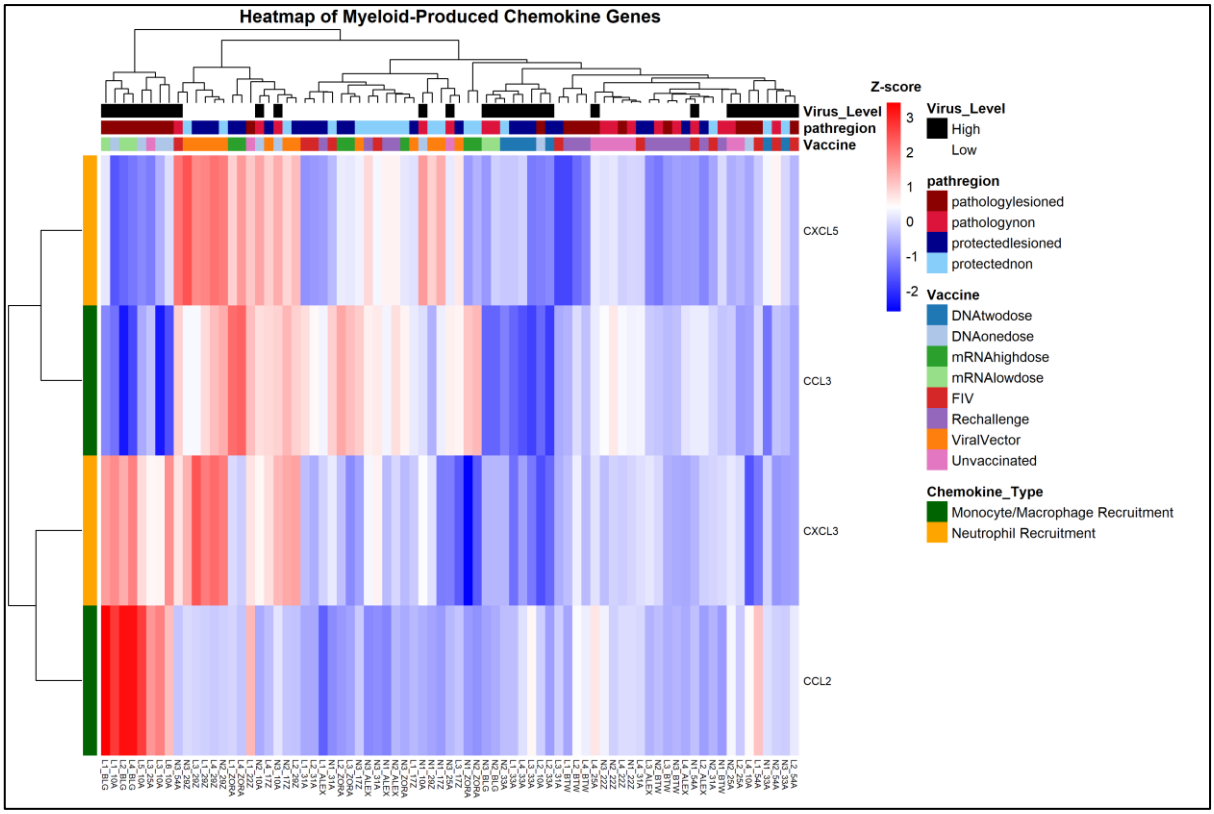

Figure 47: Heatmap of genes associated myeloid-derived chemokines, implicated in severe COVID-19. Only genes that passed earlier QC and filtration are shown. The x axis indicates the different ROIs from our dataset.

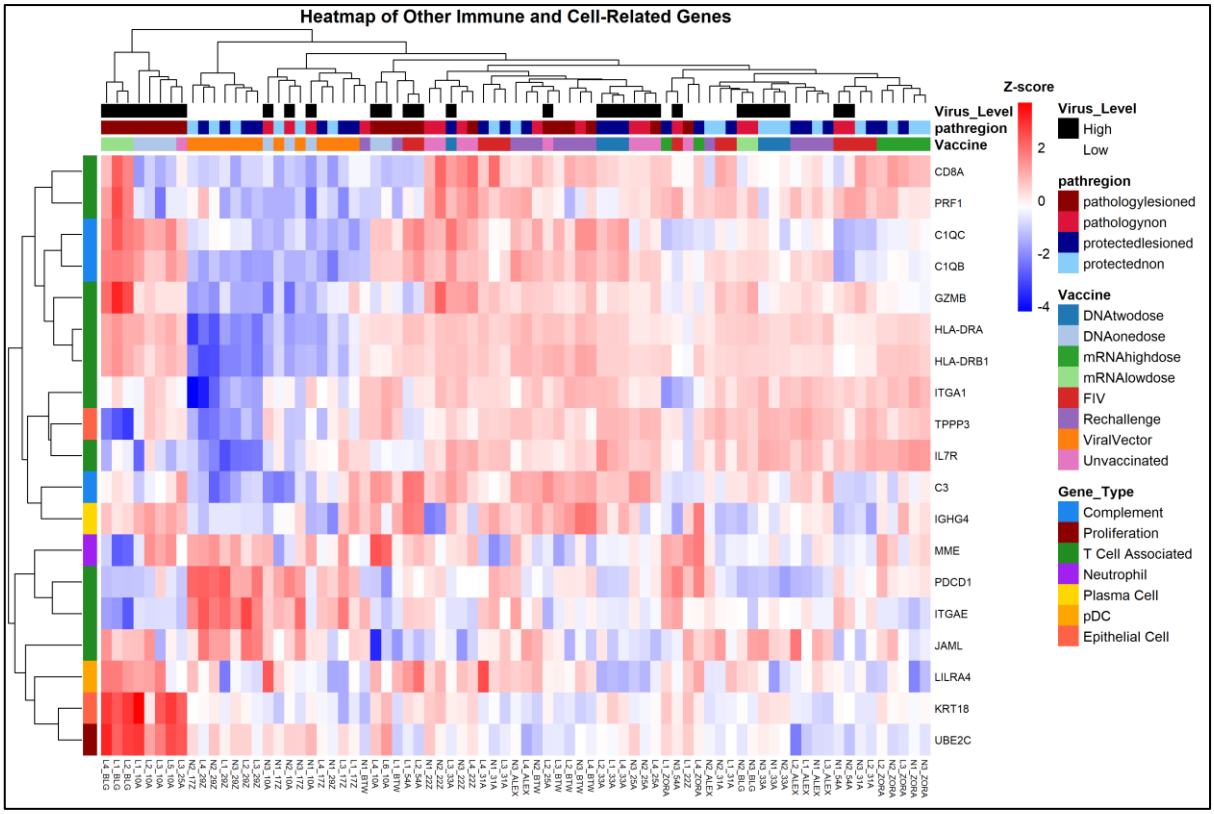

Figure 48: Heatmap of genes associated with other cell types, immune processes in human COVID-19. Only genes that passed earlier QC and filtration are shown. The x axis indicates the different ROIs from our dataset.

We used variance-stabilising transformed (VST) counts (carried out separately in the lesioned and non-lesioned areas) to examine the linear correlation between genes and the quantitative histopathology score of the NHP the gene was detected in. This is similar to how, with the Cell DIVE immunofluorescence data, to look at pathological associations we carried out both grouped comparisons (with 'pathclass' and 'pathclassregion' groups) and linear correlations (**Section 2.4**). In this case, the output of the linear correlation can be used similarly to the output of the glmQLFit function for our subsequent DGE analysis and pathway enrichment analysis (**Section 3.4**). All of the other linear models for the different category comparisons, rather than using a simple linear correlation, were fitted using the glmQLFit function from edgeR [169], according to the design matrices we set up for the different categories. The reason the glmQLFit function was used was because it does not assume that the count data is normally distributed and earlier we have shown that the count data follows a negative binomial distribution (**Figure 39**). In creating these models

for category comparisons, appropriate covariates were added to the models to remove confounding factors that may otherwise explain variation in the comparison of interest. When comparing the lesioned and non-lesioned regions, the vaccine/challenge groups ('Vaccine') and pathology class ('Pathclass') were both added as co-variates. When comparing vaccine/challenge groups, the pathology class was added as a covariate and when comparing the pathology class and region combinations, the vaccine/challenge regimen was added as a covariate. Finally, when comparing high vs low lower respiratory tract virus, 'pathregion' was added as a co-variate. Individual variation between NHPs with the same vaccine/challenge regimen could not be considered as covariates in any of the analysis due to the small sample size of these groups (n =2 or n=1 because of different dosing regimens), making it difficult to uncouple the effect of the vaccine/challenge regimen and individual variation. However, comparisons between different NHPs within each regimen were run separately to give insights into this variation. Then, contrast matrices for each comparison of interest within each broader category were created so that every analysis and graph type from this point onwards could be applied to each of these comparisons. For the NHP comparisons, as well as comparing the NHPs within the same vaccine/challenge group, we also compared 10A, the NHP with the highest pathology across all samples (**Figure 6**), to unvaccinated animals. This is because 10A was an outlier in the one dose DNA vaccine group due to its very high pathology and by comparing to unvaccinated animals, we aimed to shed light on whether 10A had a similar transcriptomic profile to the unvaccinated animals (suggesting vaccine failure), or had aberrant Th2-driven immune responses compared to unvaccinated animals (suggesting VAED).

Biological coefficient of variation (BCV) plots for each category were created and was used to visualise how the coefficient of variation of the counts depends on the frequency of the counts. Representative BCV plots are shown below (**Figure 49**), the trends for the BCV plots across the other categories were similar. Generally, highly-expressed genes appear to be contributing to more of the biological variability, as is shown by the trend line increasing over the common line at higher expression values. In our experimental context, this may be explained by the fact that

we expect genes involved in the inflammatory response to be highly-expressed in lesioned regions, particularly in high-pathology animals, whereas we expect their expression in non-lesioned regions in well-protected animals to be low. Several of the annotated genes in the BCV plot (**Figure 49**) with high BCV are involved in the antibody response, encoding for heavy chains (IGHG2 and IGHG4), the light chain (IGKC) and the joining chain of multimeric IgA and IgM (JCHAIN). This suggests that B cells and plasma cells may be present in some regions and not others, explaining the variability.

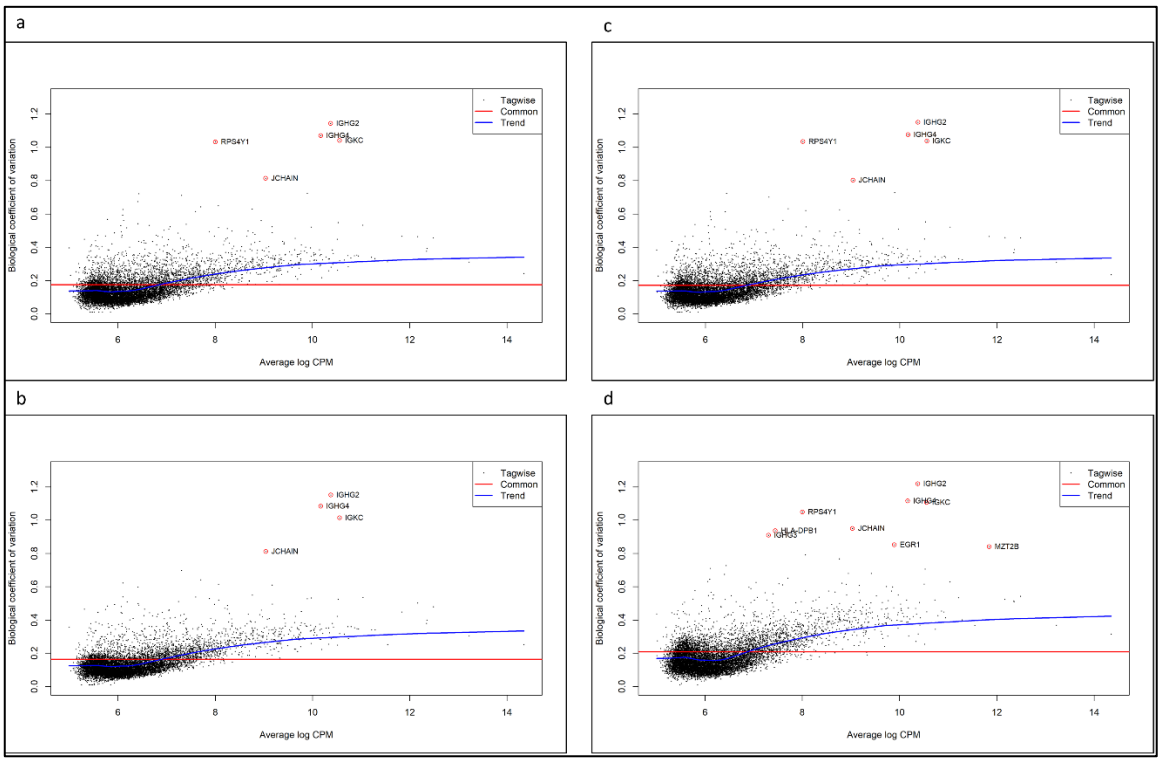

Figure 49: Representative Biological Coefficient of Variation (BCV) plots. **a.** Region category. **b.** 'Vaccinedose' category. **c.** 'PathRegion' category. **d.** 'lrt_virus' category. Genes with high BCV (> 0.8) are annotated and are likely to strongly to contribute to variation in the dataset. BCV plots for the other categories are similar and are available upon request.

Differential expression was carried out with edgeR using the previously-described linear models. A quasi-likelihood F test was carried out for each gene to determine whether it was differentially expressed in each of the comparisons. The full results table showing each gene and its associated fold change, p value and false-discovery rate (FDR)-adjusted p value etc is available upon

request. Given the large amounts of comparisons we make across all of the categories, we decided on a strict cut-off for FDR-adjusted p values of (FDR < 0.01) for genes to be referred to as significant. For the histopathology correlation, the same adjusted p value was used but in this case the p value referred to the linear correlation of a gene with histopathology score. Bar plots were created to show the number of differentially-expressed genes for different comparisons within the same category, which can be seen below (**Figure 50** to **Figure 56**). The bar plots for the 'lesioned' and 'lrt_virus' group comparisons are not shown because there would only be one comparison in each of these groups. There were 388 differentially-expressed genes in the lesioned vs non-lesioned comparison and 1216 differentially-expressed genes in the high virus vs low virus comparison. Differentially-expressed genes were also plotted onto volcano plots for every comparison across all the categories. A selection of comparisons of particular interest are shown in **Figure 57** and the other volcano plots are all available on request.

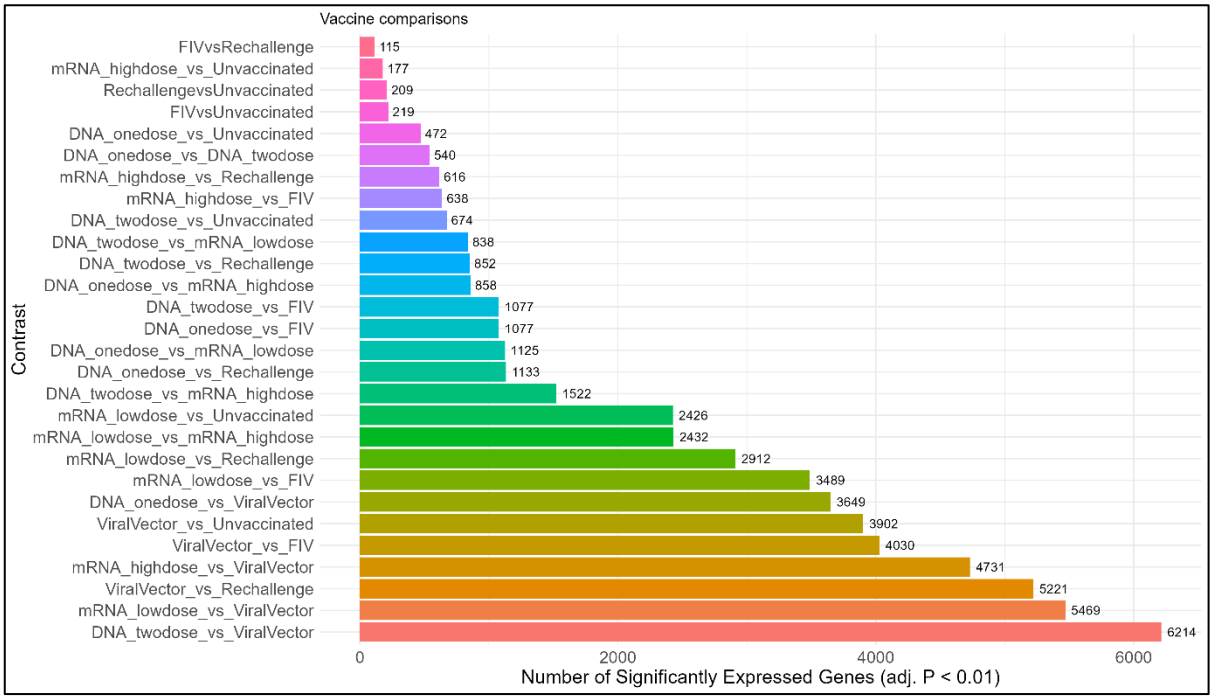

Figure 50: DGE comparison bar plot showing the number of differentially-expressed genes (adj. P < 0.01) in comparisons within the 'Vaccine' category. Each bar represents a different comparison.

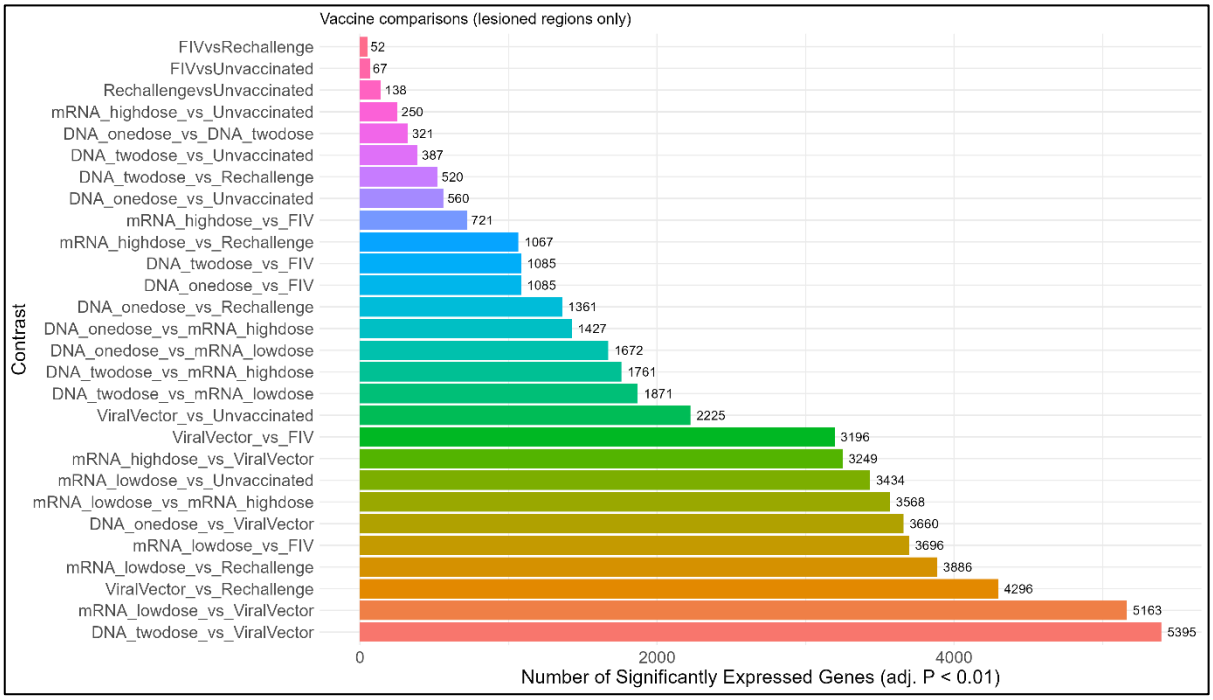

Figure 51: DGE comparison bar plot showing the number of differentially-expressed genes (adj. P < 0.01) in comparisons within the 'Vaccine' category, only in the lesioned regions.

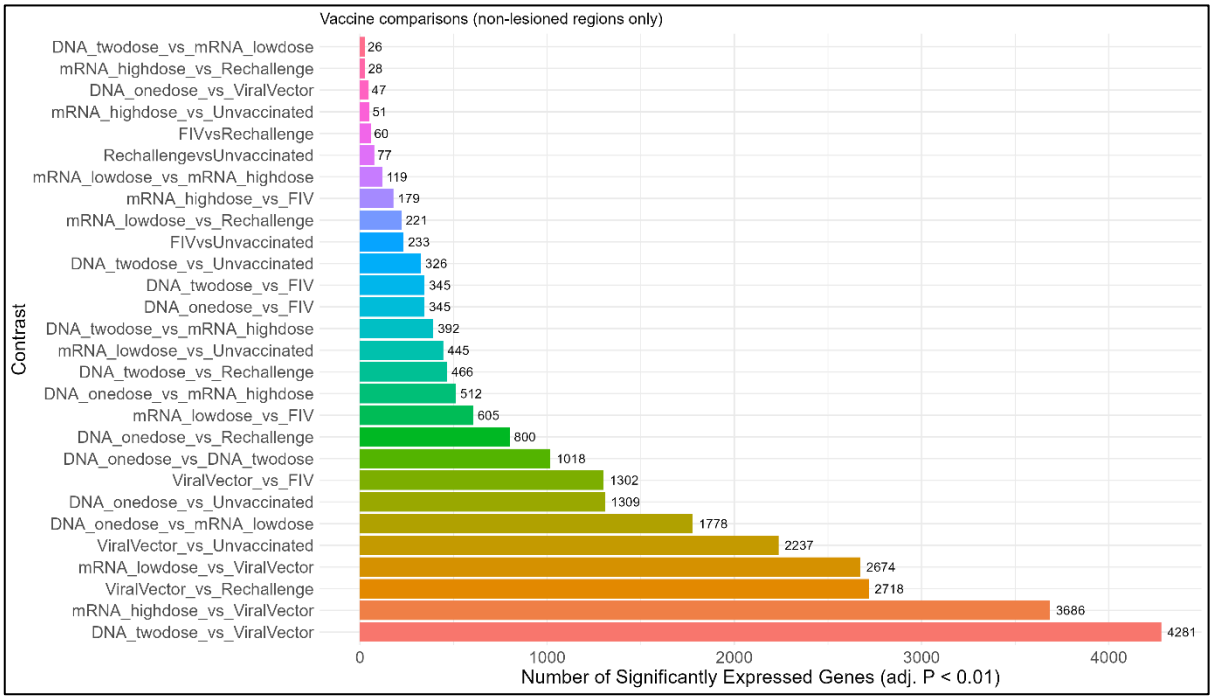

Figure 52: DGE comparison bar plot showing the number of differentially-expressed genes (adj. P < 0.01) in comparisons within the 'Vaccine' category, only in the non-lesioned regions.

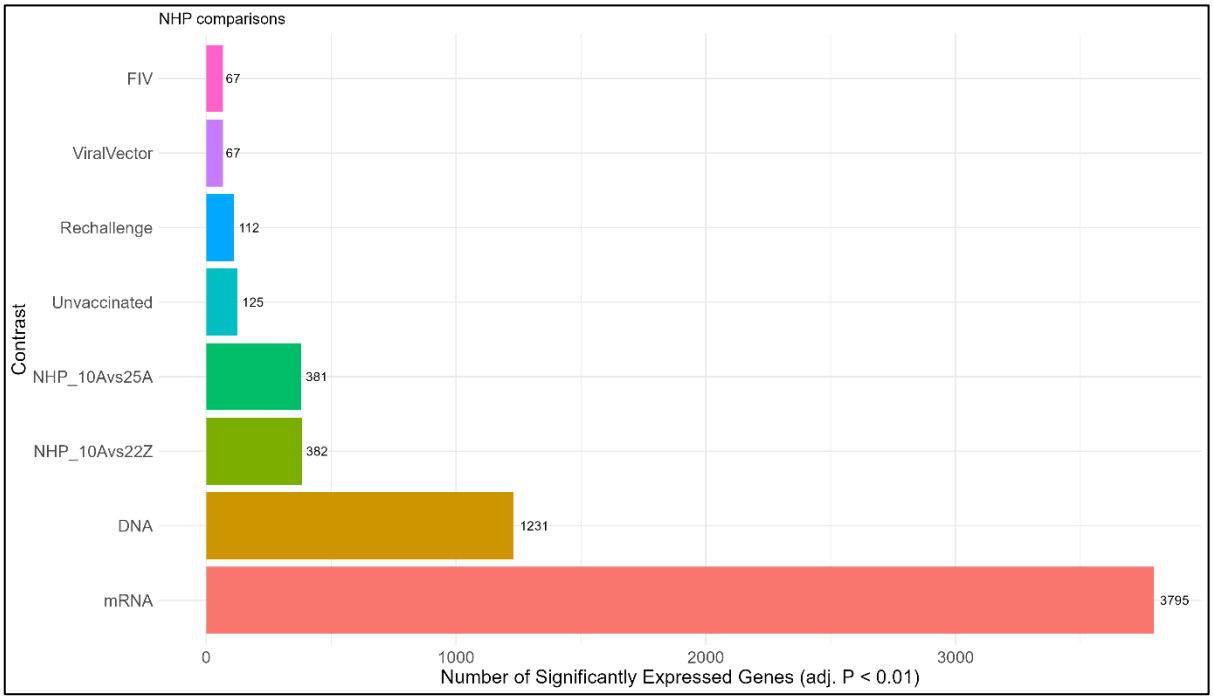

Figure 53: DGE comparison bar plot showing the number of differentially-expressed genes (adj. P < 0.01) in comparisons within the 'NHP' category.

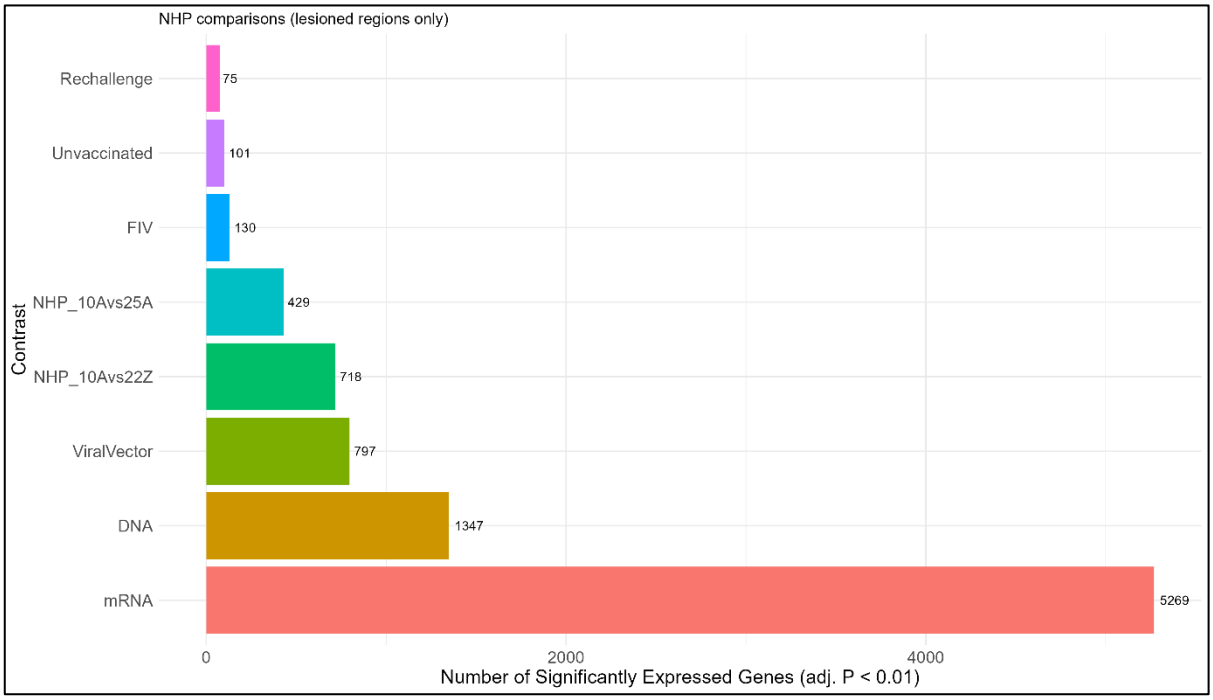

Figure 54: DGE comparison bar plot showing the number of differentially-expressed genes (adj. P < 0.01) in comparisons within the 'NHP' category, only in the lesioned regions.

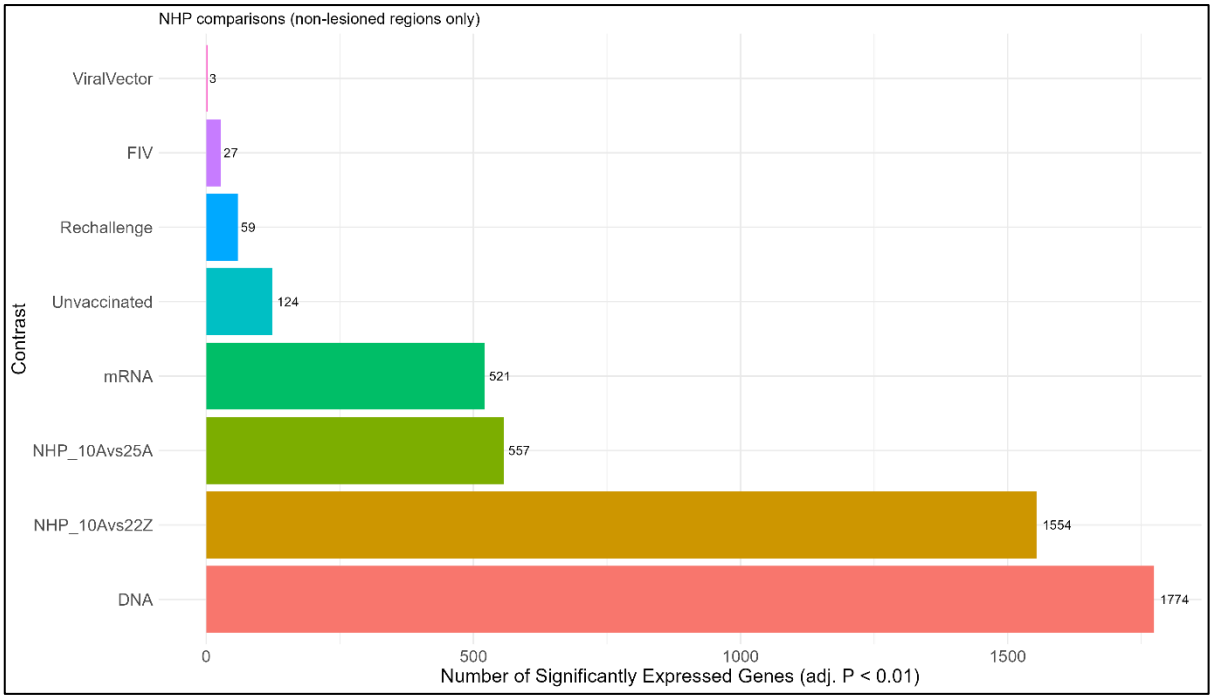

Figure 55: DGE comparison bar plot showing the number of differentially-expressed genes (adj. P < 0.01) in comparisons within the 'NHP' category, only in the non-lesioned regions.

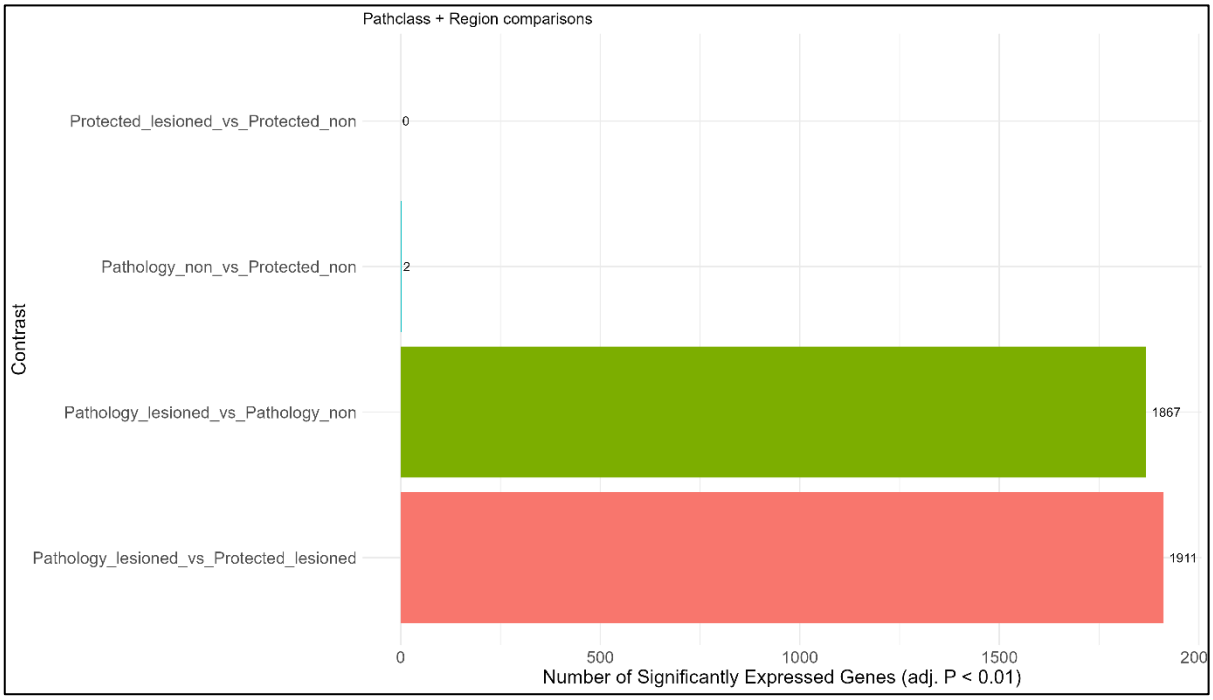

Figure 56: DGE comparison bar plot showing the number of differentially-expressed genes (adj. P < 0.01) in comparisons within the 'pathregion' category.

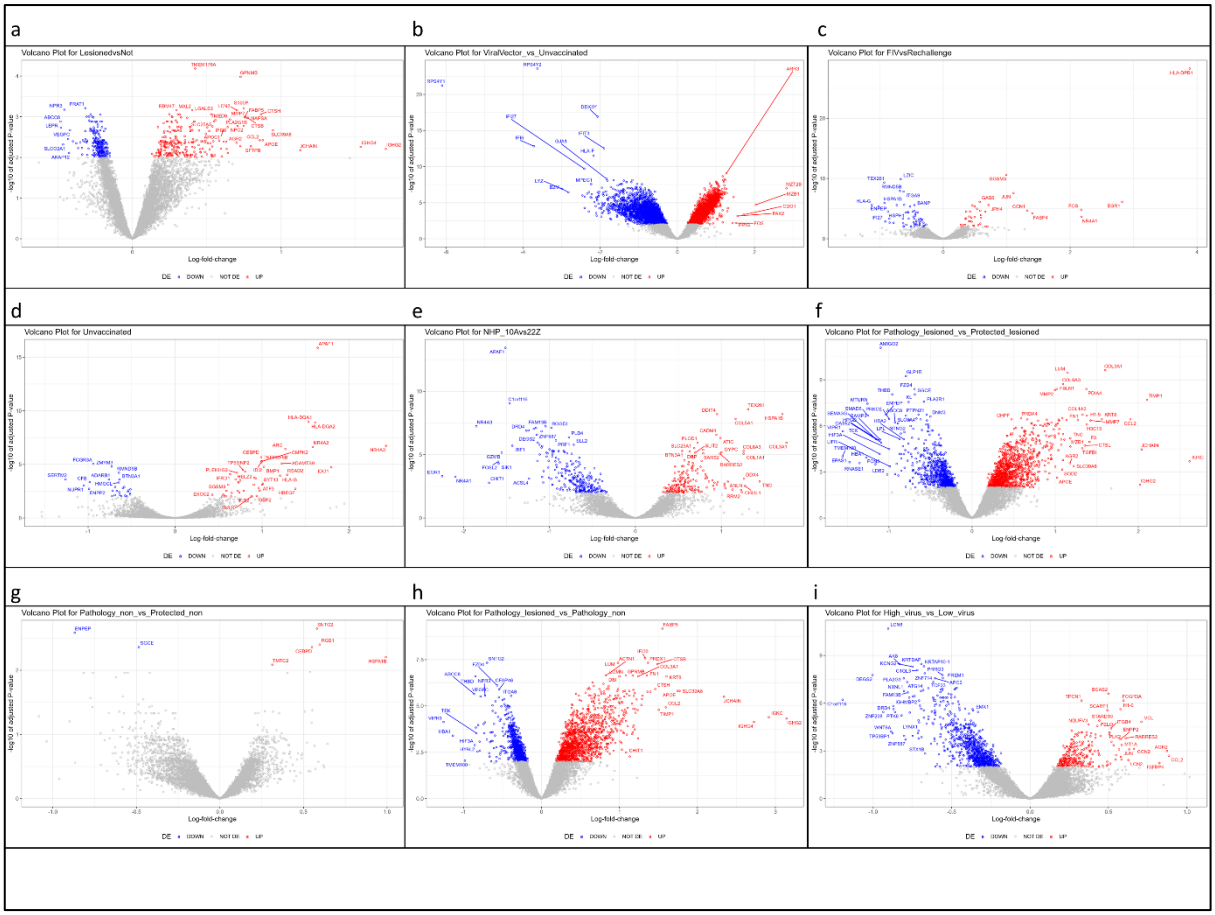

Figure 57: Volcano plots. Representative volcano plots for particular comparisons of interest. Axes are separately scaled according to the spread of the data in a given plot, with the x axis denoting fold change and the y axis denoting -log10(adjusted p value). Coloured points represent genes that are significantly (p adj. < 0.01) differentially expressed. Red colour denotes genes that are upregulated in the comparison, while blue colour denotes genes that are downregulated in the comparison. **a.** Lesioned ROIs vs non-lesioned ROIs. **b.** Viral vector vaccine ROIs vs Unvaccinated ROIs. **c.** Formalin-inactivated vaccine ROIs vs Re-challenged ROIs. **d.** ROIs from 22Z (unvaccinated animal) vs 25A (another unvaccinated animal). **e.** ROIs from 10A (highest pathology animal, one dose DNA vaccine) vs ROIs from 22Z (high pathology unvaccinated animal). **f.** Lesioned ROIs from 'pathology' (histopathology score > 6.5) animals vs lesioned ROIs from 'protected' (histopathology score < 6.5) animals. **g.** Non-lesioned ROIs from 'pathology' NHPs vs non-lesioned ROIs from 'protected' NHPs. **h.** Lesioned ROIs vs non-lesioned ROIs from 'pathology' animals. **i.** ROIs from animals with high levels of virus in the lower respiratory tract vs ROIs from animals with low levels of virus in the lower respiratory tract.

3.4. Pathway enrichment analysis

For pathway enrichment analysis there are several tools available and gene-set enrichment analysis (GSEA) methods are commonly-used for this purpose. GSEA calculates an enrichment score for pathways based on firstly ranking each gene in the dataset according to the degree of differential expression, its significance, or a combination. In our case, we ranked the genes by log fold change, which is common practice, apart from in the case of the histopathology score linear correlation, in which genes were ranked according to their correlation with histopathology score. An enrichment score for each pathway is then calculated based on whether genes in the gene sets (pathways) chosen are overrepresented at the extremes of the ranked gene lists [170]. The enrichment score is normalised for each gene to create a normalised enrichment score (NES) for the pathways. The method is described in further detail in the original publication [170]. Other pathway enrichment tools work similarly but do not involve a ranking system and instead require the list of genes in the dataset as well as a list of 'background' genes, representing the genes that could feasibly have been detected in the assay as differentially expressed. This is typically referred to as functional gene enrichment analysis. We chose to carry out GSEA, due to both its widespread use and partially because we cannot be completely certain of an appropriate background list due to unknown cross-reactivity failures between the human probe set and mRNA transcripts from NHPs. Also, because the ROIs from unchallenged animals failed, they cannot be used to generate background gene lists. To simplify integration with pathway databases, genes from the dataset were re-named according to Entrez-IDs. The c2 and gene ontology biological processes (GO-BP) gene sets were downloaded from the Molecular Signatures Database (MSigDB) and used to map genes to pathways for GSEA [170,171]. GSEA was run using the clusterprofiler package [166], once again using a strict cut-off (p.adjust < 0.01) with the Benjamini-Hochberg method to minimise false discoveries considering the many comparisons being made in this dataset. The output tables of GSEA for each comparison are available on request. Considering the many comparison plots possible across all categories, below we group comparisons as much as possible rather than show all of the one-on-one comparisons. However, some one-on-one comparisons of interest are

shown. The other one-on-one comparison plots are available upon request. The vast majority of comparisons across the dataset had over 100 or more pathways that were significantly expressed, making the data difficult to visualise. To get a sense of this scale and the general theme of the pathways, we used the rrvgo package which groups GO terms into their parental terms based on their semantic similarity and scores. Unfortunately, we were not able to do something similar for the c2 pathways. **Figure 58** to **Figure 63** are one-to-one comparison bubble plots for grouped pathways in selected comparisons of interest.

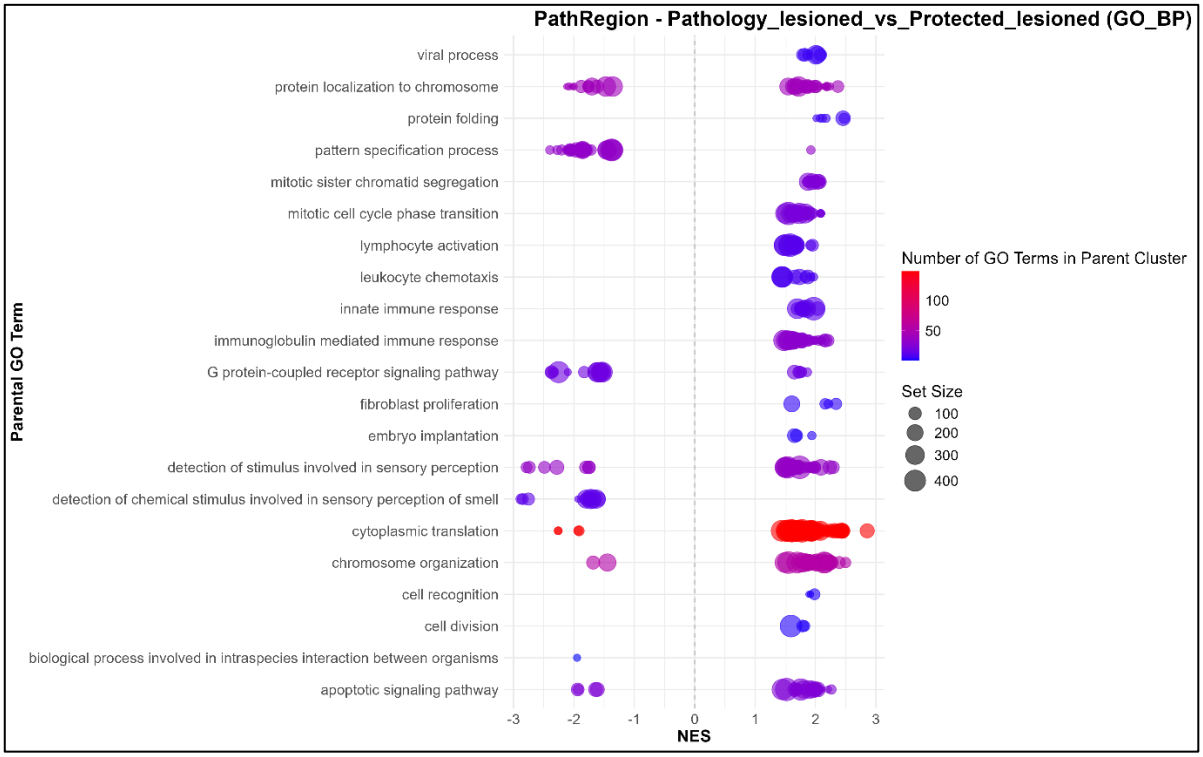

Figure 58: Grouped pathways in 'Pathology lesioned' vs 'Protected lesioned' ROIs.

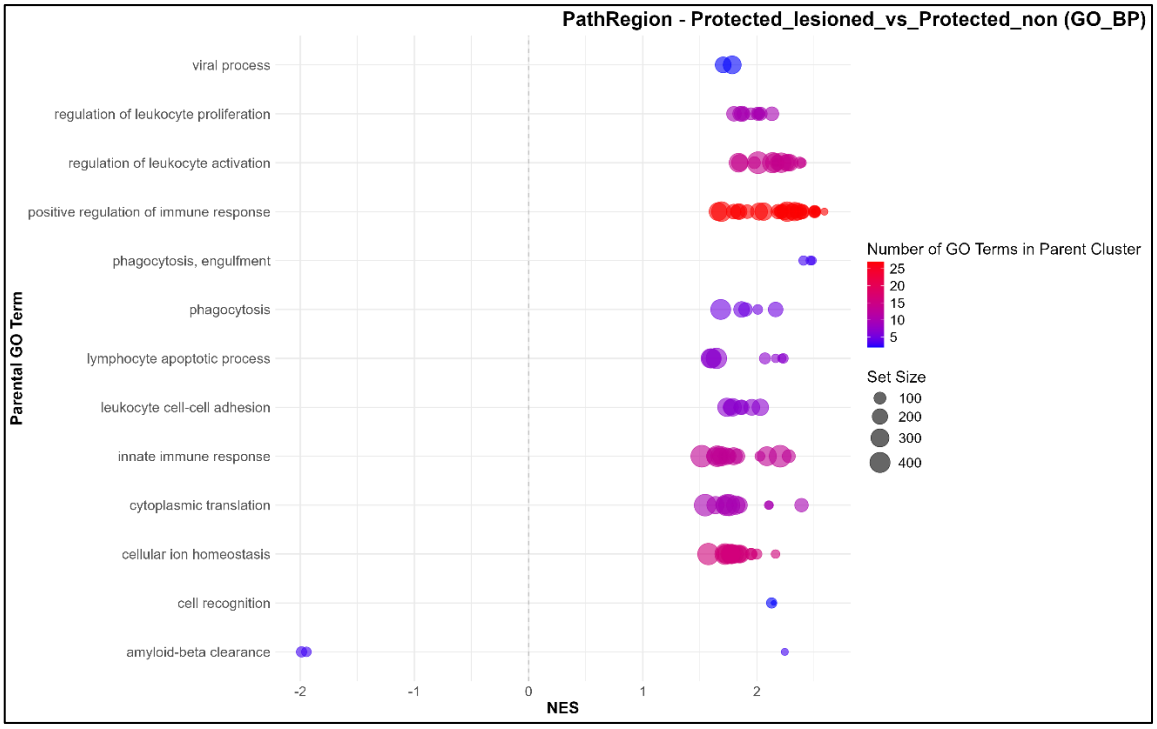

Figure 59: Grouped pathways in 'Protected lesioned' vs 'Protected non-lesioned' ROIs.

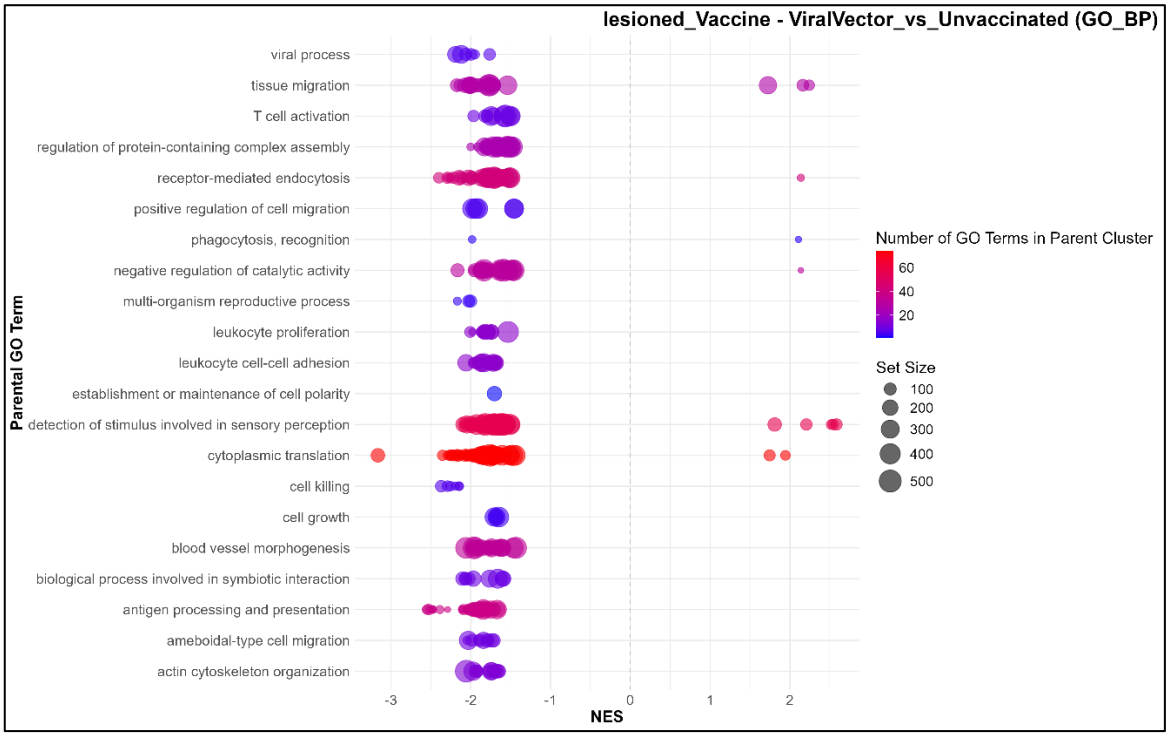

Figure 60: Grouped pathways in Viral vector vs Unvaccinated, comparing lesioned regions only.

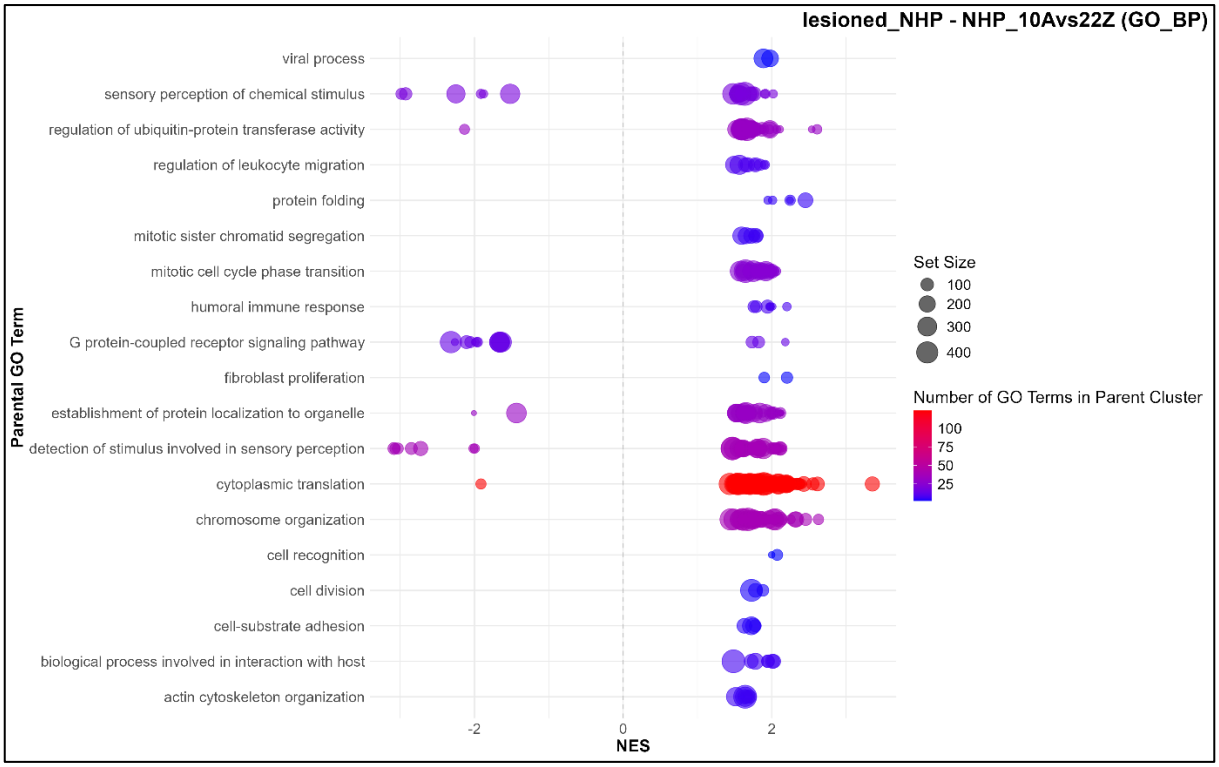

Figure 61: Grouped pathways in 10A vs 22Z NHPs, comparing lesioned regions only.

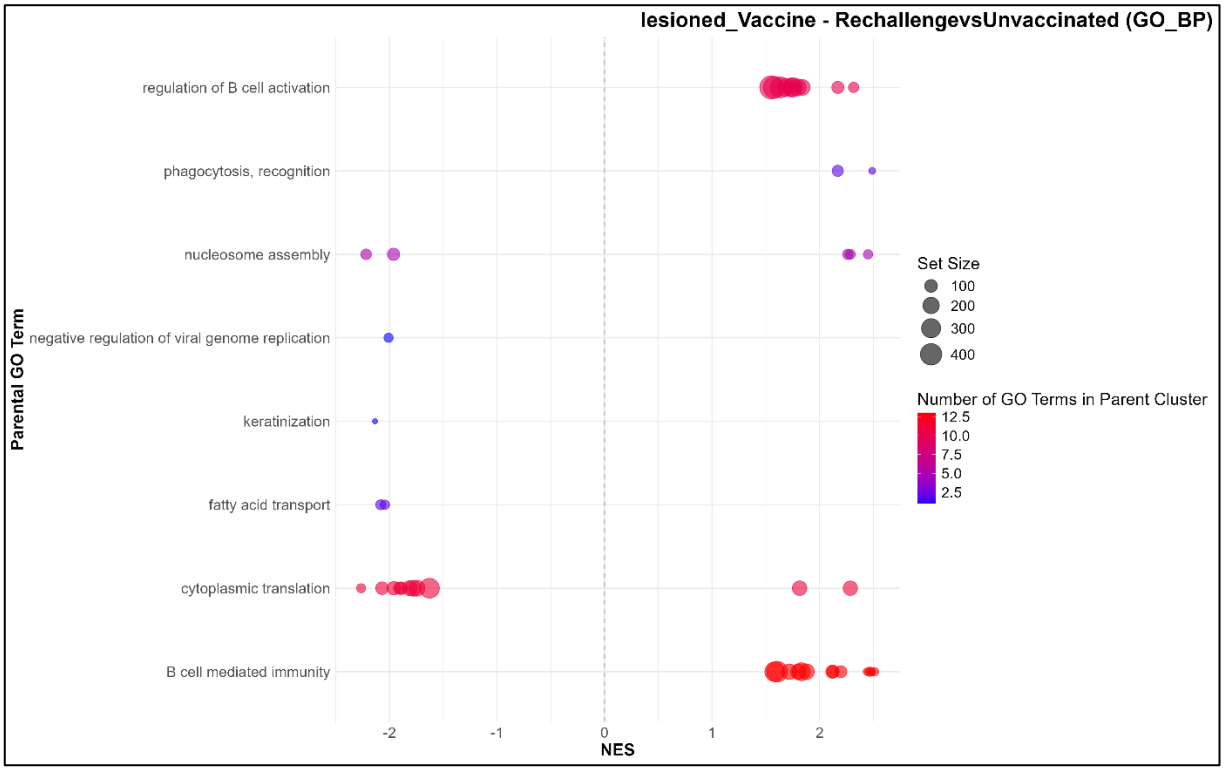

Figure 62: Grouped pathways in Re-challenge ROIs vs Unvaccinated ROIs, comparing lesioned regions only.

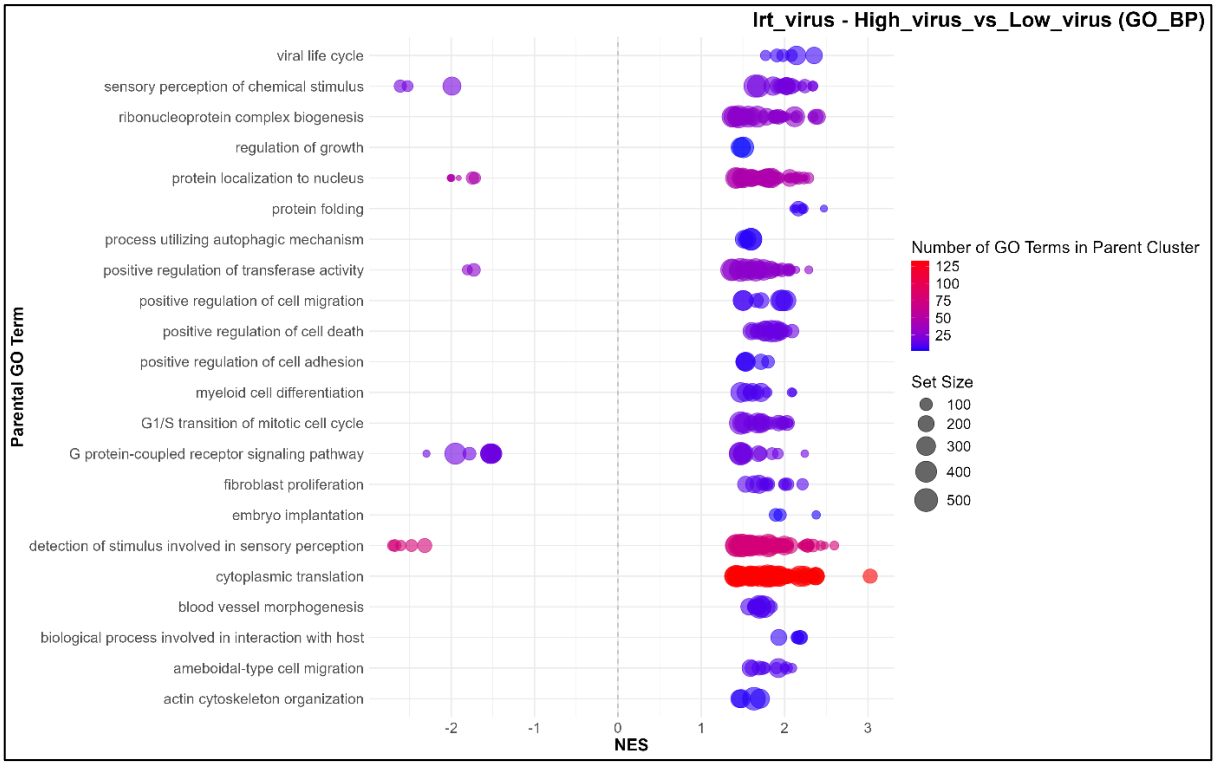

Figure 63: Grouped pathways in ROIs from NHPs with High virus vs NHPs with low virus.

For more specific pathway visualisation, pathways of interest were chosen (**Table 5**), as is common for GSEA visualisations. These pathways were selected from the GSEA results tables on the basis of relevance to viral infection, SARS-CoV-2, immunology, lung fibrosis and based on their NES. Individual one-to-one comparison bubble plots were generated for the pathways of interest from both the GO-BP and MSigDB pathways, where the x axis was the adjusted p value. This is shown for the 'region' comparisons and the 'lrt_virus' comparisons as each of these categories only has one comparison within them (**Figure 65** to **Figure 68**). We've also shown the bubble plot for the GSEA related to the linear correlation between genes and pathology scores for the c2 pathways (**Figure 64**), the GO-BP plot is not shown because none of the comparisons of interest in this database were found in this comparison. All other one-on-one comparison plots are available on request. However, as all p values had to be highly significant to be included in our GSEA output, we also grouped all of the one-on-one comparisons in each category together

in large plots for each category to simplify pathway visualisations. For the comparisons across vaccine groups and across NHPs, we have shown only comparisons related to the lesioned regions exclusively for simplicity (**Figure 69** to **Figure 72**). The plots related to the combination of lesioned and non-lesioned or only non-lesioned across all of these comparisons can be found in the supplementary data (**Supplementary Figure 6** to **Supplementary Figure 13**).

Pathway database	Pathway name
c2	REACTOME_NEUTROPHIL_DEGRANULATION
c2	REACTOME_SARS_COV_2_INFECTION
c2	REACTOME_SARS_COV_2_MODULATES_HOST_TRANSLATION_MACHINERY
c2	REACTOME_SARS_COV_2_HOST_INTERACTIONS
c2	REACTOME_CLASS_I_MHC_MEDIATED_ANTIGEN_PROCESSING_PRESENTATION
c2	REACTOME_MHC_CLASS_II_ANTIGEN_PRESENTATION
c2	REACTOME_ANTIVIRAL_MECHANISM_BY_IFN_STIMULATED_GENES
c2	KARLSSON_TGFB1_TARGETS_UP
c2	REACTOME_COMPLEMENT_CASCADE
c2	REACTOME_INTERLEUKIN_12_FAMILY_SIGNALING
c2	REACTOME_FCGAMMA_RECEPTOR_FCGR_DEPENDENT_PHAGOCYTOSIS
c2	REACTOME_INTERLEUKIN_6_SIGNALING
c2	REACTOME_TCR_SIGNALING
c2	REACTOME_DOWNSTREAM_SIGNALING_EVENTS_OF_B_CELL_RECEPTOR_BCR
c2	REACTOME_DECTIN_1_MEDIATED_NONCANONICAL_NF_KB_SIGNALING
c2	REACTOME_INTERFERON_GAMMA_SIGNALING
c2	KEGG_LEUKOCYTE_TRANSENDOTHELIAL_MIGRATION
c2	REACTOME_CYTOKINE_SIGNALING_IN_IMMUNE_SYSTEM
c2	REACTOME_TOLL_LIKE_RECEPTOR_CASCADES
c2	WP_LUNG_FIBROSIS
c2	REACTOME_INTERLEUKIN_1_FAMILY_SIGNALING
c2	WP_NETWORK_MAP_OF_SARS_COV_2_SIGNALING_PATHWAY
c2	REACTOME_VIRAL_INFECTION_PATHWAYS
c2	REACTOME_INNATE_IMMUNE_SYSTEM
c2	REACTOME_APOPTOSIS
c2	REACTOME_INTERFERON_SIGNALING
c2	REACTOME_ADAPTIVE_IMMMUNE_SYSTEM
c2	KEGG_ANTIGEN_PROCESSING_AND_PRESENTATION
c2	REACTOME_INTERLEUKIN_4_AND_INTERLEUKIN_13_SIGNALING
c2	SARRIO_EPITHELIAL_MESENCHYMAL_TRANSITION_UP
c2	REACTOME_INTERLEUKIN_17_SIGNALING
GO-BP	viral process
GO-BP	humoral immune response
GO-BP	complement activation classical pathway
GO-BP	viral life cycle
GO-BP	glycolytic process
GO-BP	B cell mediated immunity
GO-BP	antigen processing and presentation
GO-BP	antigen receptor mediated signaling pathway
GO-BP	apoptotic signaling pathway
GO-BP	lymphocyte mediated immunity
GO-BP	leukocyte chemotaxis
GO-BP	adaptive immune response
GO-BP	T cell activation
GO-BP	positive regulation of immune response
GO-BP	inflammatory response
GO-BP	immune effector process
GO-BP	cytokine production
GO-BP	fibroblast proliferation
GO-BP	type I interferon production
GO-BP	innate immune response
GO-BP	intrinsic apoptotic signaling pathway
GO-BP	phagocytosis
GO-BP	phagocytosis, engulfment
GO-BP	complement activation
GO-BP	apoptotic process
GO-BP	response to cytokine
GO-BP	T cell mediated immunity
GO-BP	T cell proliferation
GO-BP	myeloid cell differentiation

Table 5: Pathways of interest and their corresponding pathway database.

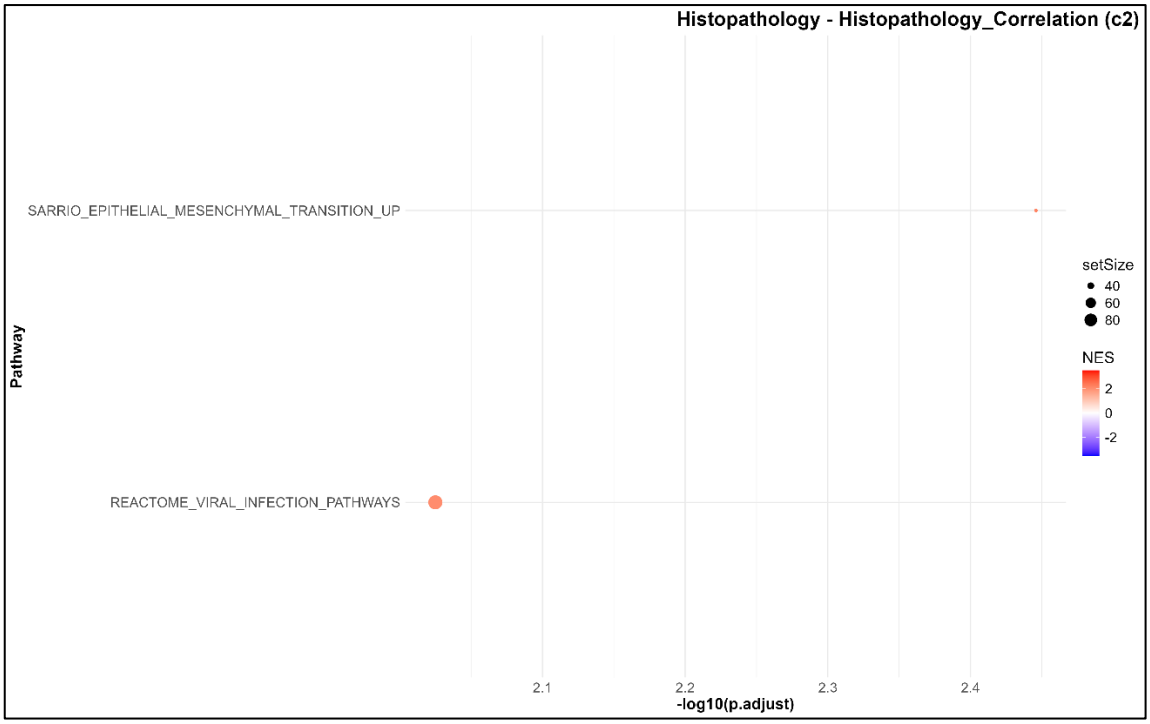

Figure 64: Bubble plot showing the detected pathways of interest from the c2 database in the histopathology score correlation.

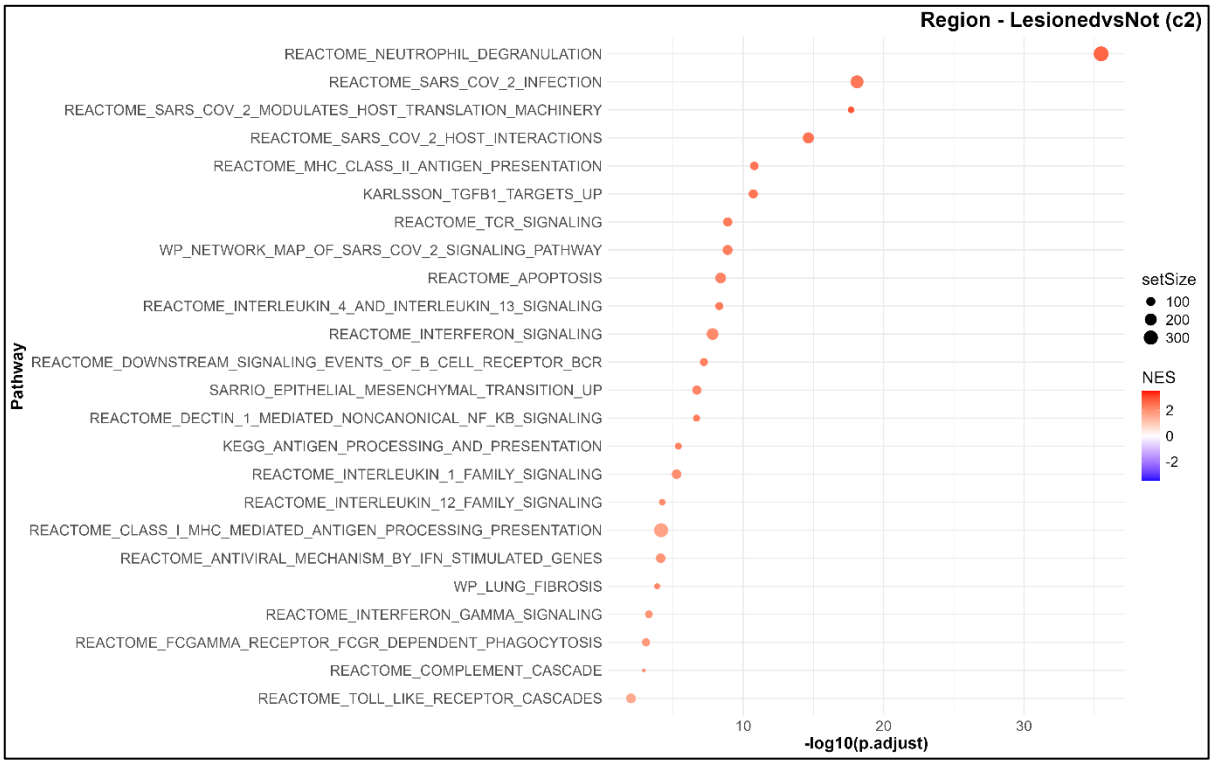

Figure 65: Bubble plot showing the detected pathways of interest from the c2 database in the lesioned vs non-lesioned comparison.

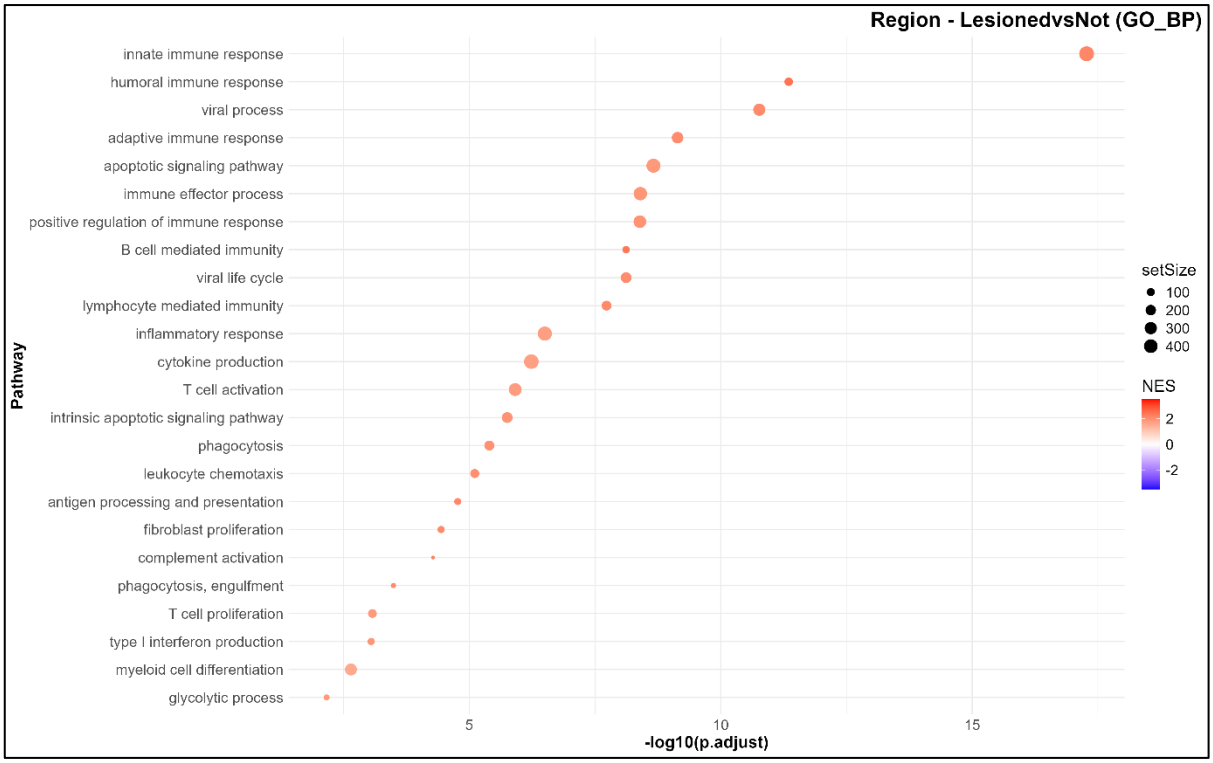

Figure 66: Bubble plot showing the detected pathways of interest from the GO-BP database in the lesioned vs non-lesioned comparison.

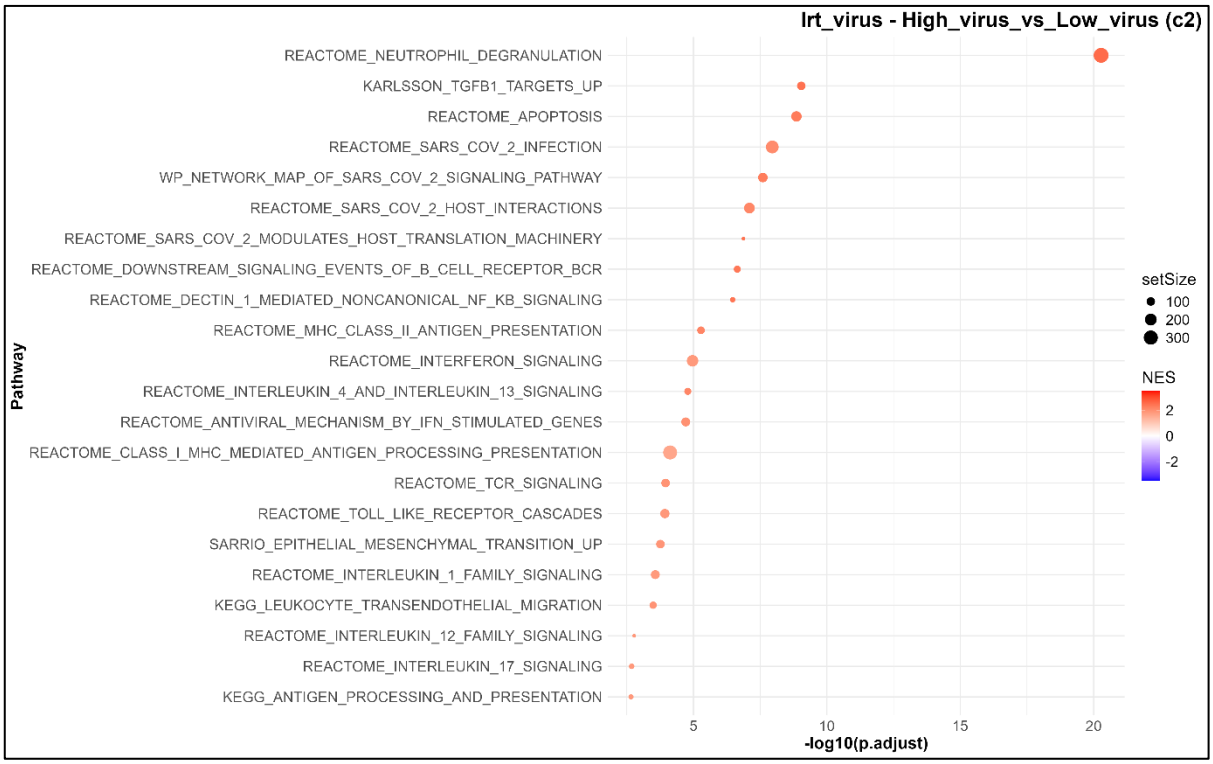

Figure 67: Bubble plot showing the detected pathways of interest from the c2 database in the high virus vs low virus comparison.

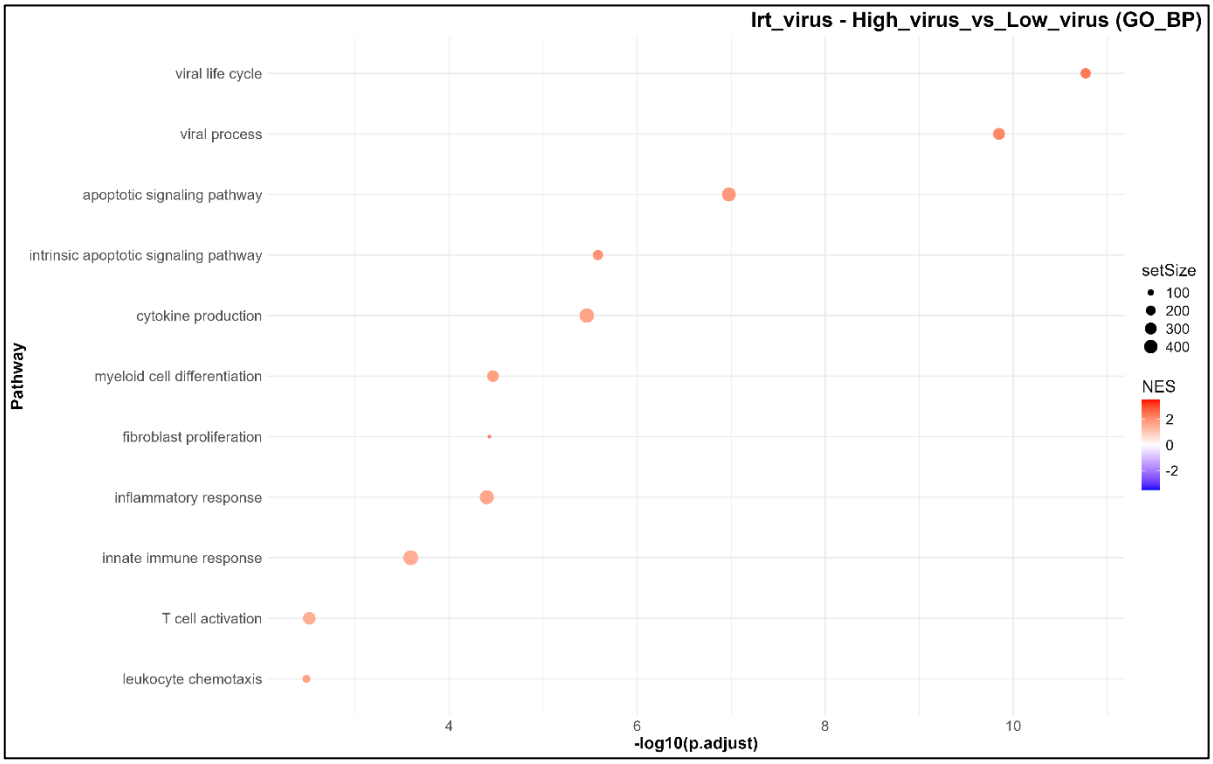

Figure 68: Bubble plot showing the detected pathways of interest from the GO-BP database in the high virus vs low virus comparison.

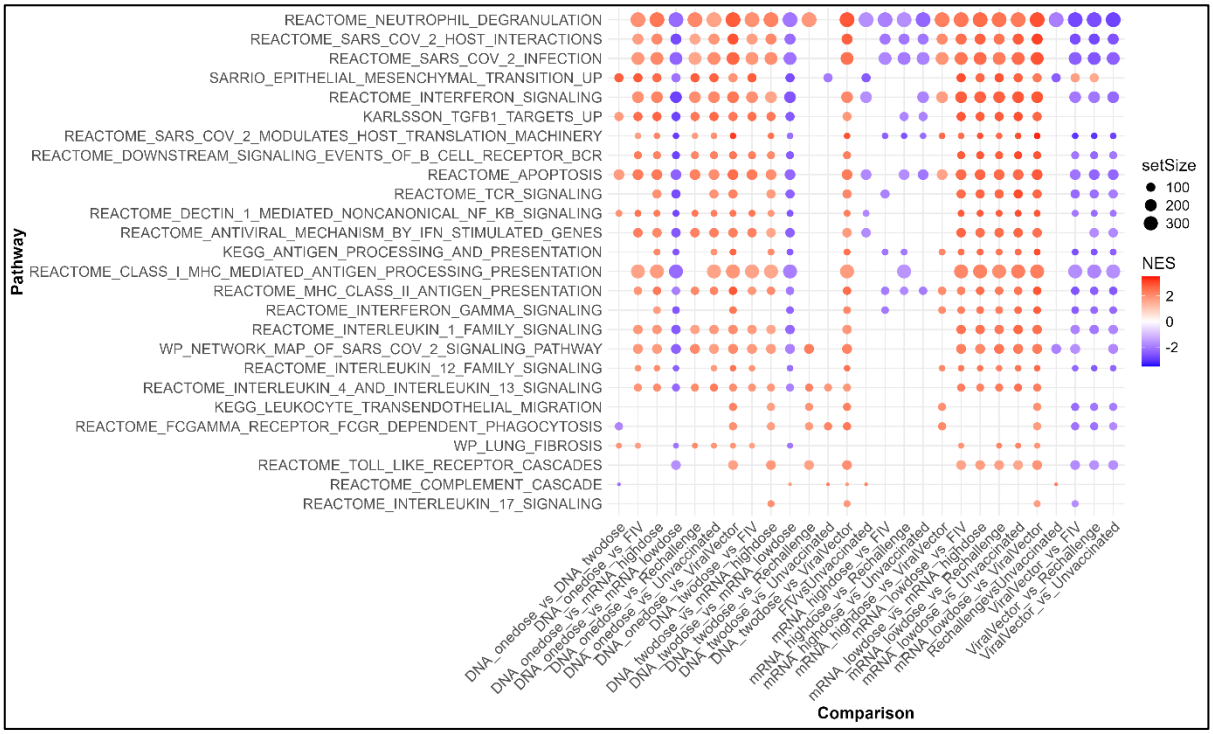

Figure 69: Bubble plot showing the detected pathways of interest from the c2 database across all of the vaccine/challenge group one-on-one comparisons, in lesioned regions only.

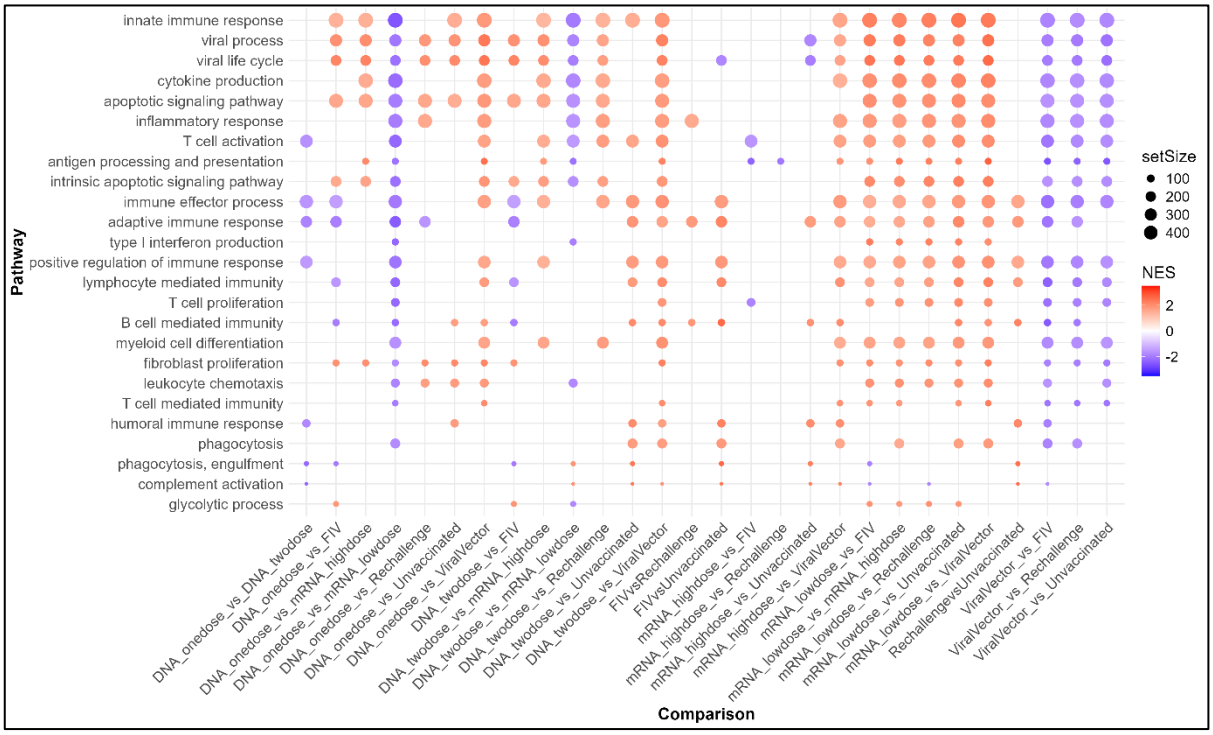

Figure 70: Bubble plot showing the detected pathways of interest from the GO-BP database across all of the vaccine/challenge group one-on-one comparisons, in lesioned regions only.

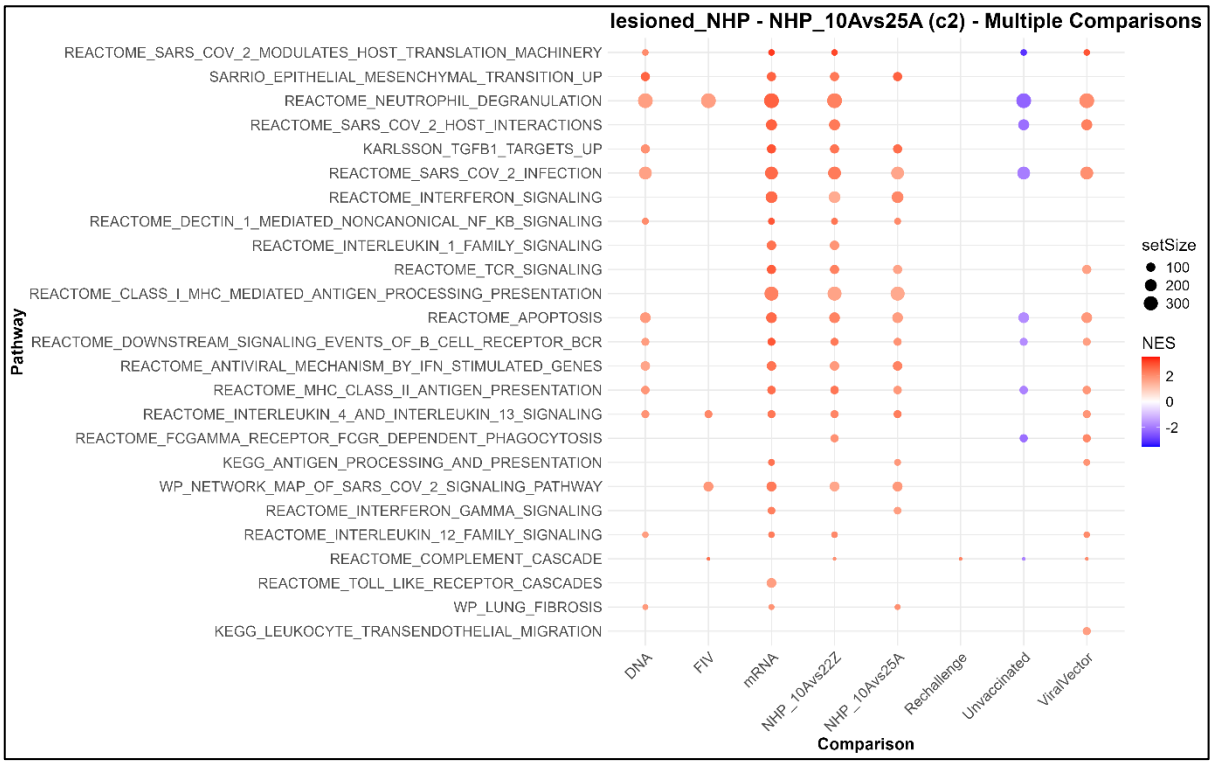

Figure 71: Bubble plot showing the detected pathways of interest from the c2 database across all of the NHP one-on-one comparisons, in lesioned regions only.

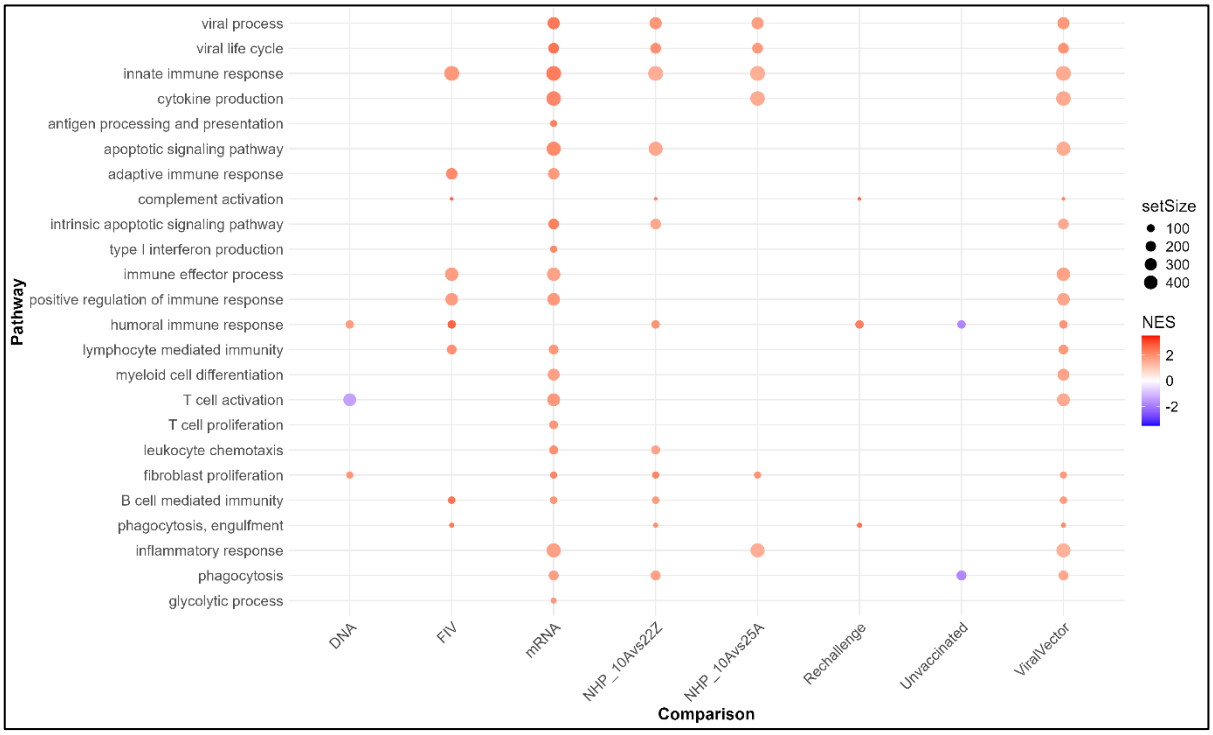

Figure 72: Bubble plot showing the detected pathways of interest from the GO-BP database across all of the NHP one-on-one comparisons, in lesioned regions only.

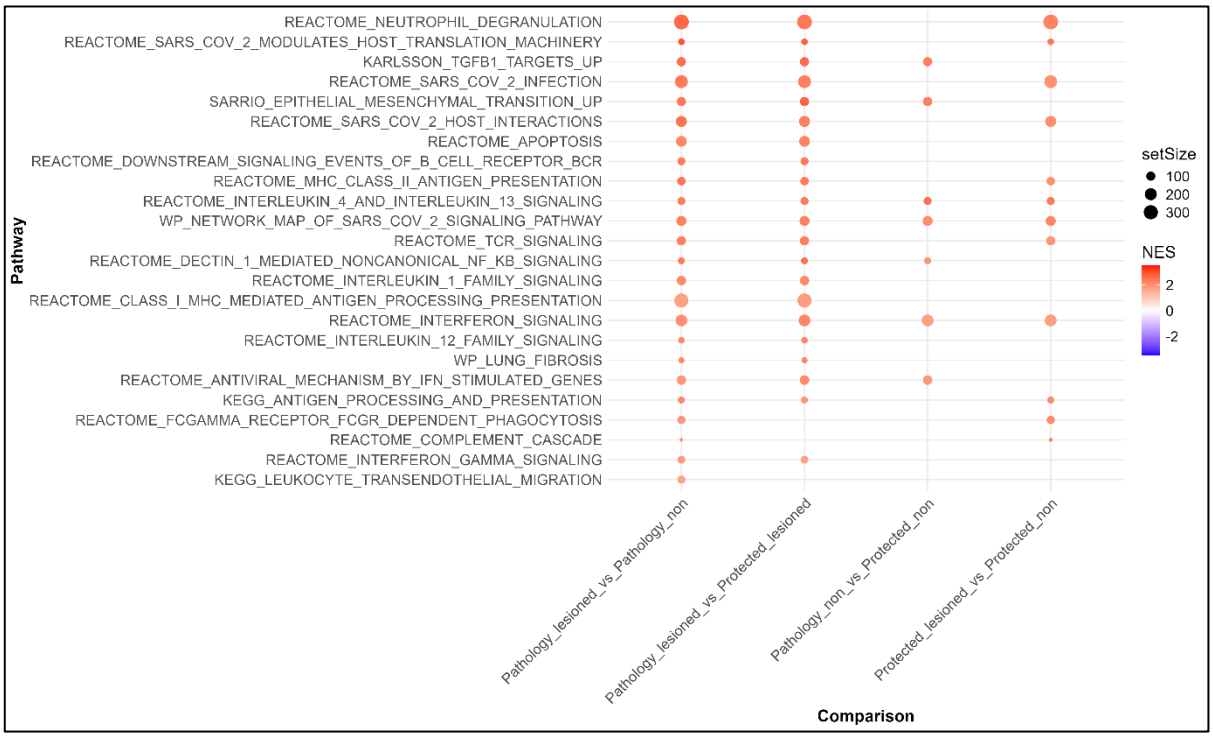

Figure 73: Bubble plot showing the detected pathways of interest from the c2 database across all of the 'pathclassregion' comparisons.

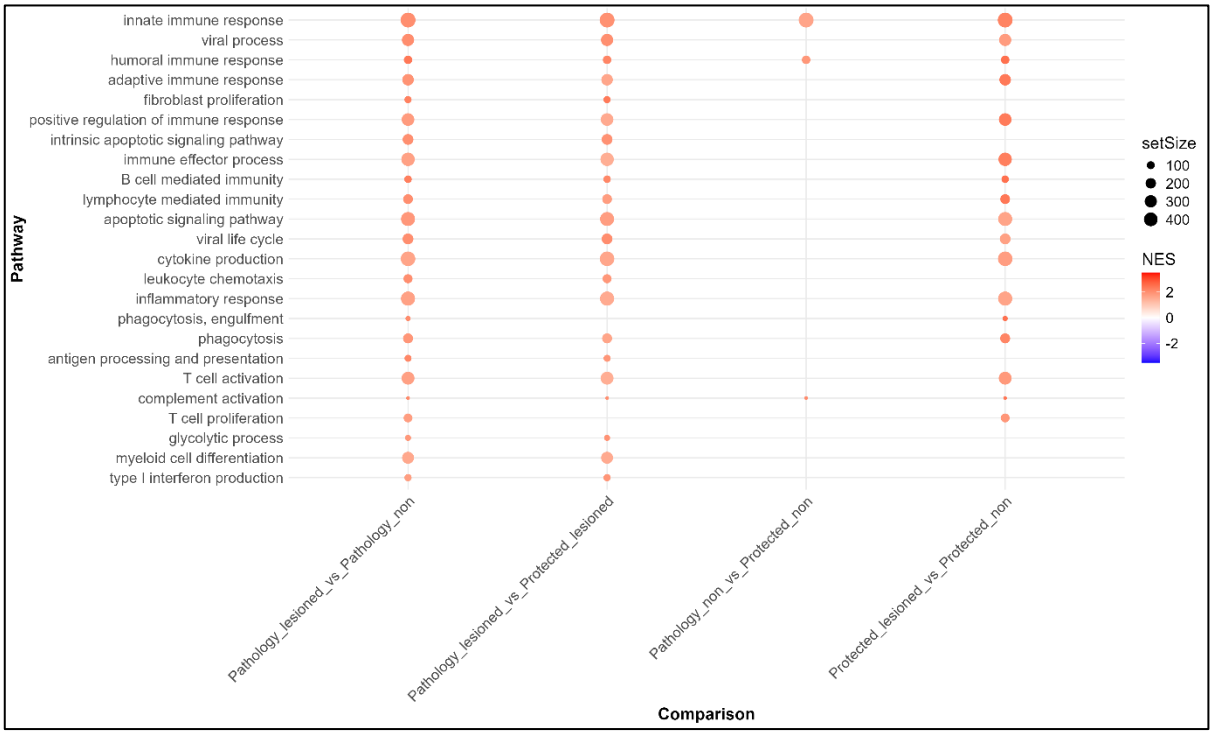

Figure 74: Bubble plot showing the detected pathways of interest from the GO-BP database across all of the 'pathclassregion' comparisons.

Heatmaps were generated for each pathway of interest to show how the gene expression (VST and z-score normalised counts) in the GeoMx experiment (after filtering and QC) varies across the regions, for each gene in the pathway that was also present in our dataset. The pathways were generated similarly to the previously-described pathways for differential gene expression (**Section 3.3**). Due to the many pathways of interest (**Table 5**) these individual pathway heatmaps are not shown but are available on request. Finally, a 'combined pathway heatmap' (**Figure 75**) was created, which took the VST and z-score normalised count values across all genes for each pathway and mapped them onto each region, with the same Euclidian clustering as previously mentioned. Based on the data from the individual pathway heatmaps (available on request as mentioned), the majority of genes in a pathway for a given region tended to be over- or under-expressed to similar extents, so averaging these expression profiles allowed for an overview of all the pathways of interest in one plot.

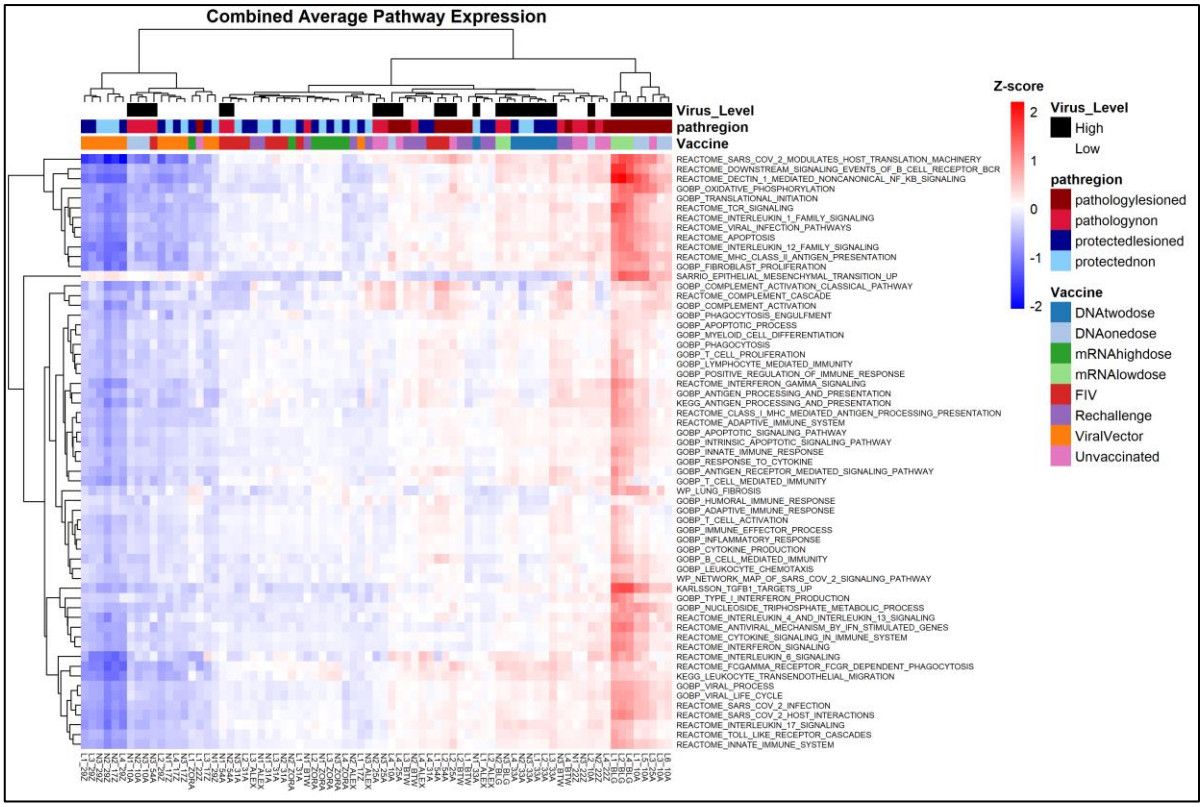

Figure 75: Combined pathway heatmap. ROIs are indicated on the x axis and pathways are shown on the y axis.

3.5. Discussion

By profiling the transcriptome in post-challenge lung tissue from NHPs in a spatially-resolved manner, we have shown that the transcriptomic response can vary widely depending on prior vaccination, the extent of pathology and whether lesioned or non-lesioned areas of the lung are sampled. Many thousands of genes were detected in our experiment due in part to the large ROI size, so the filtering steps were important in ensuring that lowly-detected genes and poorly-performing ROIs were removed (**Section 3.2**). Batch correction is commonly carried out in transcriptomic datasets. The samples that were run on a sequencing run had a smaller library size as expected (**Figure 40**) but despite this, we had many thousands of genes to analyse, even with a cut-off of 100 probe counts in a minimum of 6% of the ROIs (**Figure 38**). Based on the log CPM plots (**Figure 41**), we did not observe a major batch effect owing to the different slides or sequencing runs and the small amounts of variations were removed following TMM

normalisation (**Figure 42**). Despite the fact that different samples from the same groups were run on different slides (**Supplementary Table 4**), we found their results to be comparable (as discussed in the next paragraph). We concluded that variations were due to biological differences owing to different vaccine/challenge regimens and we did not apply batch effect corrections, as this could skew results because of the different combinations of samples on different slides. For our linear models, we ensured to include as many possible confounding variables as possible to ensure that the significant results noted for each comparison were as much as possible specific to that comparison, rather than other the other categories we compared by.

Our first look at the variation between ROIs in our dataset was through PCA dimensionality reduction (**Figure 43**). We expected that lesioned and non-lesioned ROIs might form two distinct clusters, however while there was some separation between these groups they significantly overlapped (**Figure 43a**). As most of the NHPs with high pathology also had high viral load in the respiratory tract, when we coloured the PCA by high or low viral load (**Figure 43b**), the plot was similar to grouping by pathology classification (all red vs all blue in **Figure 43d**). The PCA plots suggested that the vaccine/challenge groups (**Figure 43c**) and the combination of pathology class and region type (**Figure 43d**) explained much of the variation, as these groups tended to cluster together reasonably well. The clustering in the vaccine/challenge PCA (**Figure 43b**) was surprising given that the vaccines are all intramuscular (not expected to have tissue-specific effects) and for half of these groups (apart from the two DNA dosing groups and two mRNA dosing groups) there were two NHPs per group and these were chosen based on having relatively high and relatively low pathology within their groups to capture a spectrum of within-group pathology (**Table 1** and **Supplementary Table 1**). This suggests that despite differences in histopathology scores, there may be some consistency in the lung response following vaccination in NHPs that received the same vaccine or were previously challenged. However, it must be noted that the range of histopathology scores in the chosen NHPs within groups was sometimes quite low and in the viral vector group there were only two NHPs to choose from considering they were the only samples available at this cull timepoint (**Figure 6a**). Therefore, some of the similarities

leading to PCA clustering may be due to the NHPs having a similar level of pathology within the same vaccine/challenge groups. This could be due to consistency in the control of infection conferred by the same vaccines through peripheral and/or recruited in-situ tissue immunity. Therefore, differences between-groups in the tissue transcriptomics may reflect different levels of pathological manifestation owing to peripheral control of virus before establishment of the infection in the lungs, rather than induction of different immune mechanisms in the lung parenchyma owing to vaccination. We will discuss this in more detail later in the discussion and in the conclusions of the thesis. Within-group variation in terms of differentially-expressed genes was shown in **Figure 53** to **Figure 55**. This demonstrated relatively low within-group variation across region types, unless there was a dosing discrepancy (as there was in the DNA and mRNA groups). The PCA scree plot (**Figure 44**) demonstrated that PC1 and PC2 contributed to most of the variation across our ROIs. Based on the PCA plots (**Figure 43**), it appears that PC1 separates the well-protected animals (on the right) from the animals with higher pathology scores (on the left) while PC2 largely separates the 'pathology and lesioned' ROIs from all of the others. The distinct nature of the 'pathology and lesioned' ROIs from the others can also be notes in one of the differential gene expression comparison plots (**Figure 56**).

Many differentially expressed genes were noted across comparisons of particular interest (**Figure 57**), so pathway enrichment analysis (**Section 3.4**) was important to deconvolute this rich dataset. In the between-group pathway comparisons for lesioned regions (**Figure 69** and **Figure 70**), it is evident that many of the same pathology-associated pathways are found in almost every group but are upregulated or downregulated to different extents, suggesting a spectrum of pathology control rather than distinct in-situ immune mechanisms by the different groups, as previously mentioned. However, while there are many similarities between groups, there are some distinct patterns worth noting. For instance, the viral vector group comparisons consistently show downregulation of almost all of the pathways of interest when compared to other groups. This suggests that rather than an in-situ immune protective mechanism, this group does not activate the same responses to a large extent, perhaps due to early clearance of the virus or peripheral

control before infection establishment. Between groups, the complement cascade appears to be upregulated in the DNA two dose and mRNA low dose groups in particular. Re-challenged NHPs vs unvaccinated NHPs appear to have better adaptive responses in the tissue, as to be expected considering previous mucosal priming from their initial exposure. mRNA low dose appears to be particularly high in several immune signalling pathways including interferon, B cell receptor signalling, NF-κB signalling, IFN-γ and several interleukin families. Similarly, lung fibrosis appears to be upregulated particularly in the some of our highest-pathology NHPs, which were the NHPs from our samples of interest that received one dose of the DNA vaccine or a low dose of the mRNA vaccine (**Figure 6**). While we did not have a spike mRNA probe, viral pathways were detected across many of the comparisons as can be seen in the bubble plots, including many that are associated with SARS-CoV-2 in particular (**Figure 64** to **Figure 74**), which suggests that although viral mRNA was low (as detected in our RNAscope **Figure 14**), the knock-on effects of viral infection pathways remain at this cull timepoint. This is further shown by the parental pathway plot comparing all regions across animals with high and low viral loads in the lower respiratory tract, in which 'viral life cycle' was one of the significant parental groups and contained multiple associated pathways (**Figure 63**).

Across all of the parental pathways, while there were many immune-related pathways present, there were also more general pathways that related to cell division, apoptosis, G-protein coupled receptor signalling and translation (**Figure 64** to **Figure 74**). Translation pathways have been found to associate with severe human COVID-19 [39]. Considering the large ROI size, the high level of pathways that are not directly related to pathology could be expected. However, cell division and translation could potentially be related to repair and/or fibrosis, but single-cell resolution transcriptomics would be required to discover whether these processes were enriched in particular cell types associated with these processes, such as fibroblasts and epithelial cells. Other parental pathways that consistently came up across comparisons related to sensory perception of different stimuli, particularly those related to smell. This was initially unexpected because we were profiling the lower airway response rather than the upper airway response.

However, the signal for these pathways were among the strongest and also among the only pathways that were upregulated in protected groups (including the viral vector vaccine group) compared to groups with higher pathology, so we carried out a literature search for an explanation. We found a study that demonstrated that smooth muscle cells in the lung express olfactory cells [172] and these cells have also been found to co-express ACE2 receptors and may be associated with anosmia upon SARS-CoV-2 infection [173]. As mentioned in the introduction, olfactory receptors are thought to be downregulated in response to inflammation [21]. Therefore, while gene sets related to olfactory signalling appear to be upregulated in the lung tissue of protected animals in our analysis, we propose that the reason for this may be the downregulation of olfactory receptors on smooth muscle in the lungs of animals with greater pathology. Greater pathology is associated with increased inflammation and pathways related to interferons and other cytokines, meaning that relative to these animals, the protected animals may have greater expression of olfactory receptors in the lung. Single-cell resolution imaging studies related to olfactory receptors would be needed to confirm this hypothesis.

In our histopathology correlation, only 5 significantly-correlated genes were found in the correlation for non-lesioned regions and there were 904 significant genes in the correlation for lesioned regions. However, the only parental pathway group that was found in the lesioned correlation was for nucleosome organisation, with a limited number of GO terms associated with this and for our pathways of interest, (**Figure 64**) only two were seen. However, the correlation of genes with a quantitative histopathology is a much higher bar than an association across more general 'high' or 'low' pathology groups, so these two pathways (related to viral infection and EMT) are found to be highly correlated with progression of disease across the pathological spectrum. This confirms the utility of the rhesus macaque model to study COVID-19, as even in the context of vaccinations with varying levels of protective efficacy, EMT, which has been noted as a major driver of pathological progression in humans [29] is also strongly associated with pathological progression in this model. In the group pathway analyses, other pathways associated human severe COVID-19, including pathways related to the virus itself, TCR signalling (at least

at later timepoints [54]) and neutrophil degranulation [174]. This again validates the rhesus macaque model at the tissue level which has not been done previously aside from BAL sampling studies and to our knowledge, not at all in the context of vaccination (for humans or NHPs). On an individual gene level, similarities with human severe pathology [29,30,34,39] were noted particularly in some the highest-pathology NHPs (**Figure 45** to **Figure 48**). Given that the rhesus macaque model is typically a model of mild to moderate COVID-19 [87] these heatmaps also demonstrated the capacity for more severe disease phenotypes to be noted in rhesus macaques when analysis is focused on lesions, as these genes were typically upregulated in those regions only. Many macaques expressed at least some of the severe-associated genes in some of the heatmaps but in the heatmap with only the most severe associated genes, agnostic of cell types, only one animal (BLG) was found to have most of these genes upregulated (**Figure 45**). Given that the macaque model is not a lethal model of COVID-19 and many of the human studies have profiled the responses associated with fatal responses, it is understandable that not all of these genes would be upregulated in the macaque model, even in the lesions of a high-pathology animal. In the heatmap of genes associated with different cell types and immune processes in COVID-19 (**Figure 48**), NK cell genes, B cell genes and mDC genes were included but were not shown as these genes were not detected in our post-QC and post-filtration dataset. Only detected genes were shown in all of the other heatmaps, meaning that there are more genes related to COVID-19 that were not present in our NHP samples, at least above the strict thresholds for detection that we set.

From the pathways of interest heatmap (**Figure 75**) it was clear that pathways associated with severe human COVID-19 were generally co-expressed to very similar levels in the same ROIs and that they were highly upregulated in the highest-pathology animals (10A and BLG), in lesioned regions. The heatmap (**Figure 75**) demonstrates the spectrum pathological pathways across the ROIs clearly, showing different levels of human disease recapitulation which is often mild to moderate. Several studies have noted that expression of CD127 (also known as IL7R) on T cells in BAL is associated with less severe disease and better outcomes [54,156,160,161]. We searched

for this gene in our DGE tables and found *IL7R* to be significantly differentially expressed (FDR ≈ 0.00001) in protected lesions vs pathology lesions. While we cannot say whether this expression is within T cells and how well this corresponds to the expression of the CD127 protein, this indicates that the rhesus macaque model may recapitulate protective signatures in humans as well as pathologic ones. The data on protective lung responses in humans is limited however, as it is difficult to retrieve tissue from healthy donors as explained in **Chapter 1**.

Looking at the broad differential gene expression patterns, one of our most striking findings was that, overall, there were no differences between lesioned and non-lesioned transcriptomic profiles in 'protected' NHPs, with low histopathology score. This can be seen clearly in **Figure 56** where we note that there are no differentially-expressed genes in this comparison. Another striking finding that can be observed in **Figure 56** is that non-lesioned regions contribute little or nothing to the differences in transcriptomic responses across our comparisons. There were only two differentially-expressed genes when comparing non-lesioned regions across all of the high-pathology NHPs vs the non-lesioned regions of the 'protected' animals with low histopathology scores. Overall, this suggests that our pathology-guided spatial approach was important in picking out differentially-expressed genes that were relevant to pathological outcomes. These results also suggest that bulk sequencing may 'dilute' findings in studies that compare tissues with higher or lower pathology, as much of the tissue can be non-lesioned (particularly in milder disease) and we have shown that these parts of the tissue will not contribute largely to pathology-associated variation. Further to this point, **Figure 56** shows that if only lesioned areas are compared, there are significant differences, almost 2000 differentially-expressed genes, between 'protected' and 'pathology' groups. The vaccine/challenge group comparisons (**Figure 50**) showed that overall (and in the lesioned areas, **Figure 51**), the FIV and re-challenge groups were the most similar (with fewer differentially-expressed genes) and the viral vector group was very different to all of the other groups (high number of differentially-expressed genes). The similarity between FIV and re-challenge is interesting and might suggest a response profile associated with whole-virus exposure, as these are the only two groups that had previous exposure to the whole virus while

the other vaccine regimens encoded spike protein. The distinct nature of the viral vector group may be down to the high level of protection observed in response to this vaccine, as also noted earlier in discussion of the PCA plots.

In relation to VAED, while there were differences between the highest-pathology animal (10A) from the DNA one-dose group and the unvaccinated animals (**Figure 54**). The pathways that these differentially-expressed genes were associated with were primarily associated with cytoplasmic translation and other cellular processes (**Figure 61**). While some immune pathways were also noted (**Figure 61**) and some of our pathways of interest were upregulated, they were also found to be upregulated in other high-pathology animals such as the low-dose mRNA-vaccinated animal (**Figure 71** and **Figure 72**), which had comparable pathology to the unvaccinated NHPs (**Figure 6**). When we went through the entire pathway lists for 10A-associated comparisons, there were no aberrant immune mechanisms such as Th2-mediated pathways that would indicate VAED in this animal. Therefore, we propose that 10A's poor response to the vaccination (as evidenced also by its poor antibody response in the original publication [135]) led to more of an 'unvaccinated' phenotype and this NHP happened to be at the higher end of the unvaccinated pathology spread.

Our transcriptomic dataset contains a vast amount of information and possible comparisons, which we have summarised as best as possible with the available bioinformatic tools. Once we publish this data, it may be explored further by others to provide additional insights to the NHP lung response to SARS-CoV-2, mild to moderate pathology and the impact of vaccination on pathological outcomes – perhaps in the context of insights provided by future studies. However, there are also limitations to this data. As we have discussed earlier, we used a human probe panel and therefore there were some cross-reactivity problems, meaning that we could not detect all of the macaque transcriptome and some important genes like *IFNG* were not detected in our dataset, although pathway enrichment analysis meant that we could still detect its associated pathways due to other genes in those pathways being detectable. Transcriptomic data does not always translate to proteomic outcomes. Post-transcriptional silencing can stop proteins being produced

from their corresponding mRNA, so for mechanistic insights it is important to back up transcriptomic data with protein data. We have used protein data in the context of single-cell phenotyping in the lung tissue (**Chapter 2**) and for BAL cytokine profiling (**Chapter 4**). Here, our transcriptomic data helps to justify our hypothesis that the 'other immune' population described in chapter 2 are indeed neutrophils, as neutrophil degranulation-associated pathways appear in many of the comparisons. Another limitation is that we carried out two sequencing runs, although we have normalised to correct for the lower counts associated with this as discussed in **Section 3.2**. It was unfortunate that our unchallenged control regions failed and we hypothesise that this may be because of large air pockets in healthy lung tissue meaning there was insufficient transcriptomic material for analysis, with comparatively much fewer cells in these regions.

We hypothesised that we could determine whether high-pathology vaccinated animals experienced VAED or vaccine failure using spatial transcriptomics. As mentioned, VAED was not seen in any of the NHPs in our cohort, as we detected no Th2-biased pathway signatures and the pathways that were strongly upregulated by 10A were analogous to those present in other high-pathology animals, regardless of vaccination status. Therefore, we conclude that this animal experienced vaccine failure and not VAED. We also hypothesised that the rhesus macaque model would recapitulate human disease pathways. Despite the mild to moderate pathology evident in this model, we noted that in a high-pathology animal, BLG, several genes associated with severe human COVID-19 were upregulated (**Figure 45**) relative to the other animals. Fewer genes associated with human severe COVID-19 were upregulated or downregulated in other NHPs, which may demonstrate that this model only rarely captures a more severe profile and that mild to moderate pathology demonstrates only some features that are analogous to more severe human disease. Pathway analysis also reflected this spectrum of pathology across the NHPs, where higher-pathology animals reflected human severe COVID-19 (particularly in lesioned regions) (**Figure 75**). Finally, our hypothesis that vaccination may induce different pathways indicative of a protective profile was disproven, as highly-protected vaccinated animals did not have strong immune transcriptomic profiles and instead demonstrated a downregulation of pathological

immune pathways, hinting that perhaps pathology has already been resolved by the cull timepoint in these animals and that no ongoing protective immune response is present in the lung tissue. Alternatively, peripheral control (by antibodies for example) may have also prevented the establishment of pathological profiles in these animals, with in-situ responses in the lung parenchyma playing a limited role in protection.

Chapter 4: Soluble factors in lung tissue pathology

As we've described and shown in the previous chapters, the lung tissue parenchyma is where COVID-19 pathology primarily manifests and immune cells mediate their pro-inflammatory, anti-viral or pro-fibrotic functions which can be pathological or protective. Few studies have been able to examine the tissue parenchyma in severe COVID-19 due to difficulties in retrieving human tissue, and even when tissue is retrieved it is not possible to standardise due to different infection and death timepoints, viral loads etc. The tissue can only be retrieved upon death, making the time-course of infection very difficult to study in the native tissue context. However, other sampling methods in the airway, such as BAL fluid retrieval, can provide insights into the dynamics of immune responses in the airway over time, as well as allowing for the measurement of lung viral load in patients or animal models, as is common practice. BAL fluid contains non-adherent cells from the airways as well as soluble factors such as antibodies and cytokines [46]. In Chapters 2 and 3, we were able to study lung tissue cells and transcriptomes in their native context and in this chapter, we evaluate the cytokine profiles in BAL fluid at the cull timepoint. This allows us to put the cytokine environment of the lung in the context of what we've learned about the cellular and transcriptomic environments at the same timepoint. In this chapter we also examine another important soluble factor driving pathological or protective outcomes, the immunoglobulin response. Antibody responses (both binding and neutralisation) have been extensively evaluated in these NHP studies, with high neutralising titres in serum correlating with protective outcomes (Brady *et al*, in review). However, the potential for non-neutralising antibodies to drive pathology through AED in NHPs with poor outcomes has not been evaluated. As discussed in the introduction, a previous study described a potential role for AED as a mechanism of VAED in animal models when an improper SARS-CoV-2 antigen structure is used [132], and as a potential cause of severe disease in unvaccinated human COVID-19 patients [109,110].

Cytokine storms are a well-known feature of COVID-19 pathology [175–178]. For instance, Valle *et al*. found that high levels of serum IL-6, IL-8 and TNF-α at the time of hospitalisation correlated with COVID-19 disease severity [176]. While several pro-inflammatory cytokines have been

implicated in the cytokine storm, IL-6 has stood out as a strong predictor of severe disease outcomes [179]. However, clinical trials that block the activity of IL-6 have largely failed to show efficacy, although there may be some benefit if IL-6 is targeted early [180]. While most studies that examine the role of pro-inflammatory cytokines focus on the serum due to its relative ease of access, other studies on BAL fluid have demonstrated that the associations between high levels of pro-inflammatory cytokines (including IL-6 and IL-8) and severity of COVID-19 outcome hold true in the lung [39,181]. These cytokine levels can persist beyond the acute stage of infection, with one of these studies having measured BAL cytokines in severe COVID-19 patients a mean of 13.2 days after symptom onset [181]. As discussed previously in the introduction and Chapter 3, BAL single-cell studies have shed light on the specific cell types in the lung that produce these pro-inflammatory cytokines and chemokines, which are typically the recruited monocytes and resident lung macrophages [34,39]. While the pro-inflammatory cytokines trigger airway damage through innate immune activation, the chemokines they produce recruit monocytes and neutrophils through engaging CCR1, CCR2 and CXCR2 and T cells through CXCR3 and CXCR6 [34,39]. A study comparing blood and airway cells in COVID-19 found that cells in the BAL upregulated *IFNG*, *CCL2* and *CCL4* compared to cells in the blood, which did not [34]. Overall, whether similar correlations between cytokines, chemokines and severe outcomes exist in the NHP model is unknown, as is the impact of vaccination on BAL cytokine profiles upon infection. One NHP SARS-CoV-2 infection study quantified *IL6* mRNA in pulmonary lesions using RNAscope and found a much greater level of transcription at day 4/5 post-challenge, which had largely waned by day 14/15 post-challenge and was absent by day 18/19 post-challenge [87]. Therefore, we can expect that at least the unvaccinated rhesus macaques in our cohorts may still be producing IL-6 at the cull timepoint of day 6/7 and this will likely be detectable in BAL fluid.

In this chapter, we hypothesise that formalin inactivation alters the structure of the SARS-CoV-2 spike protein such that antibody binding to native spike protein is reduced in NHPs vaccinated with a formalin-inactivated SARS-CoV-2 vaccine. This is a concept that could theoretically lead to VAED, as discussed in **Section 1.6**. We also hypothesise that the cytokines IL-6 and IL-8, as

well as some chemokines, may be detected at higher levels in high-pathology NHPs, as is observed in human studies.

4.1. Assessment of the impact of formalin inactivation on antibody binding to SARS-CoV-2 spike protein

In this experiment, we investigated whether formalin inactivation of SARS-CoV-2 spike protein can alter its conformation to the extent at which antibodies from the NHPs differentially bind formalin-inactivated spike and native spike. If this is the case, we would expect to see that for most of the vaccinated groups, binding to native spike is higher than binding to formalin-inactivated spike, as native spike should be generated by the DNA, mRNA and viral vector vaccines. In contrast, we would expect that serum from FIV-vaccinated NHPs would show greater binding to formalin-inactivated spike than to native spike. In the context of VAED, this could indicate whether a formalin-inactivated vaccine can induce poorly-neutralising antibodies against native spike, which could theoretically lead to ADE or AED upon infection with SARS-CoV-2. As mentioned previously in the introduction, formalin inactivation has been hypothesised to alter the structure of the spike protein [117]. Serum from NHPs that received either one (10A, 30A, 24A, 21A) or two doses (42A, 33A, 9A, 12A, 45A) of the DNA vaccine were included in this assay, as was serum from NHPs that received the FIV vaccine (29A, 31A, 3A, 54A, 15A) and serum from NHPs involved in a HIV vaccine study (pre-vaccination and unchallenged healthy NHPs) as a negative control. For the vaccinated animals, the serum from day 28 post-vaccination was used.

4.1.1. Methods

SARS-CoV-2 Spike trimer (Lake Pharma, product no longer available) was diluted 2µg/mL in PBS 1X. Each plate was coated with 50 µL/well of this spike protein solution. The plates were covered and stored overnight (≥16 h) at 4 ºC. 50 µL/well of PBS was added to half of each plate, while 50 µL/well of 0.02% formaldehyde in PBS was added to the other half to formalin-inactivate the spike protein. Plates were then incubated for 1 hour at room temperature (RT). (See **Supplementary Figure 14** for a comparison of enzyme-linked immunosorbent assay

(ELISA) results for 1-hour formalin-inactivation vs 72-hour formalin-inactivation, which was used for the FIV vaccine preparation, with control human serum).

The plates were washed six times in PBS/Tween (0.05%) using the plate washer and the program 'FDA EBOV', which washes each well five times with 200 µl of wash buffer. The plates were blocked with 100 µl per well of blocking buffer (5% FBS in 0.1% PBS-Tween20). The plates were then stacked and left for 1h at RT. All samples were diluted 1/50 in 10% FBS/0.1 % PBS-Tween20. All solutions were serially diluted (1:2) down the plate (so until 1:6400) using the multichannel in a dilution plate. The plates were washed using the plate washer and the program 'FDA EBOV', the plates were then inverted and tap-dried onto paper towel. 50 µl of diluted samples were transferred from the preparation plate to the coated plates. The plates were incubated at RT for 2hrs. Goat anti-monkey IgG coupled to HRP (Invitrogen, Cat # PA1-84631) was diluted 1:10,000 in 10% FBS/0.1% PBS-Tween20. The plates were washed six times in PBS/Tween (0.05%) using the plate washer and the program 'FDA EBOV', inverted and tapped dry onto paper towel. 100ul of secondary Abs were added to the wells. The plates were incubated for 1hr at RT. The plates were washed six times in PBS/Tween (0.05%) using the plate washer and the program 'FDA EBOV', inverted and tapped dry onto paper towel. For 2 plates: one gold tablet (urea / hydrogen peroxide) in 20 ml of distilled water and just before the development, one silver tablet (OPD) was added (Sigma-Alrich P9187). The volume was adjusted according to the number of plates and the solution was kept in the dark. 100 µl of development buffer was added to each well and incubated for 5 minutes. The reaction was stopped with 1M HCl at 50µl/well. The plates were read at 490 nm on a GloMax microplate reader. Data was analysed using GraphPad Prism 9.3.1 (GraphPad Software, La Jolla, CA, USA).

4.1.2. Results

For each vaccine/challenge group, we combined all of the samples in the group and compared the binding to native spike vs formalin-inactivated spike.

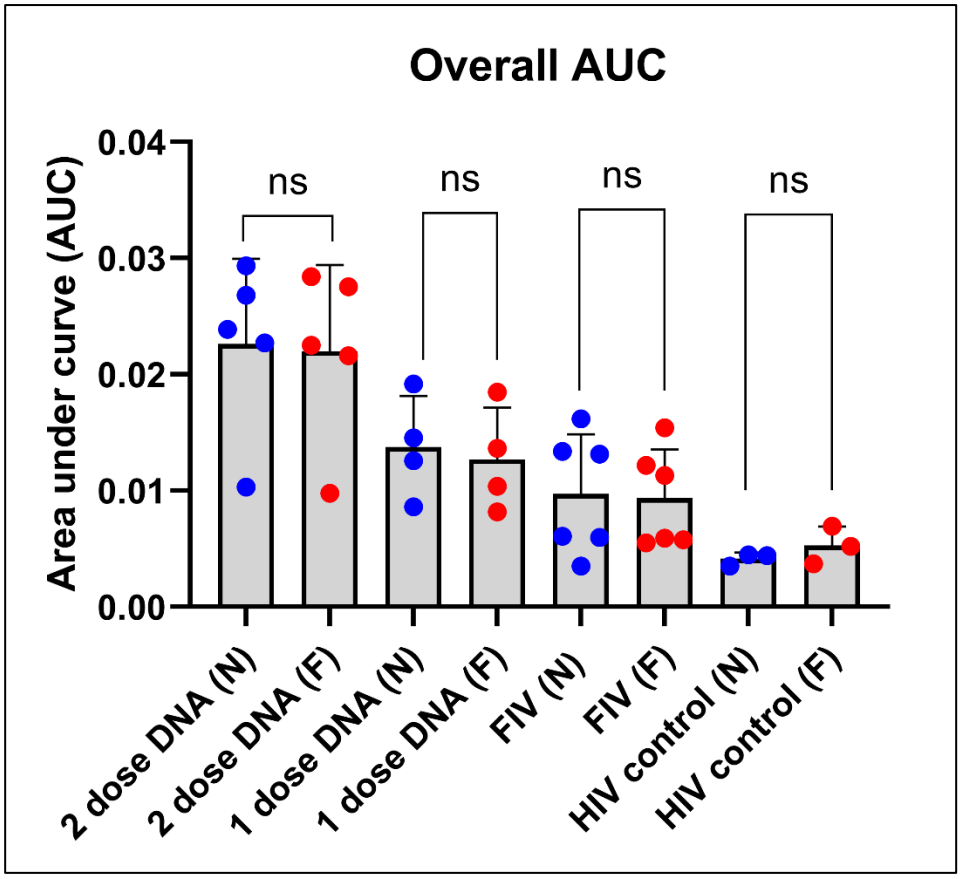

Figure 76: No effect of formalin inactivation on spike protein binding with serum from NHPs across vaccination groups. N = native spike protein. F = Formalin-inactivated spike protein. Samples in blue are from wells coated with native spike protein and samples in red are from wells coated with formalin-inactivated spike protein. Each serum sample was run on both types of spike. Area under curve (AUC) refers to the total area under the dilution curve according to optical density (OD) readout on the GloMax microplate reader. Paired t test, significance threshold is $p < 0.05$.

As expected from the respective previous vaccine studies, the two-dose DNA vaccine group had the highest level of spike binding, followed by the one-dose DNA vaccine group [135], the FIV vaccine group [117] and the negative controls. There was no significant difference observed in antibody binding to native vs formalin-inactivated spike protein across the NHP serum tested.

4.2. BAL cytokine analysis

We profiled cytokines and chemokines in BAL fluid in order to give additional insights into the immune environment at the cull timepoint. For all the NHP cohorts, BAL fluid samples were

taken from the right lung lobes at the cull timepoint with 20mL PBS after the ligation of the left primary bronchus, with the exception of the mRNA vaccine (CVnCoV) study, which also took BAL fluid samples three days post-challenge which was before the cull [136]. As the day 3 post-challenge BAL fluid from the CVnCoV study had limited material compared to the many samples across the studies at the cull timepoint, we focused exclusively on the cull timepoint BAL for cytokine analysis. We aimed to determine whether any of the cytokines implicated in severe pathology in human disease would also be associated with higher histopathology scores in our NHP cohorts. By profiling many cytokines, we also sought to search for cytokines that were associated with either protective or pathological outcomes in the context of vaccination, as human studies have not carried out BAL cytokine analysis within these conditions. However, in NHPs, BAL cytokine profiling has been carried out in the context of a mucosal vaccination study but not at a post-infection timepoint [72]. For an intramuscular vaccine used as a control in this study, there was no significant change seen in the BAL cytokine profile post-vaccination.

At the time of the initial NHP studies (over three years ago), BAL fluid was spun and the supernatant and pellets from each animal were stored separately at -80°C. To profile cytokines, we used V-PLEX NHP plates from Meso Scale Discovery (MSD) which can measure up to 10 analytes at once and were previously used to profile cytokines in NHP BAL fluid in a mucosal vaccine study [72]. We contacted the study authors, who advised using only neat BAL samples due to the dilute nature of BAL fluid, in order to maximise our ability to detect cytokines. The protocols for cytokine profiling using the MSD plates are similar to those carried out with traditional capture ELISAs but with several advantages, owing to the multiplexed nature of the assay and the electrochemiluminescence method of detection, as opposed to light absorbance [182]. Another study that used MSD and other methods for detecting cytokines found that degradation of different cytokines and chemokines following three months of freezing were not uniform and some degraded as much as 90% in samples that did not have added carrier protein, such as bovine serum albumin (BSA) [183]. The timepoint of BAL fluid collection (cull timepoint, day 6/7 post-challenge) means that findings from this work will correspond to the timepoint at which we did

the tissue work in **Chapter 2** and **Chapter 3**. This can also help to validate findings from transcriptomics, to see if predicted cytokines from transcriptomics are found in the BAL fluid.

As we sought to profile cytokines in post-challenge BAL fluid, we wrote a risk assessment (which was approved) that stated we would carry out the assay under CL3 conditions in a hood with an aspirator until the final step, which was reading the plate and was carried out at CL2 conditions. CL3 conditions were used because there would likely still be some live virus left in the BAL fluid at the cull timepoint (which was the timepoint we examined) but after all of the wash steps, we calculated that the probable amount of infectious virus particles was minimal and this was determined to be safe for CL2. The MSD plate reader could not be taken in and out of the CL3 lab, which why this final step had to be carried out at CL2. As I have not undertaken the appropriate training for solo CL3 work, the assays were carried out by Dr Stephen Laidlaw in the CL3 hood while I made up the reagents beforehand, observed the experiment in CL3 conditions and carried out the analysis.

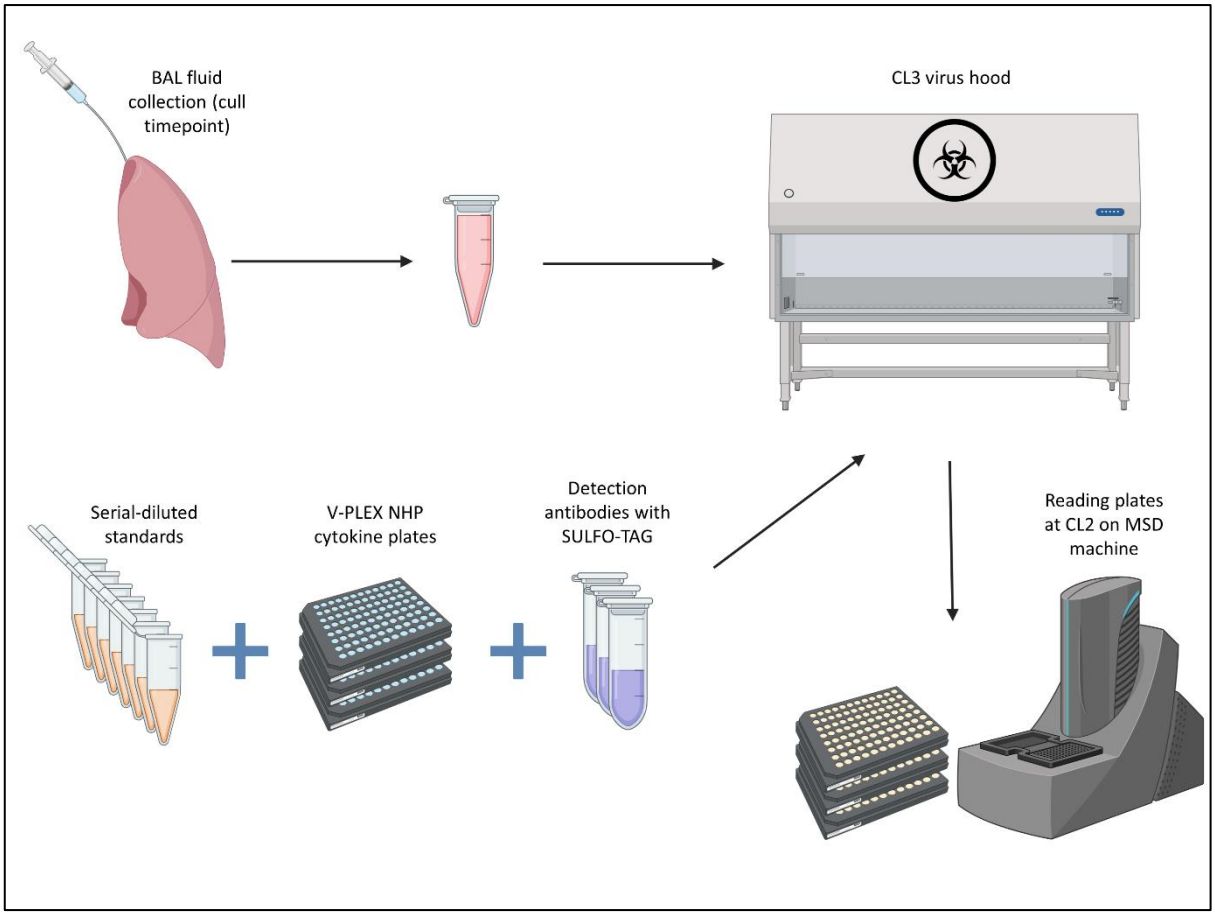

Figure 77: Overview of bronchiolar alveolar lavage (BAL) cytokine analysis protocol. BAL fluid was previously taken from each NHP at the cull timepoint, separated into a cell pellet and BAL fluid supernatant and frozen at -80°C. The BAL supernatant samples were thawed in the CL3 hood and other reagents associated with the Meso Scale Discovery V-PLEX NHP Cytokine assays were brought into the CL3 hood. The plates were read at CL2 conditions. Created with Biorender.com.

4.2.1. Methods

Cytokines from post-challenge BAL fluid were measured using three NHP cytokine kits from Meso Scale Discovery (MSD). The V-PLEX Proinflammatory Panel 1 NHP Kit (K15056D-1), the V-PLEX Cytokine Panel 1 NHP Kit (K15057D-1) and the V-PLEX Chemokine Panel 1 NHP Kit (K15055D-1). The Proinflammatory kit measured IFN-γ, IL-1β, IL-2, IL-6, IL-8 and IL-10, the Cytokine kit measured GM-CSF, IL-5, IL-7, IL-12/IL-23p40, IL-15, IL-16, IL-17A, TNF-β and VEGF-A, and the Chemokine kit measured Eotaxin-3, IL-8, IP-10, MCP-1, MCP-4, MDC, MIP-1α, MIP-1β and TARC. The MSD cytokine assays were carried out according to the

manufacturer's instructions and under containment level three (CL3) conditions, up until the point of reading the plate, which was carried out under containment level two (CL2) conditions. Briefly, the multi-analyte calibrators (which were used to generate standard curves) were prepared with seven 4-fold serial dilutions before the plate was washed three times with 150µL/well of wash buffer. 50µL of neat BAL fluid from each animal was then added to the plate in duplicate before the plate was sealed and left for two hours at room temperature with shaking. The detection antibody solutions for each plate were prepared as per the manufacturer's instructions. The plate was washed three times as before and 25µL/well of the detection antibody solution was added before the plate was sealed again and left for another two hours to incubate with shaking at room temperature. Finally, the plate was washed three times again before addition of 150µL/well of 2X read buffer T to the plate, after which the plates were removed from the CL3 lab and analysed on the MSD instrument. Standard curves and cytokine concentrations were calculated using the MSD Discovery Workbench software from MSD before the data was exported and analysis performed in R version 4.2.1 [146–150,164]. The annotated R script is available on request. Briefly, the script was used to first filter the data to remove duplicates and standards and focus on the mean interpolated concentration values for each pair of wells per sample on the plate. Then the cytokines that were below detection limits for particular samples were annotated as such. Following this several plot types were generated, including bar plots, boxplots and correlation graphs. The detection limit for the cytokines were indicated on each graph with a black dashed line and values that could not be interpolated onto the standard curve (and for which there was no estimate of concentration) were not used in the analysis.

4.2.2. Results

Standard curves were generated for each cytokine across the three plates using the MSD discovery workbench software (Meso Scale Discovery). However, only five cytokines (IL-1β, IL-2, IL-6, IL-8 and IL-10), all on the proinflammatory plate, were detected in the samples to a level that could be interpolated on their corresponding standard curves **(Supplementary Figure 15** to **Supplementary Figure 19**). We therefore restricted further analysis to these cytokines. The

raw data for every plate is available on request. The standard curves for the undetectable cytokines are shown in **Supplementary Figure 20** to **Supplementary Figure 37**. Several different plots were created for each cytokine to represent the results (**Figure 78** to **Figure 82)**. Bar plots were generated to visualise the levels of the different cytokines in each sample that had a detectable level of the given cytokine and correlation plots were generated to visualise the associations of different cytokines with pathology score (panel **b.** in **Figure 78** to **Figure 82** below) and virus level as detected by PCR in the BAL at the cull timepoint (**Supplementary Figure 38** to **Supplementary Figure 42**). Raw PCR values from each study were used for these correlations. Finally, boxplots were generated to visualise the associations of different cytokines with pathology score classifications ('Pathology' vs 'Protected') and BAL PCR virus level classifications ('High lung virus' vs 'Low lung virus').

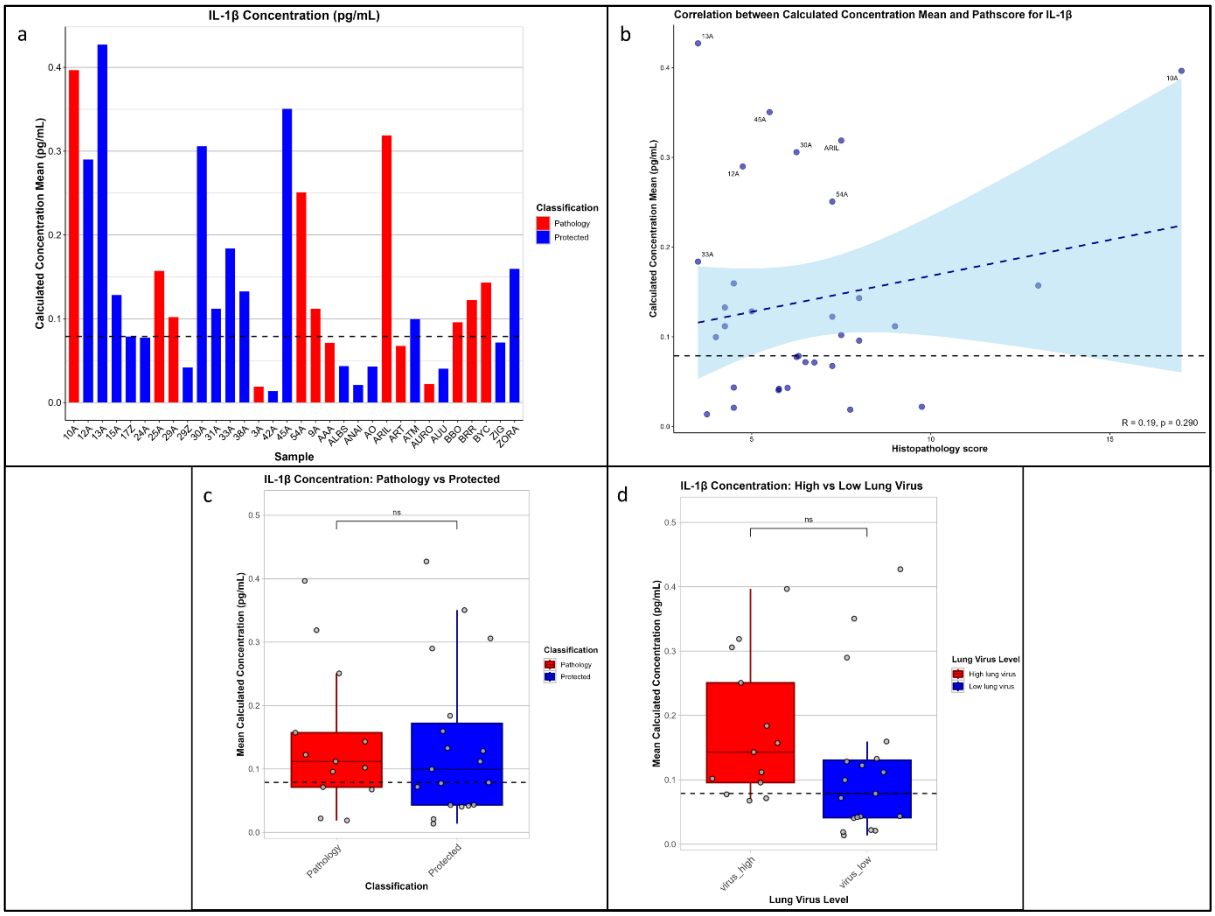

Figure 78: IL-1β BAL cytokine data. a. Bar plot showing the concentration of IL-1β in each individual NHP. **b.** Correlation plot showing the relationship between the histopathology score and cytokine

concentration. The dark blue dashed line is the regression line of the correlation between the cytokine concentration and histopathology score, while the light blue colour represents the range of the associated confidence interval. Individual samples are overlaid as blue dots, with samples in the upper quartile of cytokine concentration annotated according to NHP ID. The R value is Pearson's correlation coefficient and the p value is calculated using Pearson's correlation test. **c.** Histopathology classification boxplot. **d.** Virus level classification boxplot. Samples in **a.** and **c.** are annotated according to the pathology classification of the associated NHP, with high-pathology samples in red and low-pathology samples in blue. In **d.** samples are annotated according to the virus level classification, with 'High lung virus' in red and 'Low lung virus' in blue. In **c.** and **d.** the boxes represent the interquartile range (IQR) and the whiskers extend to the most extreme values within 1.5 times the IQR from the quartiles. The Wilcoxon rank-sum test was carried out to compare the two groups in each boxplot. Individual samples are overlaid as grey dots. In all plots, the black dashed line represents the detection limit of the machine. The samples shown below this level could still be interpolated onto the standard curve. Samples too low to be interpolated were not included.

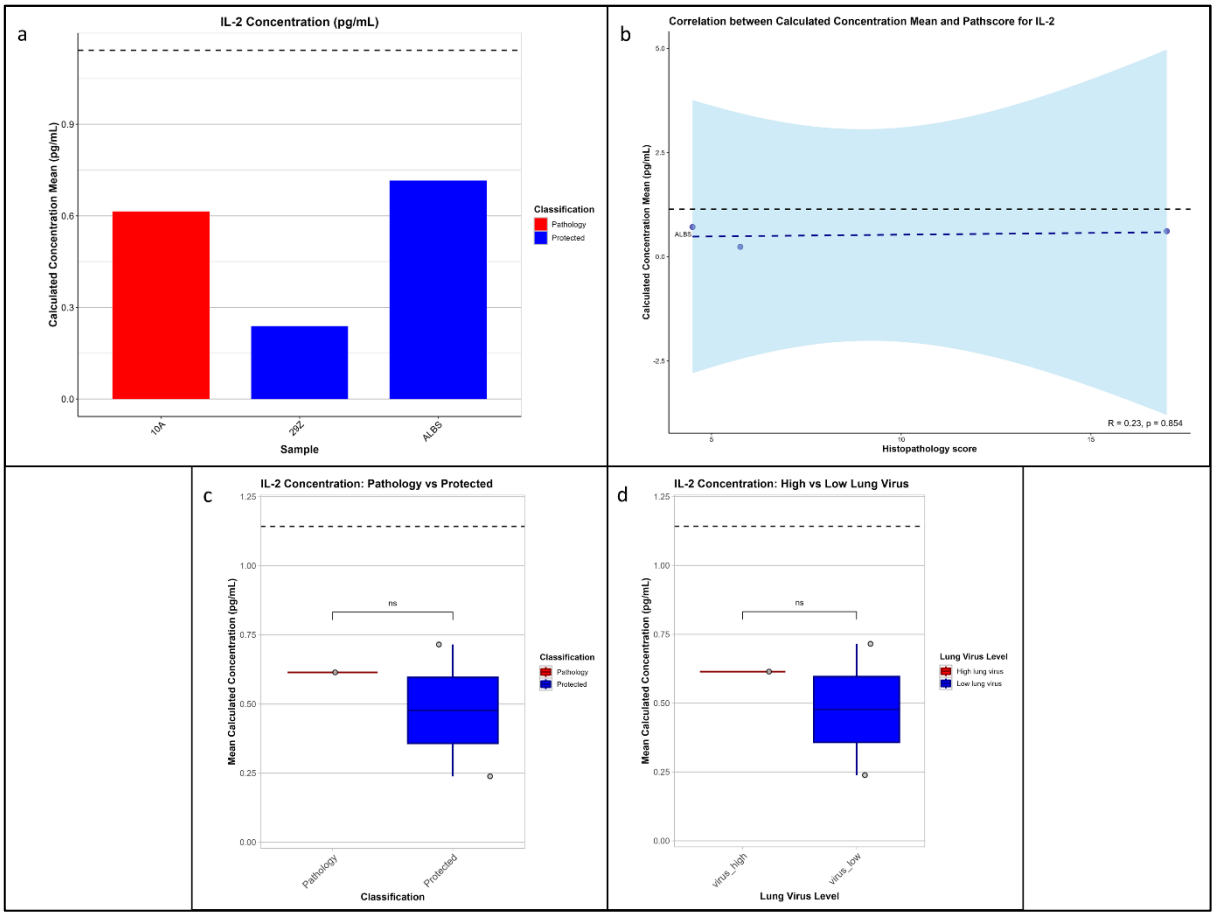

Figure 79: IL-2 BAL cytokine data. a. Bar plot showing the concentration of IL-2 in each individual NHP. **b.** Correlation plot showing the relationship between the histopathology score and cytokine concentration. The dark blue dashed line is the regression line of the correlation between the cytokine concentration and histopathology score, while the light blue colour represents the range of the associated confidence interval. Individual samples are overlaid as blue dots, with samples in the upper quartile of cytokine concentration annotated according to NHP ID. The R value is Pearson's correlation coefficient and the p value is calculated using Pearson's correlation test. **c.** Histopathology classification boxplot. **d.** Virus level classification boxplot. Samples in **a.** and **c.** are annotated according to the pathology classification of the associated NHP, with high-pathology samples in red and low-pathology samples in blue. In **d.** samples are annotated according to the virus level classification, with 'High lung virus' in red and 'Low lung virus' in blue. In **c.** and **d.** the boxes represent the interquartile range (IQR) and the whiskers extend to the most extreme values within 1.5 times the IQR from the quartiles. The Wilcoxon rank-sum test was carried out to compare the two groups in each boxplot. Individual samples are overlaid as grey dots. In all plots, the black dashed line represents the detection limit of the machine. The samples shown below this level could still be interpolated onto the standard curve. Samples too low to be interpolated were not included.

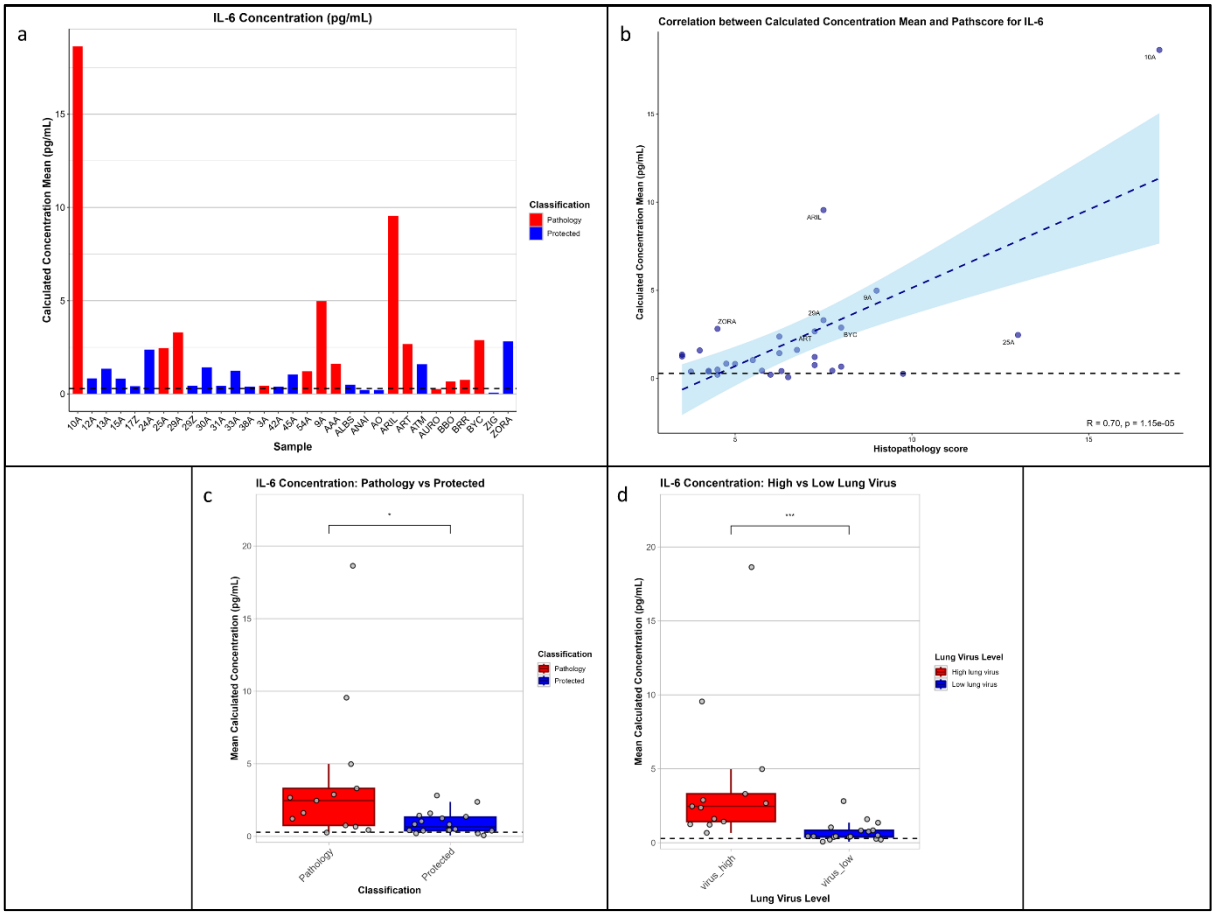

Figure 80: IL-6 BAL cytokine data. a. Bar plot showing the concentration of IL-6 in each individual NHP. **b.** Correlation plot showing the relationship between the histopathology score and cytokine concentration. The dark blue dashed line is the regression line of the correlation between the cytokine concentration and histopathology score, while the light blue colour represents the range of the associated confidence interval. Individual samples are overlaid as blue dots, with samples in the upper quartile of cytokine concentration annotated according to NHP ID. The R value is Pearson's correlation coefficient and the p value is calculated using Pearson's correlation test. **c.** Histopathology classification boxplot. **d.** Virus level classification boxplot. Samples in **a.** and **c.** are annotated according to the pathology classification of the associated NHP, with high-pathology samples in red and low-pathology samples in blue. In **d.** samples are annotated according to the virus level classification, with 'High lung virus' in red and 'Low lung virus' in blue. In **c.** and **d.** the boxes represent the interquartile range (IQR) and the whiskers extend to the most extreme values within 1.5 times the IQR from the quartiles. The Wilcoxon rank-sum test was carried out to compare the two groups in each boxplot. Individual samples are overlaid as grey dots. In all plots, the black dashed line represents the detection limit of the machine. The samples

shown below this level could still be interpolated onto the standard curve. Samples too low to be interpolated were not included.

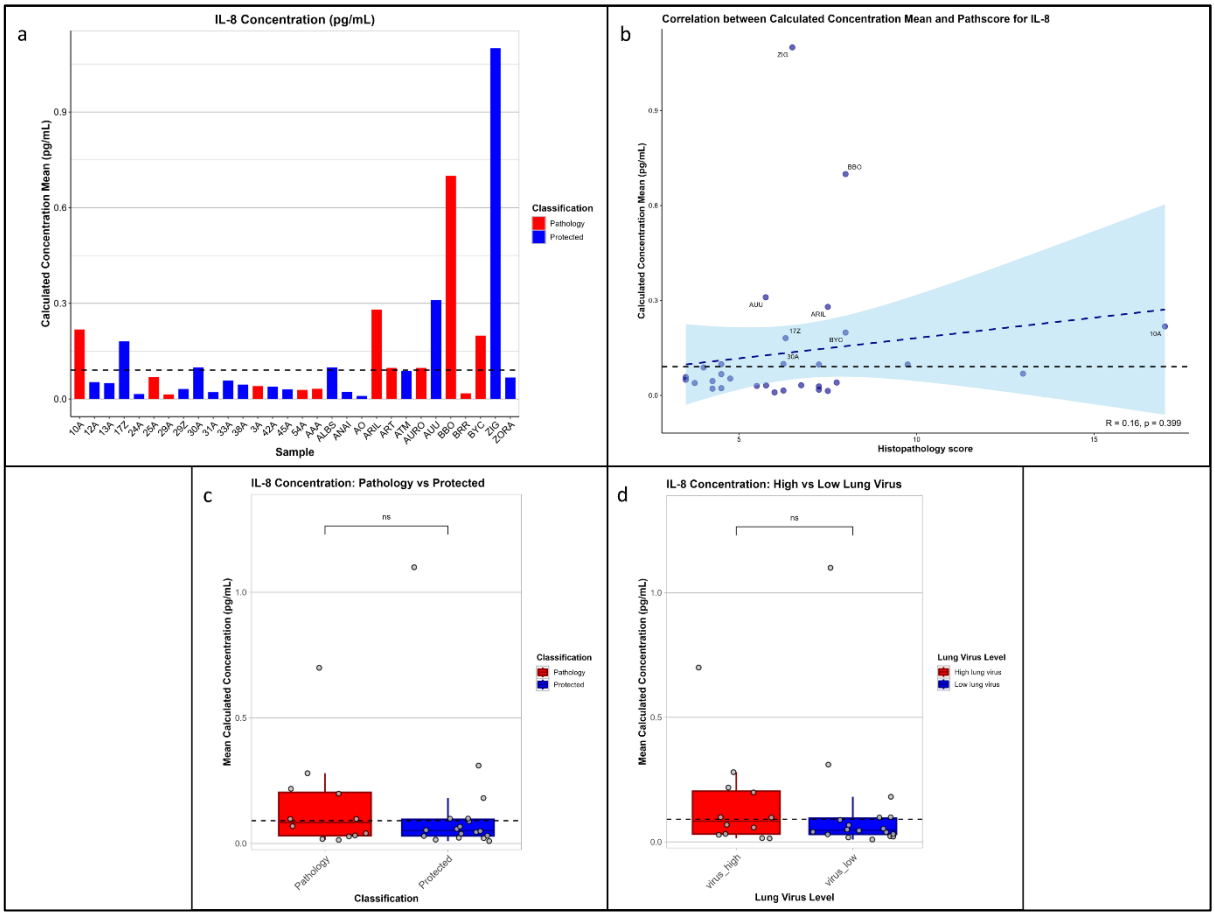

Figure 81: IL-8 BAL cytokine data. a. Bar plot showing the concentration of IL-8 in each individual NHP. **b.** Correlation plot showing the relationship between the histopathology score and cytokine concentration. The dark blue dashed line is the regression line of the correlation between the cytokine concentration and histopathology score, while the light blue colour represents the range of the associated confidence interval. Individual samples are overlaid as blue dots, with samples in the upper quartile of cytokine concentration annotated according to NHP ID. The R value is Pearson's correlation coefficient and the p value is calculated using Pearson's correlation test. **c.** Histopathology classification boxplot. **d.** Virus level classification boxplot. Samples in **a.** and **c.** are annotated according to the pathology classification of the associated NHP, with high-pathology samples in red and low-pathology samples in blue. In **d.** samples are annotated according to the virus level classification, with 'High lung virus' in red and 'Low lung virus' in blue. In **c.** and **d.** the boxes represent the interquartile range (IQR) and the whiskers extend to the most extreme values within 1.5 times the IQR from the quartiles. The Wilcoxon

rank-sum test was carried out to compare the two groups in each boxplot. Individual samples are overlaid as grey dots. In all plots, the black dashed line represents the detection limit of the machine. The samples shown below this level could still be interpolated onto the standard curve. Samples too low to be interpolated were not included.

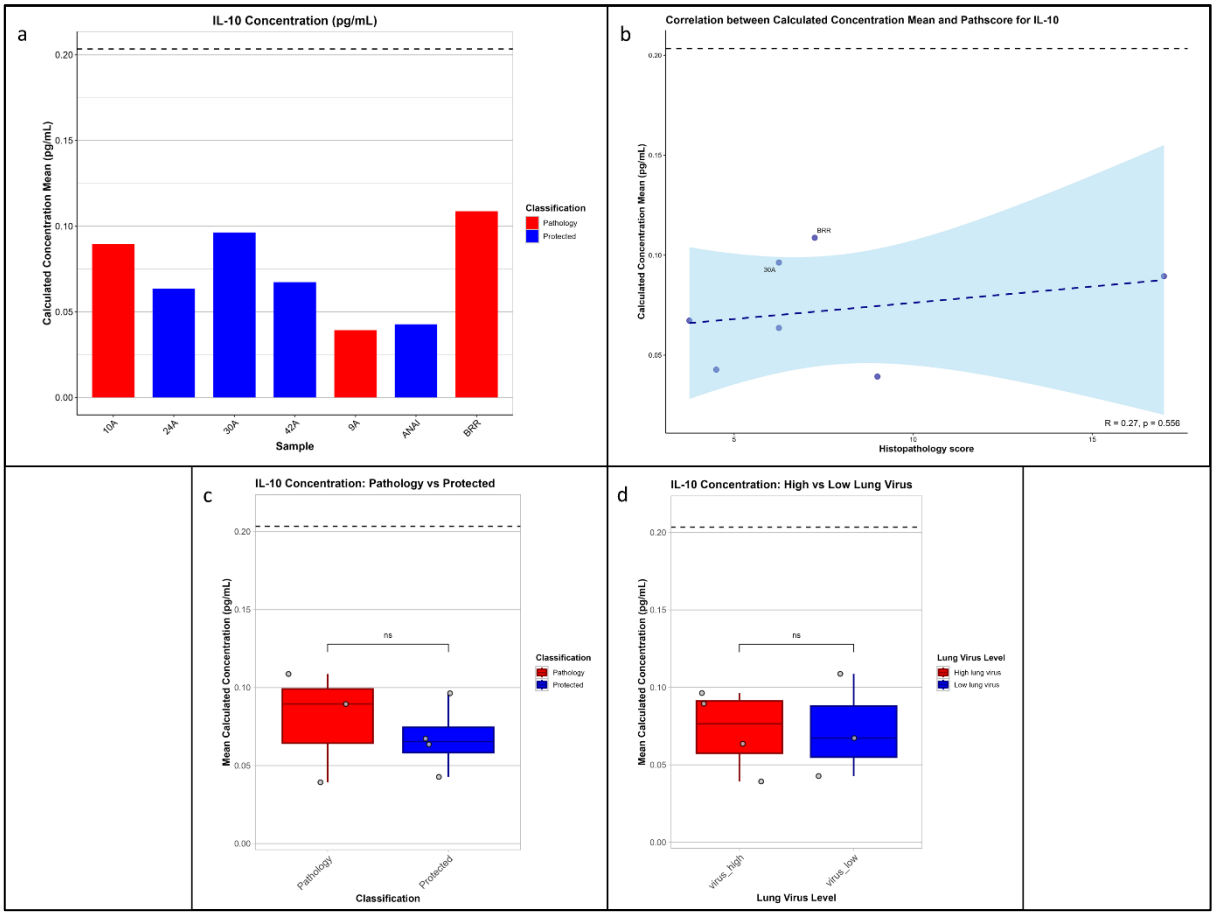

Figure 82: IL-10 BAL cytokine data. a. Bar plot showing the concentration of IL-10 in each individual NHP. **b.** Correlation plot showing the relationship between the histopathology score and cytokine concentration. The dark blue dashed line is the regression line of the correlation between the cytokine concentration and histopathology score, while the light blue colour represents the range of the associated confidence interval. Individual samples are overlaid as blue dots, with samples in the upper quartile of cytokine concentration annotated according to NHP ID. The R value is Pearson's correlation coefficient and the p value is calculated using Pearson's correlation test. **c.** Histopathology classification boxplot. **d.** Virus level classification boxplot. Samples in **a.** and **c.** are annotated according to the pathology classification of the associated NHP, with high-pathology samples in red and low-pathology samples in blue. In **d.** samples are annotated according to the virus level classification, with 'High lung virus' in red

and 'Low lung virus' in blue. In **c.** and **d.** the boxes represent the interquartile range (IQR) and the whiskers extend to the most extreme values within 1.5 times the IQR from the quartiles. The Wilcoxon rank-sum test was carried out to compare the two groups in each boxplot. Individual samples are overlaid as grey dots. In all plots, the black dashed line represents the detection limit of the machine. The samples shown below this level could still be interpolated onto the standard curve. Samples too low to be interpolated were not included.

4.3. Discussion

The lack of a significant difference in binding between native spike and formalin-inactivated spike across all of the groups (**Figure 76**) suggests that the formalin inactivation of the spike protein in the formalin-inactivated vaccine did not have a major effect on the structure of the spike protein and therefore, on the quality of antibodies generated against the native spike protein upon challenge with live virus. The data also confirms that the FIV vaccine induced lower antibody levels than the DNA vaccines in the same assay. In the context of antibody-mediated mechanisms of VAED (namely ADE and AED) it is unlikely based on this data that formalin-inactivated whole-virus vaccines would induce poorer responses to spike protein owing to the effect of the formalin inactivation. If this were the case, we would expect to see a difference between antibody binding to formalin-inactivated spike vs native spike. However, AED mechanisms are related particularly to non-neutralising antibody binding which we did not test, but the original FIV vaccine paper demonstrated the induction of neutralising antibodies (not just binding antibodies) after vaccination, which were boosted upon challenge [117]. The direct ELISA we carried out may not preserve the SARS-CoV-2 spike protein in its original native or formalin-inactivated conformation, as previous studies have demonstrated this to be the case for soluble forms of HIV-1 envelope trimers when bound to an ELISA plate [184]. While capture ELISA platforms may overcome this issue [117], we were not successful in setting up a capture ELISA for SARS-CoV-2 spike protein. While we did not study binding or neutralising capabilities of antibodies in the BAL fluid specifically, there is recent evidence that in the context of SARS-CoV-2 mucosal vaccination, the ability of binding antibodies in BAL fluid to carry out ADCP is a stronger correlate of protection than neutralising capacity [70]. This suggests that, at mucosal sites,

functional activities of SARS-CoV-2 antibodies may be more important for protection than neutralising titres. In contrast, while non-neutralising functional activities can also be pathogenic, this may be restricted to niche cases like dengue virus, which has a unique ability to co-opt antibody responses for enhancement of infection of myeloid cells [99]. We have not noted any evidence of antibody-dependent disease enhancement mechanisms in these NHP studies.

In our cytokine experiments, the majority of cytokines and chemokines to be measured were undetectable. As discussed previously, another study that detected cytokines using the MSD system found that some cytokines and chemokines degraded as much as 90% when frozen for three months without carrier protein [183]. Considering our BAL samples were frozen for almost four years before this assay was carried out and no carrier proteins were added to the samples before freezing, it is unsurprising that many cytokines were undetectable. Another reason for the low levels of cytokines could be that the cull timepoint is a few days after the peak of pathology, so there may be lower levels of cytokines in the BAL at this time anyway, as the pathology has begun to resolve. IL-8 was included in both the pro-inflammatory plate and the chemokine plate but was only detectable on the pro-inflammatory plate (although very few samples were above the detection limit), so there may have been a problem with the chemokine plate, its standards or associated reagents.

Despite the undetectable levels of many cytokines and their presumably lowered levels following frozen storage, there were strong associations between IL-6 measured in the BAL and pathological outcomes. In particular the strong correlation and significance value between the quantitative histopathology score and IL-6 (**Figure 80b**) is interesting, as it demonstrates that the rhesus macaque model recapitulates the pathological association in human studies [176]. When pathology scores are broken down into the 'Pathology' and 'Protected' categories, an association remains (**Figure 80c)**. When comparing the association of IL-6 with the 'High lung virus' and 'Low lung virus' categories (related to SARS-CoV-2 levels measured by BAL PCR, **Figure 80d**), it is even stronger. However, there is no correlation with the absolute values of the BAL PCR (**Supplementary Figure 40**), which may be due to the fact that several animals had completely

cleared the virus by the cull timepoint and so the virus level variation is skewed. Previous work demonstrated that *IL6* mRNA could be detected in pathological lesions of NHPs infected with SARS-CoV-2, as previously discussed [87]. We have now shown that the levels of IL-6 in the BAL correlate with pathological severity in this model (as it does in humans), even though this model has milder disease which is beginning to resolve by the cull timepoint.

Overall, our hypothesis that formalin inactivation would alter the spike protein structure to an extent that binding to native spike is reduced was disproven. Our other hypothesis, that cytokines associated with severe disease in BAL fluid in humans would be seen in BAL fluid from high-pathology NHPs was at least partially proven. While many cytokines and chemokines were undetectable in most samples (due to improper storage), there was a strong association between IL-6 and histopathology score, which recapitulates human severe disease studies as discussed.

Conclusions

By combining spatially-resolved in-situ profiling techniques (both transcriptomic and proteomic) and cytokine analysis, we have demonstrated that the rhesus macaque model recapitulates many features of human COVID-19 pathology. In **Chapter 2** we have shown that an immune population that we hypothesise to be neutrophils (based on their marker profiles, as discussed in **Section 2.5**) very strongly correlates with histopathology scores in our NHPs, across lesioned regions, non-lesioned regions or a combination of both. This is in line with the literature on neutrophil abundance, which has shown this increase in patients with severe disease both in BAL fluid which would be region-agnostic [39] and in lung tissue parenchyma [29]. In **Chapter 3** we have shown that neutrophil degranulation pathways are highly upregulated in more severe pathology in our NHP cohort, as is seen in human severe disease [174]. Our spatial transcriptomic analysis also revealed other human disease pathways that were recapitulated, such as EMT [29] and TCR signalling [54], as discussed in **Section 3.5**. We also discussed how some individual genes associated with human severe pathology [29,30,34,39] were also upregulated, although not all of the genes associated with human severe disease were detectable in our samples. Of those that were, they are upregulated primarily in the NHPs with the highest pathology across the entire cohort. This was also true of many human disease pathways, which overall showed a spectrum of upregulation depending on pathology and region status (**Figure 75**). Overall this demonstrates that perhaps, analogous to humans, only a subset of NHPs will experience more severe disease. Given that the NHPs in these studies were young (between 2 and 6 years old, representing a young adult cohort) and did not have known comorbidities associated with severe human COVID-19 [185], it could be that the NHP model captures the pathology of young, healthy humans quite well and that when we focus on more lesioned parts of damage, we find evidence of the more severe pathological signs, which spread more widely throughout the lung in more severe human cases. We also found $CD8^+$ T cells and an activated ($HLA\text{-}DR^+$) subset to positively correlate with histopathology scores (**Figure 28** and **Figure 29**), which lines up with human data demonstrating the elevation of $CD8^+$ T cells in post-mortem lung samples from COVID-19 patients [10]. In

Chapter 4 we have shown that the IL-6 increase seen in BAL fluid of severe human COVID-19 [39,181] is also present in NHPs upon infection and correlates strongly with histopathology score. However, while other work in NHPs has detected *IL6* in pathological lesions following challenge [87], this gene was not detected in our transcriptomics work, suggesting that the probes to this gene may not have been cross reactive between humans and NHPs or that the transcription of *IL6* had ceased by the cull timepoint, with the protein still being present in BAL.

Our central hypothesis was that peripheral vaccination could alter the response of the lung tissue parenchyma upon SARS-CoV-2 challenge by inducing protective immune responses that make their way to the lung. In our transcriptomics work (**Chapter 3**), we did not note many pathways that were specific to protection, as most were associated with pathology and were simply up- or downregulated depending on the one-to-one comparisons. We therefore noted that the transcriptomic data captures a spectrum of pathology, consistent with the different levels of peripheral immunity (and the different associated histopathology scores, see **Figure 6**) conferred by vaccination or previous challenge, with some intra-group variability noted (**Figure 53** to **Figure 55**). However, with our multiplex imaging data we noted that $CD4^+$ T cells in particular were found at greater levels in some of the vaccine groups (viral vector, high dose mRNA and FIV) and the re-challenge group compared to unvaccinated animals across all regions (**Figure 24**), suggesting some peripheral immune infiltration. An alternative explanation is that both $CD4^+$ T cells and $CD8^+$ T cells were depleted, as has been proposed to occur in the lung during severe infection, in a single-cell RNA sequencing study [33]. However, as mentioned in the introduction, the COSMIC study, which imaged lung parenchyma, found both $CD4^+$ T cells and $CD8^+$ T cells in post-mortem samples from COVID-19 patients [10]. In fact, we found $CD8^+$ T cells and their activated ($HLA\text{-}DR^+$) subset to be associated significantly with higher histopathology scores (**Figure 28** and **Figure 29**). Therefore, while further studies would be needed to confirm the hypothesis (ideally with antigen-specific single-cell profiling of lung tissue digests) we propose that vaccination primes peripheral immune cells that are recruited to the lung upon challenge. In the case of the re-challenge group, the increased abundance of T cells may be made up of a tissue-

resident profile which was established after the initial infection. However, this would also need to be proven in a separate study using antigen-specific profiling and tissue residency markers. Our transcriptomic work did not show any $CD4^+$ T cell related pathways being upregulated in protected/vaccinated animals compared to unvaccinated animals. However, this may be because the $CD4^+$ T cell activity had largely ceased by the cull timepoint (day 6/7 post-challenge) while the cells themselves remained, or because their transcriptomic activity was somewhat diluted by the relatively large (650µm diameter) circular ROIs which captured many cells. In lesioned regions, we noted an increase in the abundance of activated ($HLA\text{-}DR^+$) $CD4^+$ T cells in the viral vector vaccinated group compared to unvaccinated NHPs (**Figure 25**). This could indicate that in this highly-protected group, antigen-specific $CD4^+$ T cells were recruited from the periphery and activated in response to the virus. However, as with our other $CD4^+$ T cell associations, this was not detected in our transcriptomics and would need further work to confirm, as previously described. If this is confirmed, inducing tissue-resident $CD4^+$ T cells in the lung may be an attractive vaccine target.

An alternative hypothesis is that in cases where vaccinated animals had high histopathology scores, vaccination may have led to enhanced pathology through VAED. As discussed in **Section 1.6**, VAED in the context of coronaviruses could be mediated by a variety of mechanisms (**Figure 3**) but based on the literature, we proposed that Th2-mediated pathology or an ADE/AED mechanism (**Figure 4**) was most likely if VAED was to be observed in our NHP cohort. In our transcriptomic work, we did not see Th2 pathways in any of our comparisons, whether across vaccine groups or pathology classifications. $CD4^+$ T cell numbers did not significantly correlate with histopathology scores in any region type and the general trend was a negative (protective) association, with no high-pathology NHP outliers having high $CD4^+$ T cell abundance (**Supplementary Figure 3** to **Supplementary Figure 5**). In fact, $CD4^+$ T cells in close proximity with PanCk (epithelial) cells correlated significantly with protection in lesioned regions (**Figure 29**). In terms of ADE/AED, our transcriptomic analysis generally showed humoral responses and phagocytosis to be upregulated in a variety of vaccine groups, not just those associated with

greater pathology scores (**Figure 69** and **Figure 70**). Our ELISA of formalin-inactivated spike vs native spike demonstrated no significant change in binding affinity (**Figure 76**), despite the potential of formalin inactivation to alter antibody binding (**Figure 5**). We therefore conclude that VAED did not occur in any of the high-pathology vaccinated animals and that these NHPs instead experienced a greater level of pathology but along the expected spectrum of unvaccinated pathology, rather than due to aberrant immune responses.

In this study, we have provided rationale for pathology-guided in-situ discovery. Here we have used this to demonstrate the recapitulation of features of human COVID-19 pathology (as discussed) and to shed light on the impact of vaccination on changing the cellular profile of the post-challenge lung (**Chapter 2**) and dampening pathological pathways (**Chapter 3**). However, this framework can also be applied to study the pathogenesis of other infections, of which less is known of the pathology. While spatially-resolved methods such as multiplex imaging and spatial transcriptomics have been widely applied to study cancer [186], there is much less work on using these techniques in infectious disease, particularly in animal models. In the context of COVID-19, these methods have been used on clinical tissues from people who have succumbed to COVID-19 disease, so only the most severe cases have been studied. As we've outlined in the introduction, animal models allow for the study of tissue in the context of milder pathological states, more controlled conditions, vaccination and potentially even protective in-situ profiles. Our use of a quantitative histopathological scoring system [87] allowed us to examine linear correlations between these histopathology scores and cell types (**Chapter 2**), genes (**Chapter 3**) or cytokine levels (**Chapter 4**). The fact that many significant linear correlations were noted owing to correlations with this scoring system demonstrates its utility in identifying factors that could be used as correlates of protection or of disease severity. However, it must be noted that many of the factors we examined that were in-situ in the lung parenchyma and spatially localised to lesioned or non-lesioned areas would not be possible to sample in living people with current sampling methods. In the context of animal models, these in-situ transcriptomic or cellular features could define correlates of protection for preclinical studies (where tissue can be taken),

and provide targets for vaccines or therapeutics. Currently, the readout of protection in many studies is reduced viral load, which may not always correlate with reduced pathology, particularly in cases of VAED (see **Section 1.6**). The preclinical SARS-CoV-2 vaccine studies carried out at UKHSA used the aforementioned histopathological scoring system as well as looking at viral load. Given that viral loads can be completely cleared in some cases, even when total protection from pathology has not been achieved, as seen in our NHP cohort (**Supplementary Figure 38** to **Supplementary Figure 42**), histopathology scoring systems provide a much better quantitative readout for disease outcome, which can then be used for linear correlations. Many human studies do not use quantitative histopathology scoring systems, owing in part to the unavailability of tissue for a variety of reasons, but often classify patients by disease status (such as mild, moderate, severe, fatal). When we compared our data to two broad classifications of 'protected' and 'pathology' we also saw significant associations in each chapter. Given the wealth of FFPE tissue available in research institutions, we propose that many additional insights into tissue pathology and immunity can be gained retrospectively from previous animal studies, as we have shown in our work.

For the study of protective profiles, one particularly exciting application of these techniques is in the field of mucosal vaccination. Recent studies have demonstrated near complete levels of protection from infection (as measured by viral loads) conferred by mucosal vaccination in NHPs [71,72], particularly through aerosol delivery. While the functional activity of local mucosal antibodies has been proposed as a potential mechanism of protection, as discussed in **Section 1.3** [70], the upper and lower airway immune cells have not been examined in their native context using spatial methods. Given that mucosal vaccination is thought to induce tissue-resident immune responses (**Section 1.3**), this could be an opportunity for spatially-resolved omics methods to investigate mechanisms of protection in future work. This could potentially generate additional insights to improve future mucosal vaccinations and such future studies could help to understand why mucosal vaccinations have been relatively unsuccessful in humans thus far, with the exception of FluMist. Such animal studies would also allow for the study of the impact of

previous exposure on mucosal vaccine efficacy, as mentioned in **Section 1.4**, which is one potential explanation for their lack of success in human studies.

There are several limitations in the work associated with this thesis. In our NHP study cohort, we only studied tissue that came from day 6/7 post-challenge (**Section 1.7**). If tissue from earlier timepoints was available we would have gained insights into a more acute stage of pathology or with multiple time points we could gain insights into the course of pathology as infection progresses from acute stages to resolution. Histopathology in the rhesus macaque model has been shown to peak at 4/5 days post-challenge and begin to resolve after this timepoint [87]. We used the GeoMx DSP platform for spatial transcriptomics, although recently new platforms that provide single-cell resolution have become available [49–51], which could provide higher-resolution insights into pathology and immunity in these samples. However, across spatial transcriptomic platforms there is a lack of rhesus macaque specific probe sets and although some new technologies allow for the customisation of small probe panels, whole-transcriptome solutions (as we have used and which are not at single-cell resolution) for rhesus macaque work typically relies on a high degree of cross-reactivity between human genes and rhesus macaque genes at the probe binding sites. With this approach not all genes will cross react and some genes will not be available for analysis. Compared to the Cell DIVE, some other multiplex imaging techniques do not carry out multiple cover-slipping and de-cover-slipping steps or bleaching, meaning that they would not have the problems we experienced with tissue loss, tissue folding and poorer staining following increased numbers of bleaching rounds. Our multiplex imaging panel was relatively small, partially due to these issues and because of the lack of standardisation in NHP FFPE tissue-binding immunofluorescent antibodies. It was not possible for us to carry out spatial associations with currently available methods because of the 'holes' in our multiplex images due to the imaging artefacts and tissue movement. Therefore, we could not confirm the spatial association between $CD8^+$ T cells and APCs and whether ongoing antigen presentation to $CD8^+$ T cells in the lung drives more severe pathology (**Figure 31**). However, new methods are being developed to solve this problem. As there is currently no way to profile antigen specificity in-situ in FFPE

tissue (in fresh-frozen tissue the spatial-VDJ method can be applied [187]), we could not determine whether adaptive immune cells in our NHP tissue had arisen from previous priming by vaccination or prior infection. Other animal models such as the Syrian hamster, would have shown more severe pathology but are much less similar to humans when compared to rhesus macaque models of infection [94,95]. Our studies of the monocyte and macrophage responses, such as phagocytosis, in this model (**Supplementary Figure 46** and **Supplementary Figure 47**) were side-lined in favour of tissue studies, although this work has been used to validate bead uptake for another DPhil project and the broader goals of that research are being continued by another DPhil student.

In conclusion, our study provided novel insights into in-situ immunity and pathology in rhesus macaques lung tissue in response to SARS-CoV-2. Our work confirms the utility of this model in capturing a spectrum of pathology that can be analogous to human severe disease, particularly when lesioned areas of the lung are examined. Due to the combination of multiple standardised study cohorts, our work also has a greater sample number than many other in-situ studies, particularly those performed on post-mortem human tissue, which is rarely retrieved. This makes the significance of correlations with 'protected' and 'pathology' groups in particular (which each had high sample numbers) more robust and adds weight to our findings and suggested future directions based on these. To our knowledge, this is the only in-situ study of its kind looking at the response to peripheral vaccination upon challenge and we hope that upon publication others will explore our datasets further to generate additional insights and that we have provided a proof-of-concept for future in-situ studies of pathology and vaccination.

Bibliography

1. Worobey, M. *et al.* The Huanan Seafood Wholesale Market in Wuhan was the early epicenter of the COVID-19 pandemic. *Science (1979)* **377**, 951–959 (2022).

2. Pekar, J. E. *et al.* The molecular epidemiology of multiple zoonotic origins of SARS-CoV-2. *Science (1979)* **377**, 960–966 (2022).

3. Holmes, E. C. The Emergence and Evolution of SARS-CoV-2. *Annu Rev Virol* (2024) doi:10.1146/annurev-virology-093022-013037.

4. Crits-Christoph, A. *et al.* Genetic tracing of market wildlife and viruses at the epicenter of the COVID-19 pandemic. *Cell* **187**, 5468-5482.e11 (2024).

5. Jackson, C. B., Farzan, M., Chen, B. & Choe, H. Mechanisms of SARS-CoV-2 entry into cells. *Nature Reviews Molecular Cell Biology* vol. 23 3–20 Preprint at https://doi.org/10.1038/s41580-021-00418-x (2022).

6. Li, D., Sempowski, G. D., Saunders, K. O., Acharya, P. & Haynes, B. F. SARS-CoV-2 Neutralizing Antibodies for COVID-19 Prevention and Treatment. *Annu Rev Med* **73**, 1–16 (2022).

7. Rockx, B. *et al.* Comparative pathogenesis of COVID-19, MERS, and SARS in a nonhuman primate model. *Science* **368**, 1012–1015 (2020).

8. Carsana, L. *et al.* Pulmonary post-mortem findings in a series of COVID-19 cases from northern Italy: a two-centre descriptive study. *Lancet Infect Dis* **20**, 1135–1140 (2020).

9. Milross, L. *et al.* Post-mortem lung tissue: the fossil record of the pathophysiology and immunopathology of severe COVID-19. *Lancet Respir Med* **10**, 95–106 (2022).

10. Weeratunga, P. *et al.* Single cell spatial analysis reveals inflammatory foci of immature neutrophil and CD8 T cells in COVID-19 lungs. *Nat Commun* **14**, 7216 (2023).

11. Gupta, A. *et al.* Extrapulmonary manifestations of COVID-19. *Nat Med* **26**, 1017–1032 (2020).

12. Ahn, J. H. *et al.* Nasal ciliated cells are primary targets for SARS-CoV-2 replication in the early stage of COVID-19. *J Clin Invest* **131**, (2021).

13. Sungnak, W. *et al.* SARS-CoV-2 entry factors are highly expressed in nasal epithelial cells together with innate immune genes. *Nat Med* **26**, 681–687 (2020).

14. Killingley, B. *et al.* Safety, tolerability and viral kinetics during SARS-CoV-2 human challenge in young adults. *Nat Med* **28**, 1031–1041 (2022).

15. Altarawneh, H. N. *et al.* Protective Effect of Previous SARS-CoV-2 Infection against Omicron BA.4 and BA.5 Subvariants. *The New England journal of medicine* vol. 387 1620–1622 Preprint at https://doi.org/10.1056/NEJMc2209306 (2022).

16. Aldridge, R. W. *et al.* SARS-CoV-2 antibodies and breakthrough infections in the Virus Watch cohort. *Nat Commun* **13**, 4869 (2022).

17. Khoury, D. S. *et al.* Neutralizing antibody levels are highly predictive of immune protection from symptomatic SARS-CoV-2 infection. *Nat Med* **27**, 1205–1211 (2021).

18. Lim, J. M. E. *et al.* SARS-CoV-2 breakthrough infection in vaccinees induces virus-specific nasal-resident CD8+ and CD4+ T cells of broad specificity. *J Exp Med* **219**, (2022).

19. Swadling, L. *et al.* Pre-existing polymerase-specific T cells expand in abortive seronegative SARS-CoV-2. *Nature* (2021) doi:10.1038/s41586-021-04186-8.

20. Pozharskaya, T. & Lane, A. P. Interferon gamma causes olfactory dysfunction without concomitant neuroepithelial damage. *Int Forum Allergy Rhinol* **3**, 861–865 (2013).

21. Rodriguez, S. *et al.* Innate immune signaling in the olfactory epithelium reduces odorant receptor levels: modeling transient smell loss in COVID-19 patients. *medRxiv : the preprint server for health sciences* Preprint at https://doi.org/10.1101/2020.06.14.20131128 (2020).

22. Xydakis, M. S. *et al.* Post-viral effects of COVID-19 in the olfactory system and their implications. *Lancet Neurol* **20**, 753–761 (2021).

23. Cooper, K. W. *et al.* COVID-19 and the Chemical Senses: Supporting Players Take Center Stage. *Neuron* **107**, 219–233 (2020).

24. Lindeboom, R. G. H. *et al.* Human SARS-CoV-2 challenge uncovers local and systemic response dynamics. *Nature* **631**, 189–198 (2024).

25. Ramirez, S. I. *et al.* Immunological memory diversity in the human upper airway. *Nature* **632**, 630–636 (2024).

26. A blood atlas of COVID-19 defines hallmarks of disease severity and specificity. *Cell* **185**, 916-938.e58 (2022).

27. Stephenson, E. *et al.* Single-cell multi-omics analysis of the immune response in COVID-19. *Nat Med* **27**, 904–916 (2021).

28. Farber, D. L. Tissues, not blood, are where immune cells function. *Nature* **593**, 506–509 (2021).

29. Rendeiro, A. F. *et al.* The spatial landscape of lung pathology during COVID-19 progression. *Nature* **593**, 564–569 (2021).

30. Cross, A. R. *et al.* Spatial transcriptomic characterization of COVID-19 pneumonitis identifies immune circuits related to tissue injury. *JCI Insight* (2022) doi:10.1172/jci.insight.157837.

31. Zens, K. D., Chen, J. K. & Farber, D. L. Vaccine-generated lung tissue-resident memory T cells provide heterosubtypic protection to influenza infection. *JCI Insight* **1**, (2016).

32. Mann, E. R. *et al.* Longitudinal immune profiling reveals key myeloid signatures associated with COVID-19. *Sci Immunol* **5**, (2020).

33. Melms, J. C. *et al.* A molecular single-cell lung atlas of lethal COVID-19. *Nature* **595**, 114–119 (2021).

34. Szabo, P. A. *et al.* Longitudinal profiling of respiratory and systemic immune responses reveals myeloid cell-driven lung inflammation in severe COVID-19. *Immunity* **54**, 797-814.e6 (2021).

35. Yoo, J.-K., Kim, T. S., Hufford, M. M. & Braciale, T. J. Viral infection of the lung: host response and sequelae. *J Allergy Clin Immunol* **132**, 1263–76; quiz 1277 (2013).

36. Knoll, R., Schultze, J. L. & Schulte-Schrepping, J. Monocytes and Macrophages in COVID-19. *Front Immunol* **12**, 720109 (2021).

37. Chen, S. T. *et al.* A shift in lung macrophage composition is associated with COVID-19 severity and recovery. *Sci Transl Med* **14**, eabn5168 (2022).

38. Chua, R. L. *et al.* COVID-19 severity correlates with airway epithelium-immune cell interactions identified by single-cell analysis. *Nat Biotechnol* **38**, 970–979 (2020).

39. Liao, M. *et al.* Single-cell landscape of bronchoalveolar immune cells in patients with COVID-19. *Nat Med* **26**, 842–844 (2020).

40. Snyder, M. E. *et al.* Generation and persistence of human tissue-resident memory T cells in lung transplantation. *Sci Immunol* **4**, (2019).

41. Poon, M. M. L. *et al.* SARS-CoV-2 infection generates tissue-localized immunological memory in humans. *Sci Immunol* **6**, eabl9105 (2021).

42. Vandereyken, K., Sifrim, A., Thienpont, B. & Voet, T. Methods and applications for single-cell and spatial multi-omics. *Nat Rev Genet* **24**, 494–515 (2023).

43. Wang, S. *et al.* A single-cell transcriptomic landscape of the lungs of patients with COVID-19. *Nat Cell Biol* **23**, 1314–1328 (2021).

44. Wang, C. *et al.* Imaging Mass Cytometric Analysis of Postmortem Tissues Reveals Dysregulated Immune Cell and Cytokine Responses in Multiple Organs of COVID-19 Patients. *Front Microbiol* **11**, 600989 (2020).

45. Desai, N. *et al.* Temporal and spatial heterogeneity of host response to SARS-CoV-2 pulmonary infection. *Nat Commun* **11**, 6319 (2020).

46. Collins, A. M. *et al.* Bronchoalveolar lavage (BAL) for research; obtaining adequate sample yield. *J Vis Exp* (2014) doi:10.3791/4345.

47. Merritt, C. R. *et al.* Multiplex digital spatial profiling of proteins and RNA in fixed tissue. *Nature biotechnology* vol. 38 586–599 Preprint at https://doi.org/10.1038/s41587-020-0472-9 (2020).

48. Wang, T. *et al.* An experimental comparison of the Digital Spatial Profiling and Visium spatial transcriptomics technologies for cancer research. *bioRxiv* 2023.04.06.535805 (2023) doi:10.1101/2023.04.06.535805.

49. He, S. *et al.* High-plex imaging of RNA and proteins at subcellular resolution in fixed tissue by spatial molecular imaging. *Nat Biotechnol* **40**, 1794–1806 (2022).

50. Janesick, A. *et al.* High resolution mapping of the tumor microenvironment using integrated single-cell, spatial and in situ analysis. *Nat Commun* **14**, 8353 (2023).

51. Chen, K. H., Boettiger, A. N., Moffitt, J. R., Wang, S. & Zhuang, X. Spatially resolved, highly multiplexed RNA profiling in single cells. *Science (1979)* **348**, aaa6090 (2015).

52. Grant, R. A. *et al.* Prolonged exposure to lung-derived cytokines is associated with activation of microglia in patients with COVID-19. *JCI Insight* **9**, (2024).

53. Grant, R. A. *et al.* Circuits between infected macrophages and T cells in SARS-CoV-2 pneumonia. *Nature* **590**, 635–641 (2021).

54. Markov, N. S. *et al.* Distinctive evolution of alveolar T cell responses is associated with clinical outcomes in unvaccinated patients with SARS-CoV-2 pneumonia. *Nat Immunol* (2024) doi:10.1038/s41590-024-01914-w.

55. Mitsi, E. *et al.* Respiratory mucosal immune memory to SARS-CoV-2 after infection and vaccination. *Nat Commun* **14**, 6815 (2023).

56. Tang, J. *et al.* Respiratory mucosal immunity against SARS-CoV-2 after mRNA vaccination. *Sci Immunol* **7**, eadd4853 (2022).

57. Goltsev, Y. *et al.* Deep Profiling of Mouse Splenic Architecture with CODEX Multiplexed Imaging. *Cell* **174**, 968-981.e15 (2018).

58. Schürch, C. M. *et al.* Coordinated Cellular Neighborhoods Orchestrate Antitumoral Immunity at the Colorectal Cancer Invasive Front. *Cell* **182**, 1341-1359.e19 (2020).

59. Mothes, R. *et al.* Distinct tissue niches direct lung immunopathology via CCL18 and CCL21 in severe COVID-19. *Nat Commun* **14**, 791 (2023).

60. Rosato, P. C., Beura, L. K. & Masopust, D. Tissue resident memory T cells and viral immunity. *Curr Opin Virol* **22**, 44–50 (2017).

61. Hogan, R. J. *et al.* Protection from respiratory virus infections can be mediated by antigen-specific CD4(+) T cells that persist in the lungs. *J Exp Med* **193**, 981–986 (2001).

62. Subbarao, K. Live Attenuated Cold-Adapted Influenza Vaccines. *Cold Spring Harb Perspect Med* **11**, (2021).

63. Wu, T. *et al.* Lung-resident memory CD8 T cells (TRM) are indispensable for optimal cross-protection against pulmonary virus infection. *J Leukoc Biol* **95**, 215–224 (2014).

64. Keeton, R. *et al.* T cell responses to SARS-CoV-2 spike cross-recognize Omicron. *Nature* **603**, 488–492 (2022).

65. Naranbhai, V. *et al.* T cell reactivity to the SARS-CoV-2 Omicron variant is preserved in most but not all individuals. *Cell* **185**, 1041-1051.e6 (2022).

66. McMaster, S. R., Wilson, J. J., Wang, H. & Kohlmeier, J. E. Airway-Resident Memory CD8 T Cells Provide Antigen-Specific Protection against Respiratory Virus Challenge through Rapid IFN-γ Production. *J Immunol* **195**, 203–209 (2015).

67. Kumar, B. V *et al.* Human Tissue-Resident Memory T Cells Are Defined by Core Transcriptional and Functional Signatures in Lymphoid and Mucosal Sites. *Cell Rep* **20**, 2921–2934 (2017).

68. Connors, T. J. *et al.* Site-specific development and progressive maturation of human tissue-resident memory T cells over infancy and childhood. *Immunity* **56**, 1894-1909.e5 (2023).

69. Wu, N. *et al.* Long-term effectiveness of COVID-19 vaccines against infections, hospitalisations, and mortality in adults: findings from a rapid living systematic evidence synthesis and meta-analysis up to December, 2022. *Lancet Respir Med* **11**, 439–452 (2023).

70. Tong, X. *et al.* Compartment-Specific Antibody Correlates of Protection to SARS-CoV-2 Omicron in Macaques. *iScience* (2024).

71. Gagne, M. *et al.* Mucosal adenovirus vaccine boosting elicits IgA and durably prevents XBB.1.16 infection in nonhuman primates. *Nat Immunol* (2024) doi:10.1038/s41590-024-01951-5.

72. McMahan, K. *et al.* Mucosal boosting enhances vaccine protection against SARS-CoV-2 in macaques. *Nature* **626**, 385–391 (2024).

73. Levin, E. G. *et al.* Waning Immune Humoral Response to BNT162b2 Covid-19 Vaccine over 6 Months. *N Engl J Med* **385**, e84 (2021).

74. Tut, G. *et al.* Strong peak immunogenicity but rapid antibody waning following third vaccine dose in older residents of care homes. *Nat Aging* **3**, 93–104 (2023).

75. Szabo, P. A., Miron, M. & Farber, D. L. Location, location, location: Tissue resident memory T cells in mice and humans. *Sci Immunol* **4**, (2019).

76. Swanson, P. A. 2nd *et al.* AZD1222/ChAdOx1 nCoV-19 vaccination induces a polyfunctional spike protein-specific T(H)1 response with a diverse TCR repertoire. *Sci Transl Med* **13**, eabj7211 (2021).

77. Painter, M. M. *et al.* Prior vaccination promotes early activation of memory T cells and enhances immune responses during SARS-CoV-2 breakthrough infection. *Nat Immunol* **24**, 1711–1724 (2023).

78. Sette, A. & Crotty, S. Immunological memory to SARS-CoV-2 infection and COVID-19 vaccines. *Immunol Rev* **310**, 27–46 (2022).

79. Hasenkrug, K. J. *et al.* Recovery from Acute SARS-CoV-2 Infection and Development of Anamnestic Immune Responses in T Cell-Depleted Rhesus Macaques. *mBio* **12**, e0150321 (2021).

80. McMahan, K. *et al.* Correlates of protection against SARS-CoV-2 in rhesus macaques. *Nature* **590**, 630–634 (2021).

81. Zhao, J. *et al.* Airway Memory CD4(+) T Cells Mediate Protective Immunity against Emerging Respiratory Coronaviruses. *Immunity* **44**, 1379–1391 (2016).

82. van Doremalen, N. *et al.* Intranasal ChAdOx1 nCoV-19/AZD1222 vaccination reduces viral shedding after SARS-CoV-2 D614G challenge in preclinical models. *Sci Transl Med* **13**, (2021).

83. Mao, T. *et al.* Unadjuvanted intranasal spike vaccine elicits protective mucosal immunity against sarbecoviruses. *Science* **378**, eabo2523 (2022).

84. Madhavan, M. *et al.* Tolerability and immunogenicity of an intranasally-administered adenovirus-vectored COVID-19 vaccine: An open-label partially-randomised ascending dose phase I trial. *EBioMedicine* **85**, 104298 (2022).

85. Wu, Z. & McGoogan, J. M. Characteristics of and Important Lessons From the Coronavirus Disease 2019 (COVID-19) Outbreak in China: Summary of a Report of 72 314 Cases From the Chinese Center for Disease Control and Prevention. *JAMA* **323**, 1239–1242 (2020).

86. Liu, Y. *et al.* Association between age and clinical characteristics and outcomes of COVID-19. *The European respiratory journal* vol. 55 Preprint at https://doi.org/10.1183/13993003.01112-2020 (2020).

87. Salguero, F. J. *et al.* Comparison of rhesus and cynomolgus macaques as an infection model for COVID-19. *Nat Commun* **12**, (2021).

88. Singh, D. K. *et al.* Responses to acute infection with SARS-CoV-2 in the lungs of rhesus macaques, baboons and marmosets. *Nat Microbiol* **6**, 73–86 (2021).

89. Rockx, B. *et al.* Comparative pathogenesis of COVID-19, MERS, and SARS in a nonhuman primate model. *Science* **368**, 1012–1015 (2020).

90. Brady, C., Tipton, T., Longet, S. & Carroll, M. W. Pre-clinical models to define correlates of protection for SARS-CoV-2. *Front Immunol* **14**, 1166664 (2023).

91. Goldblatt, D., Alter, G., Crotty, S. & Plotkin, S. A. Correlates of protection against SARS-CoV-2 infection and COVID-19 disease. *Immunol Rev* **310**, 6–26 (2022).

92. Watson, O. J. *et al.* Global impact of the first year of COVID-19 vaccination: a mathematical modelling study. *Lancet Infect Dis* (2022) doi:10.1016/S1473-3099(22)00320-6.

93. Bjornson-Hooper, Z. B. *et al.* A Comprehensive Atlas of Immunological Differences Between Humans, Mice, and Non-Human Primates. *Front Immunol* **13**, 867015 (2022).

94. Muñoz-Fontela, C. *et al.* Advances and gaps in SARS-CoV-2 infection models. *PLoS Pathog* **18**, e1010161 (2022).

95. Muñoz-fontela, C. *et al.* Animal models for COVID-19. **586**, (2020).

96. Nelson, C. E. *et al.* Mild SARS-CoV-2 infection in rhesus macaques is associated with viral control prior to antigen-specific T cell responses in tissues. *Sci Immunol* eabo0535 (2022) doi:10.1126/sciimmunol.abo0535.

97. Chandrashekar, A. *et al.* SARS-CoV-2 infection protects against rechallenge in rhesus macaques. *Science* **369**, 812–817 (2020).

98. Deng, W. *et al.* Primary exposure to SARS-CoV-2 protects against reinfection in rhesus macaques. *Science* **369**, 818–823 (2020).

99. Gartlan, C. *et al.* Vaccine-Associated Enhanced Disease and Pathogenic Human Coronaviruses. *Front Immunol* **13**, 882972 (2022).

100. Munoz, F. M. *et al.* Vaccine-associated enhanced disease: Case definition and guidelines for data collection, analysis, and presentation of immunization safety data. *Vaccine* **39**, 3053–3066 (2021).

101. Sridhar, S. *et al.* Effect of Dengue Serostatus on Dengue Vaccine Safety and Efficacy. *New England Journal of Medicine* 327–340 (2018) doi:10.1056/nejmoa1800820.

102. Kim, H. W. H. A. *et al.* Respiratory syncytial virus disease in infants despite prior administration of antigenic inactivated vaccine. *Am J Epidemiol* **89**, 422–434 (1969).

103. Fulginiti, V. A., Eller, J. J., Downie, A. W. & Kempe, C. H. Altered Reactivity to Measles Virus: Atypical Measles in Children Previously Immunized With Inactivated Measles Virus Vaccines. *JAMA* **202**, 1075–1080 (1967).

104. Iwasaki, A. & Yang, Y. The potential danger of suboptimal antibody responses in COVID-19. *Nat Rev Immunol* **20**, 339–341 (2020).

105. Graham, B. B. S. Rapid COVID-19 vaccine development. *Science (1979)* **368**, 945–946 (2020).

106. Shaw, C. A. *et al.* The role of non-viral antigens in the cotton rat model of respiratory syncytial virus vaccine-enhanced disease. *Vaccine* **31**, 306–312 (2013).

107. Feng, S. *et al.* Correlates of protection against symptomatic and asymptomatic SARS-CoV-2 infection. *Nat Med* **27**, 2032–2040 (2021).

108. ben Mkaddem, S., Benhamou, M. & Monteiro, R. C. Understanding Fc Receptor Involvement in Inflammatory Diseases: From Mechanisms to New Therapeutic Tools. *Front Immunol* **10**, 811 (2019).

109. Junqueira, C. *et al.* FcγR-mediated SARS-CoV-2 infection of monocytes activates inflammation. *Nature* **606**, 576–584 (2022).

110. Sefik, E. *et al.* Inflammasome activation in infected macrophages drives COVID-19 pathology. *Nature* **606**, 585–593 (2022).

111. Lu, L. L., Suscovich, T. J., Fortune, S. M. & Alter, G. Beyond binding: antibody effector functions in infectious diseases. *Nat Rev Immunol* **18**, 46–61 (2018).

112. Bournazos, S. *et al.* Antibody fucosylation predicts disease severity in secondary dengue infection. *Science (1979)* **372**, 1102–1105 (2021).

113. Larsen, M. D. *et al.* Afucosylated IgG characterizes enveloped viral responses and correlates with COVID-19 severity. *Science (1979)* **371**, (2021).

114. Katzelnick, L. C. *et al.* Antibody-dependent enhancement of severe dengue disease in humans. *Science (1979)* **358**, 929–932 (2017).

115. Yamanaka, A. *et al.* Antibody-dependent enhancement representing in vitro infective progeny virus titer correlates with the viremia level in dengue patients. *Sci Rep* **11**, 1–11 (2021).

116. Screaton, G., Mongkolsapaya, J., Yacoub, S. & Roberts, C. New insights into the immunopathology and control of dengue virus infection. *Nat Rev Immunol* **15**, 745–759 (2015).

117. Bewley, K. R. *et al.* Immunological and pathological outcomes of SARS-CoV-2 challenge following formalin-inactivated vaccine in ferrets and rhesus macaques. *Sci. Adv* **7**, 7996 (2021).

118. Moghaddam, A. *et al.* A potential molecular mechanism for hypersensitivity caused by formalin-inactivated vaccines. *Nat Med* **12**, 905–907 (2006).

119. Polack, F. P. *et al.* A role for immune complexes in enhanced respiratory syncytial virus disease. *J Exp Med* **196**, 859–865 (2002).

120. Hohdatsu, T. *et al.* Antibody-Dependent Enhancement of Feline Infectious Peritonitis Virus Infection in Feline Alveolar Macrophages and Human Monocyte Cell Line U937 by Serum of Cats Experimentally or Naturally Infected with Feline Coronavirus. *Journal of Veterinary Medical Science* **60**, 49–55 (1998).

121. Rottier, P. J. M., Nakamura, K., Schellen, P., Volders, H. & Haijema, B. J. Acquisition of macrophage tropism during the pathogenesis of feline infectious peritonitis is determined by mutations in the feline coronavirus spike protein. *J Virol* **79**, 14122–14130 (2005).

122. Takano, T., Kawakami, C., Yamada, S., Satoh, R. & Hohdatsu, T. Antibody-dependent enhancement occurs upon re-infection with the identical serotype virus in feline infectious peritonitis virus infection. *Journal of Veterinary Medical Science* **70**, 1315–1321 (2008).

123. Pedersen, N. C. An update on feline infectious peritonitis: Virology and immunopathogenesis. *The Veterinary Journal* **201**, 123–132 (2014).

124. Emmler, L. *et al.* Feline coronavirus with and without spike gene mutations detected by real-time RT-PCRs in cats with feline infectious peritonitis. *J Feline Med Surg* **22**, 791–799 (2020).

125. Huang, A. T. *et al.* A systematic review of antibody mediated immunity to coronaviruses: kinetics, correlates of protection, and association with severity. *Nat Commun* **11**, 1–16 (2020).

126. Hui, K. P. Y. *et al.* Tropism, replication competence, and innate immune responses of the coronavirus SARS-CoV-2 in human respiratory tract and conjunctiva: an analysis in ex-vivo and in-vitro cultures. *Lancet Respir Med* **8**, 687–695 (2020).

127. Niles, M. A. *et al.* Macrophages and Dendritic Cells Are Not the Major Source of Pro-Inflammatory Cytokines Upon SARS-CoV-2 Infection. *Front Immunol* **12**, (2021).

128. Ankerhold, J. *et al.* Circulating multimeric immune complexes contribute to immunopathology in COVID-19. *Nat Commun* **13**, 5654 (2022).

129. Li, C. *et al.* Absence of Vaccine-enhanced Disease With Unexpected Positive Protection Against severe acute respiratory syndrome coronavirus 2 (SARS-CoV-2) by Inactivated Vaccine Given Within 3 Days of Virus Challenge in Syrian Hamster Model. *Clinical Infectious Diseases* **73**, e719–e734 (2021).

130. Dillard, J. A. *et al.* Adjuvant-dependent impact of inactivated SARS-CoV-2 vaccines during heterologous infection by a SARS-related coronavirus. *Nat Commun* **15**, 3738 (2024).

131. Walls, A. C. *et al.* Structure, Function, and Antigenicity of the SARS-CoV-2 Spike Glycoprotein. *Cell* **181**, 281-292.e6 (2020).

132. Ebenig, A. *et al.* Vaccine-associated enhanced respiratory pathology in COVID-19 hamsters after TH2-biased immunization. *Cell Rep* **40**, 111214 (2022).

133. Hörner, C. *et al.* A highly immunogenic and effective measles virus-based Th1-biased COVID-19 vaccine. *Proc Natl Acad Sci U S A* **117**, 32657–32666 (2020).

134. Mühlebach, M. *et al.* Hamster Model of Severe COVID-19 Demonstrates Differential Efficacy of first Licensed Western Vaccines in the Absence of Immunopathogenesis. *Preprint (version 1), available at Research square* (2024) doi:10.21203/rs.3.rs-4151277/v1.

135. Gooch, K. E. *et al.* One or two dose regimen of the SARS-CoV-2 synthetic DNA vaccine INO-4800 protects against respiratory tract disease burden in nonhuman primate challenge model. *Vaccine* **39**, 4885–4894 (2021).

136. Rauch, S. *et al.* mRNA vaccine CVnCoV protects non-human primates from SARS-CoV-2 challenge infection. *bioRxiv* 2020.12.23.424138 (2020) doi:10.1101/2020.12.23.424138.

137. Lambe, T. *et al.* ChAdOx1 nCoV-19 protection against SARS-CoV-2 in rhesus macaque and ferret challenge models. *Commun Biol* **4**, 915 (2021).

138. Hunter, L., Hingley-Wilson, S., Stewart, G. R., Sharpe, S. A. & Salguero, F. J. Dynamics of Macrophage, T and B Cell Infiltration Within Pulmonary Granulomas Induced by Mycobacterium tuberculosis in Two Non-Human Primate Models of Aerosol Infection. *Front Immunol* **12**, 776913 (2021).

139. Randall, T. D. Bronchus-associated lymphoid tissue (BALT) structure and function. *Adv Immunol* **107**, 187–241 (2010).

140. Pabst, R. The bronchus-associated-lymphoid tissue (BALT) an unique lymphoid organ in man and animals. *Annals of anatomy - Anatomischer Anzeiger* **240**, 151833 (2022).

141. Reusch, N. *et al.* Neutrophils in COVID-19. *Front Immunol* **12**, 652470 (2021).

142. Radtke, A. J. *et al.* IBEX: an iterative immunolabeling and chemical bleaching method for high-content imaging of diverse tissues. *Nat Protoc* **17**, 378–401 (2022).

143. Black, S. *et al.* CODEX multiplexed tissue imaging with DNA-conjugated antibodies. *Nat Protoc* **16**, 3802–3835 (2021).

144. Bankhead, P. *et al.* QuPath: Open source software for digital pathology image analysis. *Sci Rep* **7**, 16878 (2017).

145. Greenwald, N. F. *et al.* Whole-cell segmentation of tissue images with human-level performance using large-scale data annotation and deep learning. *Nat Biotechnol* **40**, 555–565 (2022).

146. Team, R. C. R: A Language and Environment for Statistical Computing. Preprint at https://www.r-project.org/ (2022).

147. Constantin, A.-E. & Patil, I. ggsignif: R Package for Displaying Significance Brackets for 'ggplot2'. *PsyArxiv* Preprint at https://doi.org/10.31234/osf.io/7awm6 (2021).

148. Wickham, H., François, R., Henry, L., Müller, K. & Vaughan, D. dplyr: A Grammar of Data Manipulation. Preprint at https://cran.r-project.org/package=dplyr (2023).

149. Wickham, H. ggplot2: Elegant Graphics for Data Analysis. Preprint at https://ggplot2.tidyverse.org (2016).

150. Slowikowski, K. ggrepel: Automatically Position Non-Overlapping Text Labels with 'ggplot2'. Preprint at https://cran.r-project.org/package=ggrepel (2023).

151. Hothorn, T., Bretz, F. & Westfall, P. Simultaneous inference in general parametric models. *Biom J* **50**, 346–63 (2008).

152. Mortlock, R. D. *et al.* Tissue Trafficking Kinetics of Rhesus Macaque Natural Killer Cells Measured by Serial Intravascular Staining. *Front Immunol* **12**, 772332 (2021).

153. Rogers, K. A., Scinicariello, F. & Attanasio, R. Identification and characterization of macaque CD89 (immunoglobulin A Fc receptor). *Immunology* **113**, 178–86 (2004).

154. Rogers, K. A., Scinicariello, F. & Attanasio, R. IgG Fc receptor III homologues in nonhuman primate species: genetic characterization and ligand interactions. *J Immunol* **177**, 3848–56 (2006).

155. Veglia, F., Sanseviero, E. & Gabrilovich, D. I. Myeloid-derived suppressor cells in the era of increasing myeloid cell diversity. *Nat Rev Immunol* **21**, 485–498 (2021).

156. Neidleman, J. *et al.* Distinctive features of SARS-CoV-2-specific T cells predict recovery from severe COVID-19. *Cell Rep* **36**, 109414 (2021).

157. Kuri-Cervantes, L. *et al.* Comprehensive mapping of immune perturbations associated with severe COVID-19. *Sci Immunol* **5**, (2020).

158. Laing, A. G. *et al.* A dynamic COVID-19 immune signature includes associations with poor prognosis. *Nat Med* **26**, 1623–1635 (2020).

159. Chen, S. T. *et al.* A shift in lung macrophage composition is associated with COVID-19 severity and recovery. *Sci Transl Med* **14**, eabn5168 (2022).

160. Bergamaschi, L. *et al.* Longitudinal analysis reveals that delayed bystander CD8+ T cell activation and early immune pathology distinguish severe COVID-19 from mild disease. *Immunity* **54**, 1257-1275.e8 (2021).

161. Mathew, D. *et al.* Deep immune profiling of COVID-19 patients reveals distinct immunotypes with therapeutic implications. *Science* **369**, (2020).

162. Rao, A., Barkley, D., França, G. S. & Yanai, I. Exploring tissue architecture using spatial transcriptomics. *Nature* **596**, 211–220 (2021).

163. Moses, L. & Pachter, L. Museum of spatial transcriptomics. *Nat Methods* **19**, 534–546 (2022).

164. Wickham, H. *et al.* Welcome to the tidyverse. *Journal of Open Source Software* vol. 4 1686 Preprint at https://doi.org/10.21105/joss.01686 (2019).

165. Righelli, D. *et al.* SpatialExperiment: infrastructure for spatially-resolved transcriptomics data in R using Bioconductor. *Bioinformatics* **38**, 3128–3131 (2022).

166. Wu, T. *et al.* clusterProfiler 4.0: A universal enrichment tool for interpreting omics data. *Innovation (Cambridge (Mass.))* **2**, 100141 (2021).

167. Love, M. I., Huber, W. & Anders, S. Moderated estimation of fold change and dispersion for RNA-seq data with DESeq2. *Genome Biol* **15**, 550 (2014).

168. Liu, N. *et al.* standR: spatial transcriptomic analysis for GeoMx DSP data. *Nucleic Acids Res* **52**, e2 (2024).

169. Robinson, M. D., McCarthy, D. J. & Smyth, G. K. edgeR: a Bioconductor package for differential expression analysis of digital gene expression data. *Bioinformatics* **26**, 139–40 (2010).

170. Subramanian, A. *et al.* Gene set enrichment analysis: a knowledge-based approach for interpreting genome-wide expression profiles. *Proc Natl Acad Sci U S A* **102**, 15545–15550 (2005).

171. Liberzon, A. *et al.* Molecular signatures database (MSigDB) 3.0. *Bioinformatics* **27**, 1739–1740 (2011).

172. Kalbe, B. *et al.* Olfactory Receptors Modulate Physiological Processes in Human Airway Smooth Muscle Cells. *Front Physiol* **7**, 339 (2016).

173. Brann, D. H. *et al.* Non-neuronal expression of SARS-CoV-2 entry genes in the olfactory system suggests mechanisms underlying COVID-19-associated anosmia. *Sci Adv* **6**, (2020).

174. LaSalle, T. J. *et al.* Longitudinal characterization of circulating neutrophils uncovers phenotypes associated with severity in hospitalized COVID-19 patients. *Cell Rep Med* **3**, 100779 (2022).

175. Mehta, P. *et al.* COVID-19: consider cytokine storm syndromes and immunosuppression. *Lancet (London, England)* vol. 395 1033–1034 Preprint at https://doi.org/10.1016/S0140-6736(20)30628-0 (2020).

176. Del Valle, D. M. *et al.* An inflammatory cytokine signature predicts COVID-19 severity and survival. *Nat Med* **26**, 1636–1643 (2020).

177. Herold, T. *et al.* Elevated levels of IL-6 and CRP predict the need for mechanical ventilation in COVID-19. *J Allergy Clin Immunol* **146**, 128-136.e4 (2020).

178. Wu, C. *et al.* Risk Factors Associated With Acute Respiratory Distress Syndrome and Death in Patients With Coronavirus Disease 2019 Pneumonia in Wuhan, China. *JAMA Intern Med* **180**, 934–943 (2020).

179. Coomes, E. A. & Haghbayan, H. Interleukin-6 in Covid-19: A systematic review and meta-analysis. *Rev Med Virol* **30**, 1–9 (2020).

180. Jones, S. A. & Hunter, C. A. Is IL-6 a key cytokine target for therapy in COVID-19? *Nat Rev Immunol* **21**, 337–339 (2021).

181. Reynolds, D. *et al.* Comprehensive Immunologic Evaluation of Bronchoalveolar Lavage Samples from Human Patients with Moderate and Severe Seasonal Influenza and Severe COVID-19. *J Immunol* **207**, 1229–1238 (2021).

182. Stefura, W. P., Graham, C., Lotoski, L. & HayGlass, K. T. Improved Methods for Quantifying Human Chemokine and Cytokine Biomarker Responses: Ultrasensitive ELISA and Meso Scale Electrochemiluminescence Assays. in *Allergy: Methods and Protocols* (eds. Lympany, P. & Jones, M. G.) 91–114 (Springer New York, New York, NY, 2019). doi:10.1007/978-1-4939-9591-2_7.

183. Zhang, Y., Li, X. & Di, Y. P. Fast and Efficient Measurement of Clinical and Biological Samples Using Immunoassay-Based Multiplexing Systems. in *Molecular Toxicology Protocols* (eds. Keohavong, P., Singh, K. P. & Gao, W.) 129–147 (Springer US, New York, NY, 2020). doi:10.1007/978-1-0716-0223-2_6.

184. Schiffner, T. *et al.* Chemical Cross-Linking Stabilizes Native-Like HIV-1 Envelope Glycoprotein Trimer Antigens. *J Virol* **90**, 813–828 (2016).

185. Russell, C. D., Lone, N. I. & Baillie, J. K. Comorbidities, multimorbidity and COVID-19. *Nat Med* **29**, 334–343 (2023).

186. Lewis, S. M. *et al.* Spatial omics and multiplexed imaging to explore cancer biology. *Nat Methods* **18**, 997–1012 (2021).

187. Engblom, C. *et al.* Spatial transcriptomics of B cell and T cell receptors reveals lymphocyte clonal dynamics. *Science* **382**, eadf8486 (2023).

Appendix

Supplementary tables and figures

Vaccine study (manufacturer)	NHP ID	Vaccination strategy	Sex	Cull day*	Lung histopathology score
Viral vector (Oxford-Astrazeneca)	17Z	Single dose	M	Standard	6.31
	13Z	Single dose	M	Late	2.96
	45Z	Single dose	M	Late	2.55
	29Z	Single dose	F	Standard	5.76
	26Z	Single dose	F	Late	5.21
	36Z	Single dose	F	Late	2.45
DNA (Inovio)	10A	Single dose	M	Standard	17
	30A	Single dose	M	Standard	6.25
	24A	Single dose	M	Standard	6.25
	21A	Single dose	F	Standard	5
	5A	Single dose	F	Standard	3.25
	38A	Single dose	F	Standard	4.25
	9A	Two dose	M	Standard	9
	12A	Two dose	M	Standard	4.75
	45A	Two dose	M	Standard	5.5
	42A	Two dose	F	Standard	3.75
	33A	Two dose	F	Standard	3.5
	13A	Two dose	F	Standard	3.5
Formalin inactivated vaccine	29A	Single dose	M	Standard	7.5
	31A	Single dose	M	Standard	4.25
	3A	Single dose	M	Standard	7.75
	2A	Single dose	F	Standard	3.25
	54A	Single dose	F	Standard	7.25
	15A	Single dose	F	Standard	5
mRNA (Curevac)	BLG	Two low doses (2 x 0.5µg)	M	Standard	11.5
	BBO	Two low doses (2 x 0.5µg)	M	Standard	8
	BRR	Two low doses (2 x 0.5µg)	M	Standard	7.25
	ARIL	Two low doses (2 x 0.5µg)	F	Standard	6.75
	BYC	Two low doses (2 x 0.5µg)	F	Standard	7.5
	AAA	Two low doses (2 x 0.5µg)	F	Standard	8
	ATM	Two high doses (2 x 8µg)	M	Standard	5.75
	AUU	Two high doses (2 x 8µg)	M	Standard	4
	ALBS	Two high doses (2 x 8µg)	M	Standard	4.5
	ANAI	Two high doses (2 x 8µg)	F	Standard	6
	ZORA	Two high doses (2 x 8µg)	F	Standard	4.5
	AO	Two high doses (2 x 8µg)	F	Standard	4.5
Re-challenge	ALEX	Unvaccinated	M	Standard	4.92
	APOLL	Unvaccinated	M	Standard	8.91
	ANKI	Unvaccinated	M	Standard	5.88
	BTW	Unvaccinated	F	Standard	8.63
	BINKY	Unvaccinated	F	Standard	6
	BDC	Unvaccinated	F	Standard	8.54
Unvaccinated	22Z	Unvaccinated (PBS)	M	Standard	15.46
	31Z	Unvaccinated (PBS)	M	Late	5.31
	4Z	Unvaccinated (PBS)	M	Late	8.47
	18Z	Unvaccinated (PBS)	F	Late	5.4
	24Z	Unvaccinated (PBS)	F	Standard	5.12
	53Z	Unvaccinated (PBS)	F	Late	4.28
	25A	Unvaccinated (PBS)	M	Standard	13
	8A	Unvaccinated (PBS)	M	Standard	11
	28A	Unvaccinated (PBS)	M	Standard	8.75
	50A	Unvaccinated (PBS)	F	Standard	11
	19A	Unvaccinated (PBS)	F	Standard	6.75
	14A	Unvaccinated (PBS)	F	Standard	8.75
	AMIS	Unvaccinated (PBS)	M	Standard	7.25
	ART	Unvaccinated (PBS)	M	Standard	6.5
	ZIG	Unvaccinated (PBS)	M	Standard	8.5
	APRIL	Unvaccinated (PBS)	F	Standard	9.75
	ASE	Unvaccinated (PBS)	F	Standard	9.5
	AURO	Unvaccinated (PBS)	F	Standard	7.25

Supplementary Table 1: Information on the NHPs in the preclinical vaccine studies conducted at Porton Down. **Standard cull day is day 6 or 7, while the late cull day is day 13, 14 or 15.*

Marker	Clone	Fluoresence channel	Supplier	Cat number	Concentration (µg/mL)	Staining round	Suitable?
Anti-Mouse IgG1	Polyclonal	Cy5 (AF647)	Abcam	ab150107	5	1	NA
Anti-Rabbit	Polyclonal	Cy3 (AF555)	Abcam	ab150078	5	1	NA
Calprotectin	MAC387	FITC (AF488). Manually conjugated	Abcam	ab22506	10	3	No
CD10	EPR22865-73	FITC (AF488). Manually conjugated	Abcam	ab256767	10	2	No
CD103	EPR4166(2)	Cy5 (AF647)	Abcam	ab225153	10	3	No
CD107a/LAMP1	H4A3	Cy5 (AF647)	Biolegend	328601	10	2	No
CD16	EPR16784	Cy5 (AF647)	Abcam	ab283695	10	4	Yes
CD20	EP459Y	FITC (AF488)	Abcam	ab198941	5	5	Yes
CD3	SP162	Cy3 (AF555)	Abcam	ab307335	5	5	Yes
CD31	JC70/A (anti-mouse IgG1)	NA	GeneTex	GTX34495	10	1	No
CD4	EPR6855	Cy5 (AF647)	Abcam	ab196147	10	5	Yes
CD45	RM1007	Cy3 (AF555). Manually conjugated	Abcam	ab282747	10	2	Yes
CD56	EPR2566	FITC (AF488)	Abcam	ab200333	10	4	No
CD68	EPR20545	Cy3 (AF555)	Abcam	ab280860	5	3	No
DAPI (nuclear)	NA	DAPI	Thermo Fisher	62247	NA	All	Yes
FOXP3 (nuclear)	D2W8E	Cy3 (AF555). Manually conjugated	Cell Signaling Technology	74816SF	14	4	Yes
HLADR	TAL 1B5	Cy3 (AF546)	Santa Cruz Biotechnology	sc-53319	10	6	Yes
Ki67 (nuclear)	Polyclonal rabbit	NA	Abcam	ab15580	5	1	No
PanCk	AE1+AE3	eF660 (AF647)	Thermo Fisher	50-9003-82	2	6	Yes

Supplementary Table 2: Antibody list for multiplex immunofluorescence (Cell DIVE) experiment. The table includes the staining round the antibody was included in, as well as whether or not the antibody was suitable for analysis.

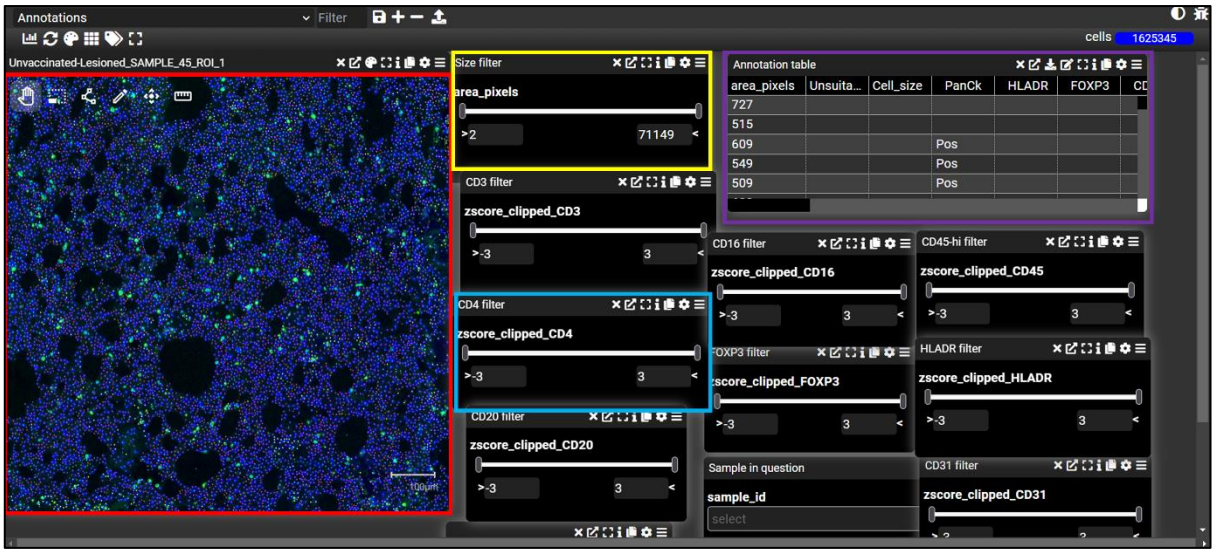

Supplementary Figure 1: Multi-Dimensional Viewer (MDV) annotations overview. Showing a browsable view of a sample (red box), a filter for the size of segmented cells (yellow box), a filter for one of the markers of interest, CD4 (blue box) and the annotation table (purple box). The filters were used to annotate segmented cells of appropriate size and categorise them according to marker positivity, all within the annotation. Unsuitable areas for analysis were annotated using the drawing feature in the red box and added to the annotation table. In the red box, DAPI is blue and CD3 is green. Screenshot taken from MDV.

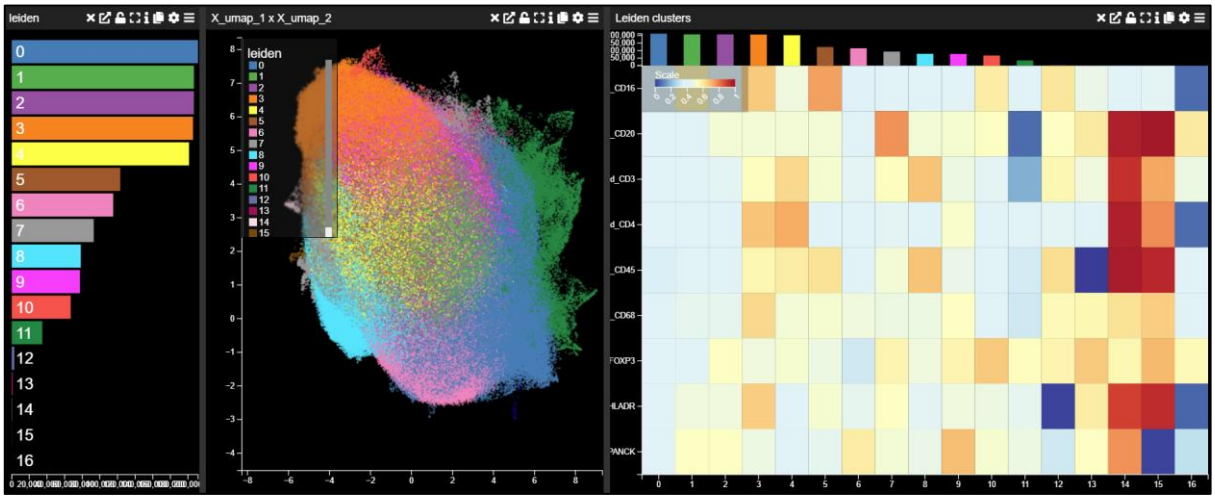

Supplementary Figure 2: Leiden clustering in Multi-Dimensional Viewer (MDV). Showing the relative abundances of the clusters (on the left-most box), a UMAP of the cell clusters (middle box) and the relative expression of markers of interest (right-most box). Screenshot taken from MDV.

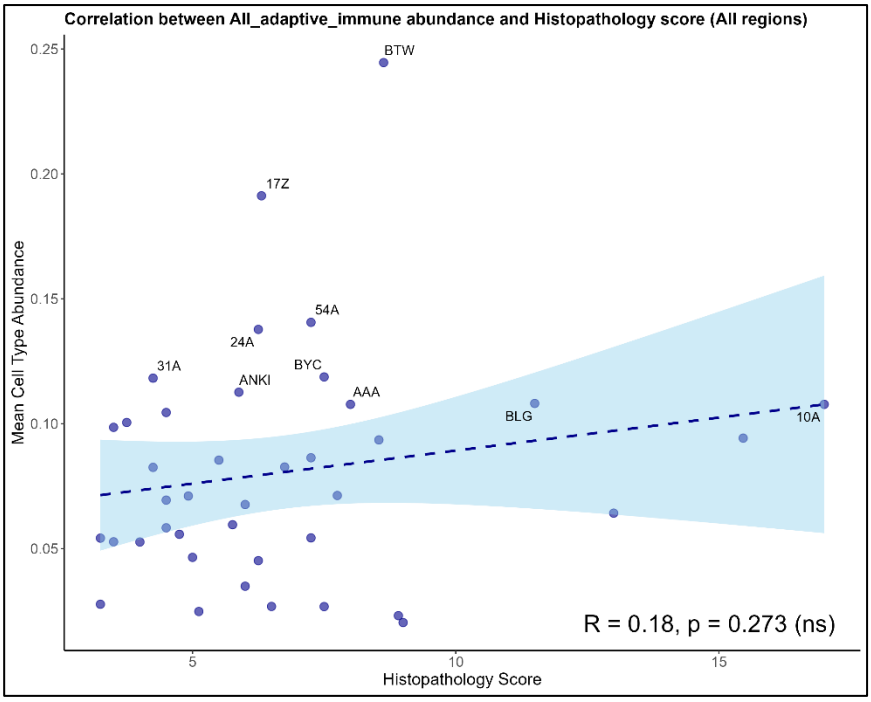
Correlation between All_adaptive_immune abundance and Histopathology score (All regions)
Mean Cell Type Abundance
Histopathology Score
0.25
0.20
0.15
0.10
0.05
5
10
15
BTW
17Z
54A
24A
31A
BYC
ANKI
AAA
BLG
10A
R = 0.18, p = 0.273 (ns)

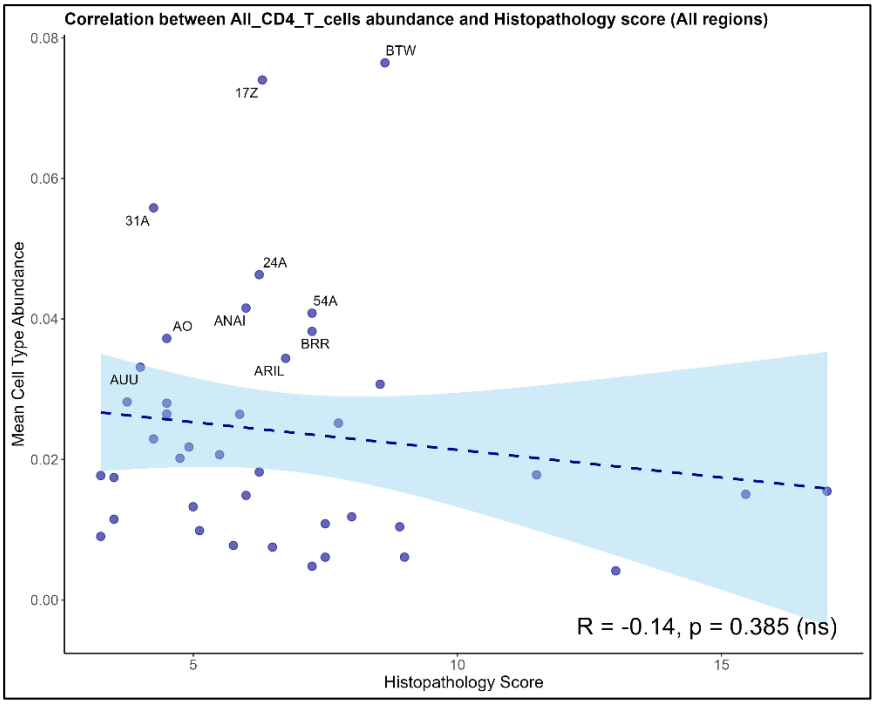
Correlation between All_CD4_T_cells abundance and Histopathology score (All regions)
Mean Cell Type Abundance
Histopathology Score
0.08
0.06
0.04
0.02
0.00
5
10
15
BTW
17Z
31A
24A
54A
ANAI
AO
BRR
ARIL
AUU
R = -0.14, p = 0.385 (ns)

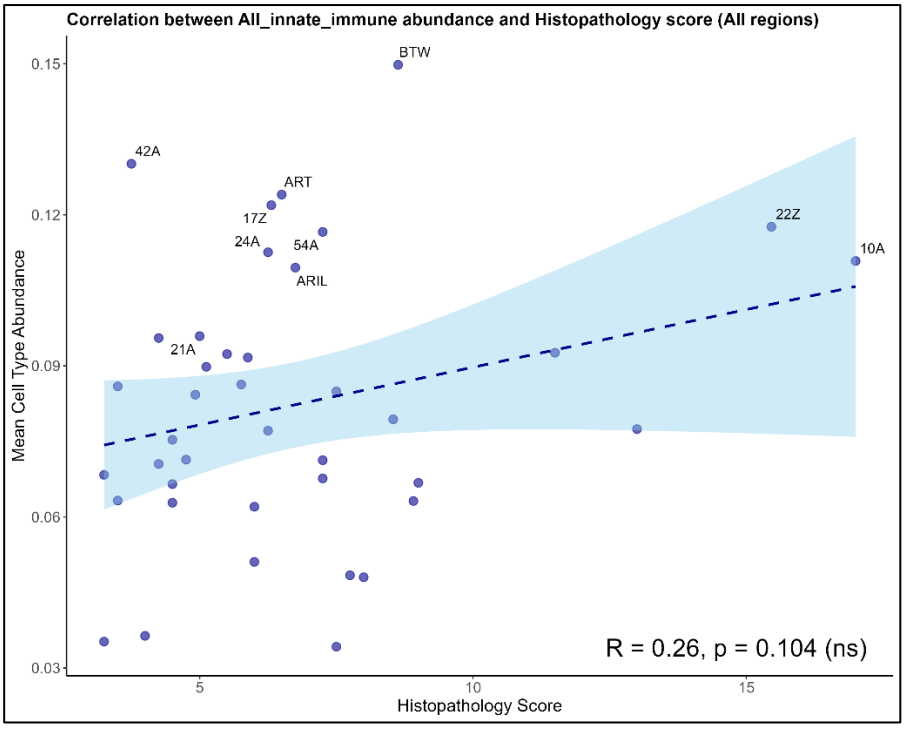
Correlation between All_innate_immune abundance and Histopathology score (All regions)
Mean Cell Type Abundance
Histopathology Score
0.15
0.12
0.09
0.06
0.03
5
10
15
BTW
42A
ART
17Z
24A
54A
ARIL
22Z
10A
21A
R = 0.26, p = 0.104 (ns)

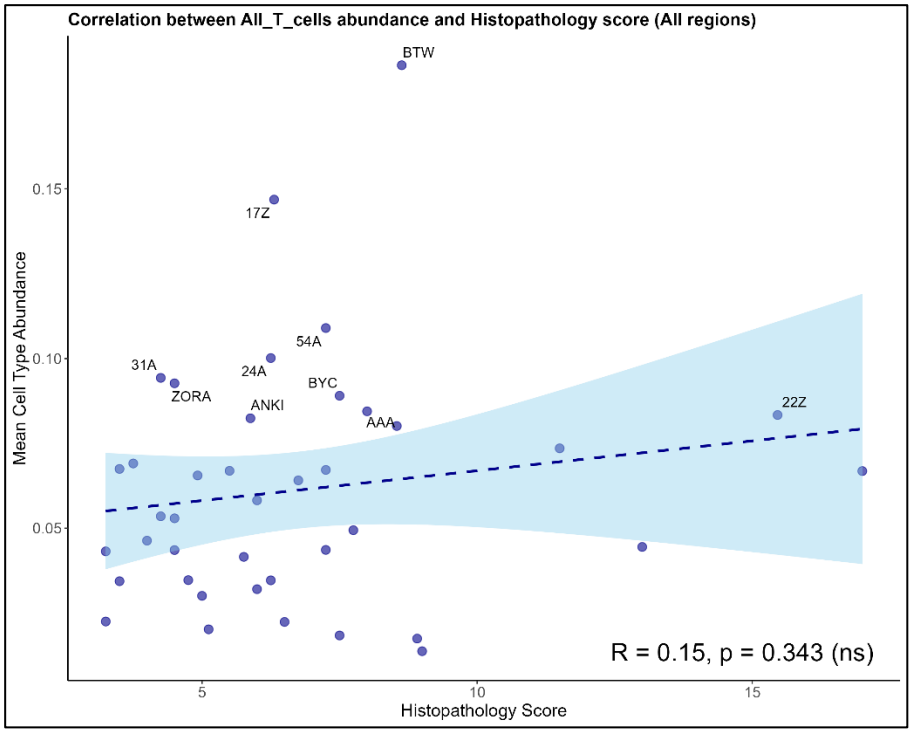
Correlation between All_T_cells abundance and Histopathology score (All regions)
Mean Cell Type Abundance
Histopathology Score
0.15
0.10
0.05
5
10
15
BTW
17Z
54A
31A
24A
BYC
ZORA
ANKI
AAA
22Z
R = 0.15, p = 0.343 (ns)

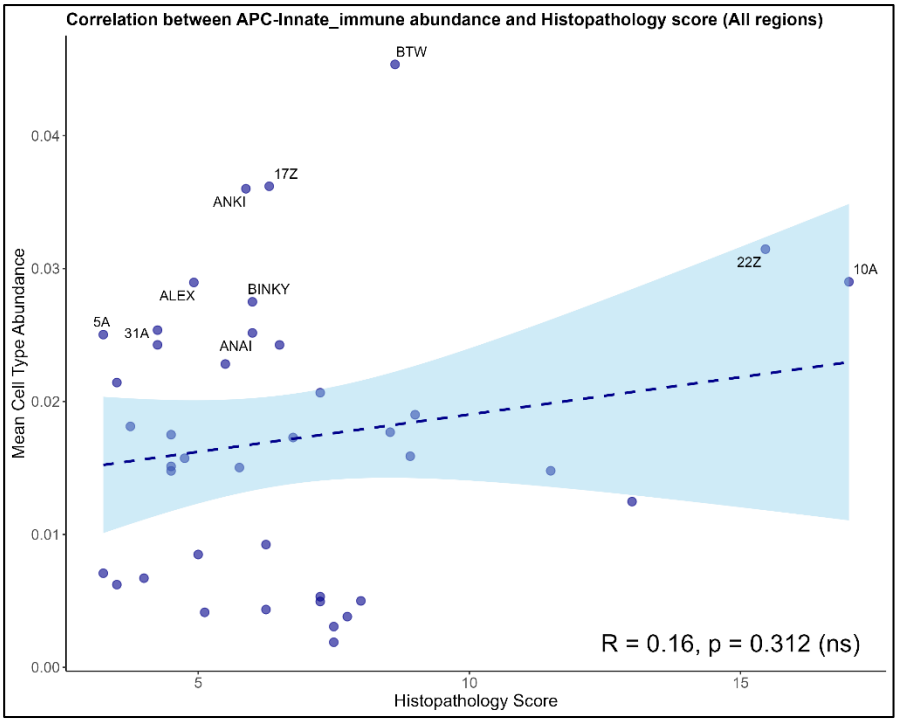
Correlation between APC-Innate_immune abundance and Histopathology score (All regions)
Mean Cell Type Abundance
Histopathology Score
0.00
0.01
0.02
0.03
0.04
5
10
15
BTW
17Z
ANKI
22Z
10A
ALEX
BINKY
5A
31A
ANAI
R = 0.16, p = 0.312 (ns)

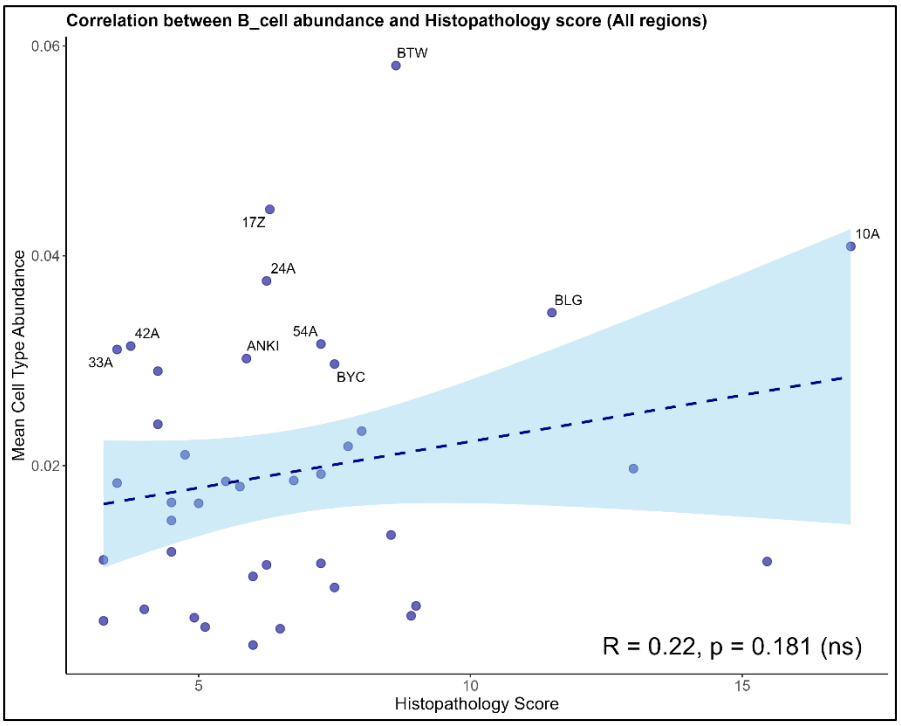
Correlation between B_cell abundance and Histopathology score (All regions)
Mean Cell Type Abundance
Histopathology Score
0.02
0.04
0.06
5
10
15
BTW
17Z
10A
24A
BLG
42A
54A
33A
ANKI
BYC
R = 0.22, p = 0.181 (ns)

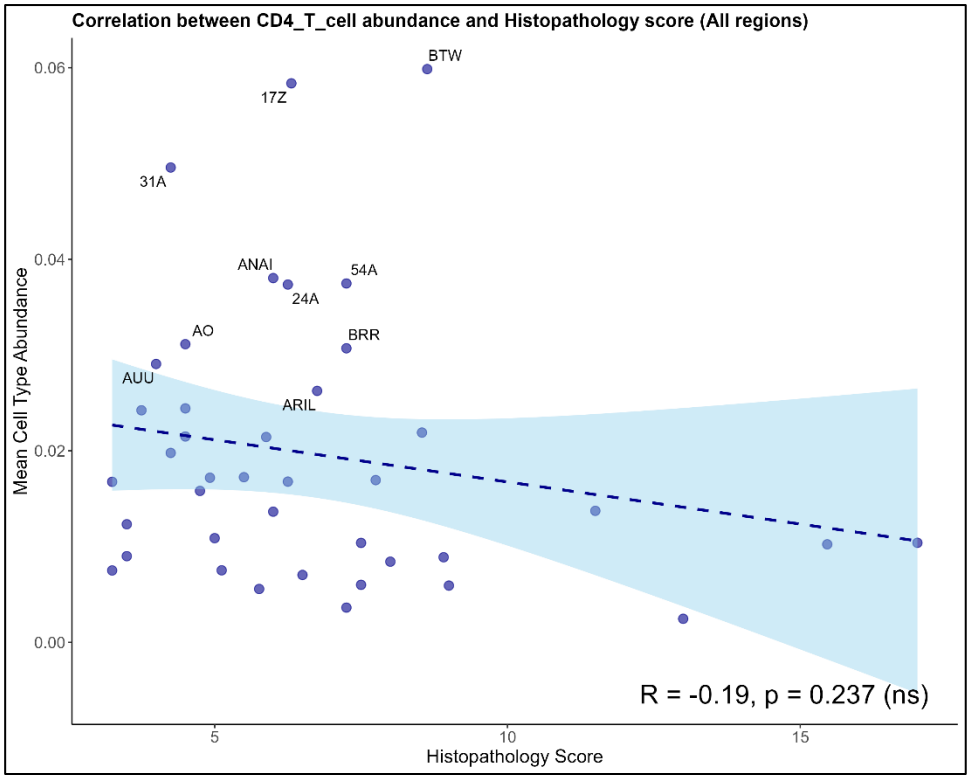
Correlation between CD4_T_cell abundance and Histopathology score (All regions)
Mean Cell Type Abundance
Histopathology Score
0.06
0.04
0.02
0.00
5
10
15
BTW
17Z
31A
ANAI
54A
24A
AO
BRR
AUU
ARIL
R = -0.19, p = 0.237 (ns)

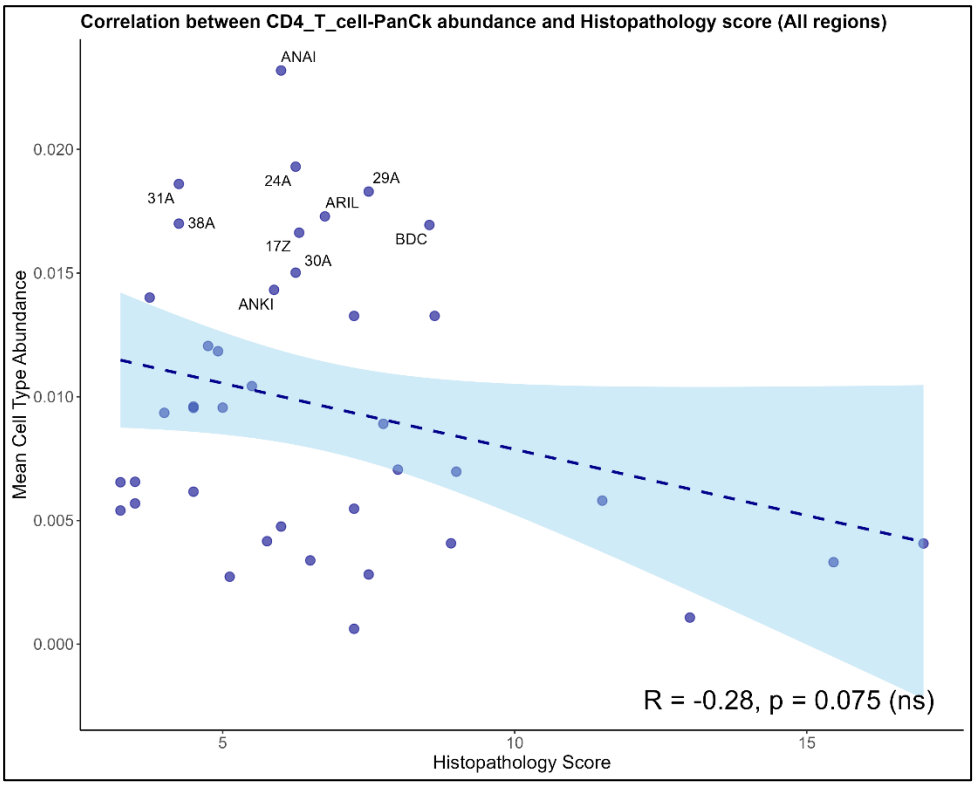
Correlation between CD4_T_cell-PanCk abundance and Histopathology score (All regions)
Mean Cell Type Abundance
Histopathology Score
0.020
0.015
0.010
0.005
0.000
5
10
15
ANAI
24A
29A
31A
ARIL
38A
BDC
17Z
30A
ANKI
R = -0.28, p = 0.075 (ns)

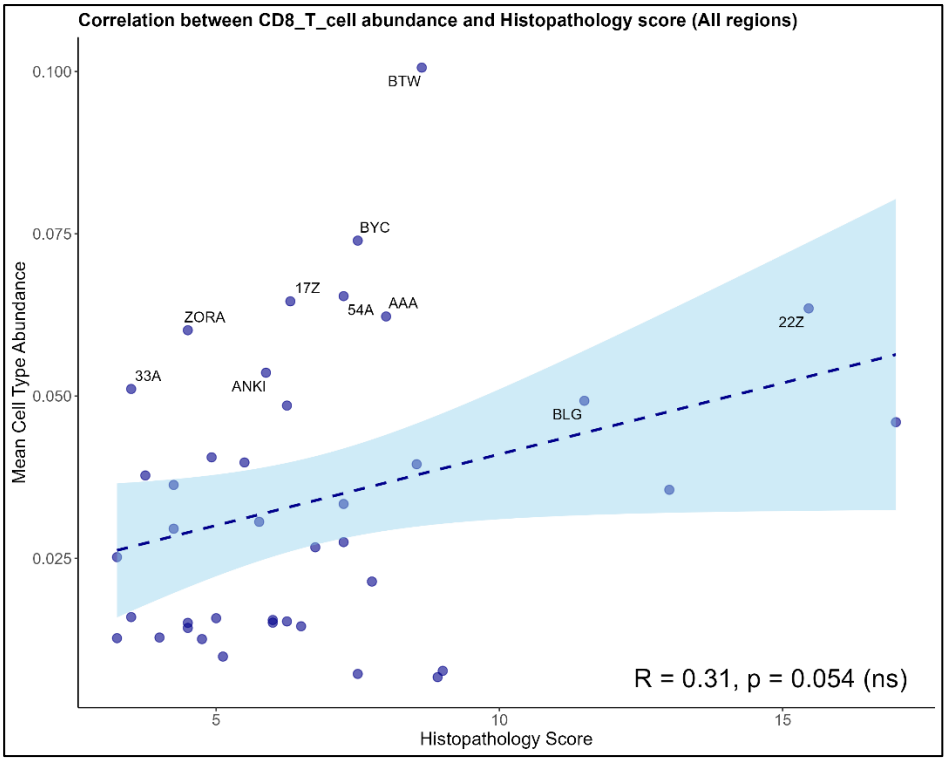
Correlation between CD8_T_cell abundance and Histopathology score (All regions)
Mean Cell Type Abundance
0.100
0.075
0.050
0.025
BTW
BYC
17Z
54A
AAA
ZORA
22Z
33A
ANKI
BLG
R = 0.31, p = 0.054 (ns)
5
10
15
Histopathology Score

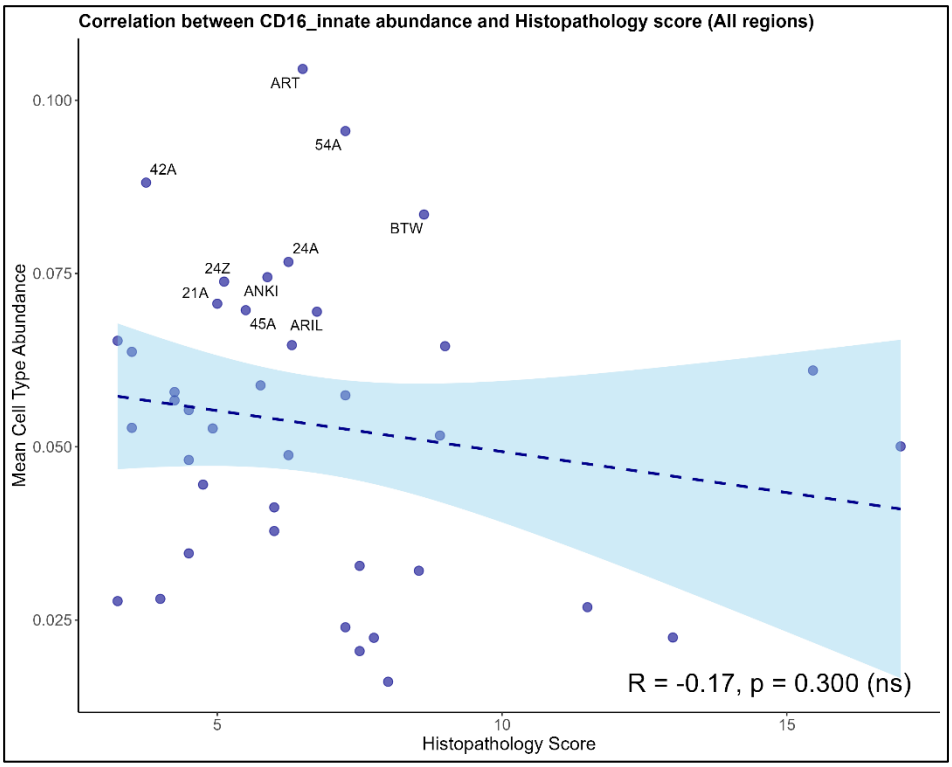
Correlation between CD16_innate abundance and Histopathology score (All regions)
Mean Cell Type Abundance
0.100
0.075
0.050
0.025
ART
54A
42A
BTW
24A
24Z
21A
ANKI
45A
ARIL
R = -0.17, p = 0.300 (ns)
5
10
15
Histopathology Score

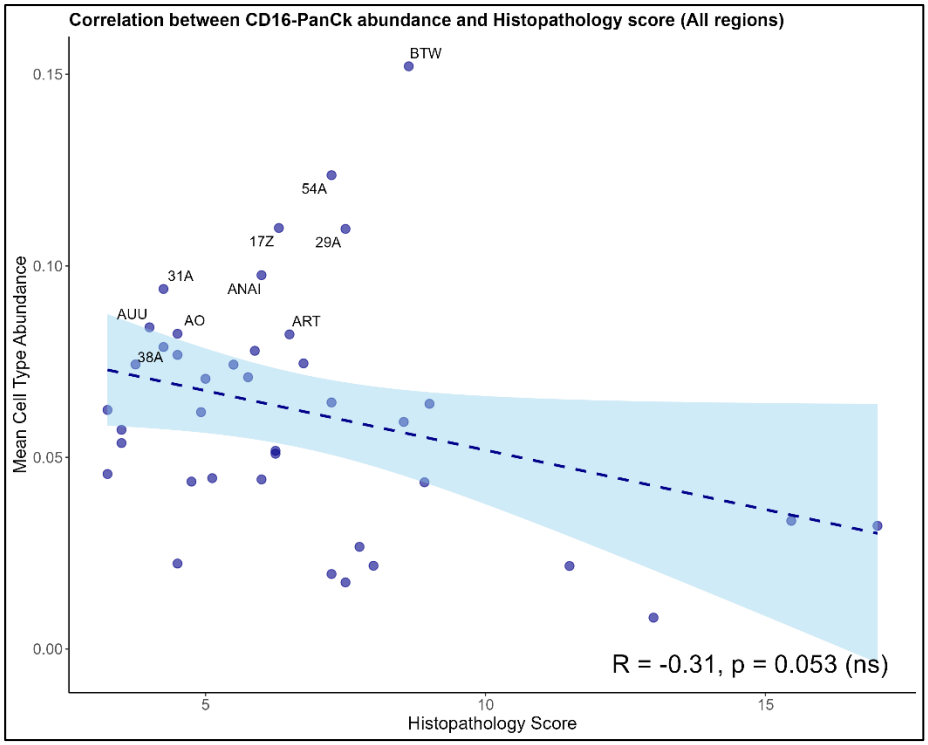
Correlation between CD16-PanCk abundance and Histopathology score (All regions)
Mean Cell Type Abundance
Histopathology Score
BTW
54A
17Z
29A
31A
ANAI
AUU
AO
ART
38A
R = -0.31, p = 0.053 (ns)

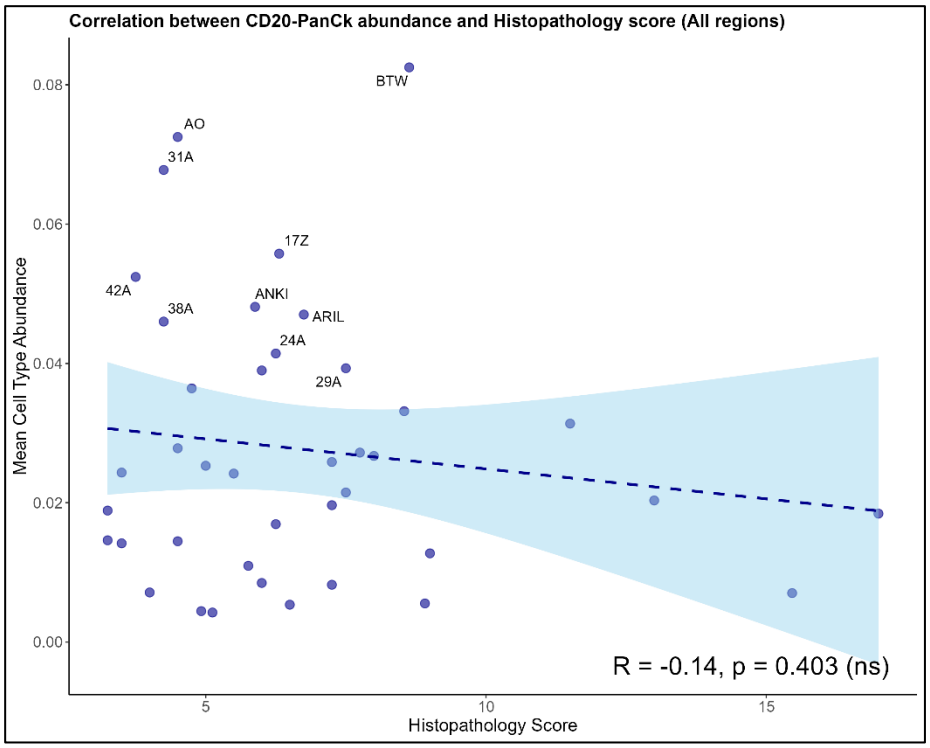
Correlation between CD20-PanCk abundance and Histopathology score (All regions)
Mean Cell Type Abundance
Histopathology Score
BTW
AO
31A
17Z
42A
ANKI
38A
ARIL
24A
29A
R = -0.14, p = 0.403 (ns)

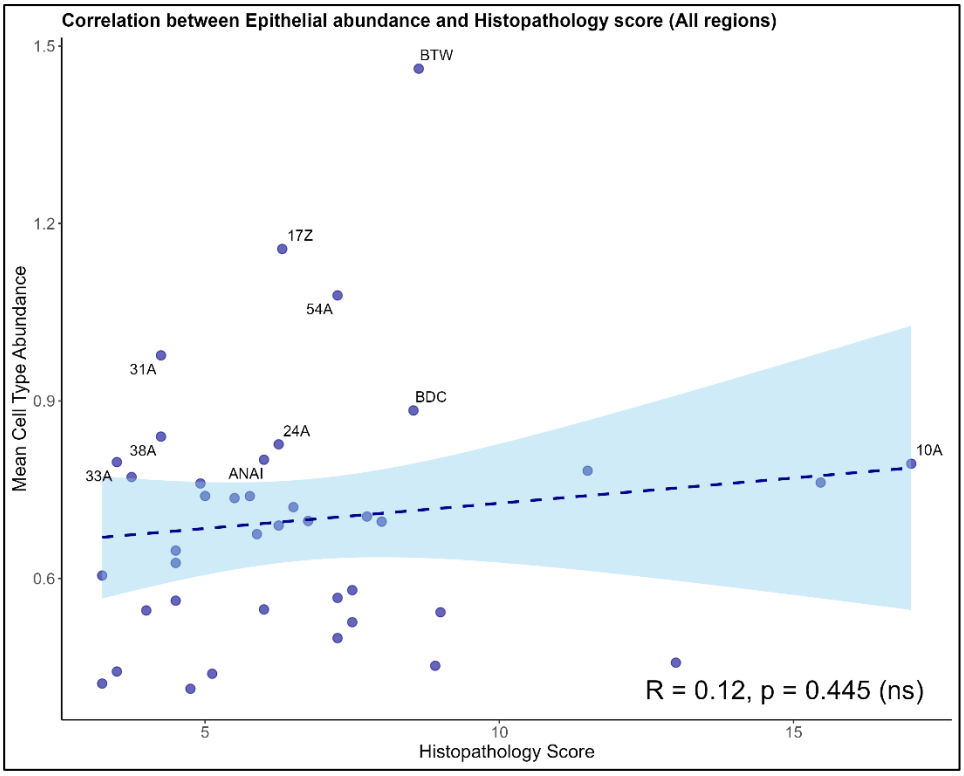
Correlation between Epithelial abundance and Histopathology score (All regions)
Mean Cell Type Abundance
Histopathology Score
BTW
17Z
54A
31A
BDC
24A
38A
33A
ANAI
10A
R = 0.12, p = 0.445 (ns)

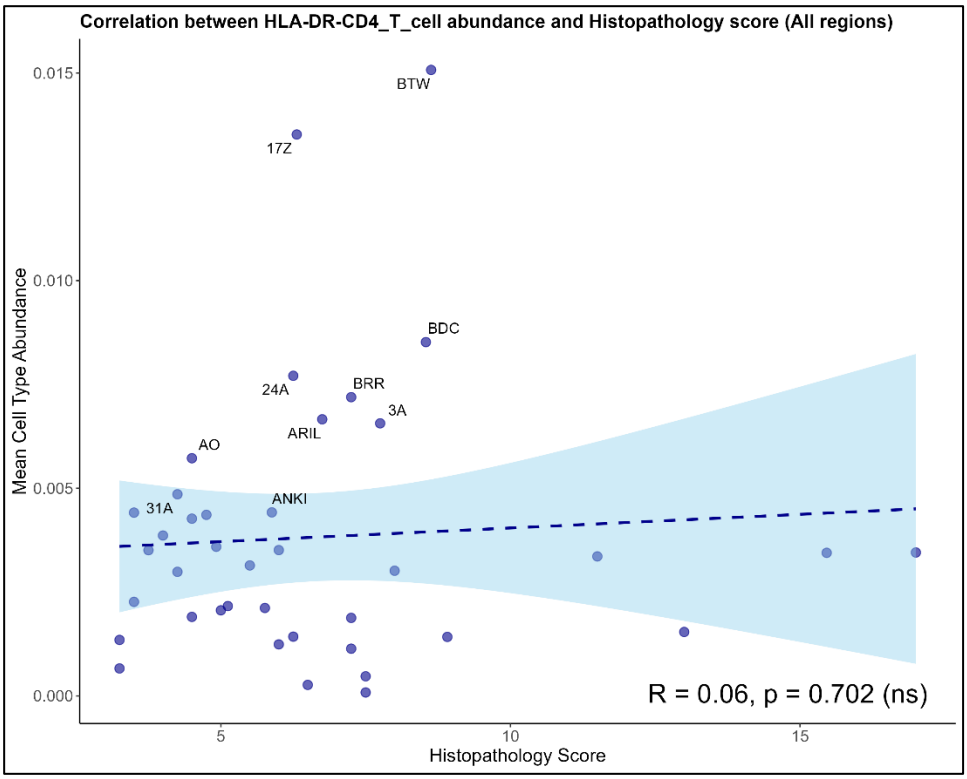
Correlation between HLA-DR-CD4_T_cell abundance and Histopathology score (All regions)
Mean Cell Type Abundance
Histopathology Score
BTW
17Z
BDC
24A
BRR
3A
ARIL
AO
ANKI
31A
R = 0.06, p = 0.702 (ns)

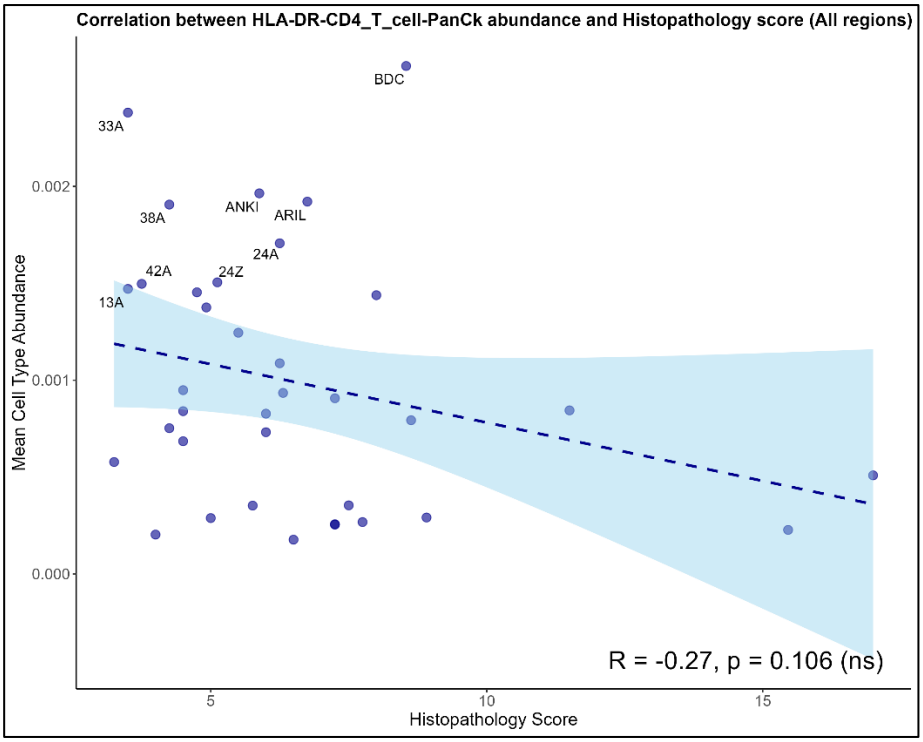
Correlation between HLA-DR-CD4_T_cell-PanCk abundance and Histopathology score (All regions)
BDC
33A
ANKI
ARIL
38A
24A
42A
24Z
13A
0.002
0.001
0.000
Mean Cell Type Abundance
R = -0.27, p = 0.106 (ns)
5
10
15
Histopathology Score

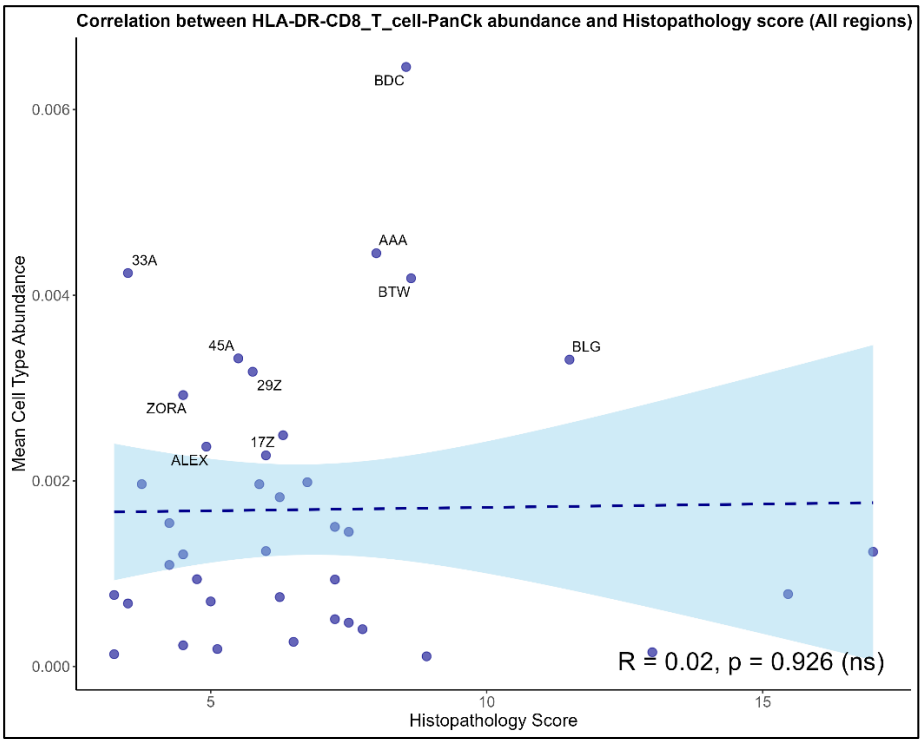
Correlation between HLA-DR-CD8_T_cell-PanCk abundance and Histopathology score (All regions)
BDC
0.006
AAA
33A
BTW
0.004
45A
BLG
29Z
ZORA
17Z
ALEX
0.002
0.000
Mean Cell Type Abundance
R = 0.02, p = 0.926 (ns)
5
10
15
Histopathology Score

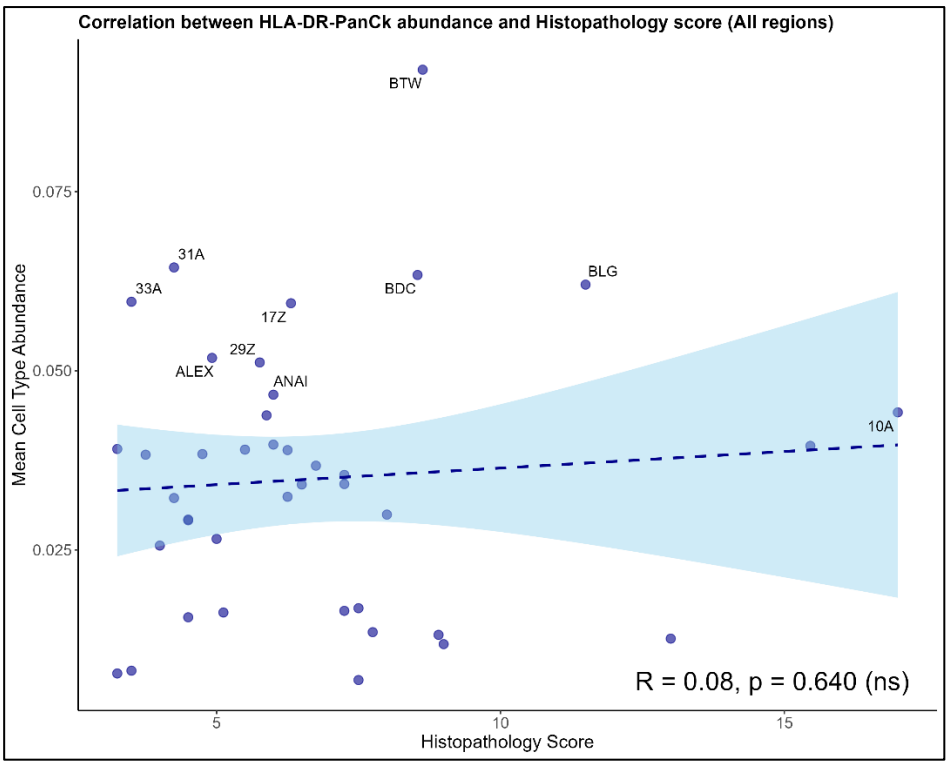
Correlation between HLA-DR-PanCk abundance and Histopathology score (All regions)
Mean Cell Type Abundance
Histopathology Score
0.075
0.050
0.025
5
10
15
BTW
31A
33A
BDC
BLG
17Z
29Z
ALEX
ANAI
10A
R = 0.08, p = 0.640 (ns)

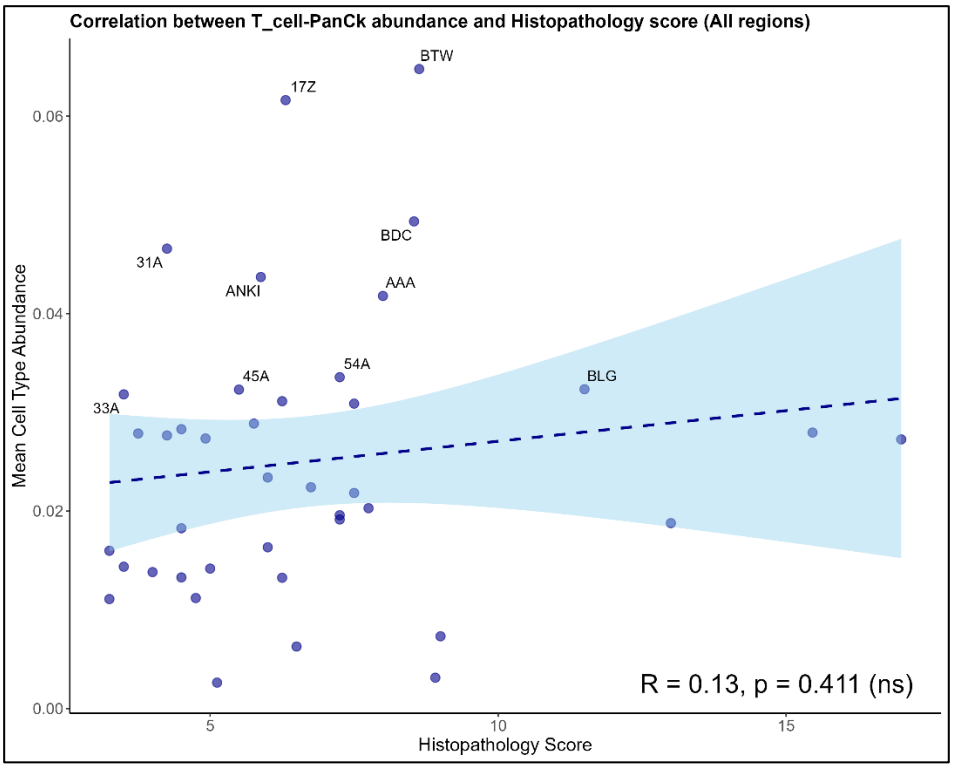
Correlation between T_cell-PanCk abundance and Histopathology score (All regions)
Mean Cell Type Abundance
Histopathology Score
0.06
0.04
0.02
0.00
5
10
15
BTW
17Z
BDC
31A
ANKI
AAA
45A
54A
BLG
33A
R = 0.13, p = 0.411 (ns)

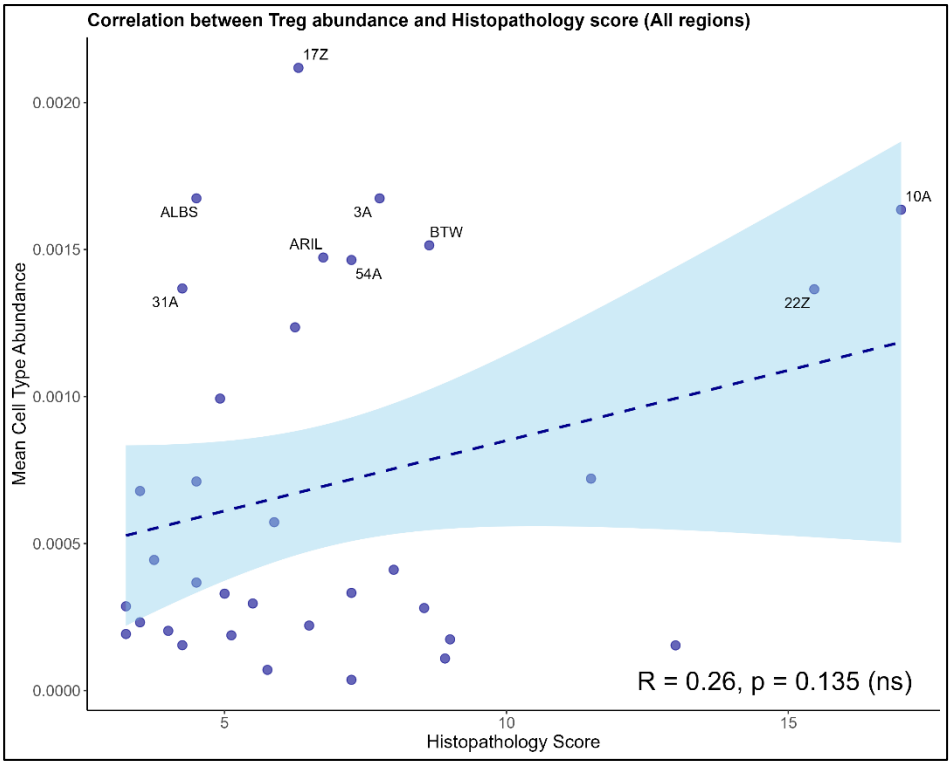
Correlation between Treg abundance and Histopathology score (All regions)
Mean Cell Type Abundance
Histopathology Score
0.0020
0.0015
0.0010
0.0005
0.0000
5
10
15
17Z
ALBS
3A
BTW
ARIL
54A
31A
10A
22Z
R = 0.26, p = 0.135 (ns)

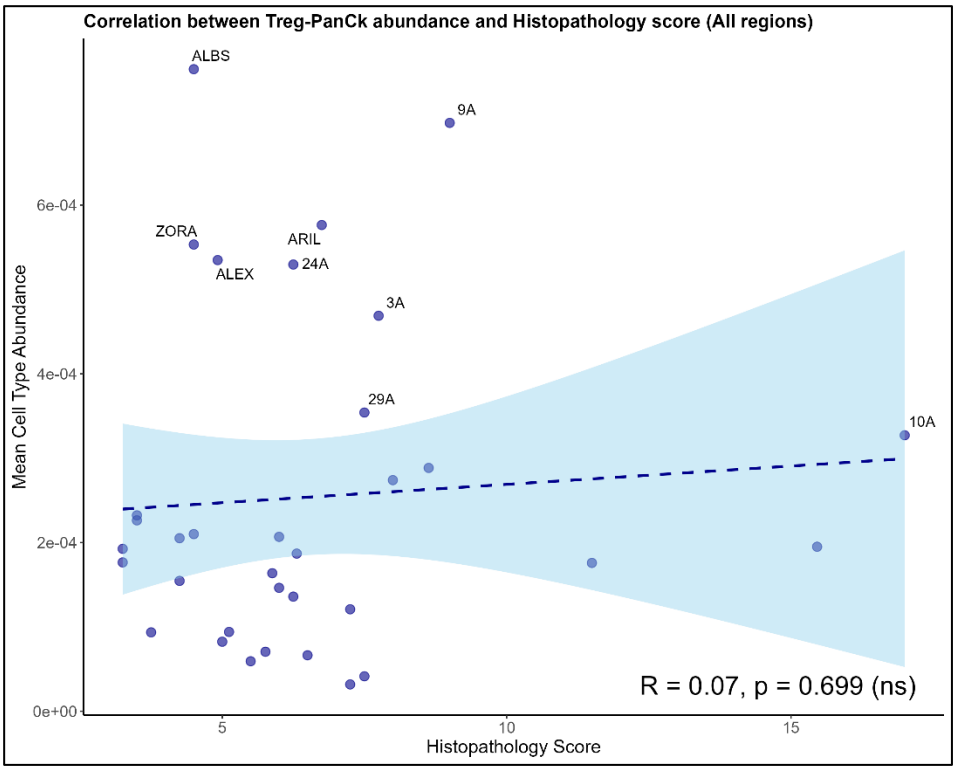
Correlation between Treg-PanCk abundance and Histopathology score (All regions)
Mean Cell Type Abundance
Histopathology Score
6e-04
4e-04
2e-04
0e+00
5
10
15
ALBS
9A
ZORA
ARIL
24A
ALEX
3A
29A
10A
R = 0.07, p = 0.699 (ns)

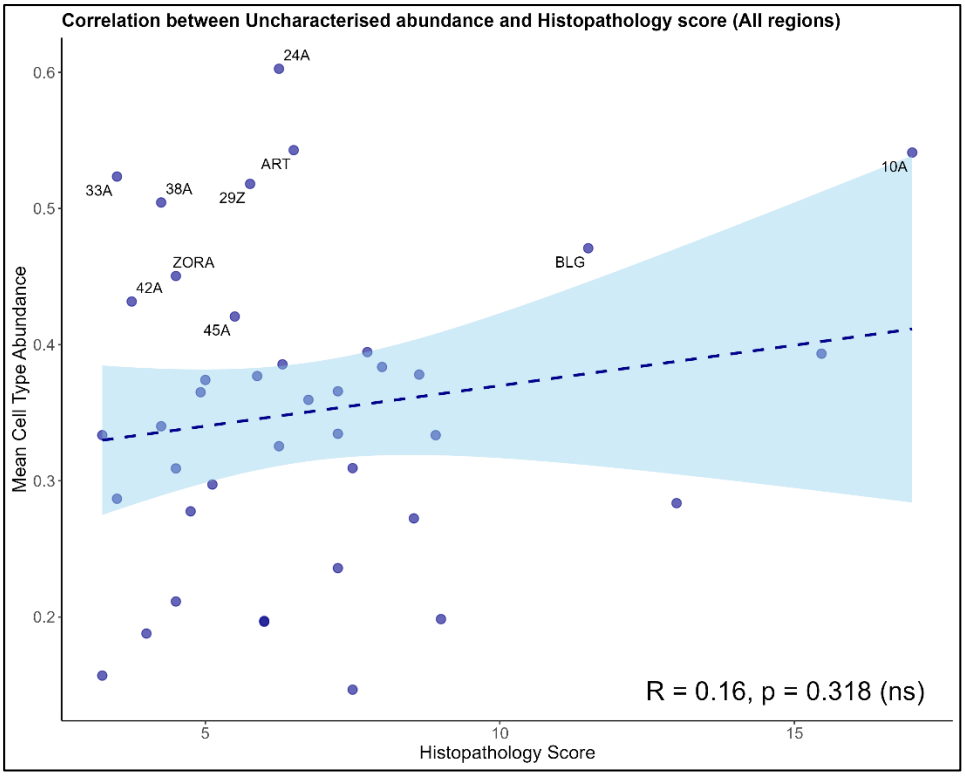

Supplementary Figure 3: All non-significant correlations between cell type abundances and histopathology scores (as described in Section 2.4) across all region types. The dark blue dashed line is the regression line of the correlation between the cell type abundance and histopathology score, while the light blue colour represents the range of the associated confidence interval. Individual samples are overlaid as blue dots, with samples in the upper quartile of cell type abundance annotated according to NHP ID. The R value is Pearson's correlation coefficient and the p value is calculated using Pearson's correlation test. The cell type abundance in question is shown in each individual plot title.

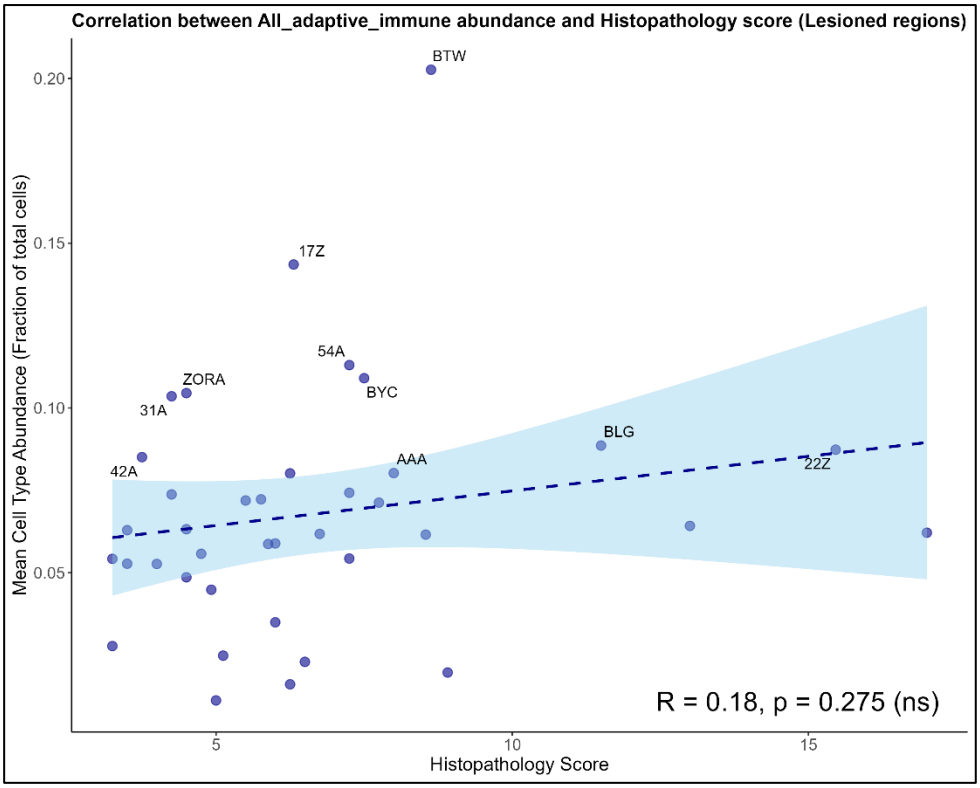
Correlation between All_adaptive_immune abundance and Histopathology score (Lesioned regions)
Mean Cell Type Abundance (Fraction of total cells)
Histopathology Score
0.20
0.15
0.10
0.05
5
10
15
BTW
17Z
54A
ZORA
BYC
31A
BLG
AAA
42A
22Z
R = 0.18, p = 0.275 (ns)

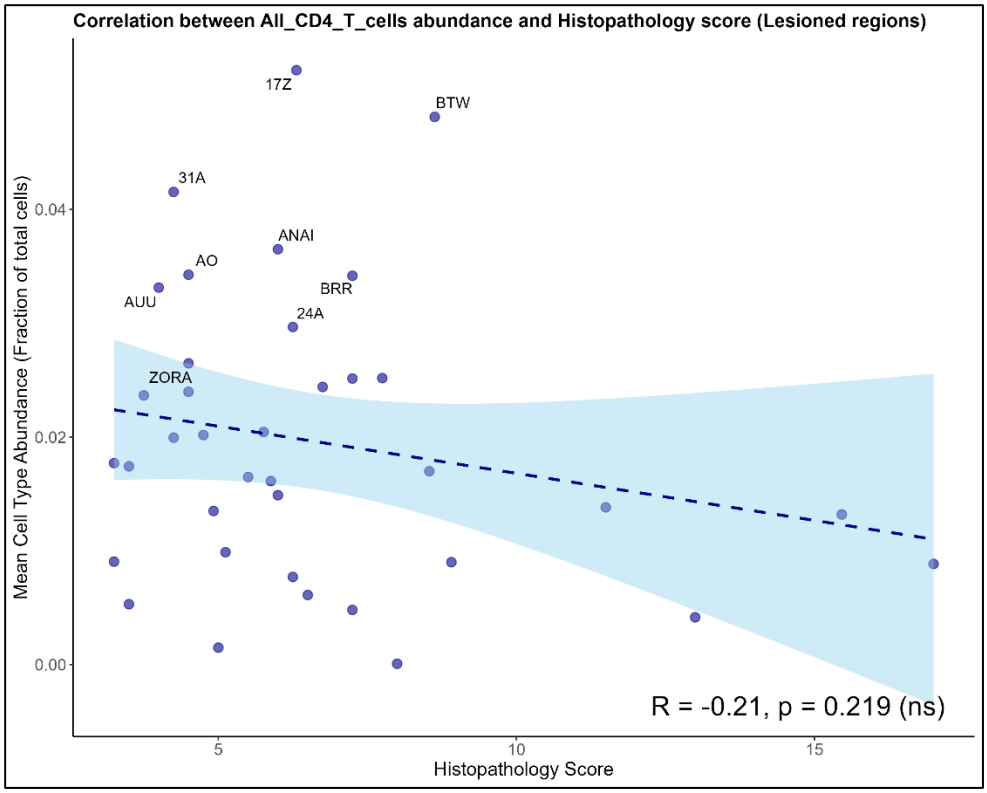
Correlation between All_CD4_T_cells abundance and Histopathology score (Lesioned regions)
Mean Cell Type Abundance (Fraction of total cells)
Histopathology Score
0.04
0.02
0.00
5
10
15
17Z
BTW
31A
ANAI
AO
BRR
AUU
24A
ZORA
R = -0.21, p = 0.219 (ns)

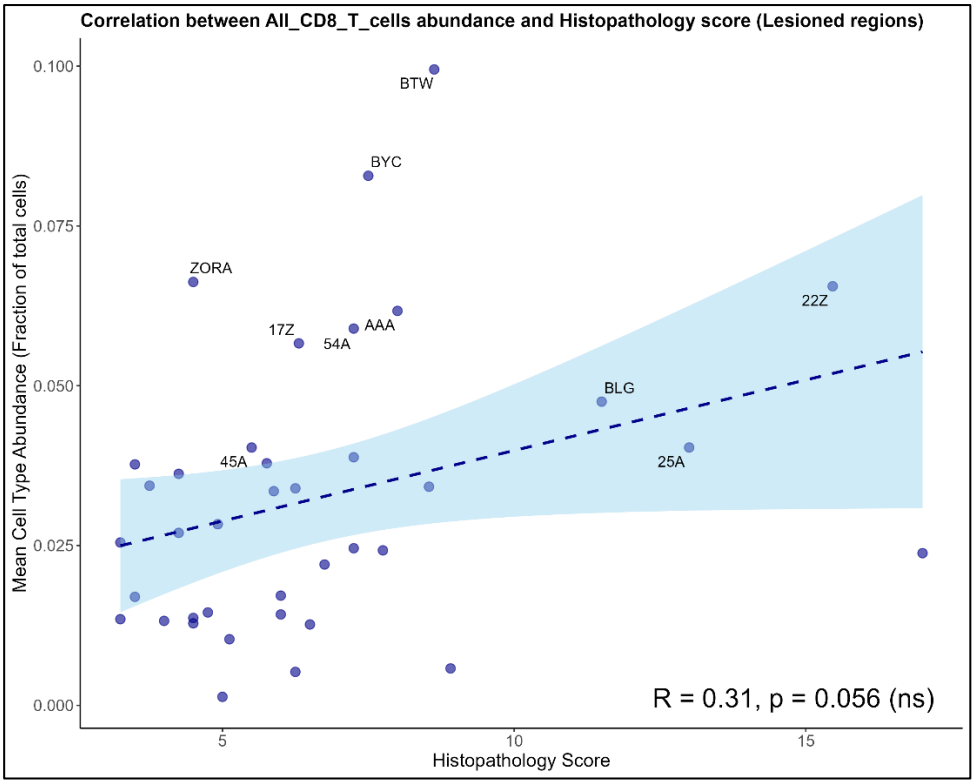
Correlation between All_CD8_T_cells abundance and Histopathology score (Lesioned regions)
Mean Cell Type Abundance (Fraction of total cells)
0.100
0.075
0.050
0.025
0.000
BTW
BYC
ZORA
17Z
AAA
54A
22Z
BLG
45A
25A
R = 0.31, p = 0.056 (ns)
5
10
15
Histopathology Score

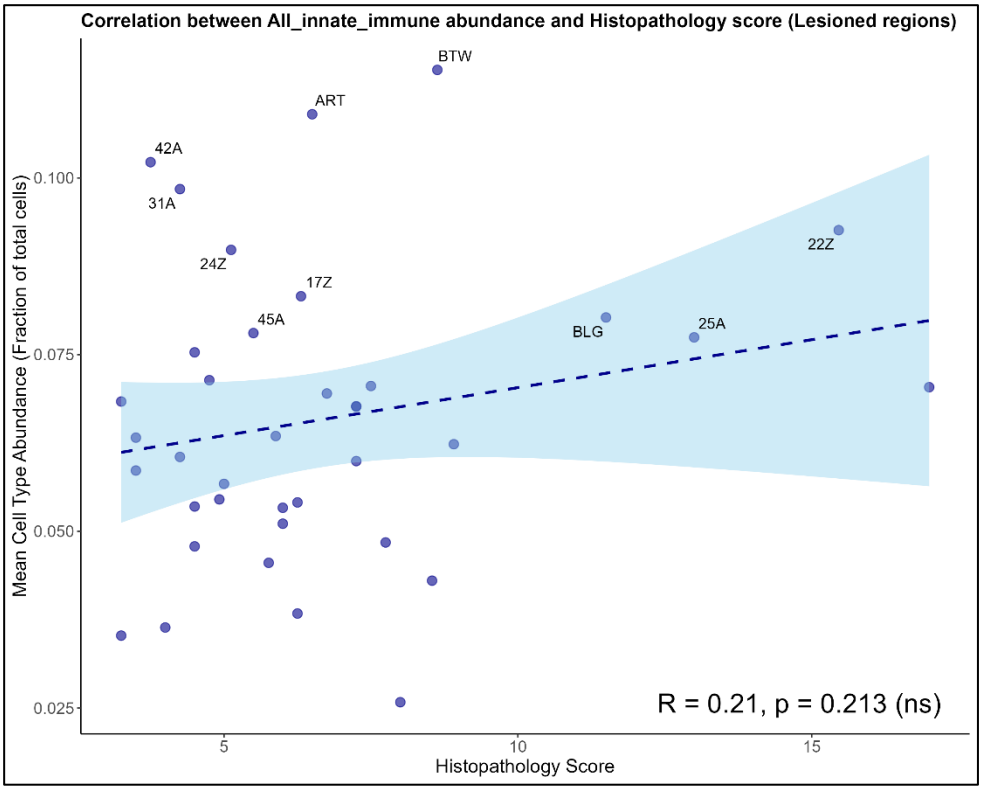
Correlation between All_innate_immune abundance and Histopathology score (Lesioned regions)
Mean Cell Type Abundance (Fraction of total cells)
0.100
0.075
0.050
0.025
BTW
ART
42A
31A
24Z
17Z
45A
22Z
BLG
25A
R = 0.21, p = 0.213 (ns)
5
10
15
Histopathology Score

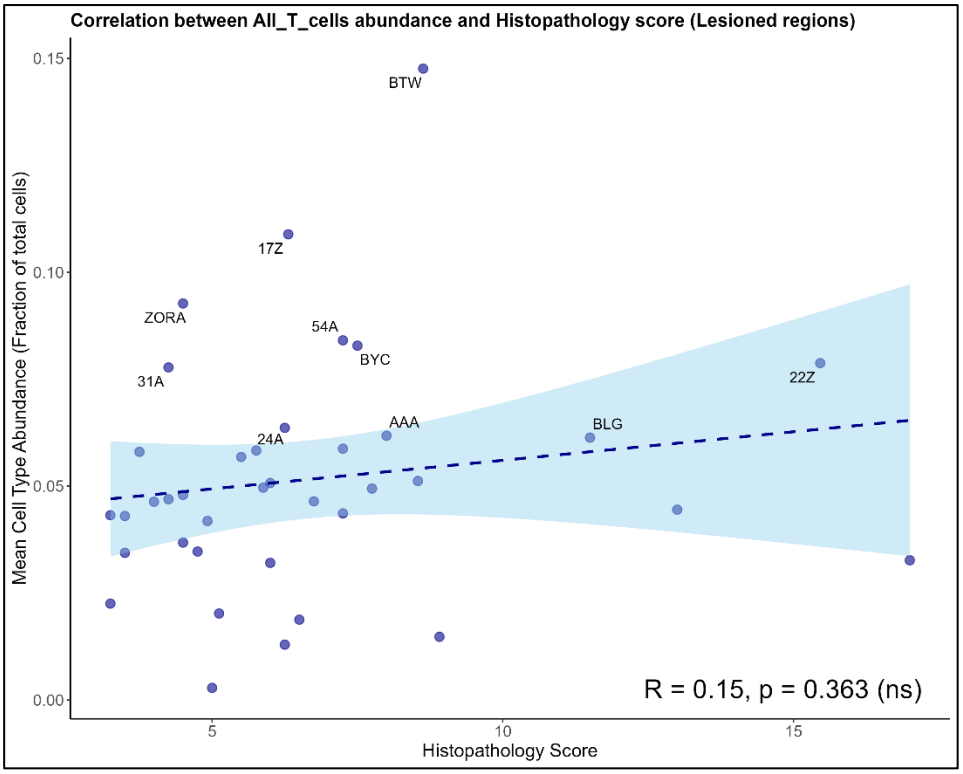
Correlation between All_T_cells abundance and Histopathology score (Lesioned regions)
Mean Cell Type Abundance (Fraction of total cells)
Histopathology Score
0.15
0.10
0.05
0.00
5
10
15
BTW
17Z
ZORA
54A
BYC
31A
22Z
AAA
BLG
24A
R = 0.15, p = 0.363 (ns)

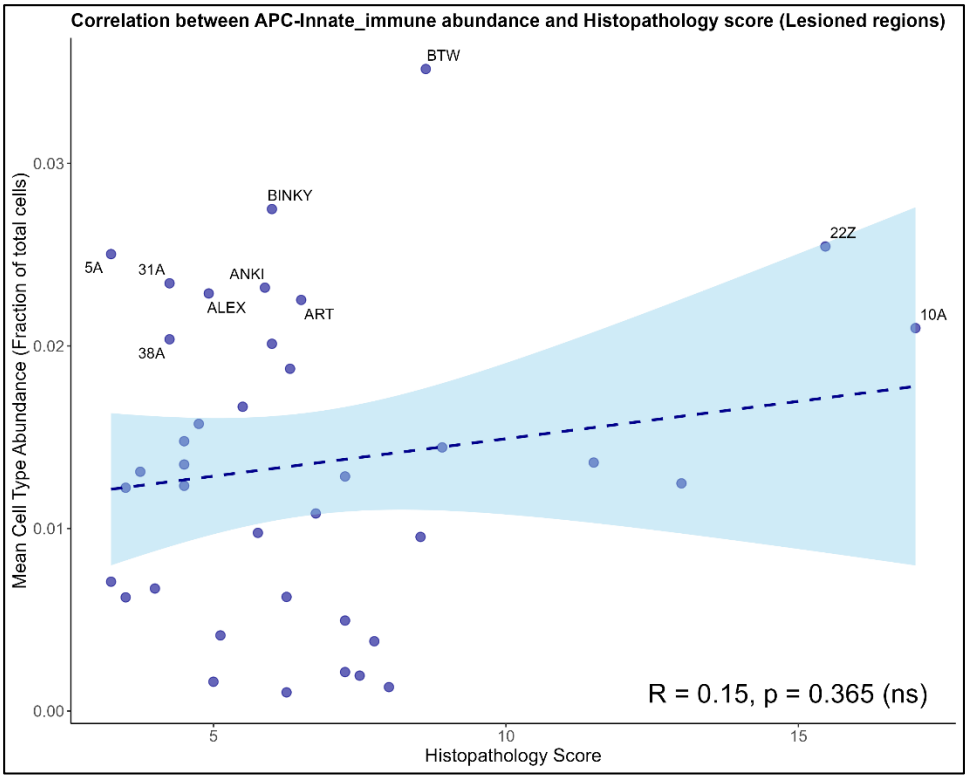
Correlation between APC-Innate_immune abundance and Histopathology score (Lesioned regions)
Mean Cell Type Abundance (Fraction of total cells)
Histopathology Score
0.03
0.02
0.01
0.00
5
10
15
BTW
BINKY
22Z
5A
31A
ANKI
ALEX
ART
10A
38A
R = 0.15, p = 0.365 (ns)

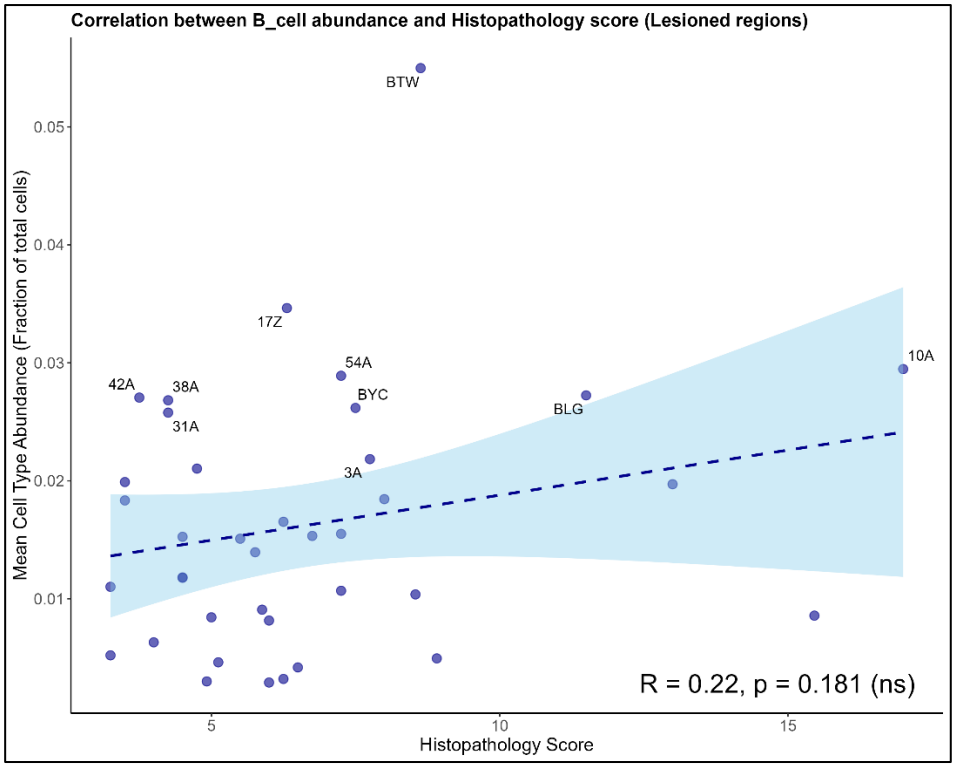
Correlation between B_cell abundance and Histopathology score (Lesioned regions)
Mean Cell Type Abundance (Fraction of total cells)
Histopathology Score
BTW
17Z
54A
10A
42A
38A
BYC
BLG
31A
3A
R = 0.22, p = 0.181 (ns)

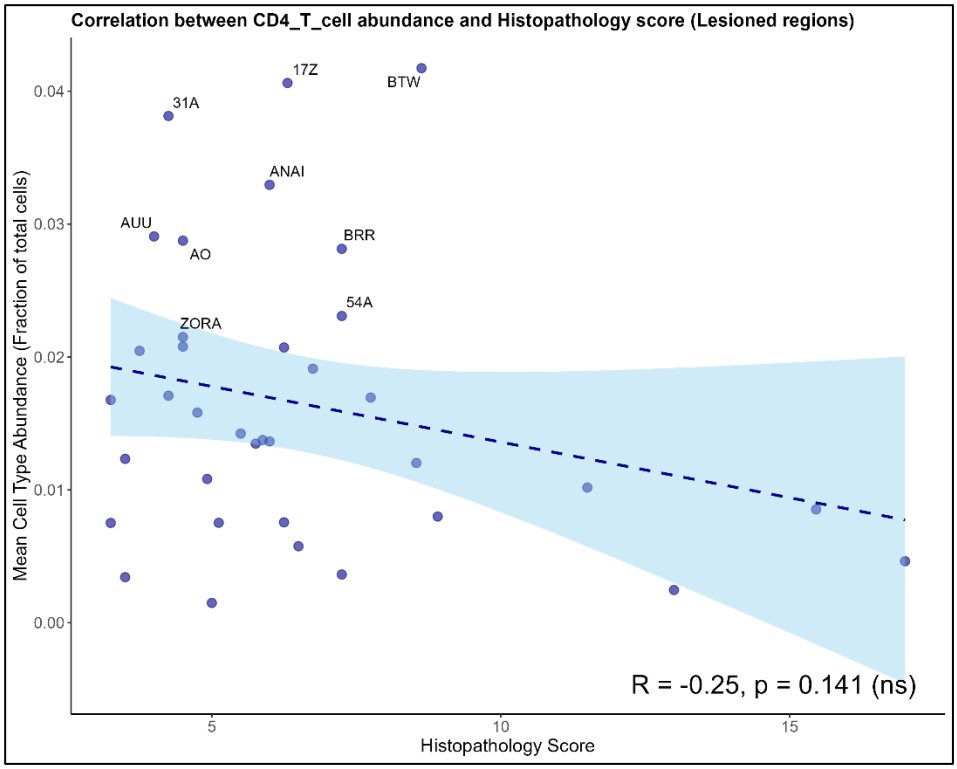
Correlation between CD4_T_cell abundance and Histopathology score (Lesioned regions)
Mean Cell Type Abundance (Fraction of total cells)
Histopathology Score
17Z
BTW
31A
ANAI
AUU
BRR
AO
54A
ZORA
R = -0.25, p = 0.141 (ns)

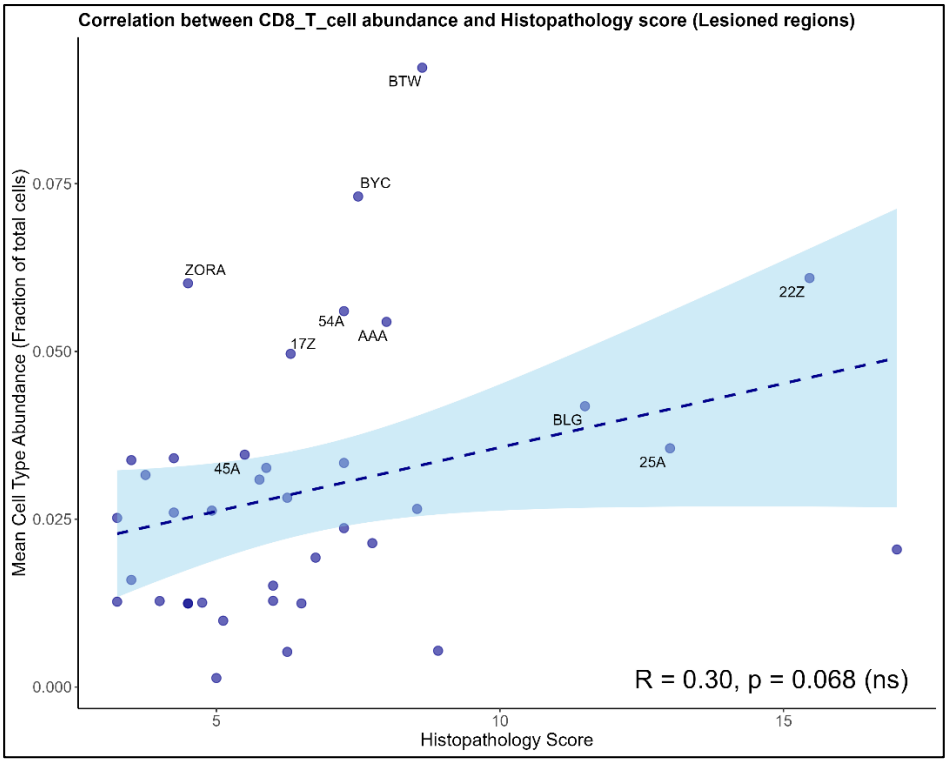
Correlation between CD8_T_cell abundance and Histopathology score (Lesioned regions)
Mean Cell Type Abundance (Fraction of total cells)
Histopathology Score
0.000
0.025
0.050
0.075
5
10
15
BTW
BYC
ZORA
22Z
54A
AAA
17Z
BLG
25A
45A
R = 0.30, p = 0.068 (ns)

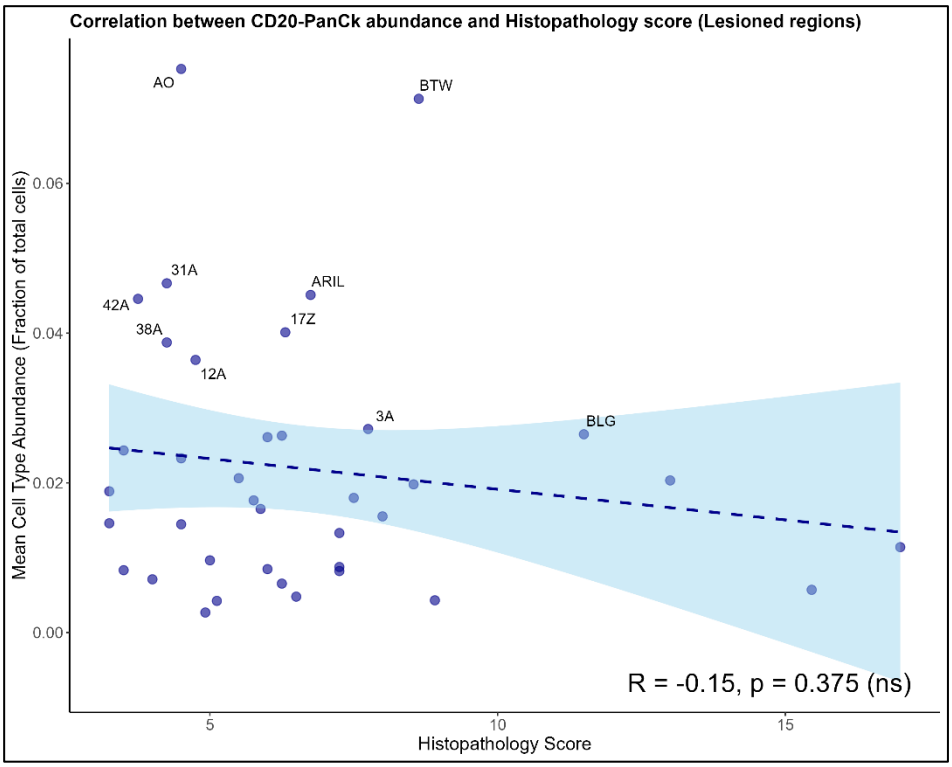
Correlation between CD20-PanCk abundance and Histopathology score (Lesioned regions)
Mean Cell Type Abundance (Fraction of total cells)
Histopathology Score
0.00
0.02
0.04
0.06
5
10
15
AO
BTW
31A
ARIL
42A
17Z
38A
12A
3A
BLG
R = -0.15, p = 0.375 (ns)

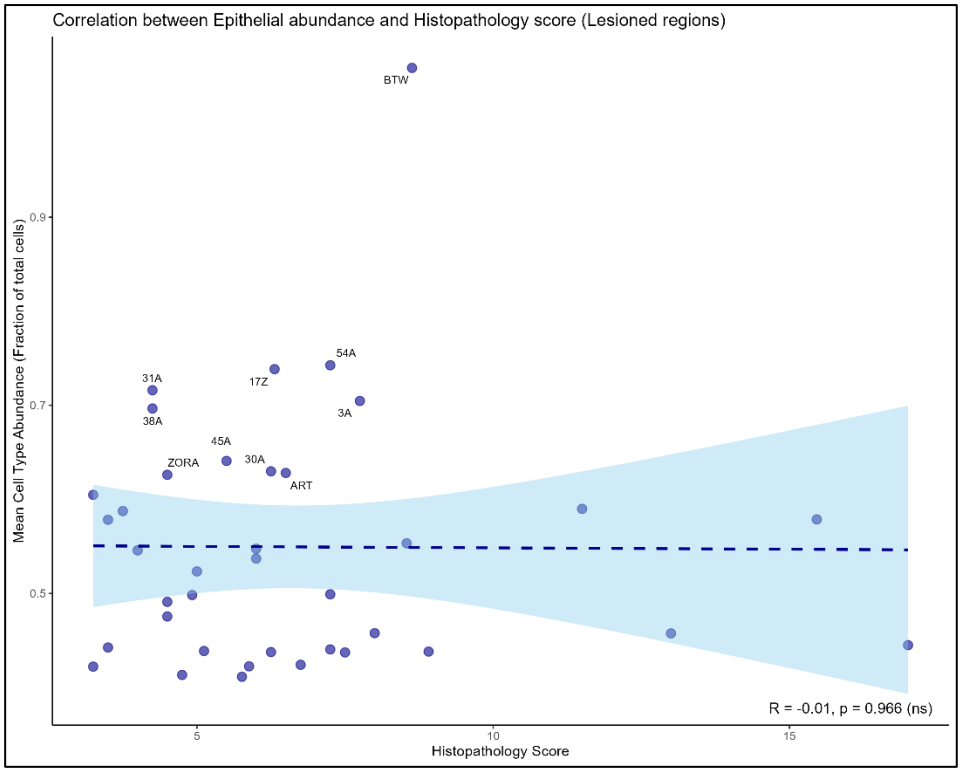
Correlation between Epithelial abundance and Histopathology score (Lesioned regions)
Mean Cell Type Abundance (Fraction of total cells)
Histopathology Score
BTW
54A
31A
17Z
3A
38A
45A
ZORA
30A
ART
0.9
0.7
0.5
5
10
15
R = -0.01, p = 0.966 (ns)

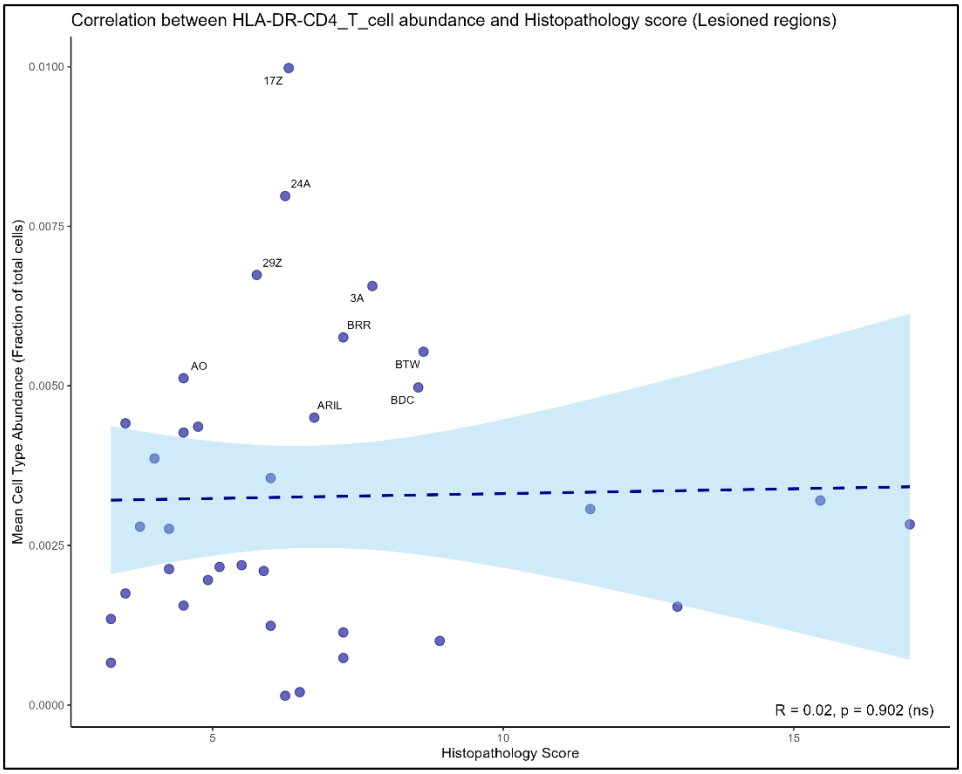
Correlation between HLA-DR-CD4_T_cell abundance and Histopathology score (Lesioned regions)
Mean Cell Type Abundance (Fraction of total cells)
Histopathology Score
17Z
24A
29Z
3A
BRR
BTW
AO
BDC
ARIL
0.0100
0.0075
0.0050
0.0025
0.0000
5
10
15
R = 0.02, p = 0.902 (ns)

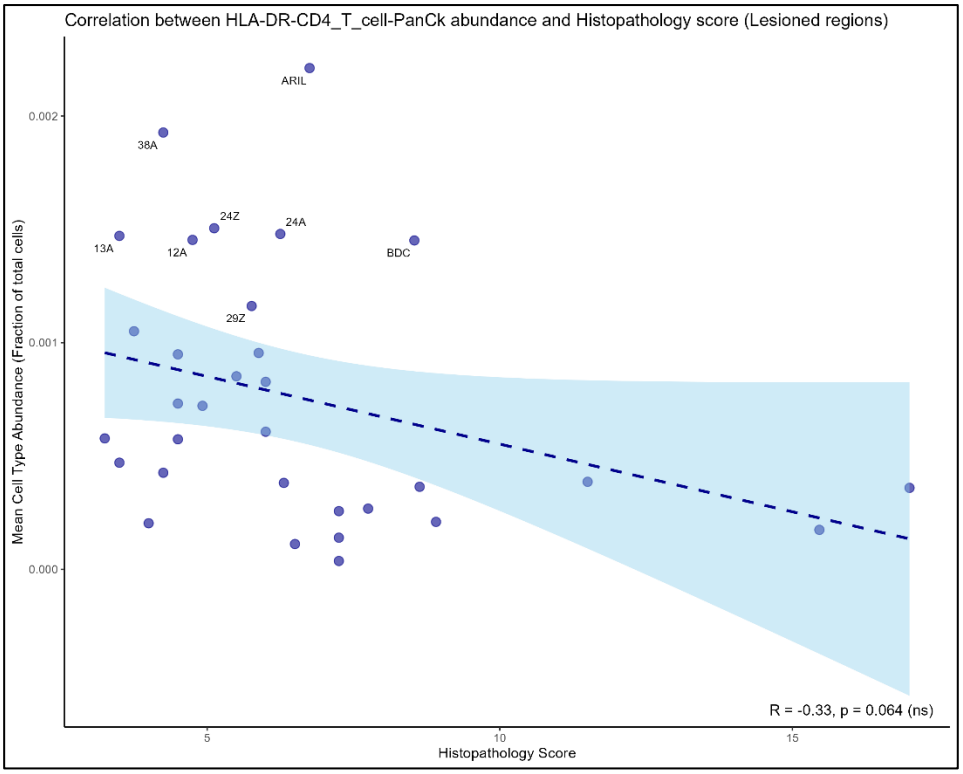
Correlation between HLA-DR-CD4_T_cell-PanCk abundance and Histopathology score (Lesioned regions)
Mean Cell Type Abundance (Fraction of total cells)
0.002
0.001
0.000
ARIL
38A
24Z
24A
13A
12A
BDC
29Z
R = -0.33, p = 0.064 (ns)
5
10
15
Histopathology Score

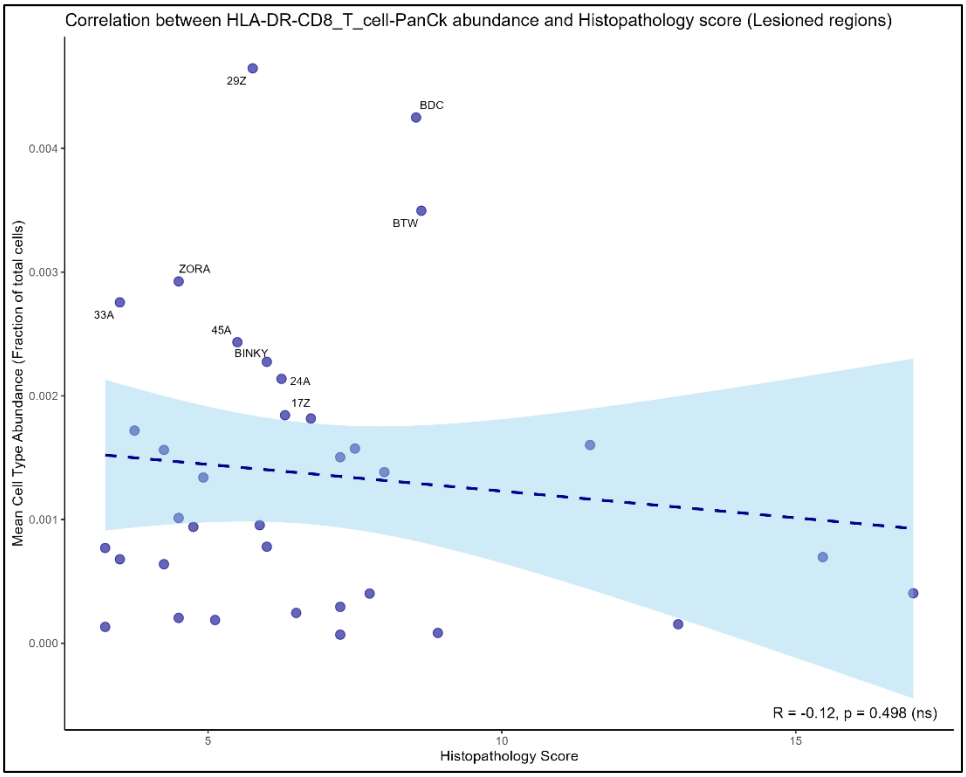
Correlation between HLA-DR-CD8_T_cell-PanCk abundance and Histopathology score (Lesioned regions)
Mean Cell Type Abundance (Fraction of total cells)
0.004
0.003
0.002
0.001
0.000
29Z
BDC
BTW
ZORA
33A
45A
BINKY
24A
17Z
R = -0.12, p = 0.498 (ns)
5
10
15
Histopathology Score

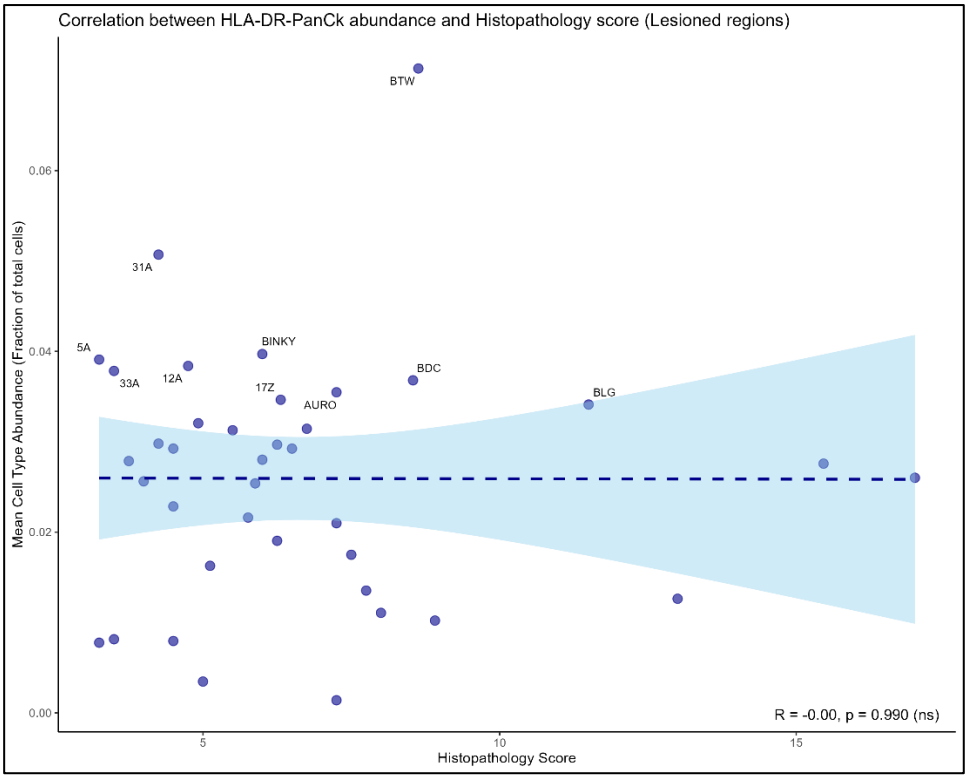
Correlation between HLA-DR-PanCk abundance and Histopathology score (Lesioned regions)
Mean Cell Type Abundance (Fraction of total cells)
Histopathology Score
BTW
31A
5A
33A
12A
BINKY
17Z
AURO
BDC
BLG
0.00
0.02
0.04
0.06
5
10
15
R = -0.00, p = 0.990 (ns)

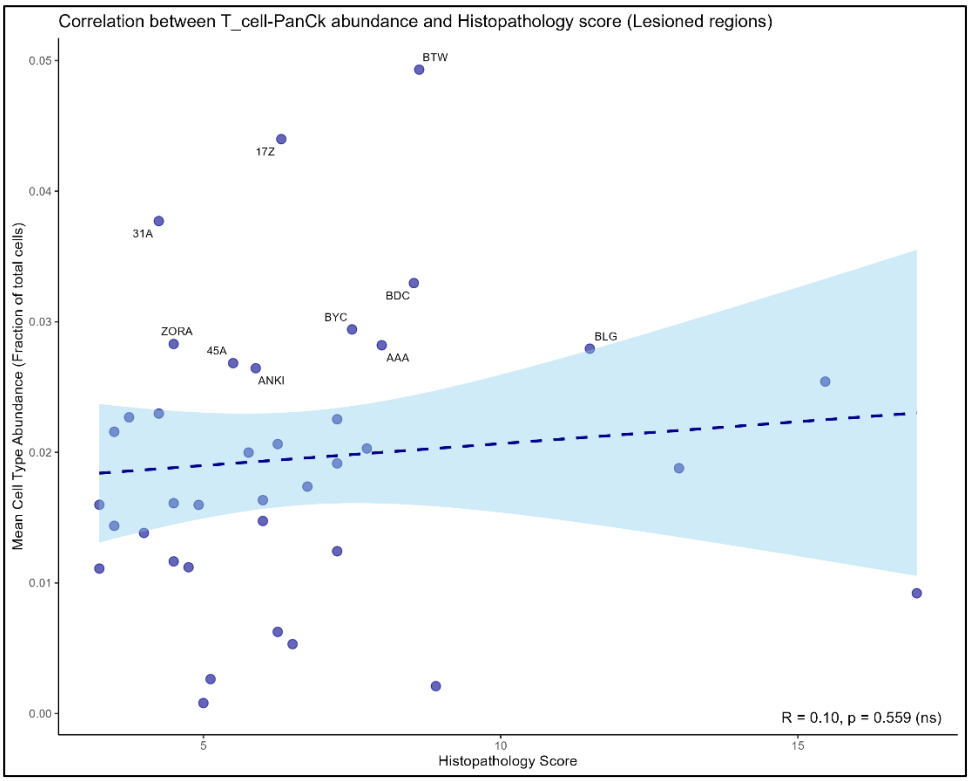
Correlation between T_cell-PanCk abundance and Histopathology score (Lesioned regions)
Mean Cell Type Abundance (Fraction of total cells)
Histopathology Score
BTW
17Z
31A
BDC
BYC
ZORA
45A
ANKI
AAA
BLG
0.00
0.01
0.02
0.03
0.04
0.05
5
10
15
R = 0.10, p = 0.559 (ns)

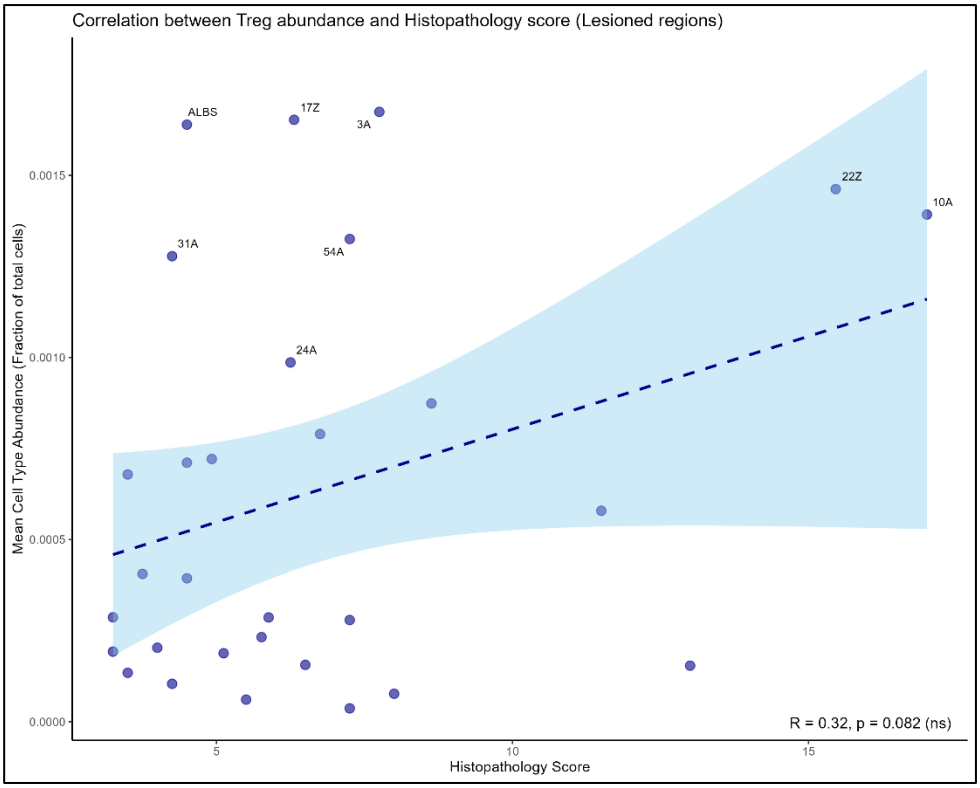
Correlation between Treg abundance and Histopathology score (Lesioned regions)
Mean Cell Type Abundance (Fraction of total cells)
0.0015
0.0010
0.0005
0.0000
ALBS
17Z
3A
22Z
10A
31A
54A
24A
R = 0.32, p = 0.082 (ns)
5
10
15
Histopathology Score

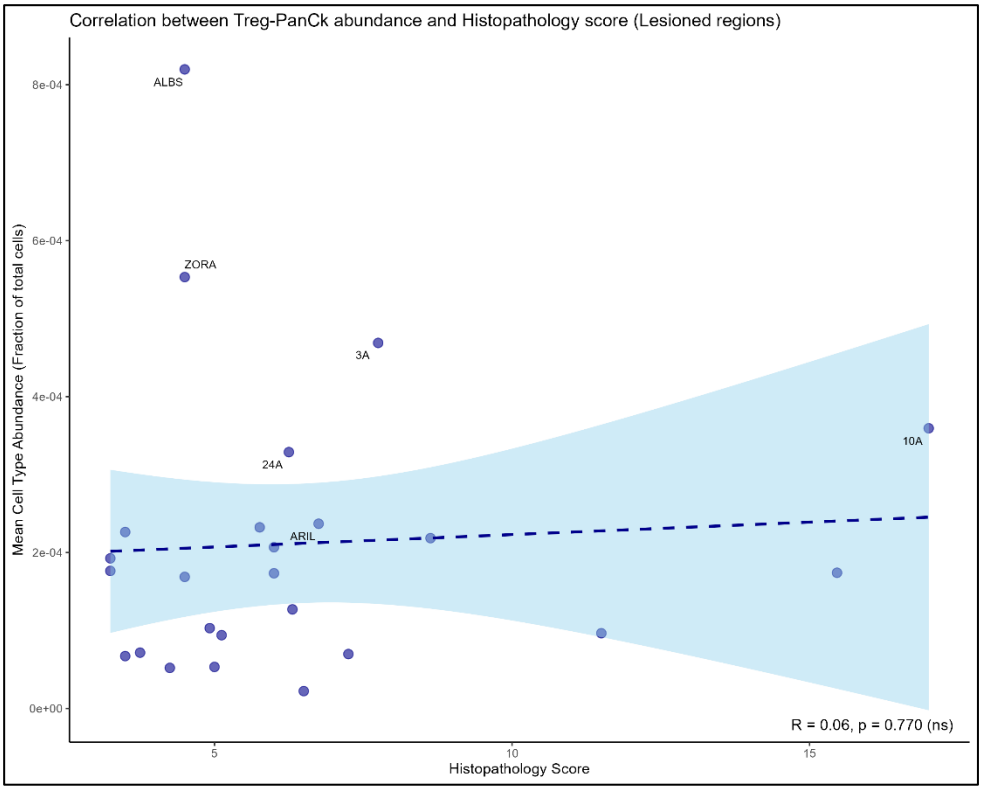
Correlation between Treg-PanCk abundance and Histopathology score (Lesioned regions)
Mean Cell Type Abundance (Fraction of total cells)
8e-04
6e-04
4e-04
2e-04
0e+00
ALBS
ZORA
3A
10A
24A
ARIL
R = 0.06, p = 0.770 (ns)
5
10
15
Histopathology Score

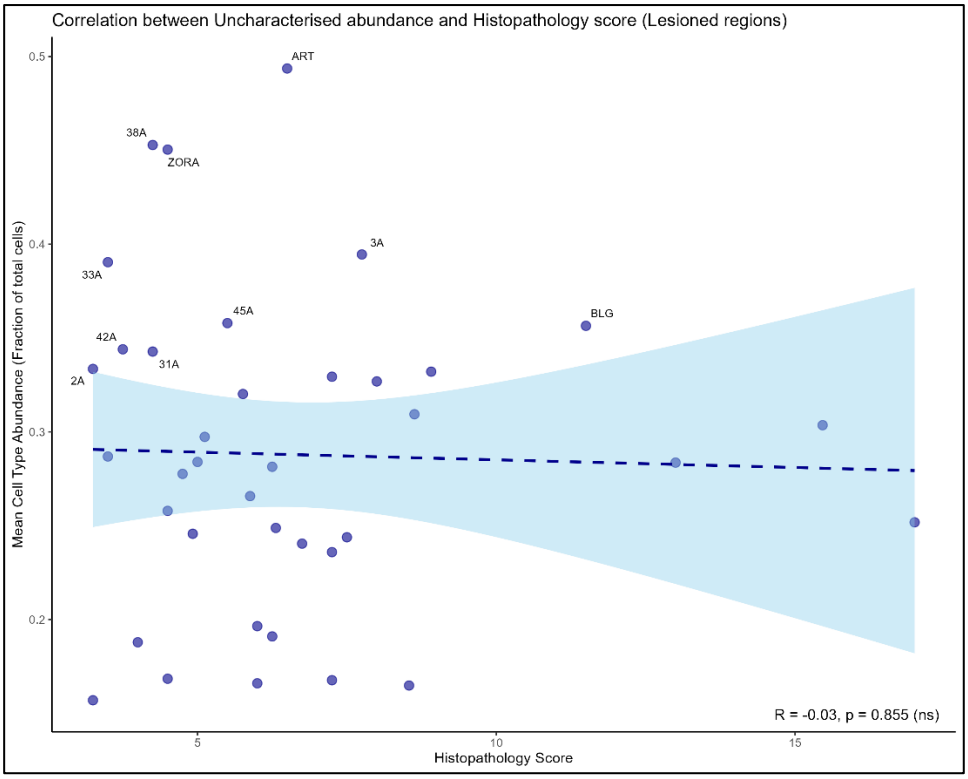

Supplementary Figure 4: All non-significant correlations between cell type abundances and histopathology scores (as described in Section 2.4) across lesioned regions. The dark blue dashed line is the regression line of the correlation between the cell type abundance and histopathology score, while the light blue colour represents the range of the associated confidence interval. Individual samples are overlaid as blue dots, with samples in the upper quartile of cell type abundance annotated according to NHP ID. The R value is Pearson's correlation coefficient and the p value is calculated using Pearson's correlation test. The cell type abundance in question is shown in each individual plot title.

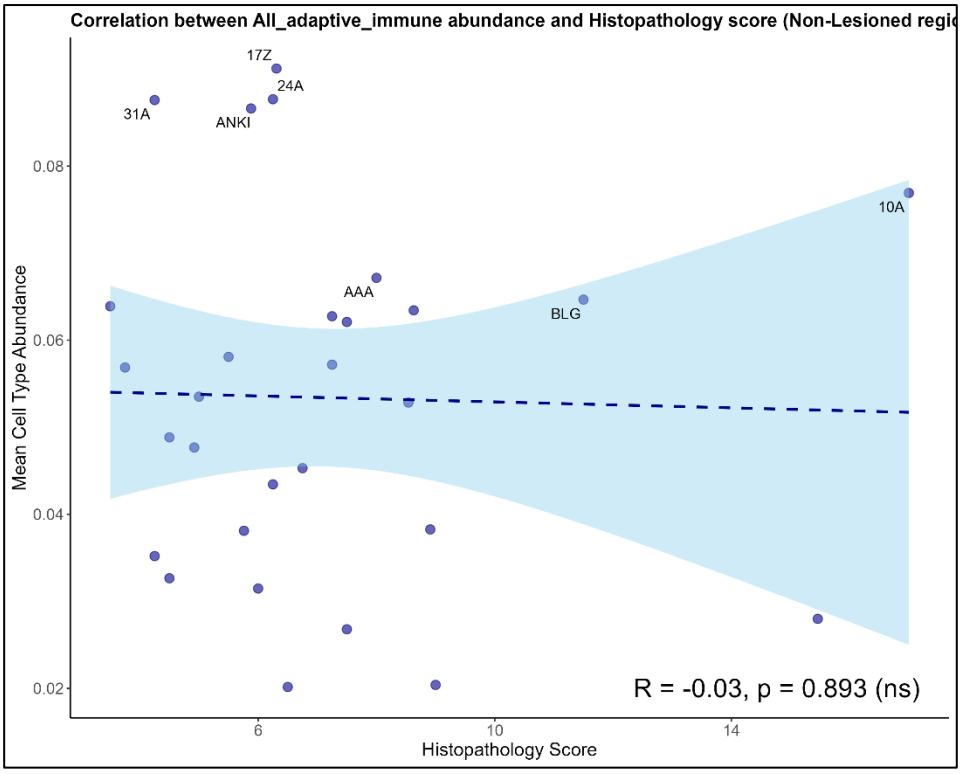
Correlation between All_adaptive_immune abundance and Histopathology score (Non-Lesioned regi
17Z
24A
31A
ANKI
10A
AAA
BLG
Mean Cell Type Abundance
0.08
0.06
0.04
0.02
6
10
14
Histopathology Score
R = -0.03, p = 0.893 (ns)

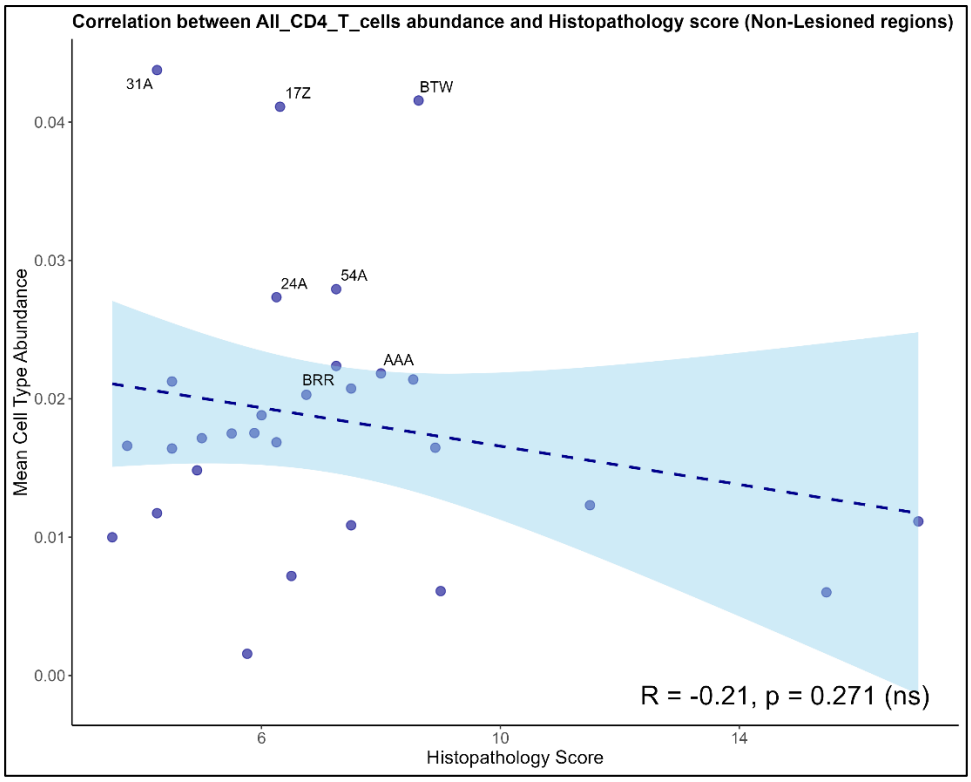
Correlation between All_CD4_T_cells abundance and Histopathology score (Non-Lesioned regions)
31A
17Z
BTW
24A
54A
AAA
BRR
Mean Cell Type Abundance
0.04
0.03
0.02
0.01
0.00
6
10
14
Histopathology Score
R = -0.21, p = 0.271 (ns)

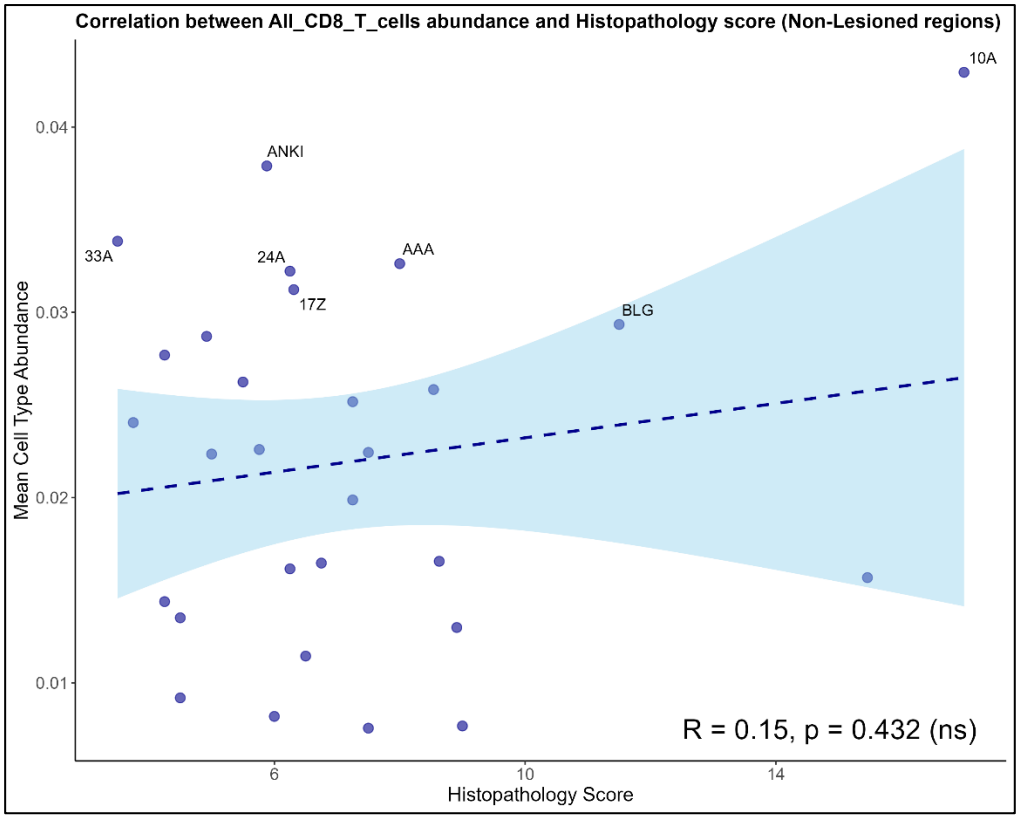
Correlation between All_CD8_T_cells abundance and Histopathology score (Non-Lesioned regions)
Mean Cell Type Abundance
Histopathology Score
0.04
0.03
0.02
0.01
6
10
14
10A
ANKI
33A
24A
AAA
17Z
BLG
R = 0.15, p = 0.432 (ns)

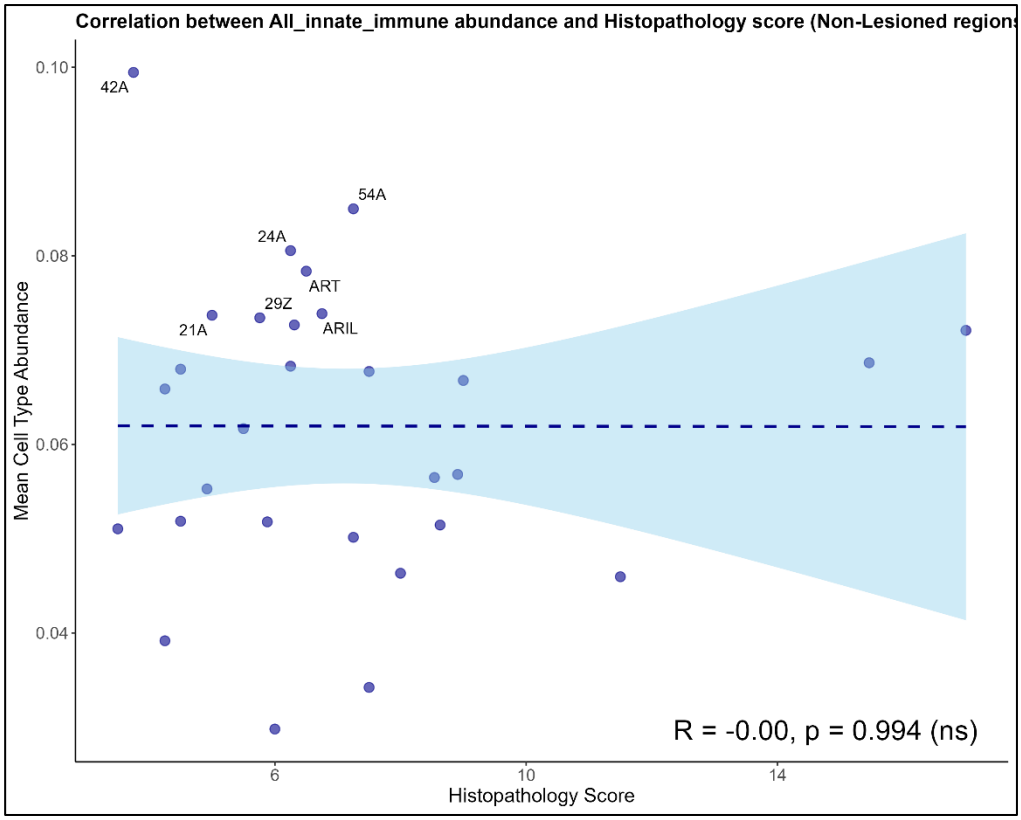
Correlation between All_innate_immune abundance and Histopathology score (Non-Lesioned regions
Mean Cell Type Abundance
Histopathology Score
0.10
0.08
0.06
0.04
6
10
14
42A
54A
24A
ART
29Z
21A
ARIL
R = -0.00, p = 0.994 (ns)

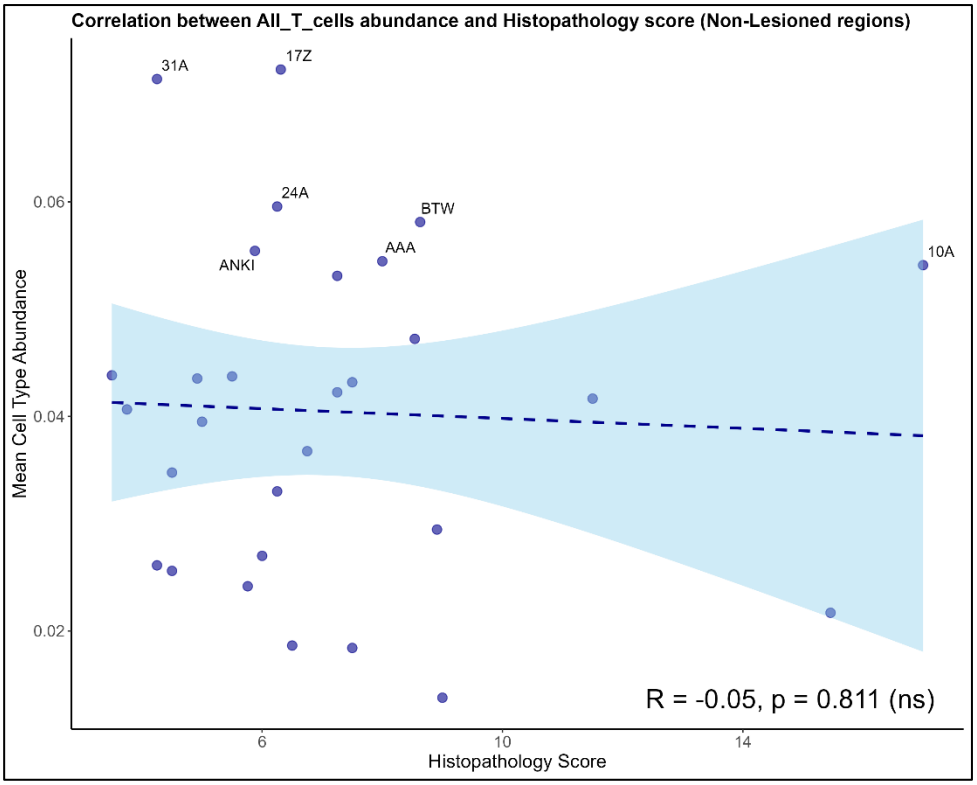
Correlation between All_T_cells abundance and Histopathology score (Non-Lesioned regions)
Mean Cell Type Abundance
Histopathology Score
0.02
0.04
0.06
6
10
14
31A
17Z
24A
BTW
AAA
ANKI
10A
R = -0.05, p = 0.811 (ns)

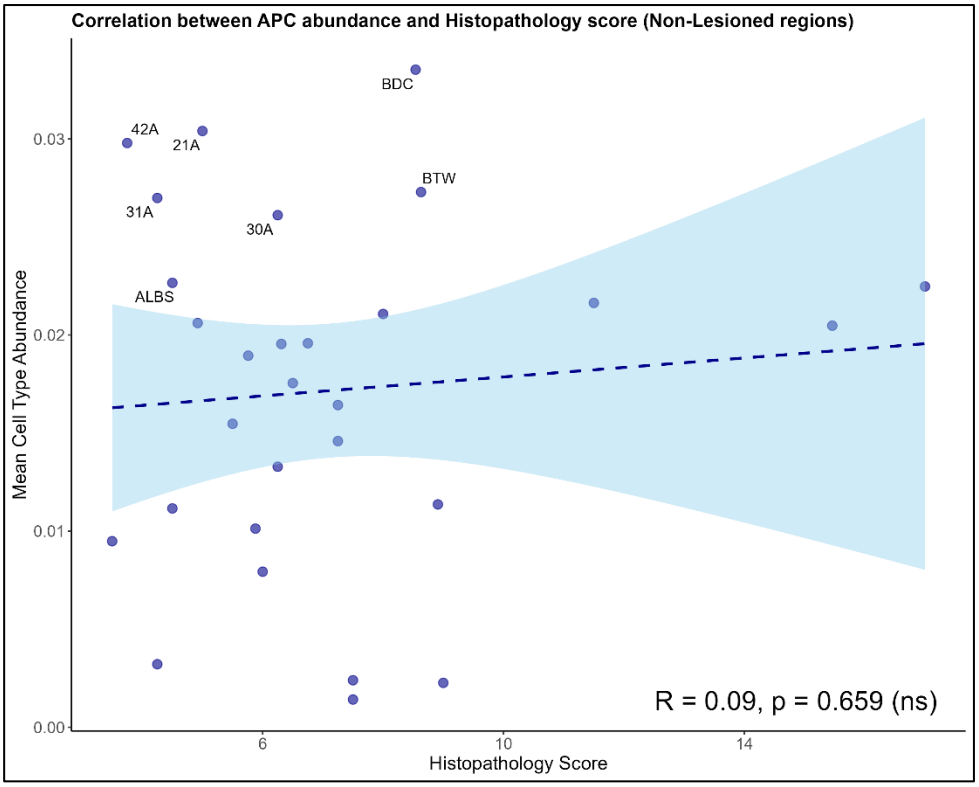
Correlation between APC abundance and Histopathology score (Non-Lesioned regions)
Mean Cell Type Abundance
Histopathology Score
0.00
0.01
0.02
0.03
6
10
14
BDC
42A
21A
BTW
31A
30A
ALBS
R = 0.09, p = 0.659 (ns)

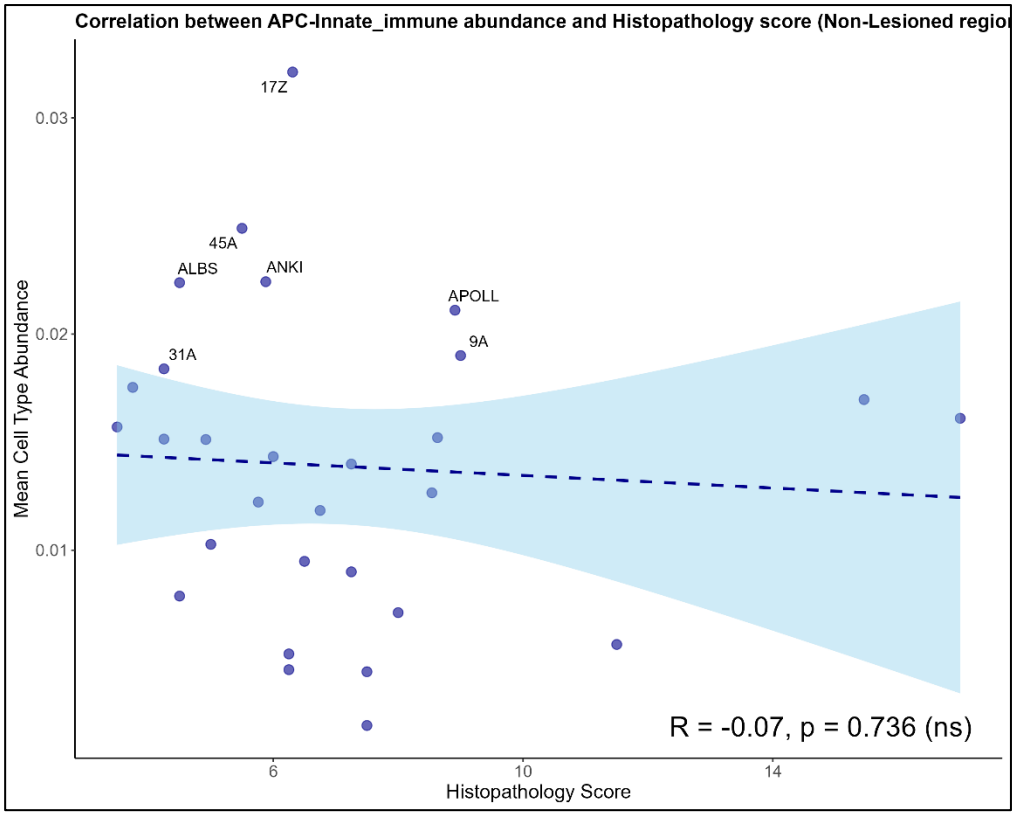
Correlation between APC-Innate_immune abundance and Histopathology score (Non-Lesioned regio
17Z
45A
ALBS
ANKI
APOLL
9A
31A
0.03
0.02
0.01
Mean Cell Type Abundance
R = -0.07, p = 0.736 (ns)
6
10
14
Histopathology Score

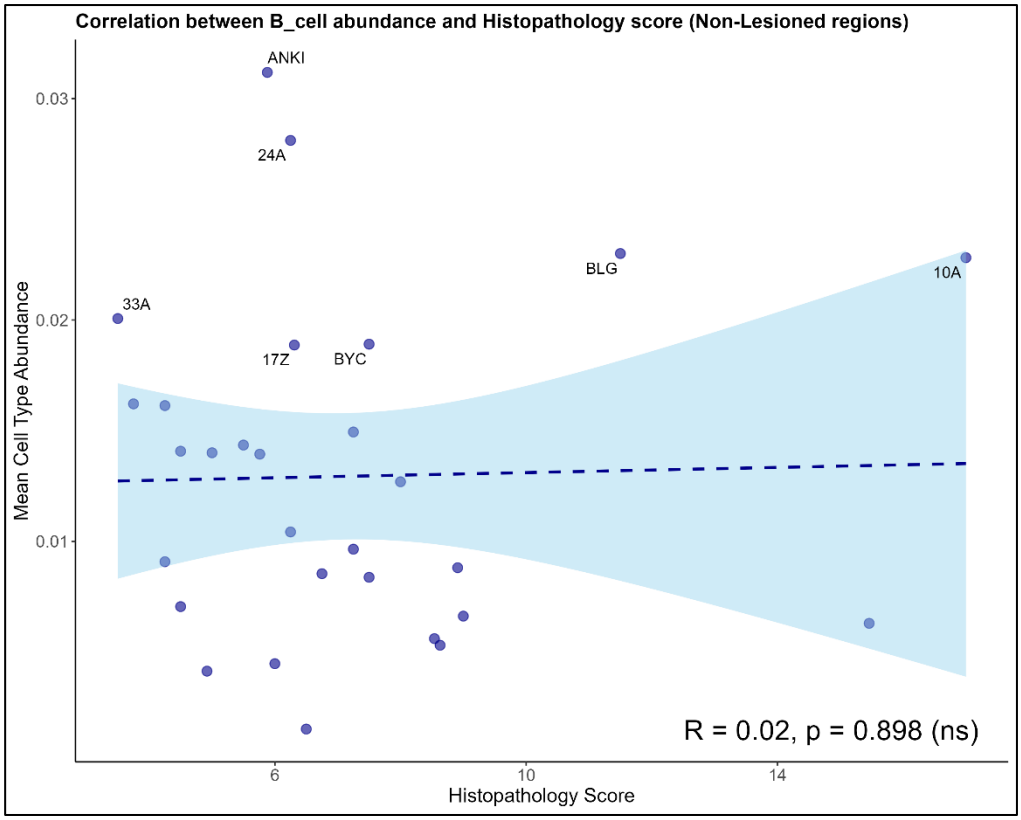
Correlation between B_cell abundance and Histopathology score (Non-Lesioned regions)
ANKI
24A
BLG
10A
33A
17Z
BYC
0.03
0.02
0.01
Mean Cell Type Abundance
R = 0.02, p = 0.898 (ns)
6
10
14
Histopathology Score

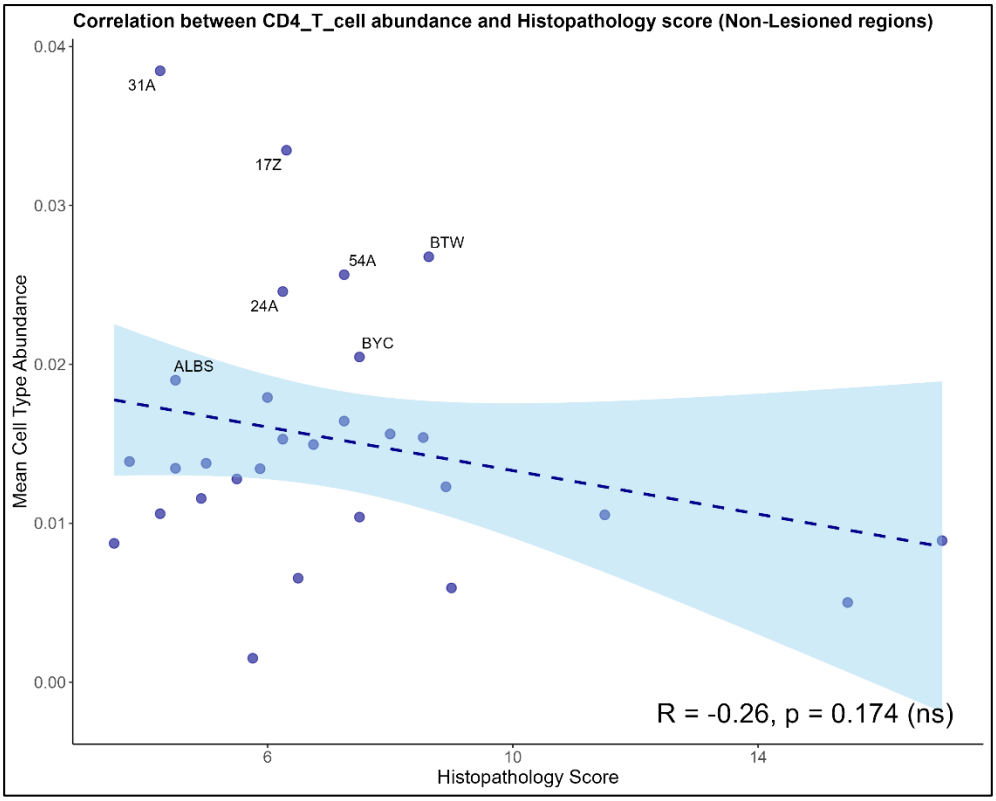
Correlation between CD4_T_cell abundance and Histopathology score (Non-Lesioned regions)
Mean Cell Type Abundance
Histopathology Score
0.04
0.03
0.02
0.01
0.00
6
10
14
31A
17Z
BTW
54A
24A
BYC
ALBS
R = -0.26, p = 0.174 (ns)

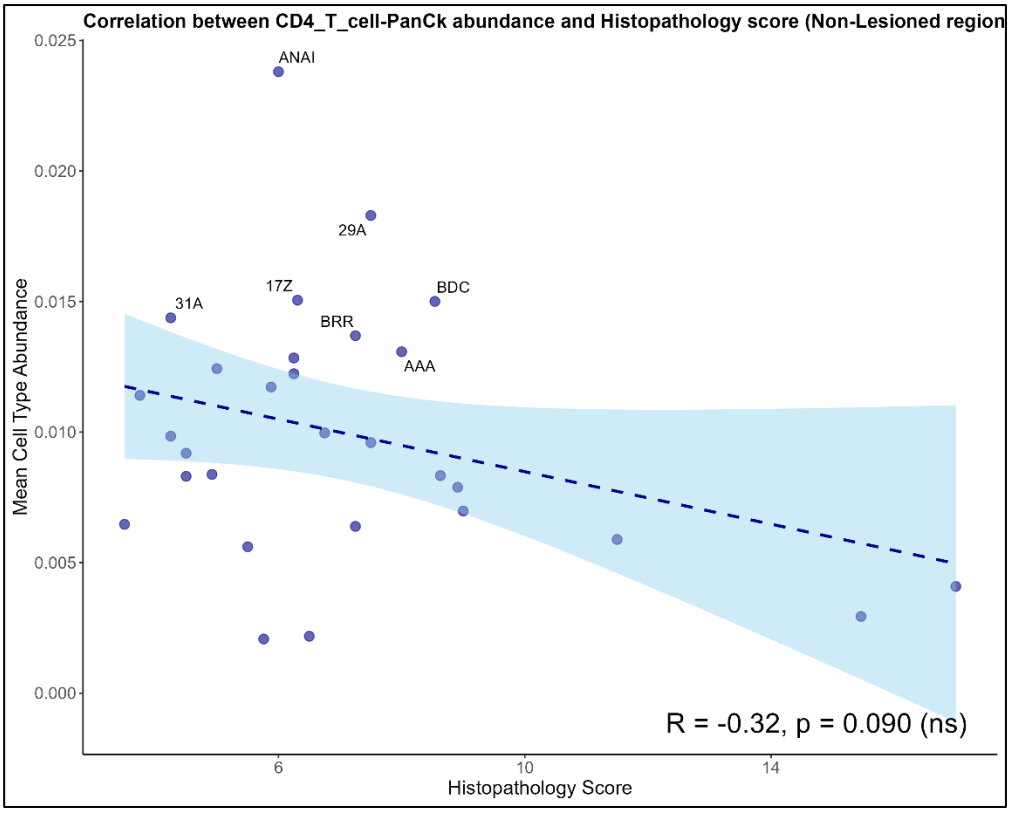
Correlation between CD4_T_cell-PanCk abundance and Histopathology score (Non-Lesioned region
Mean Cell Type Abundance
Histopathology Score
0.025
0.020
0.015
0.010
0.005
0.000
6
10
14
ANAI
29A
17Z
BDC
31A
BRR
AAA
R = -0.32, p = 0.090 (ns)

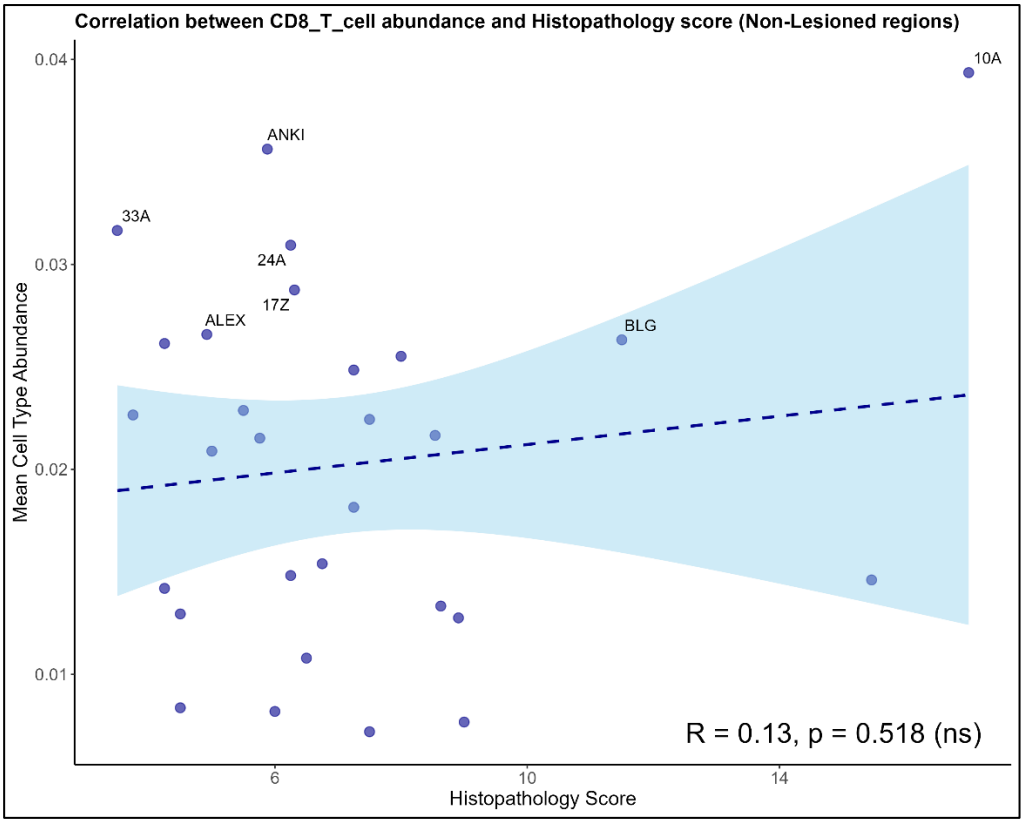
Correlation between CD8_T_cell abundance and Histopathology score (Non-Lesioned regions)
Mean Cell Type Abundance
Histopathology Score
0.04
0.03
0.02
0.01
6
10
14
10A
ANKI
33A
24A
17Z
ALEX
BLG
R = 0.13, p = 0.518 (ns)

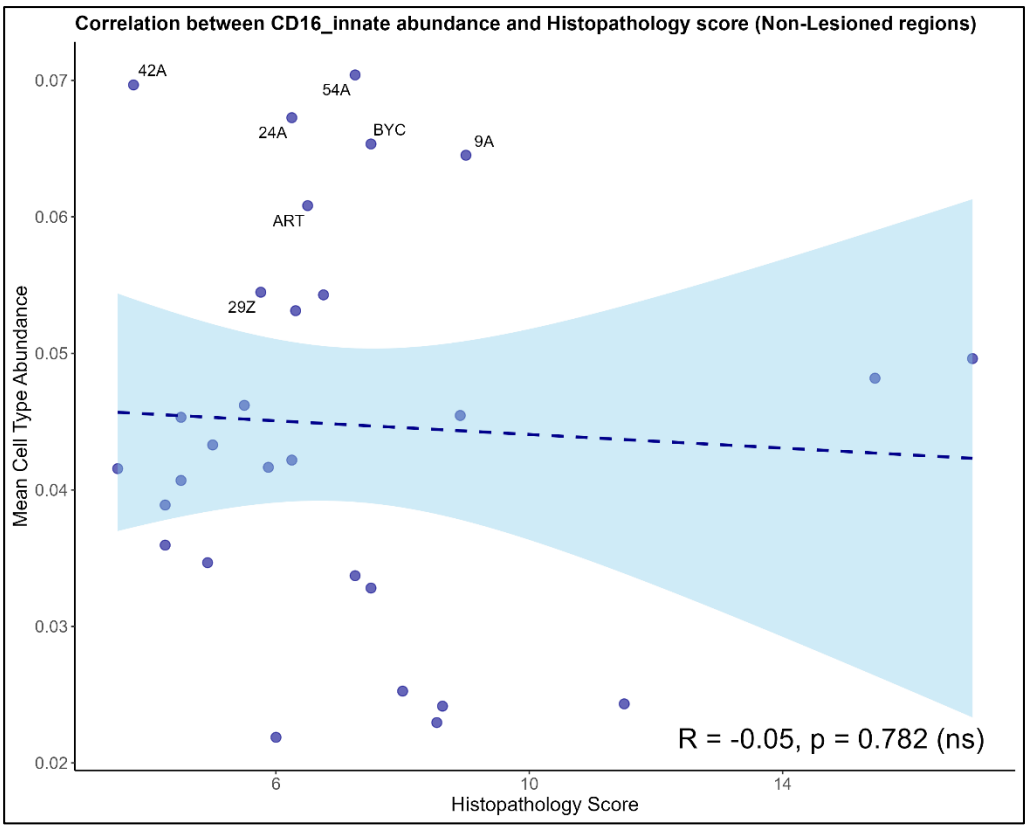
Correlation between CD16_innate abundance and Histopathology score (Non-Lesioned regions)
Mean Cell Type Abundance
Histopathology Score
0.07
0.06
0.05
0.04
0.03
0.02
6
10
14
42A
54A
24A
BYC
9A
ART
29Z
R = -0.05, p = 0.782 (ns)

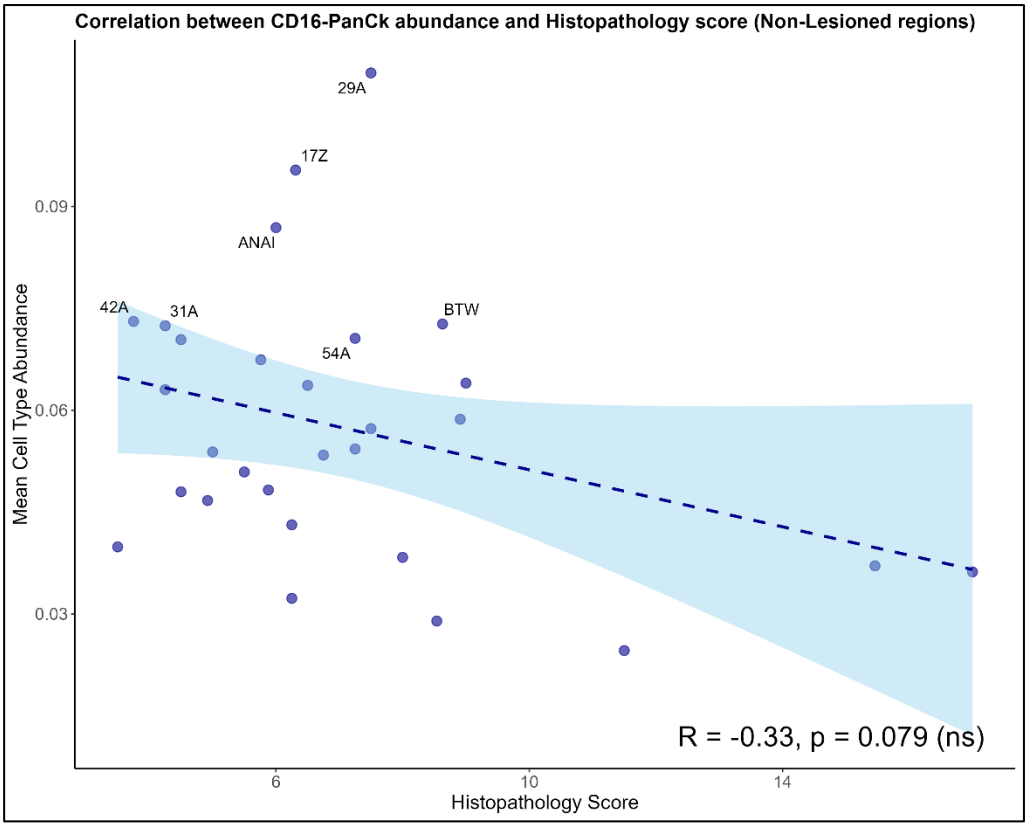
Correlation between CD16-PanCk abundance and Histopathology score (Non-Lesioned regions)
29A
17Z
ANAI
42A
31A
BTW
54A
0.09
0.06
0.03
Mean Cell Type Abundance
R = -0.33, p = 0.079 (ns)
6
10
14
Histopathology Score

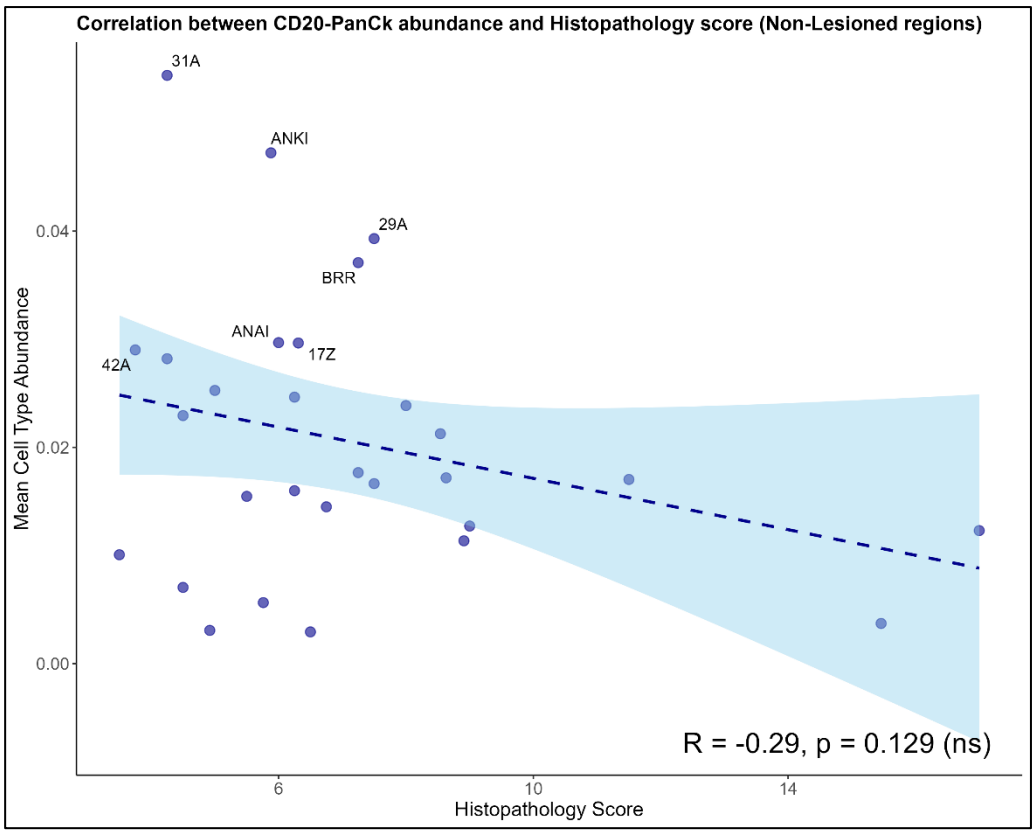
Correlation between CD20-PanCk abundance and Histopathology score (Non-Lesioned regions)
31A
ANKI
29A
BRR
ANAI
17Z
42A
0.04
0.02
0.00
Mean Cell Type Abundance
R = -0.29, p = 0.129 (ns)
6
10
14
Histopathology Score

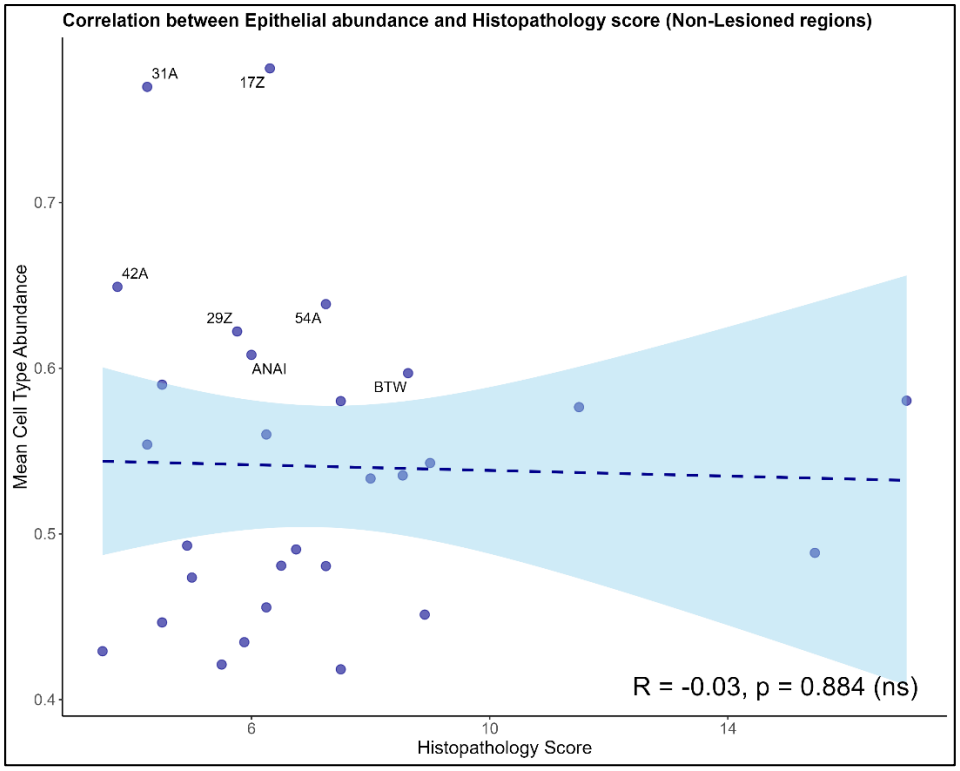
Correlation between Epithelial abundance and Histopathology score (Non-Lesioned regions)
31A
17Z
42A
29Z
54A
ANAI
BTW
0.7
0.6
0.5
0.4
Mean Cell Type Abundance
R = -0.03, p = 0.884 (ns)
6
10
14
Histopathology Score

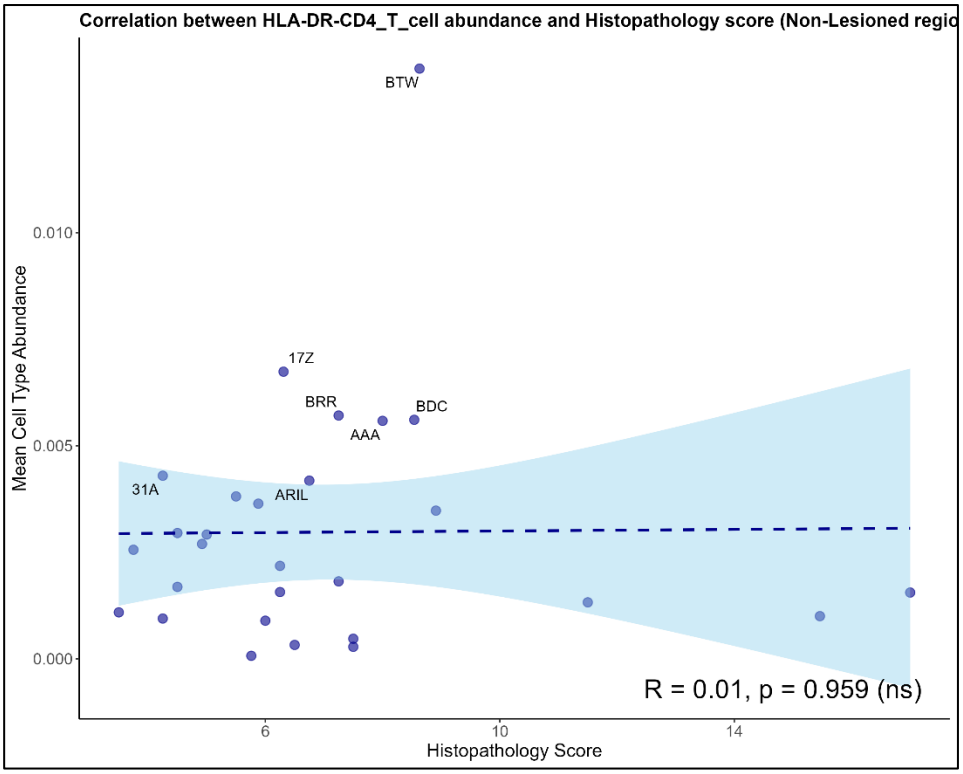
Correlation between HLA-DR-CD4_T_cell abundance and Histopathology score (Non-Lesioned regio
BTW
0.010
0.005
0.000
Mean Cell Type Abundance
17Z
BRR
BDC
AAA
31A
ARIL
R = 0.01, p = 0.959 (ns)
6
10
14
Histopathology Score

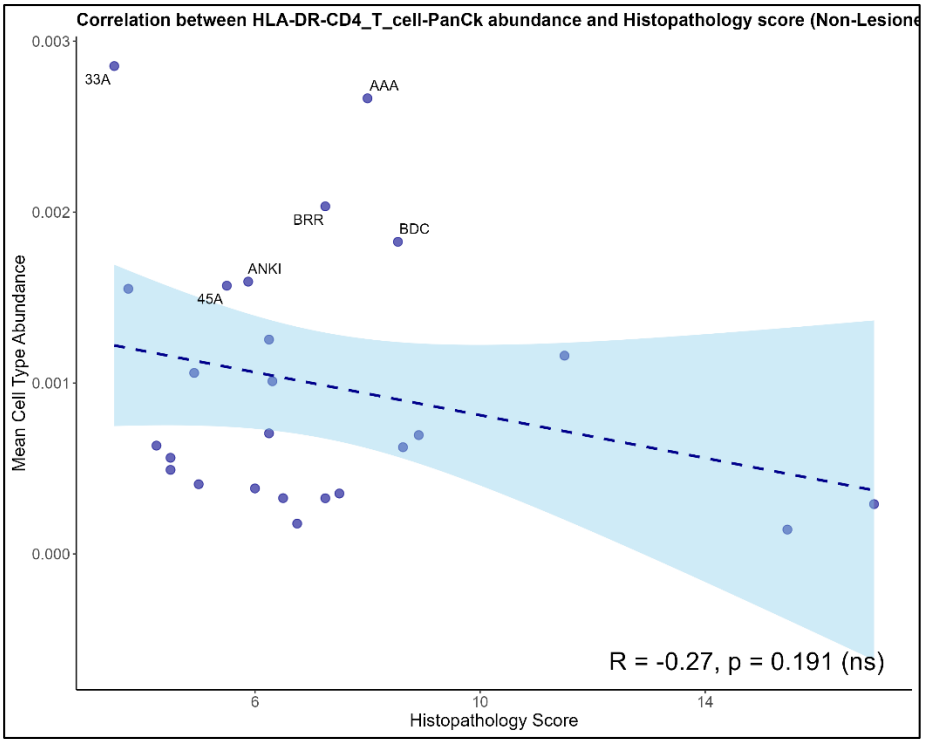
Correlation between HLA-DR-CD4_T_cell-PanCk abundance and Histopathology score (Non-Lesione
Mean Cell Type Abundance
0.003
0.002
0.001
0.000
33A
AAA
BRR
BDC
ANKI
45A
6
10
14
Histopathology Score
R = -0.27, p = 0.191 (ns)

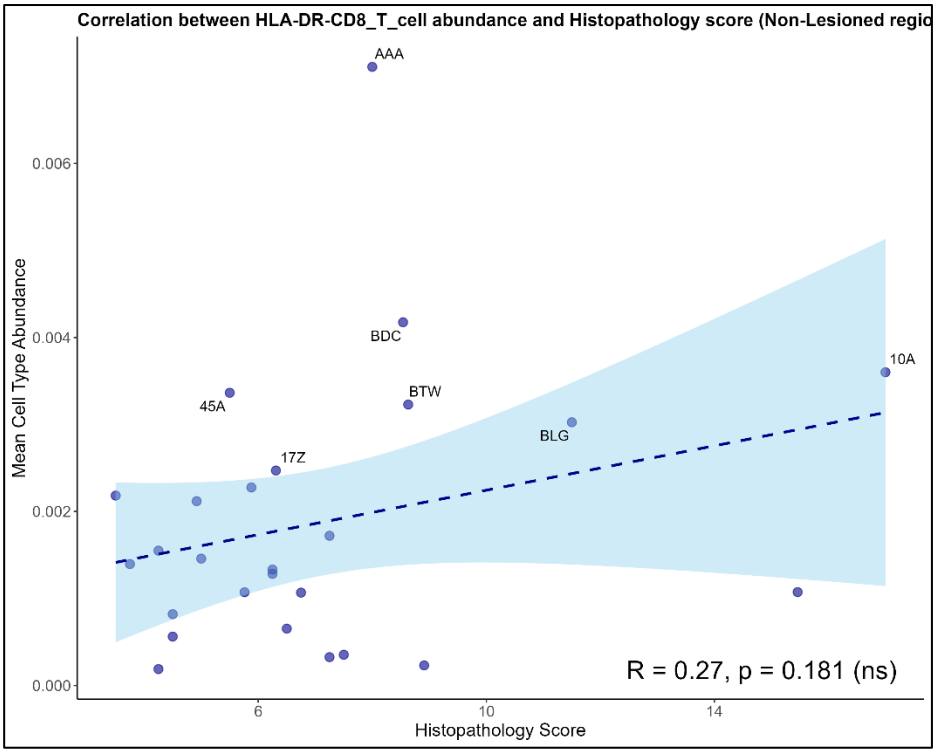
Correlation between HLA-DR-CD8_T_cell abundance and Histopathology score (Non-Lesioned regio
Mean Cell Type Abundance
0.006
0.004
0.002
0.000
AAA
BDC
10A
45A
BTW
BLG
17Z
6
10
14
Histopathology Score
R = 0.27, p = 0.181 (ns)

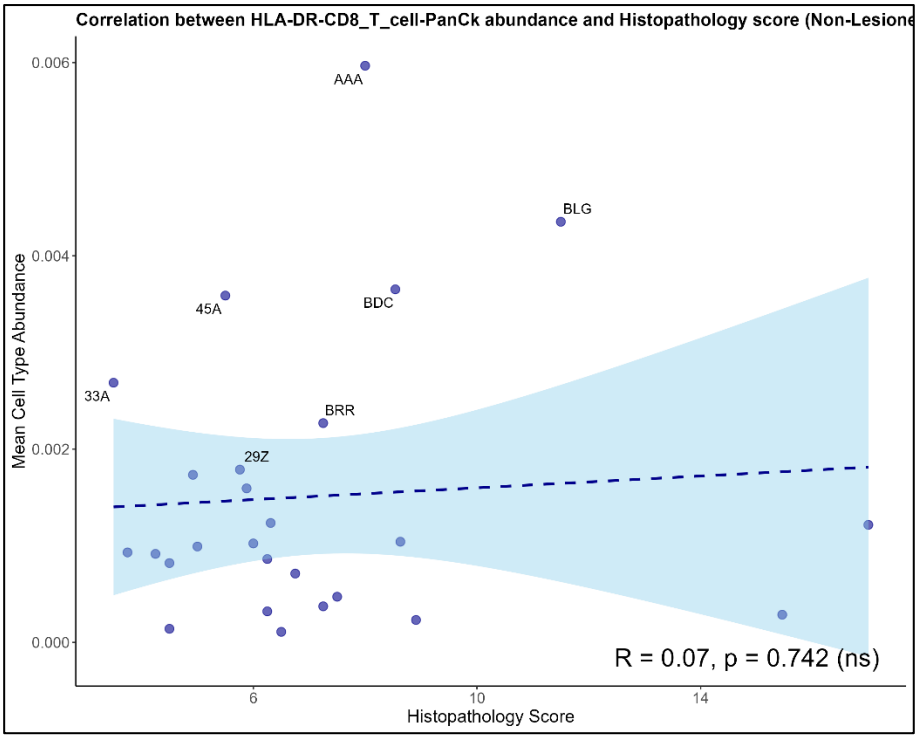
Correlation between HLA-DR-CD8_T_cell-PanCk abundance and Histopathology score (Non-Lesione
Mean Cell Type Abundance
0.006
0.004
0.002
0.000
AAA
BLG
45A
BDC
33A
BRR
29Z
R = 0.07, p = 0.742 (ns)
6
10
14
Histopathology Score

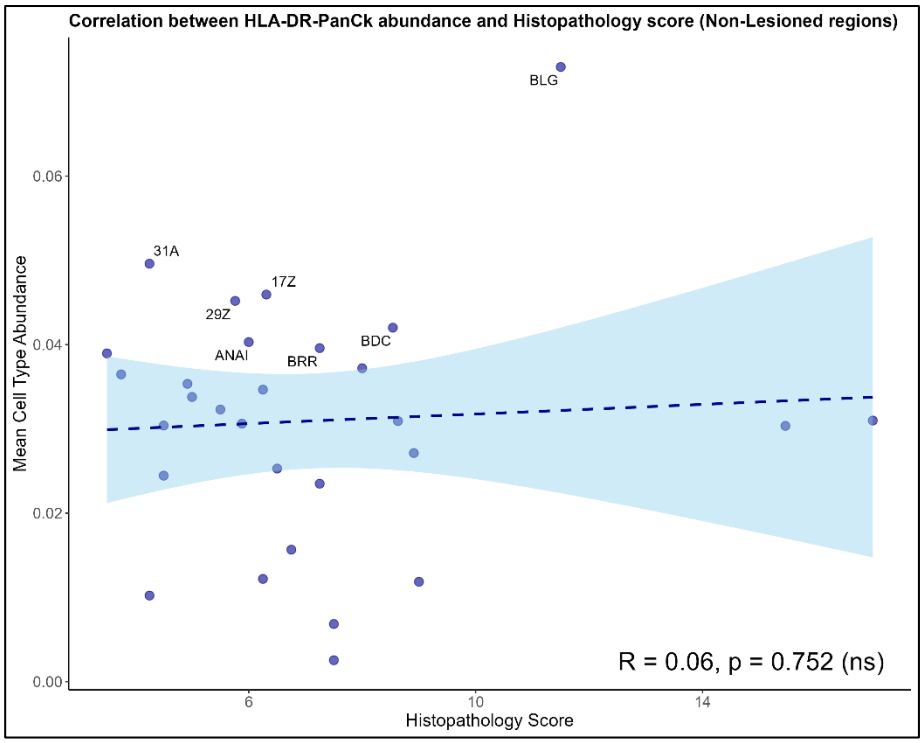
Correlation between HLA-DR-PanCk abundance and Histopathology score (Non-Lesioned regions)
Mean Cell Type Abundance
0.06
0.04
0.02
0.00
BLG
31A
17Z
29Z
ANAl
BRR
BDC
R = 0.06, p = 0.752 (ns)
6
10
14
Histopathology Score

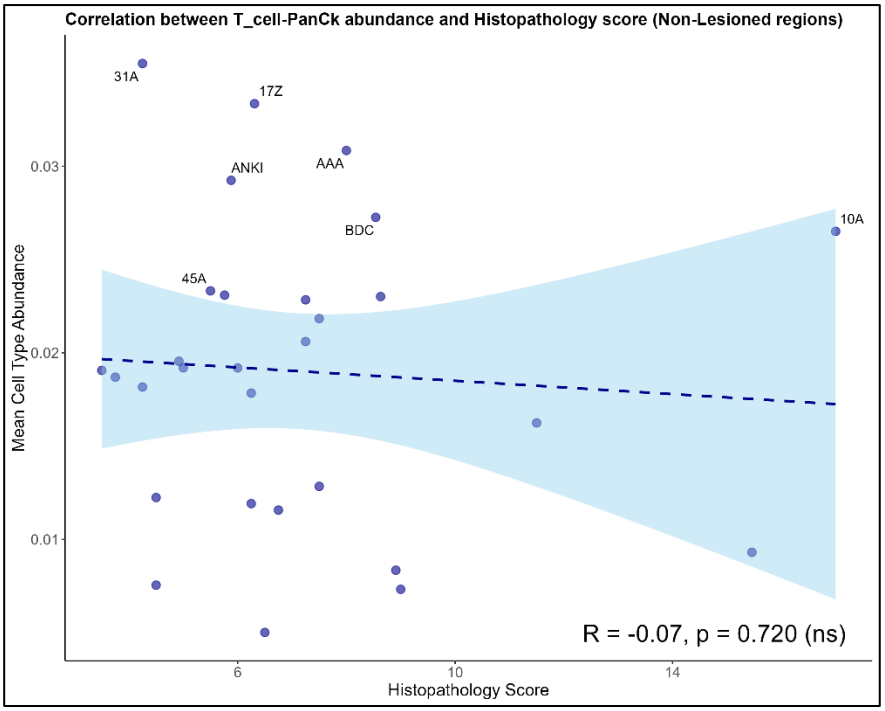
Correlation between T_cell-PanCk abundance and Histopathology score (Non-Lesioned regions)
31A
17Z
ANKI
AAA
BDC
10A
45A
0.03
0.02
0.01
Mean Cell Type Abundance
R = -0.07, p = 0.720 (ns)
6
10
14
Histopathology Score

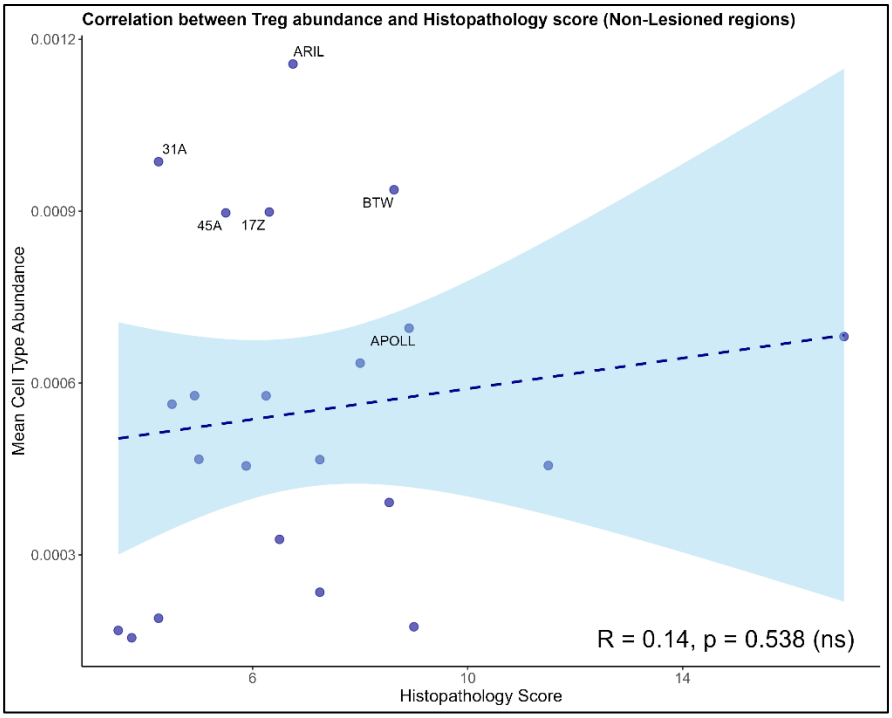
Correlation between Treg abundance and Histopathology score (Non-Lesioned regions)
0.0012
0.0009
0.0006
0.0003
Mean Cell Type Abundance
ARIL
31A
BTW
45A
17Z
APOLL
R = 0.14, p = 0.538 (ns)
6
10
14
Histopathology Score

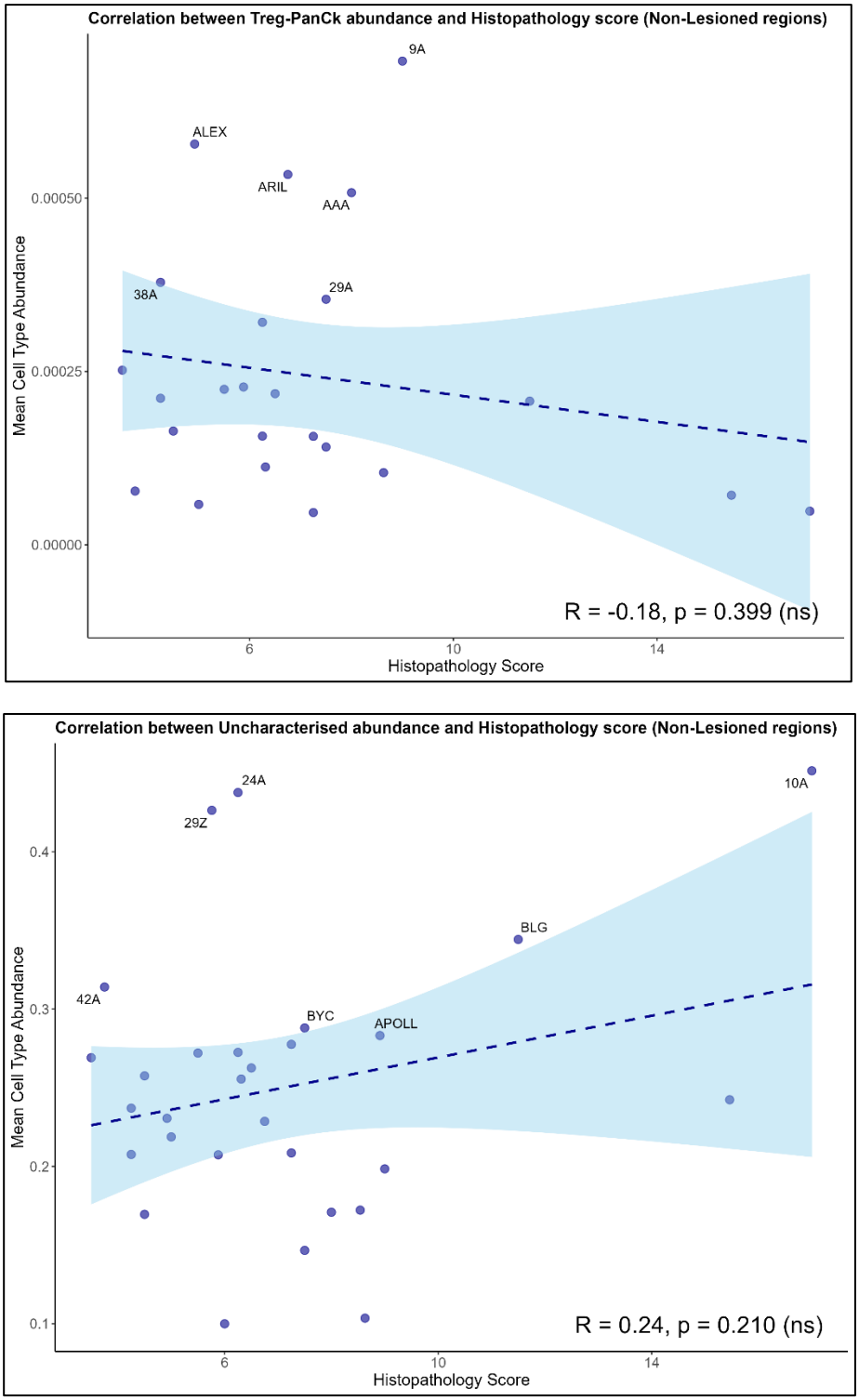

Supplementary Figure 5: All non-significant correlations between cell type abundances and histopathology scores (as described in Section 2.4) across non-lesioned regions. The dark blue dashed line is the regression line of the correlation between the cell type abundance and histopathology score, while the light blue colour represents the range of the associated confidence interval. Individual samples are overlaid as blue dots, with samples in the upper quartile of cell type abundance annotated according

to NHP ID. The R value is Pearson's correlation coefficient and the p value is calculated using Pearson's correlation test. The cell type abundance in question is shown in each individual plot title.

Marker	Clone	Concentration (µg/mL)	Cat number	Fluoresence	Supplier
Nuclei	SYTO 13	NA	S7575	488	Invitrogen
CD68	KP1	5	sc-20060	594	Santa Cruz Biotechnolog
PanCk	AE1 + AE3	2	NBP2-29429	532	Novus Biologicals

Supplementary Table 3: Antibody list for GeoMx experiment.

SlideName	nhp	roi	vaccine	region
No Template Control	na	na	na	na
GeoMx 1	10A	1	DNA	Pathology
GeoMx 1	10A	2	DNA	Pathology
GeoMx 1	10A	3	DNA	Pathology
GeoMx 1	10A	4	DNA	Not
GeoMx 1	10A	5	DNA	Pathology
GeoMx 1	10A	6	DNA	Not
GeoMx 1	10A	7	DNA	Not
GeoMx 1	BLG	8	mRNA	Pathology
GeoMx 1	BLG	9	mRNA	Pathology
GeoMx 1	BLG	10	mRNA	Pathology
GeoMx 1	BLG	11	mRNA	Pathology
GeoMx 1	BLG	12	mRNA	Not
GeoMx 1	BLG	13	mRNA	Not
GeoMx 1	BLG	14	mRNA	Not
GeoMx 1	33A	15	DNA	Not
GeoMx 1	33A	16	DNA	Not
GeoMx 1	33A	17	DNA	Not
GeoMx 1	33A	18	DNA	Pathology
GeoMx 1	33A	19	DNA	Pathology
GeoMx 1	33A	20	DNA	Pathology
GeoMx 1	33A	21	DNA	Pathology
GeoMx 1	Archive230	22	Unchallenged	Not
GeoMx 1	Archive230	23	Unchallenged	Not
GeoMx 1	Archive230	24	Unchallenged	Not
GeoMx 1	10A	25	DNA	Pathology
GeoMx 1	10A	26	DNA	Pathology
GeoMx 2	ZORA	1	mRNA	Pathology
GeoMx 2	ZORA	2	mRNA	Pathology
GeoMx 2	ZORA	3	mRNA	Pathology
GeoMx 2	ZORA	4	mRNA	Not
GeoMx 2	ZORA	5	mRNA	Not
GeoMx 2	ZORA	6	mRNA	Not
GeoMx 2	22Z	7	Unvaccinated	Pathology
GeoMx 2	22Z	8	Unvaccinated	Not
GeoMx 2	22Z	9	Unvaccinated	Pathology
GeoMx 2	22Z	10	Unvaccinated	Pathology
GeoMx 2	22Z	11	Unvaccinated	Not
GeoMx 2	22Z	12	Unvaccinated	Not
GeoMx 2	22Z	13	Unvaccinated	Pathology
GeoMx 2	ALEX	14	Rechallenge	Pathology
GeoMx 2	ALEX	15	Rechallenge	Not
GeoMx 2	ALEX	16	Rechallenge	Not
GeoMx 2	ALEX	17	Rechallenge	Pathology
GeoMx 2	ALEX	18	Rechallenge	Pathology
GeoMx 2	ALEX	19	Rechallenge	Not
GeoMx 2	ALEX	20	Rechallenge	Pathology
GeoMx 2	25A	21	Unvaccinated	Pathology
GeoMx 2	25A	22	Unvaccinated	Not
GeoMx 2	25A	23	Unvaccinated	Not
GeoMx 2	25A	24	Unvaccinated	Pathology
GeoMx 2	25A	25	Unvaccinated	Not
GeoMx 2	25A	26	Unvaccinated	Pathology
GeoMx 2	25A	27	Unvaccinated	Pathology
GeoMx 2	ZORA	28	mRNA	Pathology
GeoMx 3	31A	1	FIV	Pathology
GeoMx 3	31A	2	FIV	Not
GeoMx 3	31A	3	FIV	Not
GeoMx 3	31A	4	FIV	Not
GeoMx 3	31A	5	FIV	Pathology
GeoMx 3	31A	6	FIV	Pathology
GeoMx 3	31A	7	FIV	Pathology
GeoMx 3	17Z	8	Viral vector	Pathology
GeoMx 3	17Z	9	Viral vector	Pathology
GeoMx 3	17Z	10	Viral vector	Pathology
GeoMx 3	17Z	11	Viral vector	Not
GeoMx 3	17Z	12	Viral vector	Pathology
GeoMx 3	17Z	13	Viral vector	Not
GeoMx 3	17Z	14	Viral vector	Not
GeoMx 3	54A	15	FIV	Pathology
GeoMx 3	54A	16	FIV	Pathology
GeoMx 3	54A	17	FIV	Pathology
GeoMx 3	54A	18	FIV	Pathology
GeoMx 3	54A	19	FIV	Not
GeoMx 3	54A	20	FIV	Not
GeoMx 3	54A	21	FIV	Not
GeoMx 3	BTW	22	Rechallenge	Pathology
GeoMx 3	BTW	23	Rechallenge	Pathology
GeoMx 3	BTW	24	Rechallenge	Pathology
GeoMx 3	BTW	25	Rechallenge	Not
GeoMx 3	BTW	26	Rechallenge	Not
GeoMx 3	BTW	27	Rechallenge	Not
GeoMx 3	BTW	28	Rechallenge	Pathology
GeoMx 4	Archive231	1	Unchallenged	Not
GeoMx 4	Archive231	2	Unchallenged	Not
GeoMx 4	Archive231	3	Unchallenged	Not
GeoMx 4	29Z	4	Viral vector	Pathology
GeoMx 4	29Z	5	Viral vector	Pathology
GeoMx 4	29Z	6	Viral vector	Pathology
GeoMx 4	29Z	7	Viral vector	Pathology
GeoMx 4	29Z	8	Viral vector	Not
GeoMx 4	29Z	9	Viral vector	Not
GeoMx 4	10A2	10	DNA	Pathology
GeoMx 4	29Z	11	Viral vector	Not
GeoMx 4	10A2	12	DNA	Pathology
GeoMx 4	10A2	13	DNA	Pathology

Supplementary Table 4: Details on NHPs and region types taken for the GeoMx experiment. 10A2 refers to a spare tissue from NHP 10A. After filtering, some of these ROIs were removed as described in **Section 3.2**. Regions labelled as ‘Pathology’ were later renamed as ‘Lesioned’.

SlideName	nhp	roi	vaccine	region
No Template Control	na	na	na	na
GeoMx 1	A10	1	DNA	Lesioned
GeoMx 1	A10	2	DNA	Lesioned
GeoMx 1	A10	3	DNA	Lesioned
GeoMx 1	A10	4	DNA	Not
GeoMx 1	A10	5	DNA	Lesioned
GeoMx 1	A10	6	DNA	Not
GeoMx 1	A10	7	DNA	Not
GeoMx 1	BLG	8	mRNA	Lesioned
GeoMx 1	BLG	9	mRNA	Lesioned
GeoMx 1	BLG	10	mRNA	Lesioned
GeoMx 1	BLG	11	mRNA	Lesioned
GeoMx 1	BLG	12	mRNA	Not
GeoMx 1	BLG	13	mRNA	Not
GeoMx 1	BLG	14	mRNA	Not
GeoMx 1	A33	15	DNA	Not
GeoMx 1	A33	16	DNA	Not
GeoMx 1	A33	17	DNA	Not
GeoMx 1	A33	18	DNA	Lesioned
GeoMx 1	A33	19	DNA	Lesioned
GeoMx 1	A33	20	DNA	Lesioned
GeoMx 1	A33	21	DNA	Lesioned
GeoMx 1	A10	25	DNA	Lesioned
GeoMx 1	A10	26	DNA	Lesioned
GeoMx 2	ZORA	1	mRNA	Lesioned
GeoMx 2	ZORA	2	mRNA	Lesioned
GeoMx 2	ZORA	3	mRNA	Lesioned
GeoMx 2	ZORA	4	mRNA	Not
GeoMx 2	ZORA	5	mRNA	Not
GeoMx 2	ZORA	6	mRNA	Not
GeoMx 2	Z22	7	Unvaccinated	Lesioned
GeoMx 2	Z22	8	Unvaccinated	Not
GeoMx 2	Z22	9	Unvaccinated	Lesioned
GeoMx 2	Z22	10	Unvaccinated	Lesioned
GeoMx 2	Z22	11	Unvaccinated	Not
GeoMx 2	Z22	12	Unvaccinated	Not
GeoMx 2	Z22	13	Unvaccinated	Lesioned
GeoMx 2	ALEX	14	Rechallenge	Lesioned
GeoMx 2	ALEX	15	Rechallenge	Not
GeoMx 2	ALEX	16	Rechallenge	Not
GeoMx 2	ALEX	17	Rechallenge	Lesioned
GeoMx 2	ALEX	18	Rechallenge	Lesioned
GeoMx 2	ALEX	19	Rechallenge	Not
GeoMx 2	ALEX	20	Rechallenge	Lesioned
GeoMx 2	A25	21	Unvaccinated	Lesioned
GeoMx 2	A25	22	Unvaccinated	Not
GeoMx 2	A25	23	Unvaccinated	Not
GeoMx 2	A25	24	Unvaccinated	Lesioned
GeoMx 2	A25	25	Unvaccinated	Not
GeoMx 2	A25	26	Unvaccinated	Lesioned
GeoMx 2	A25	27	Unvaccinated	Lesioned
GeoMx 2	ZORA	28	mRNA	Lesioned
GeoMx 3	A31	1	FIV	Lesioned
GeoMx 3	A31	2	FIV	Not
GeoMx 3	A31	3	FIV	Not
GeoMx 3	A31	4	FIV	Not
GeoMx 3	A31	5	FIV	Lesioned
GeoMx 3	A31	6	FIV	Lesioned
GeoMx 3	A31	7	FIV	Lesioned
GeoMx 3	Z17	8	ViralVector	Lesioned
GeoMx 3	Z17	9	ViralVector	Lesioned
GeoMx 3	Z17	10	ViralVector	Lesioned
GeoMx 3	Z17	11	ViralVector	Not
GeoMx 3	Z17	12	ViralVector	Lesioned
GeoMx 3	Z17	13	ViralVector	Not
GeoMx 3	Z17	14	ViralVector	Not
GeoMx 3	A54	15	FIV	Lesioned
GeoMx 3	A54	16	FIV	Lesioned
GeoMx 3	A54	17	FIV	Lesioned
GeoMx 3	A54	18	FIV	Lesioned
GeoMx 3	A54	19	FIV	Not
GeoMx 3	A54	20	FIV	Not
GeoMx 3	A54	21	FIV	Not
GeoMx 3	BTW	22	Rechallenge	Lesioned
GeoMx 3	BTW	23	Rechallenge	Lesioned
GeoMx 3	BTW	24	Rechallenge	Lesioned
GeoMx 3	BTW	25	Rechallenge	Not
GeoMx 3	BTW	26	Rechallenge	Not
GeoMx 3	BTW	27	Rechallenge	Not
GeoMx 3	BTW	28	Rechallenge	Lesioned
GeoMx 4	Z29	4	ViralVector	Lesioned
GeoMx 4	Z29	5	ViralVector	Lesioned
GeoMx 4	Z29	6	ViralVector	Lesioned
GeoMx 4	Z29	7	ViralVector	Lesioned
GeoMx 4	Z29	8	ViralVector	Not
GeoMx 4	Z29	9	ViralVector	Not
GeoMx 4	Z29	11	ViralVector	Not

Supplementary Table 5: Details on NHPs and region types used for GeoMx analysis, post-filtering.

Filtering of ROIs was described in **Section 3.2**. NHP names were modified to start with letters rather than

numbers to avoid being misread as a numerical data type in R.

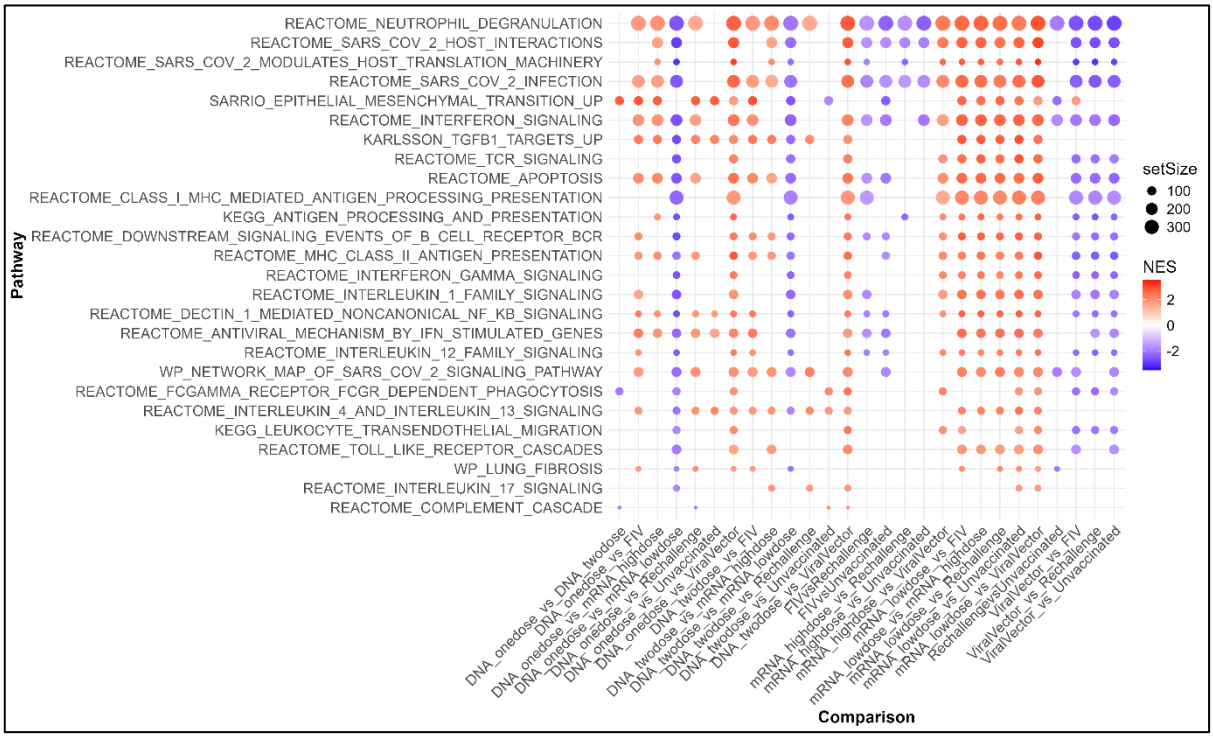

Supplementary Figure 6: Bubble plot showing the detected pathways of interest from the c2 database across all of the vaccine/challenge group one-on-one comparisons, in all region types.

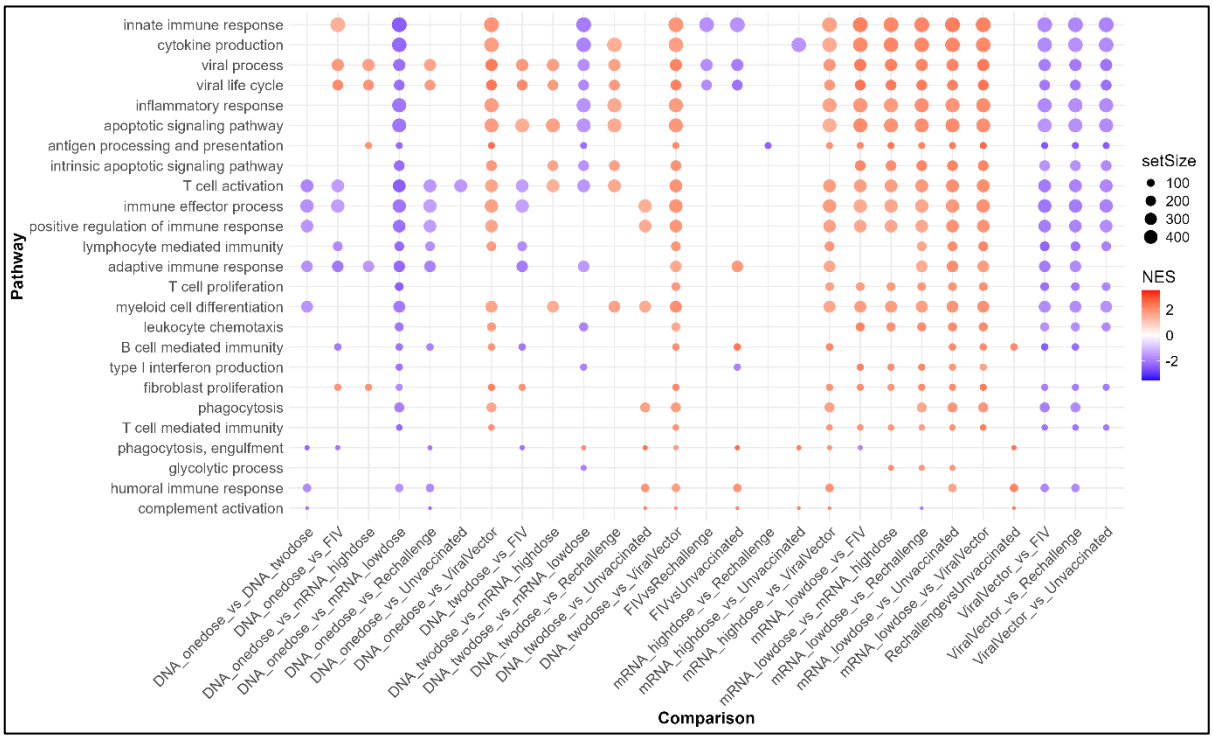

Supplementary Figure 7: Bubble plot showing the detected pathways of interest from the GO-BP database across all of the vaccine/challenge group one-on-one comparisons, in all region types.

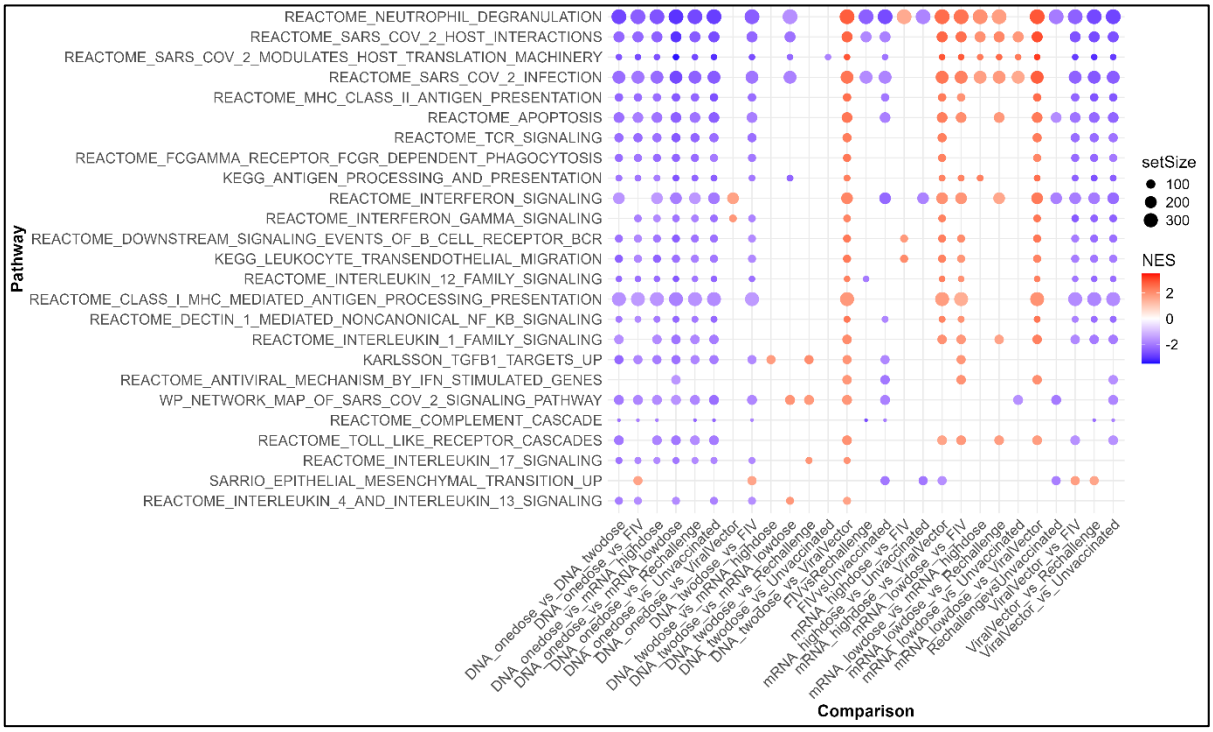

Supplementary Figure 8: Bubble plot showing the detected pathways of interest from the c2 database across all of the vaccine/challenge group one-on-one comparisons, in non-lesioned regions.

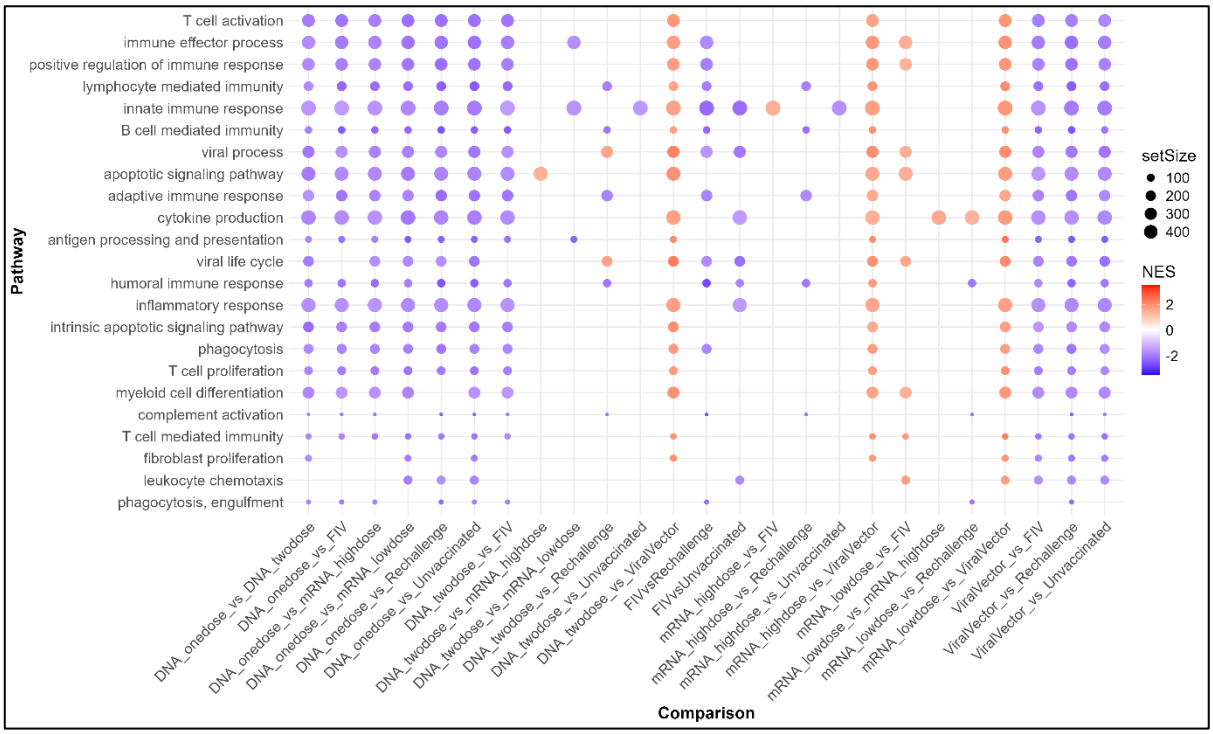

Supplementary Figure 9: Bubble plot showing the detected pathways of interest from the GO-BP database across all of the vaccine/challenge group one-on-one comparisons, in all non-lesioned regions.

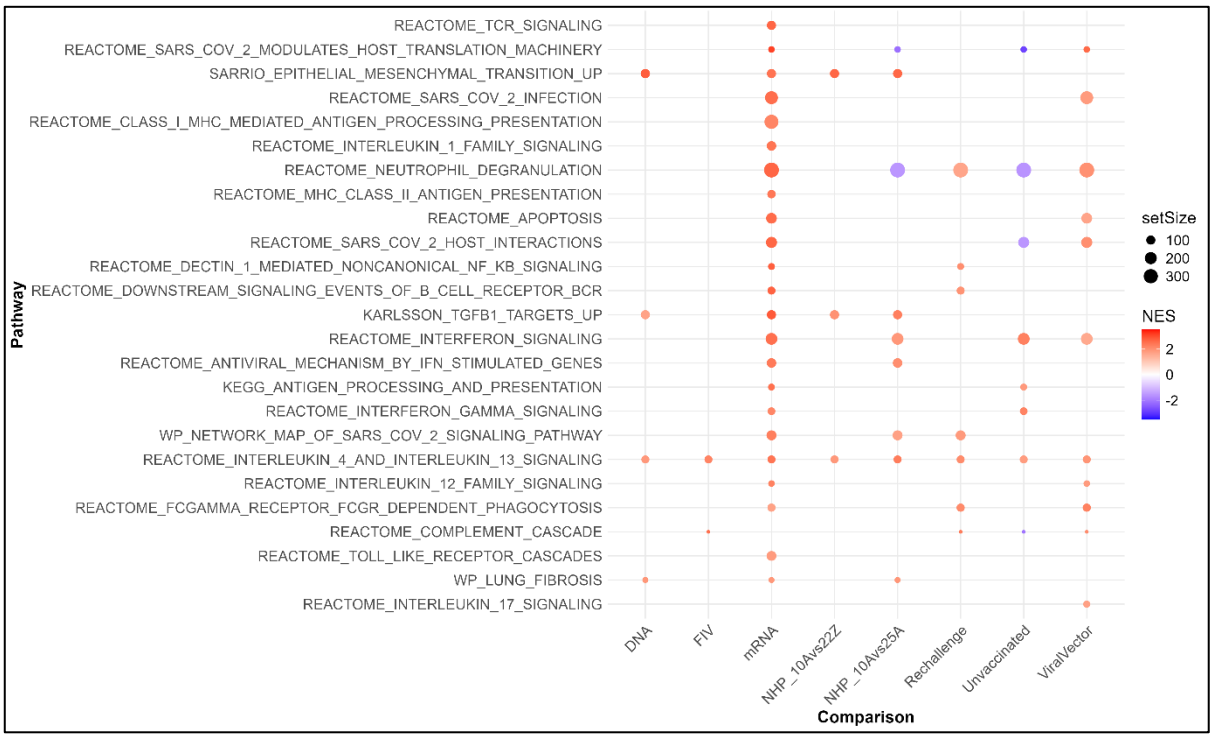

Supplementary Figure 10: Bubble plot showing the detected pathways of interest from the c2 database across all of the NHP one-on-one comparisons, in all region types.

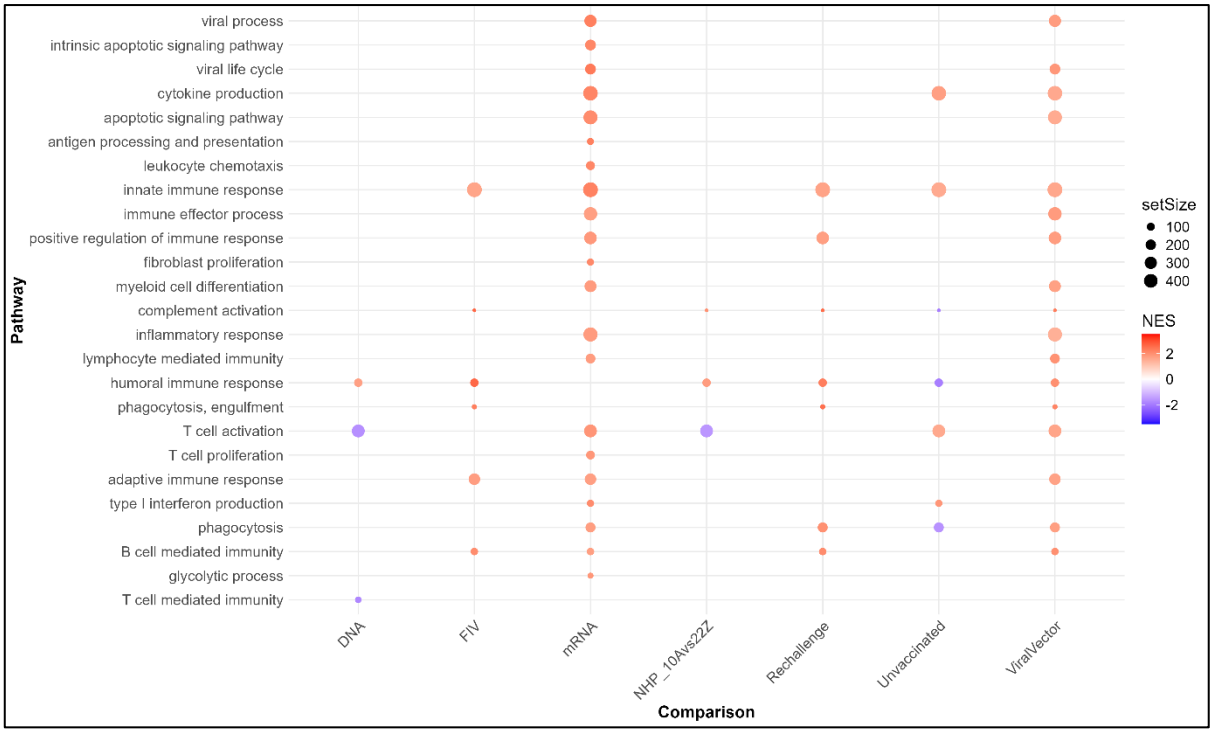

Supplementary Figure 11: Bubble plot showing the detected pathways of interest from the GO-BP database across all of the NHP one-on-one comparisons, in all region types.

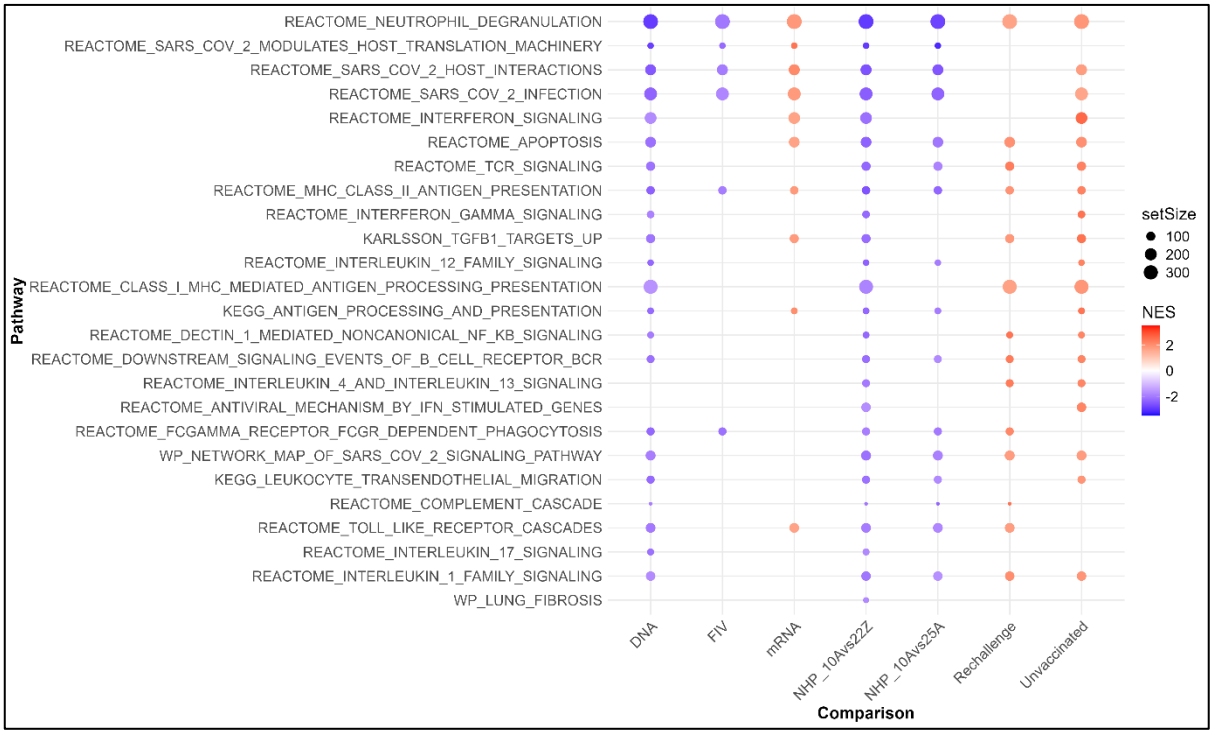

Supplementary Figure 12: Bubble plot showing the detected pathways of interest from the c2 database across all of the NHP one-on-one comparisons, in non-lesioned regions.

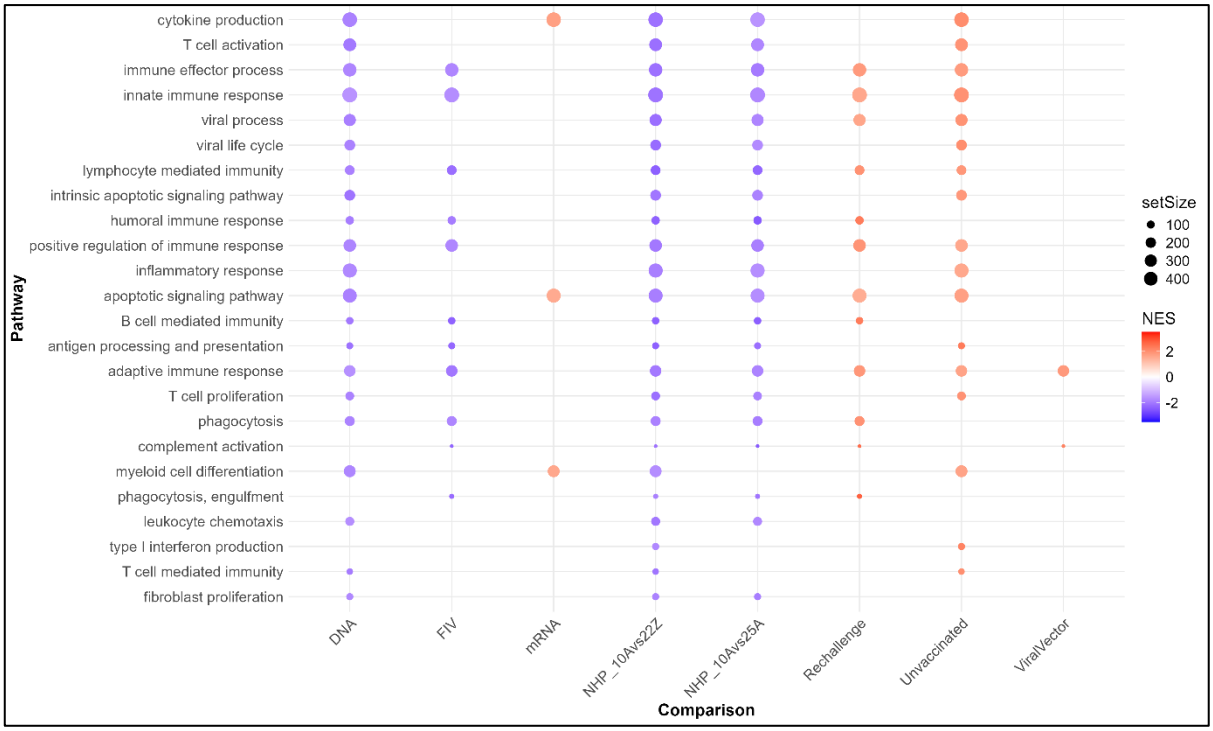

Supplementary Figure 13: Bubble plot showing the detected pathways of interest from the GO-BP database across all of the NHP one-on-one comparisons, in non-lesioned regions.

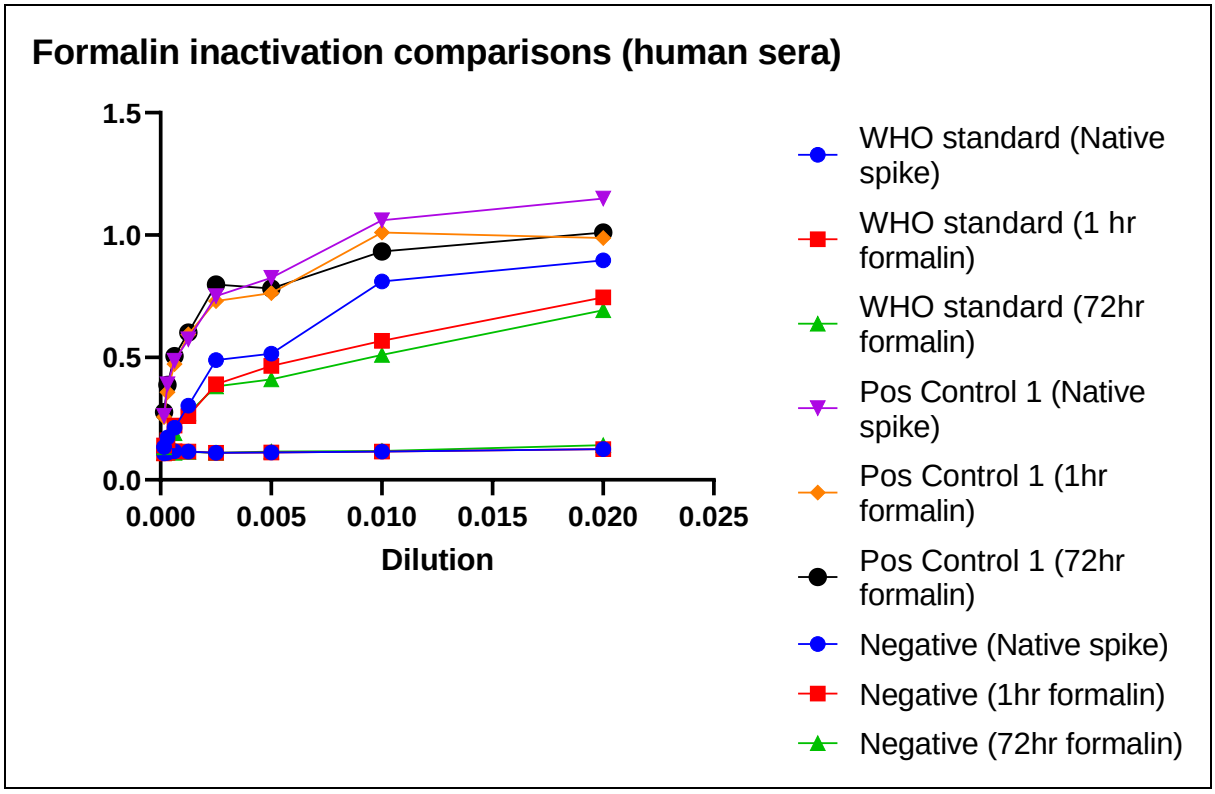

Supplementary Figure 14: Comparison of OD readout from anti-SARS-CoV-2 spike ELISA when using native vs formalin-inactivated spike protein (inactivated for 1hr or 72hr), with different human sera (WHO positive standard, positive control from convalescent individual and negative control).

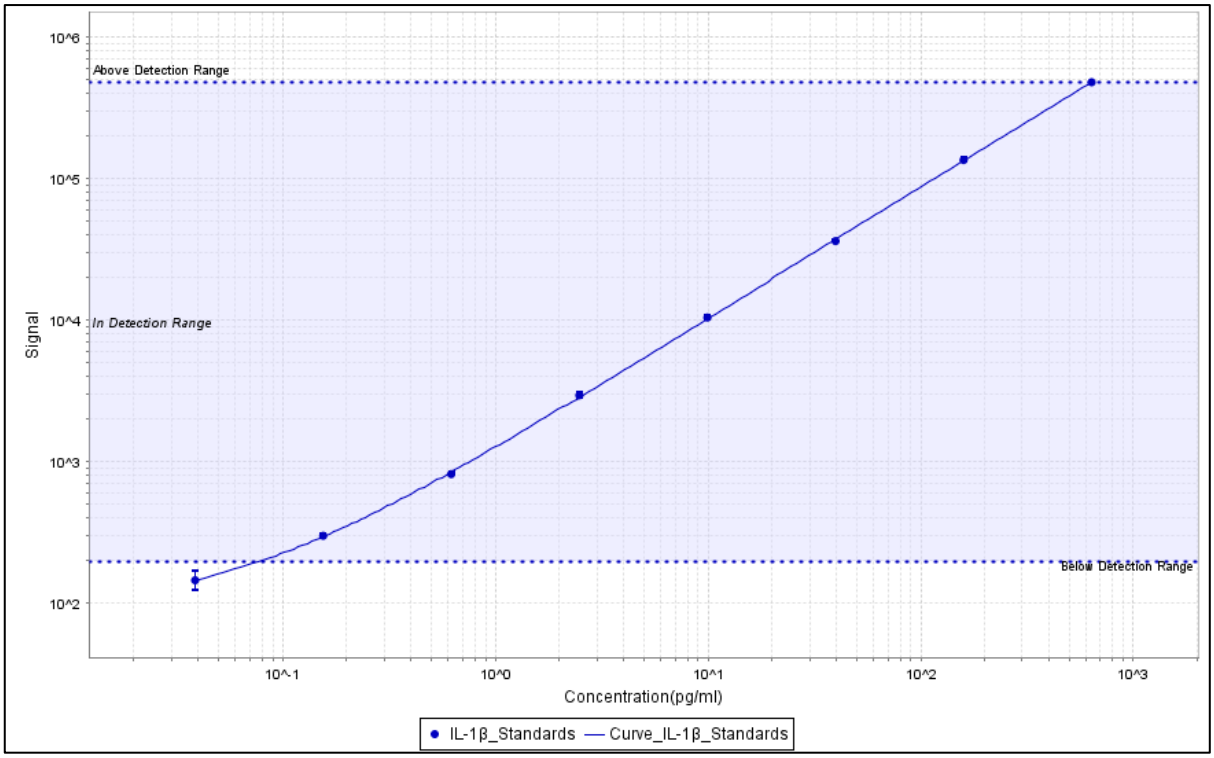

Supplementary Figure 15: IL-1β standard curve. Generated using the MSD discovery workbench software (Meso Scale Discovery).

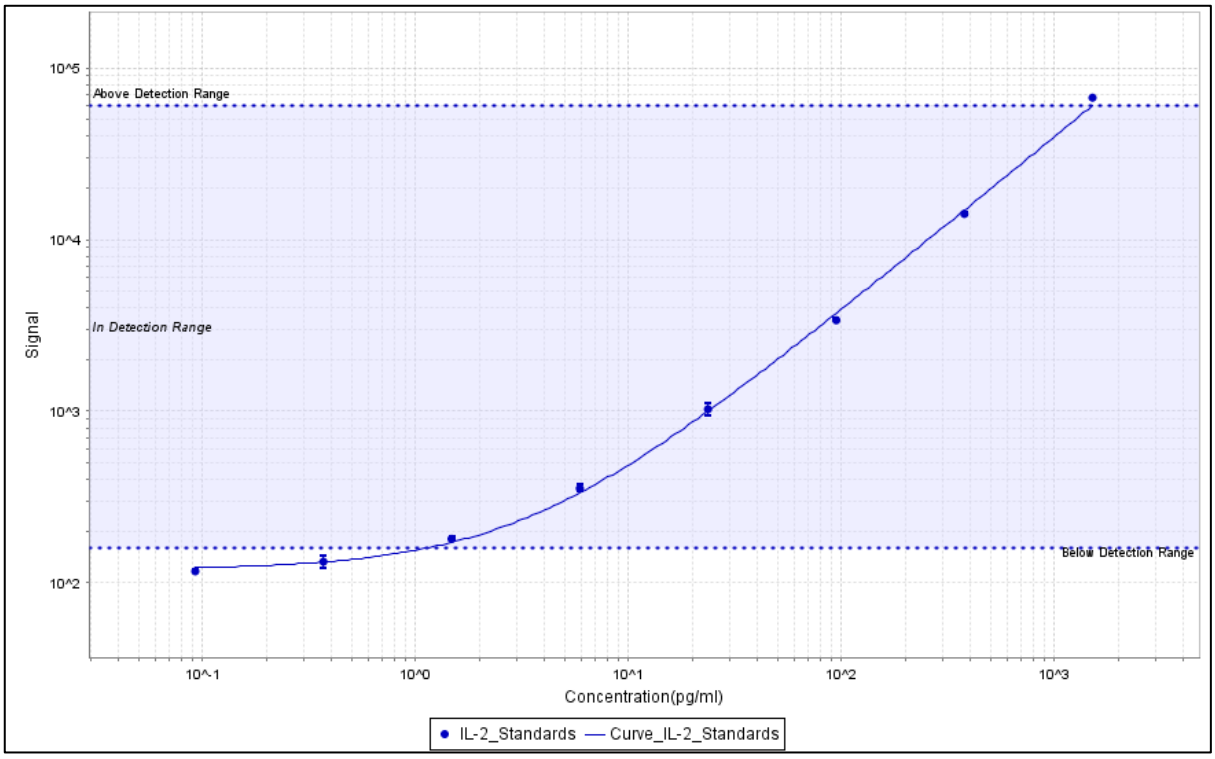

Supplementary Figure 16: IL-2 standard curve. Generated using the MSD discovery workbench software (Meso Scale Discovery).

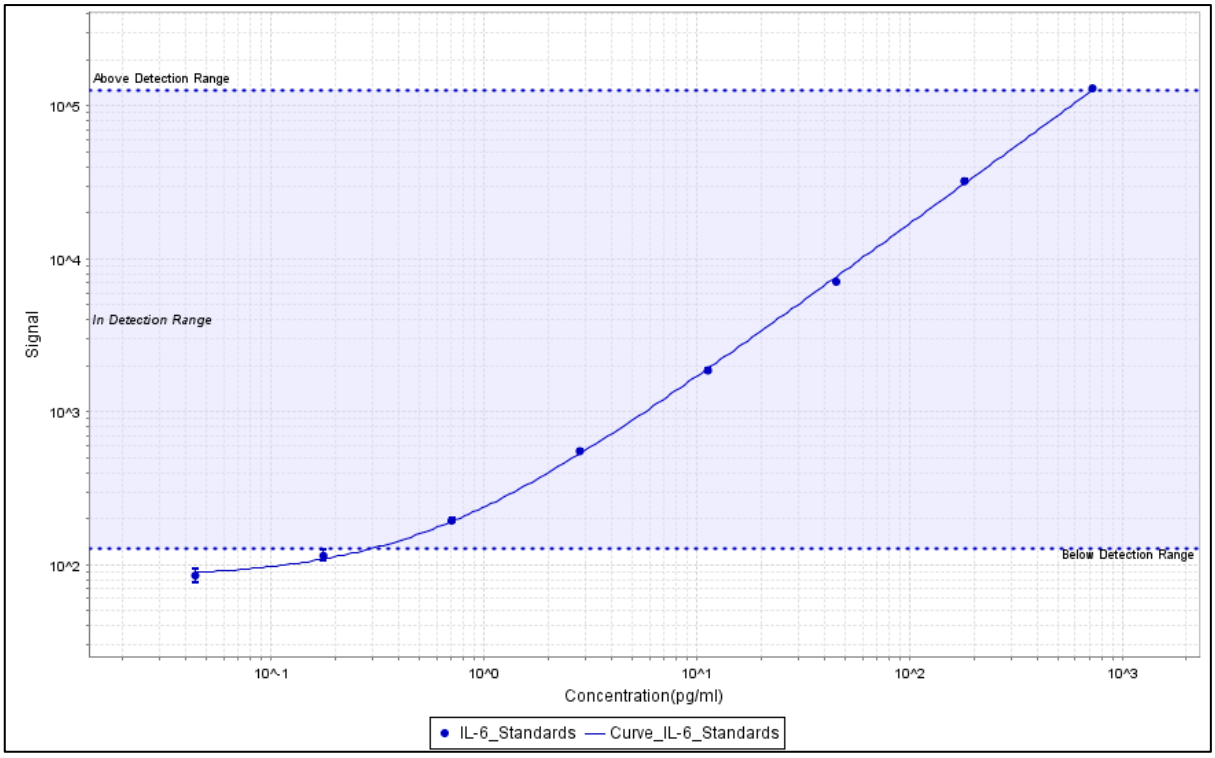

Supplementary Figure 17: IL-6 standard curve. Generated using the MSD discovery workbench software (Meso Scale Discovery).

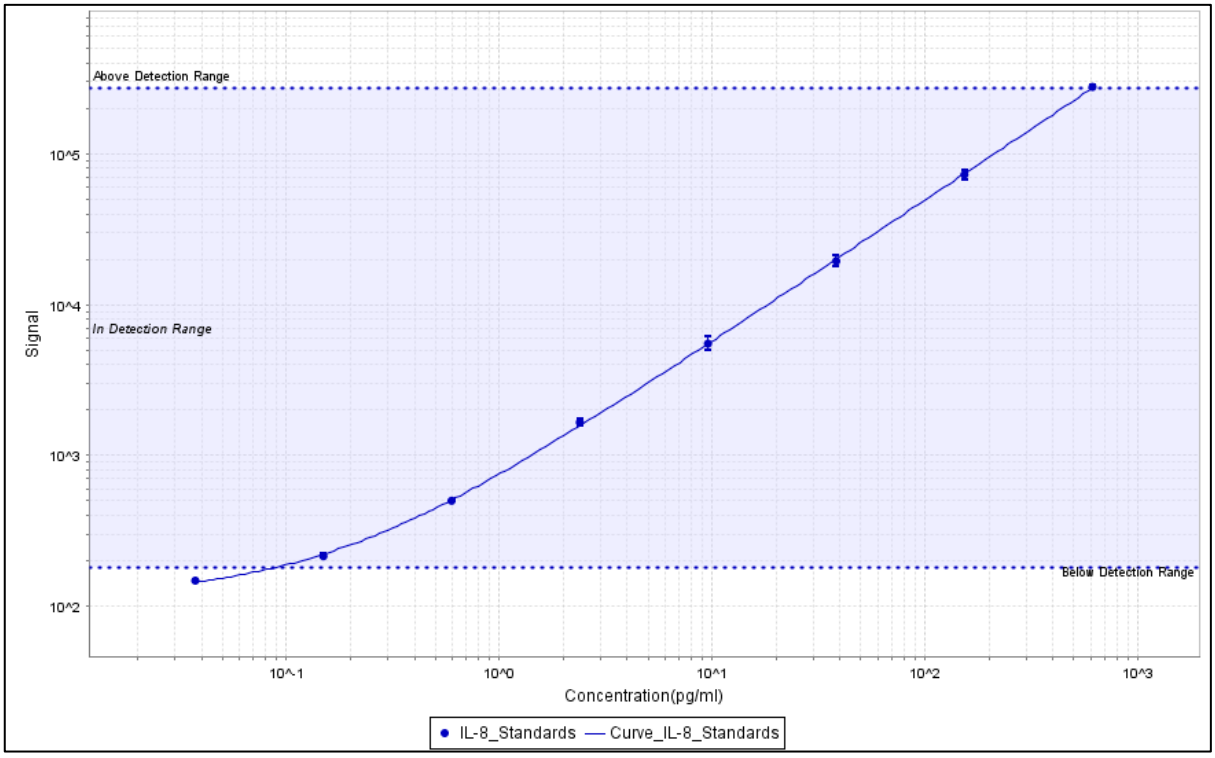

Supplementary Figure 18: IL-8 standard curve. Generated using the MSD discovery workbench software (Meso Scale Discovery).

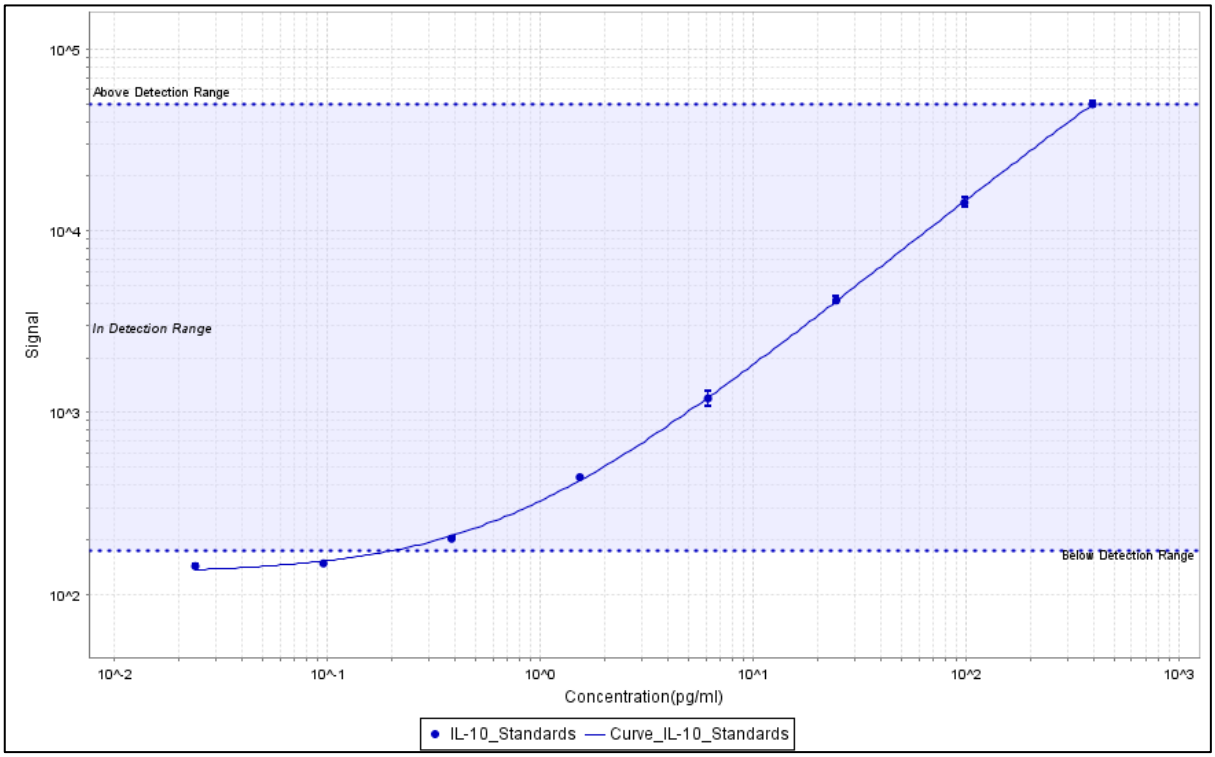

Supplementary Figure 19: IL-10 standard curve. Generated using the MSD discovery workbench software (Meso Scale Discovery).

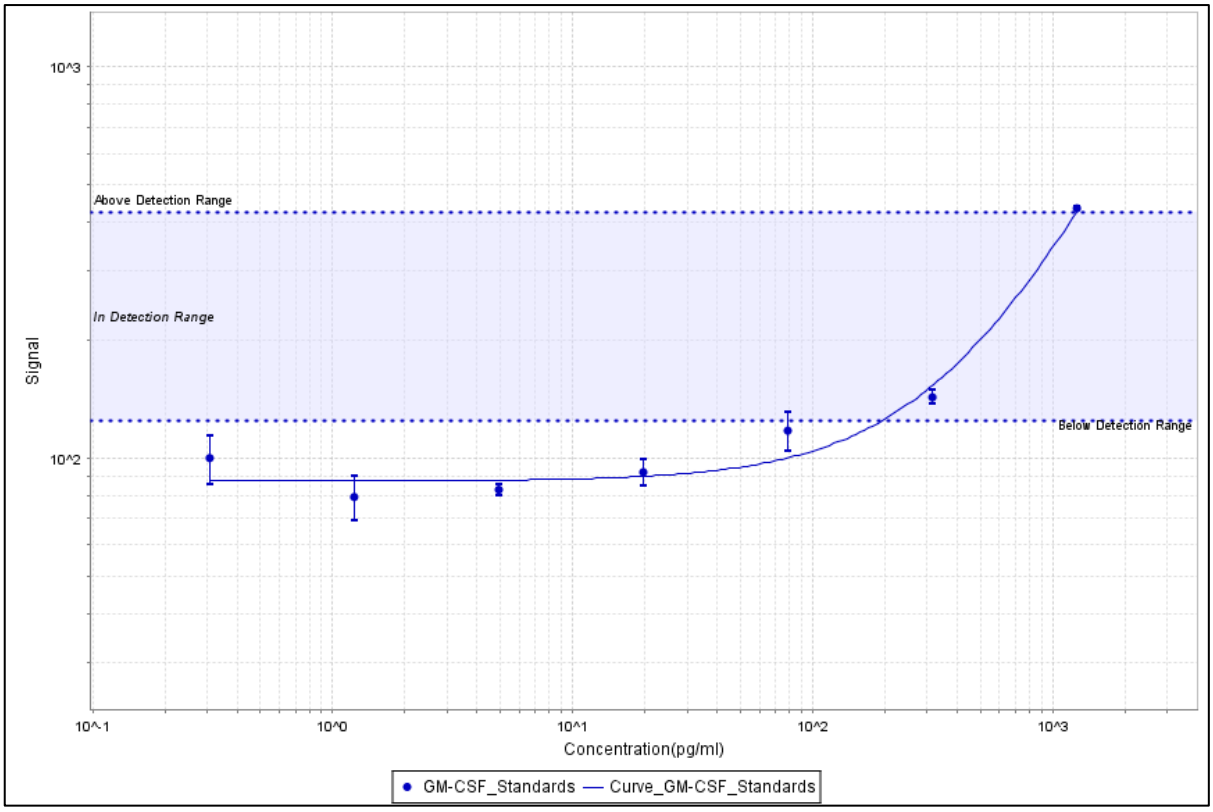

Supplementary Figure 20: GM-CSF standard curve. Generated using the MSD discovery workbench software (Meso Scale Discovery).

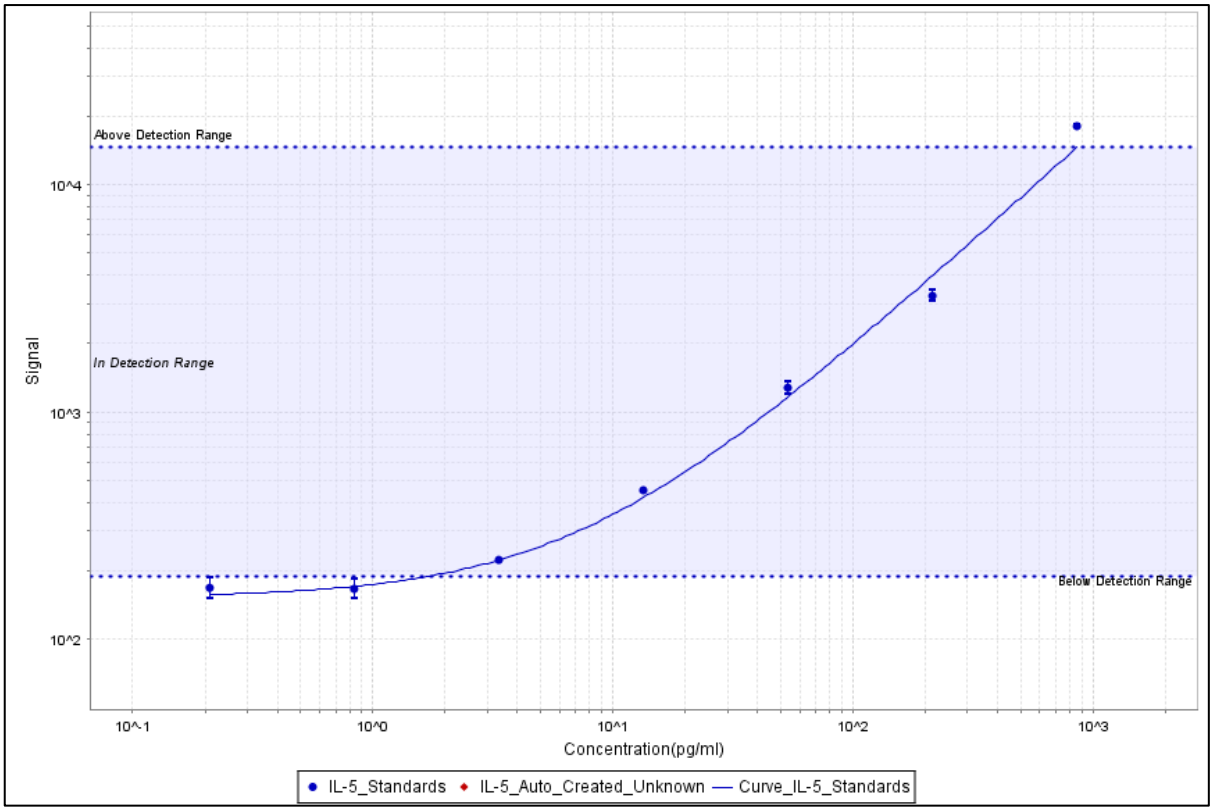

Supplementary Figure 21: IL-5 standard curve. Generated using the MSD discovery workbench software (Meso Scale Discovery).

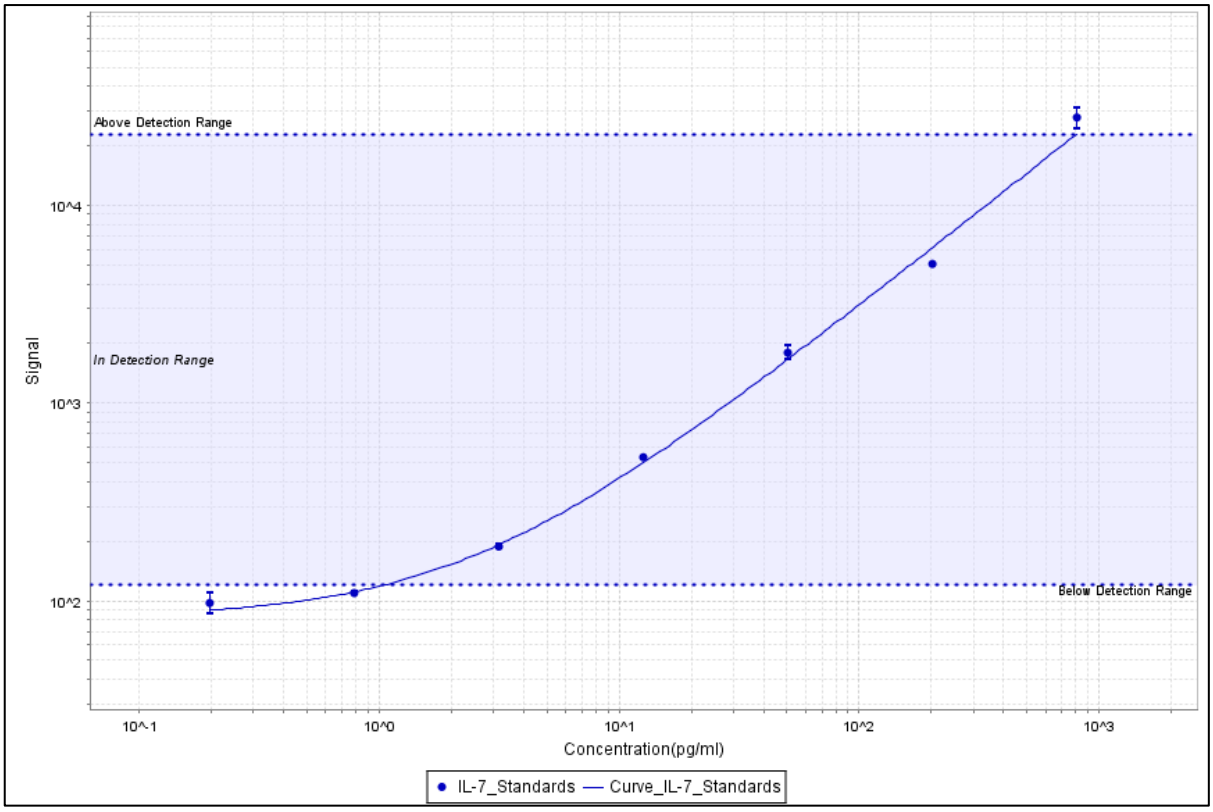

Supplementary Figure 22: IL-7 standard curve. Generated using the MSD discovery workbench software (Meso Scale Discovery).

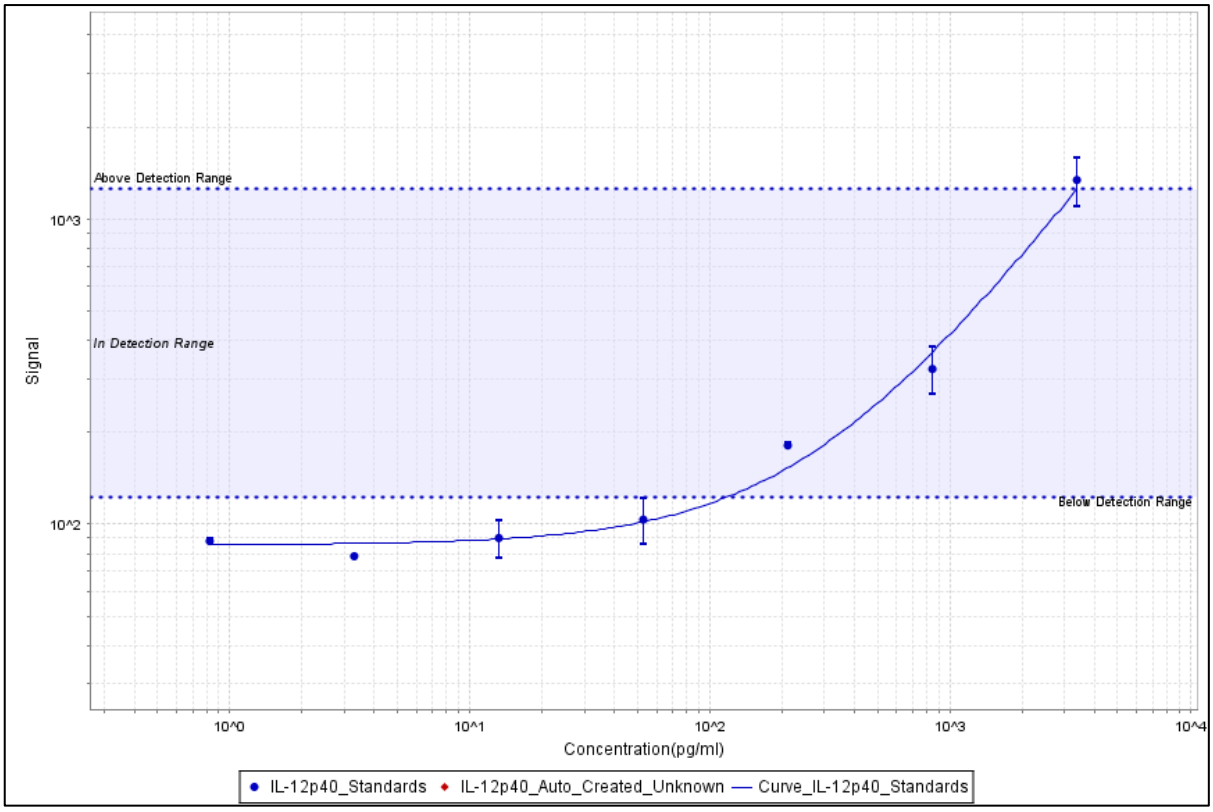

Supplementary Figure 23: IL-12p40 standard curve. Generated using the MSD discovery workbench software (Meso Scale Discovery).

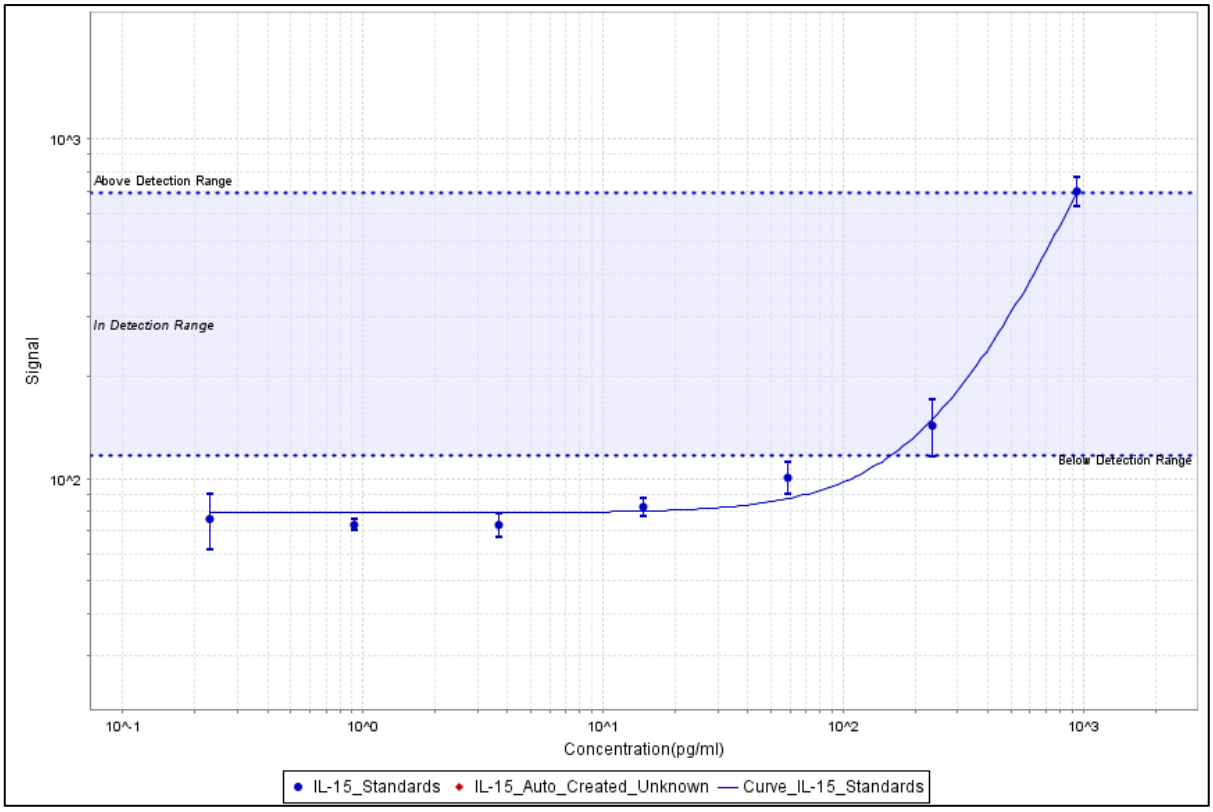

Supplementary Figure 24: IL-15 standard curve. Generated using the MSD discovery workbench software (Meso Scale Discovery).

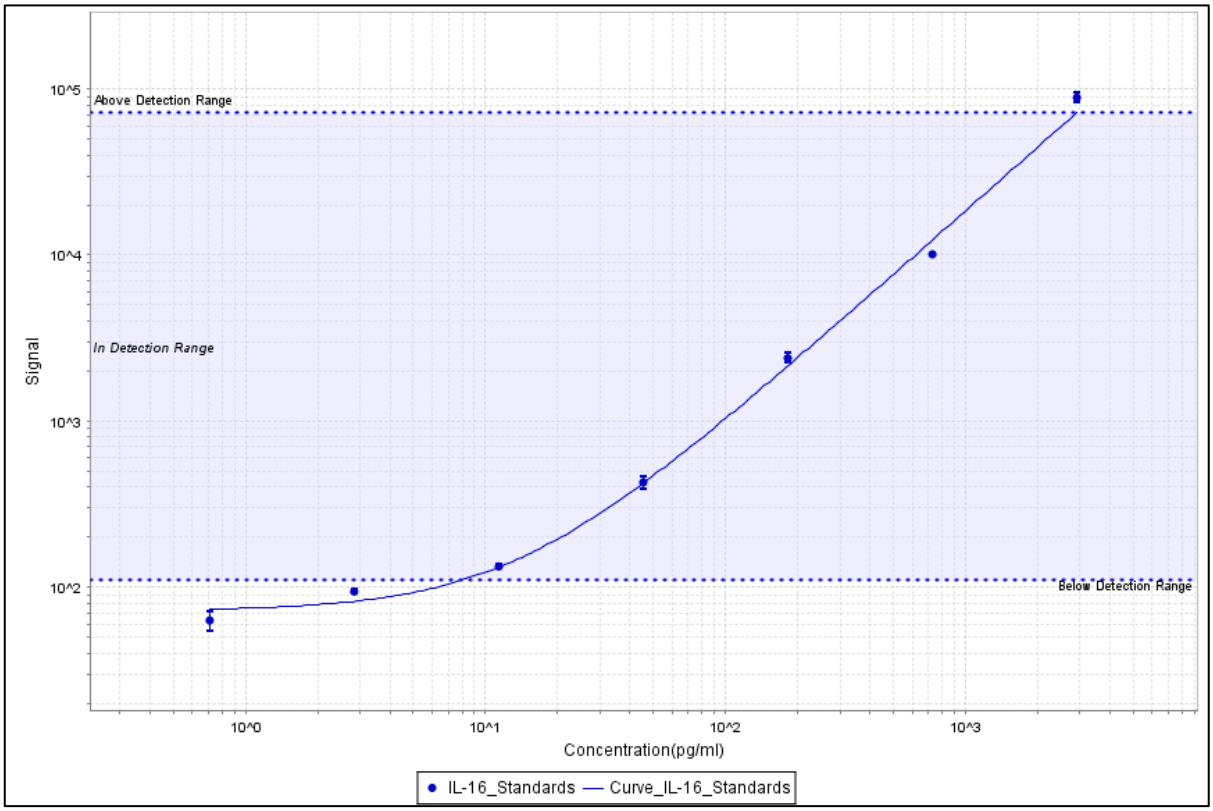

Supplementary Figure 25: IL-16 standard curve. Generated using the MSD discovery workbench software (Meso Scale Discovery).

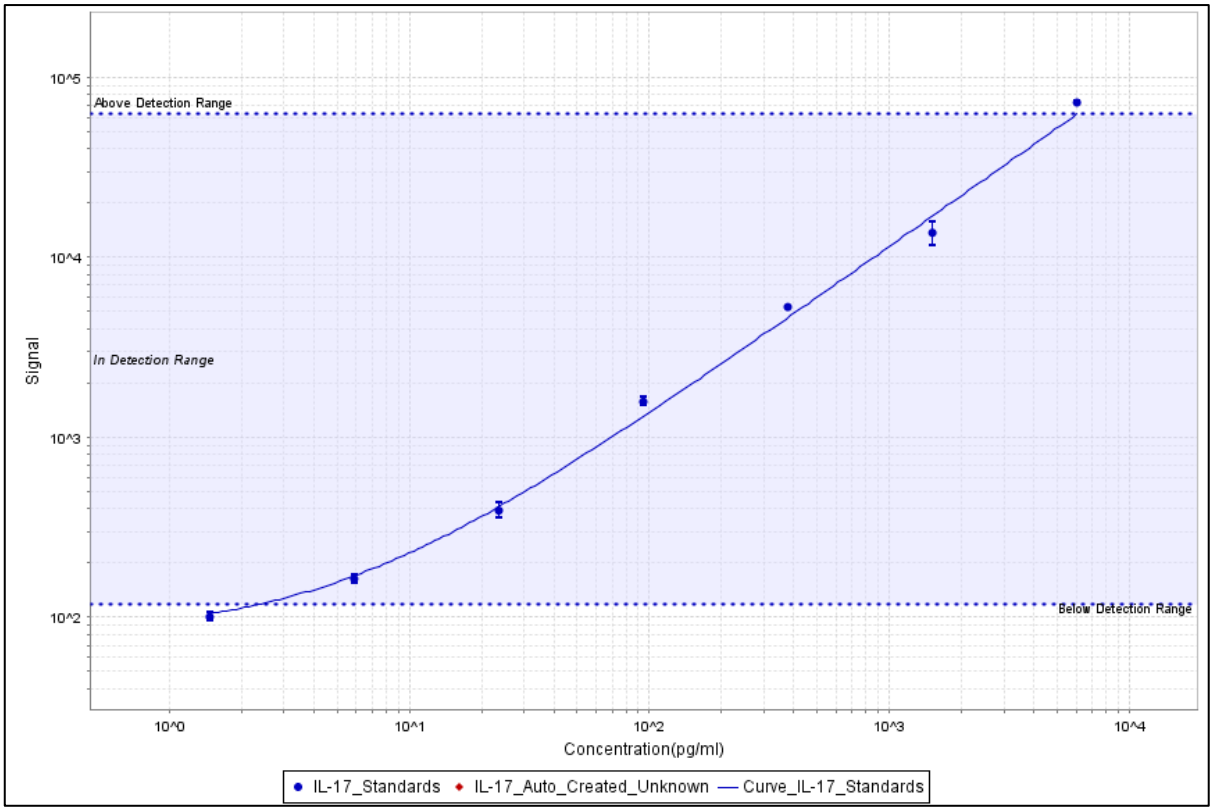

Supplementary Figure 26: IL-17 standard curve. Generated using the MSD discovery workbench software (Meso Scale Discovery).

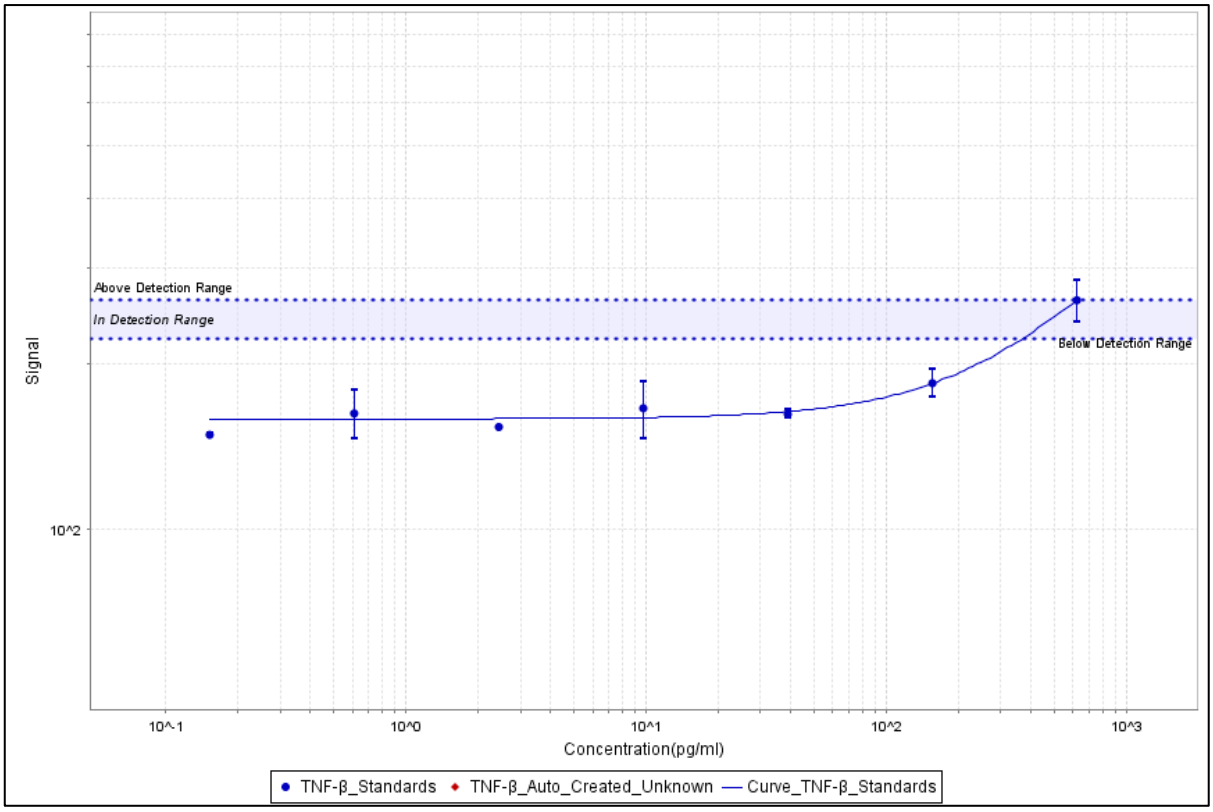

Supplementary Figure 27: TNF-β standard curve. Generated using the MSD discovery workbench software (Meso Scale Discovery).

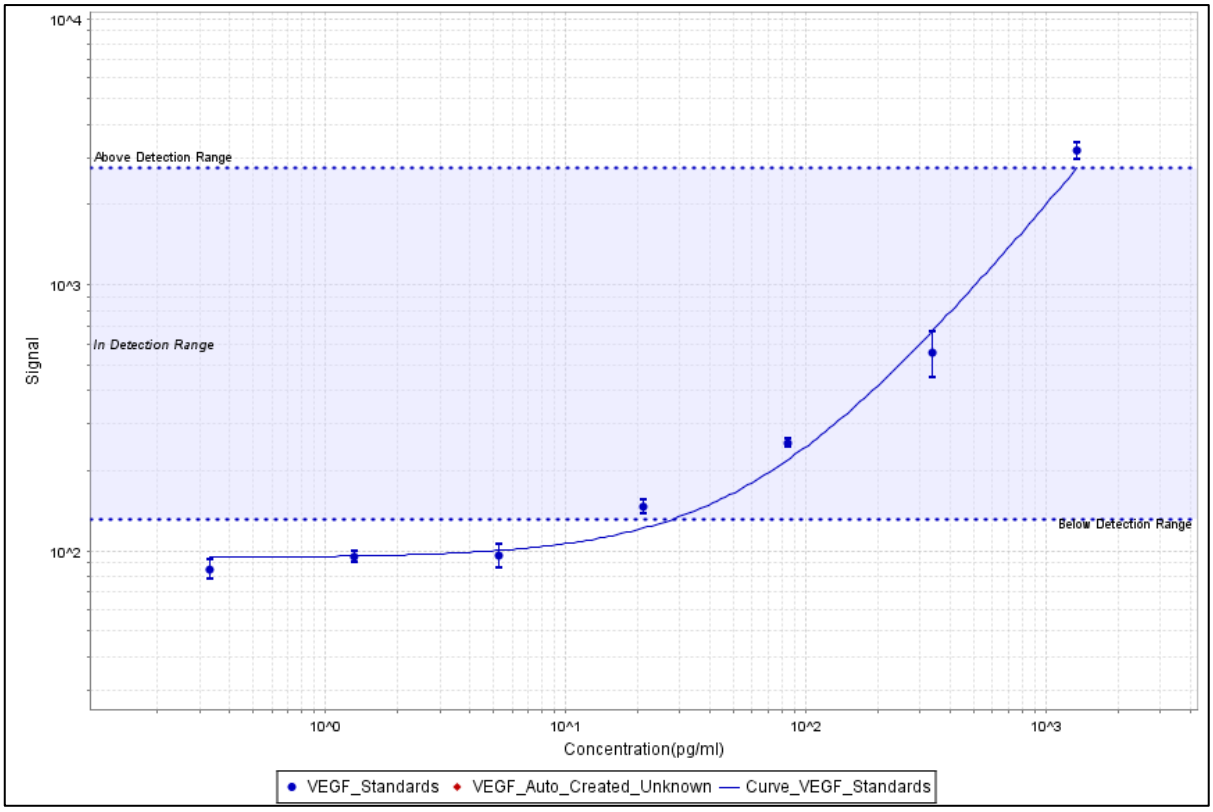

Supplementary Figure 28: VEGF standard curve. Generated using the MSD discovery workbench software (Meso Scale Discovery).

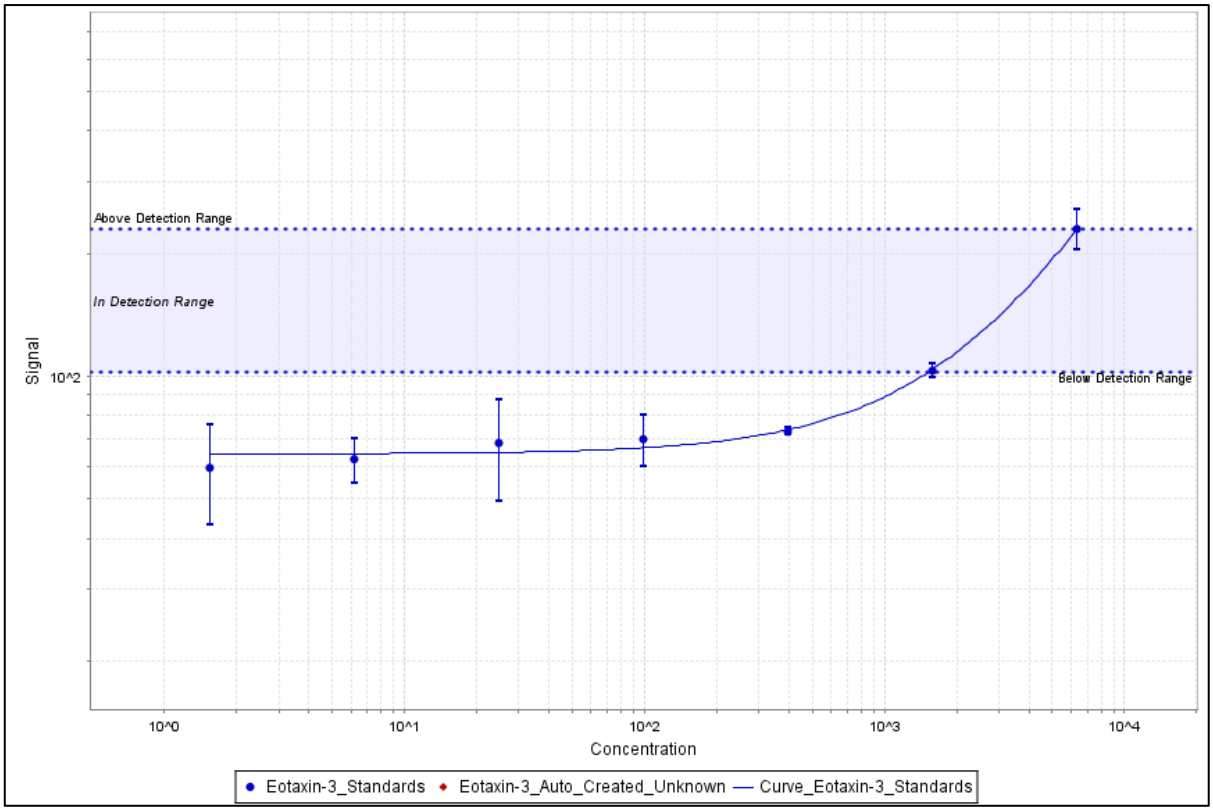

Supplementary Figure 29: Eotaxin-3 standard curve. Generated using the MSD discovery workbench software (Meso Scale Discovery).

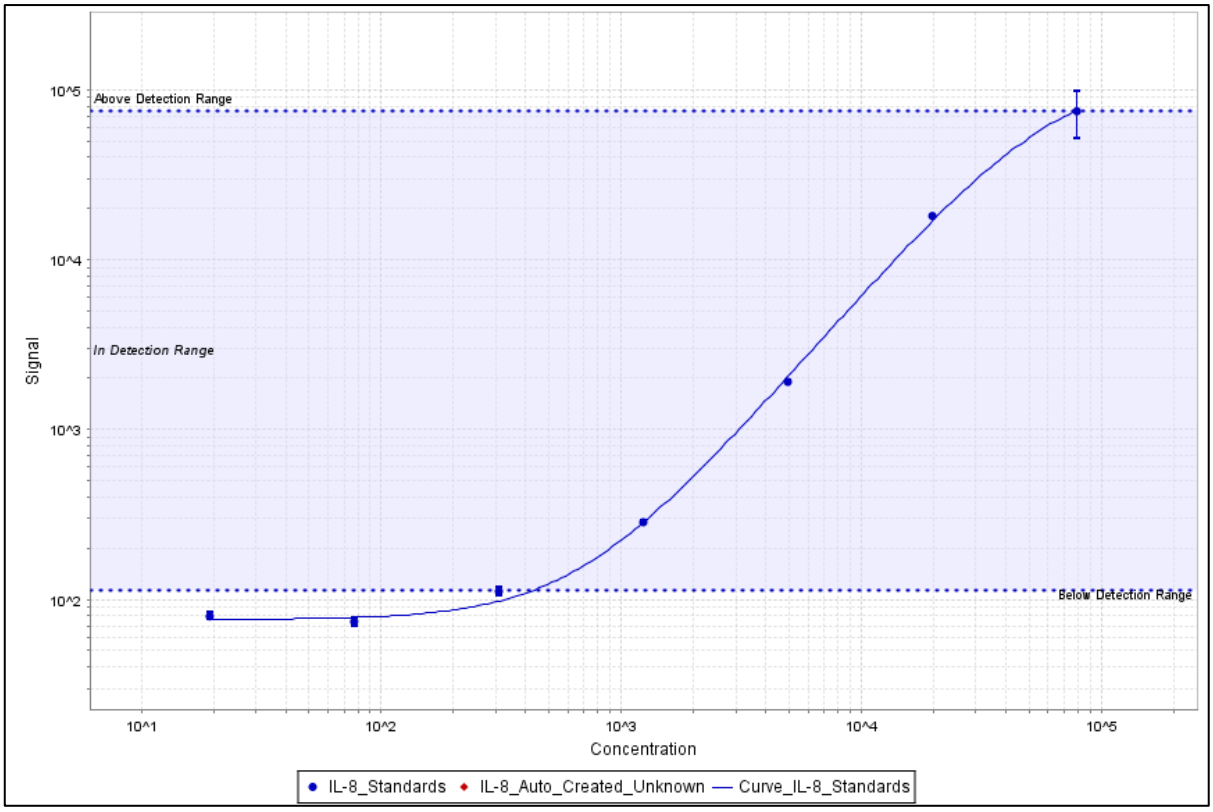

Supplementary Figure 30: IL-8 standard curve (from the chemokine plate). Generated using the MSD discovery workbench software (Meso Scale Discovery).

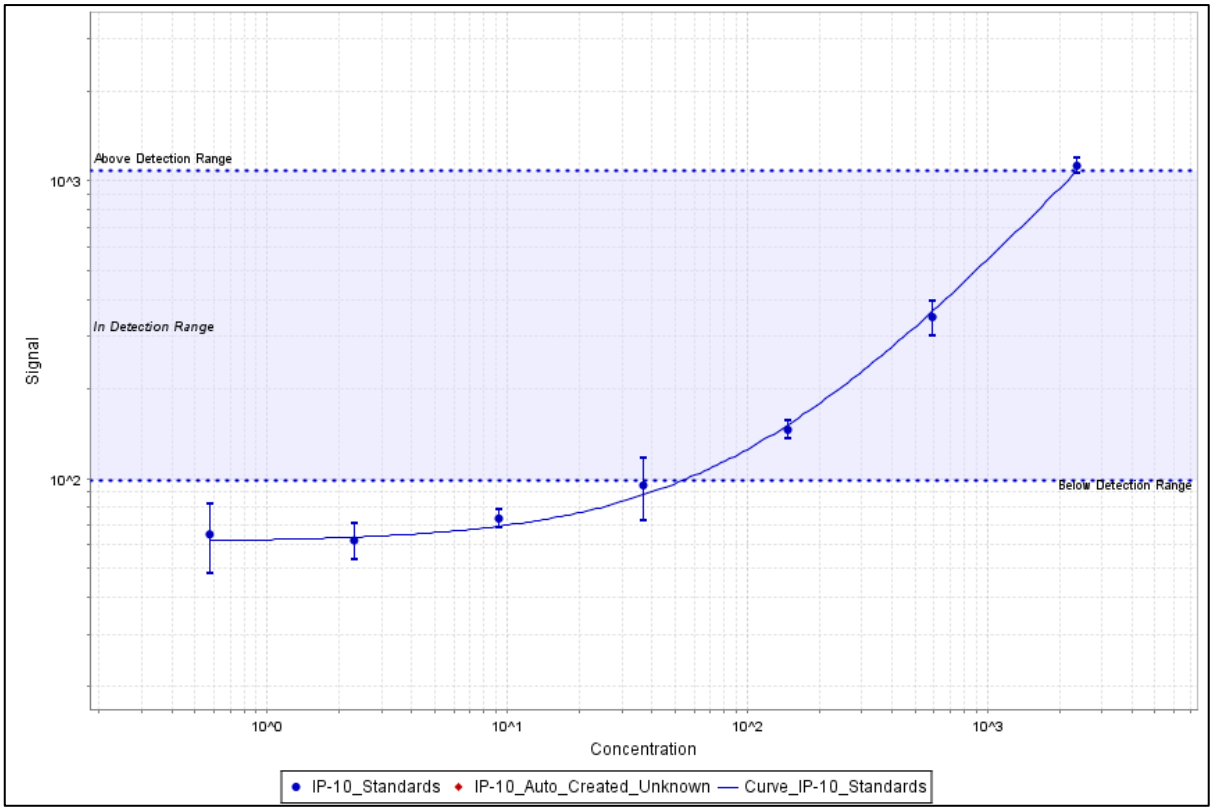

Supplementary Figure 31: IP-10 standard curve. Generated using the MSD discovery workbench software (Meso Scale Discovery).

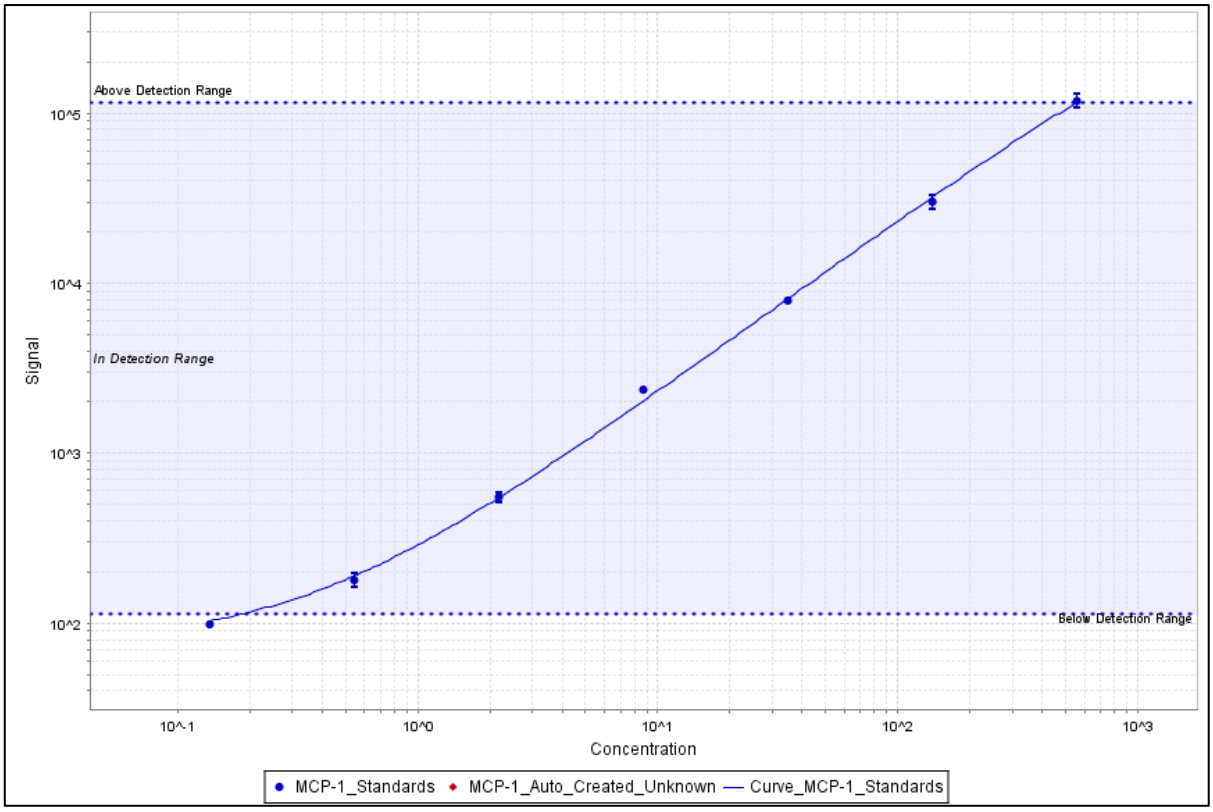

Supplementary Figure 32: MCP-1 standard curve. Generated using the MSD discovery workbench software (Meso Scale Discovery).

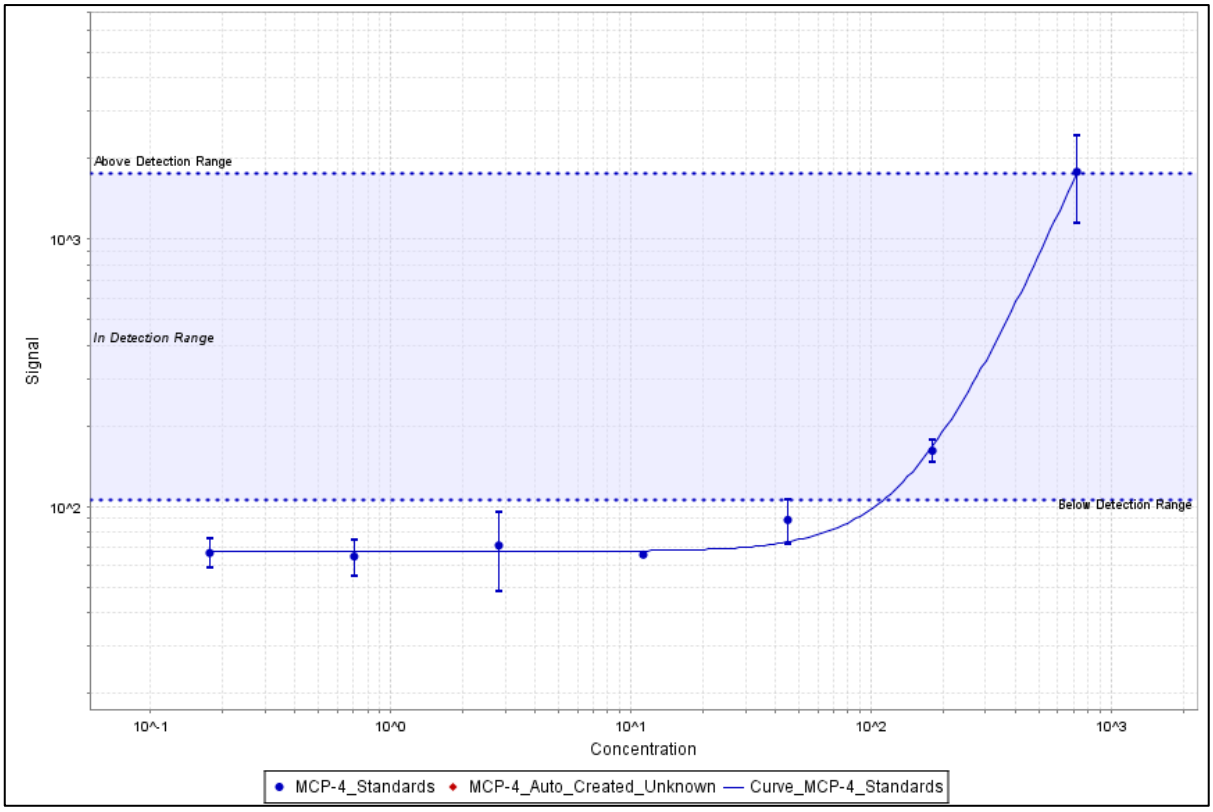

Supplementary Figure 33: MCP-4 standard curve. Generated using the MSD discovery workbench software (Meso Scale Discovery).

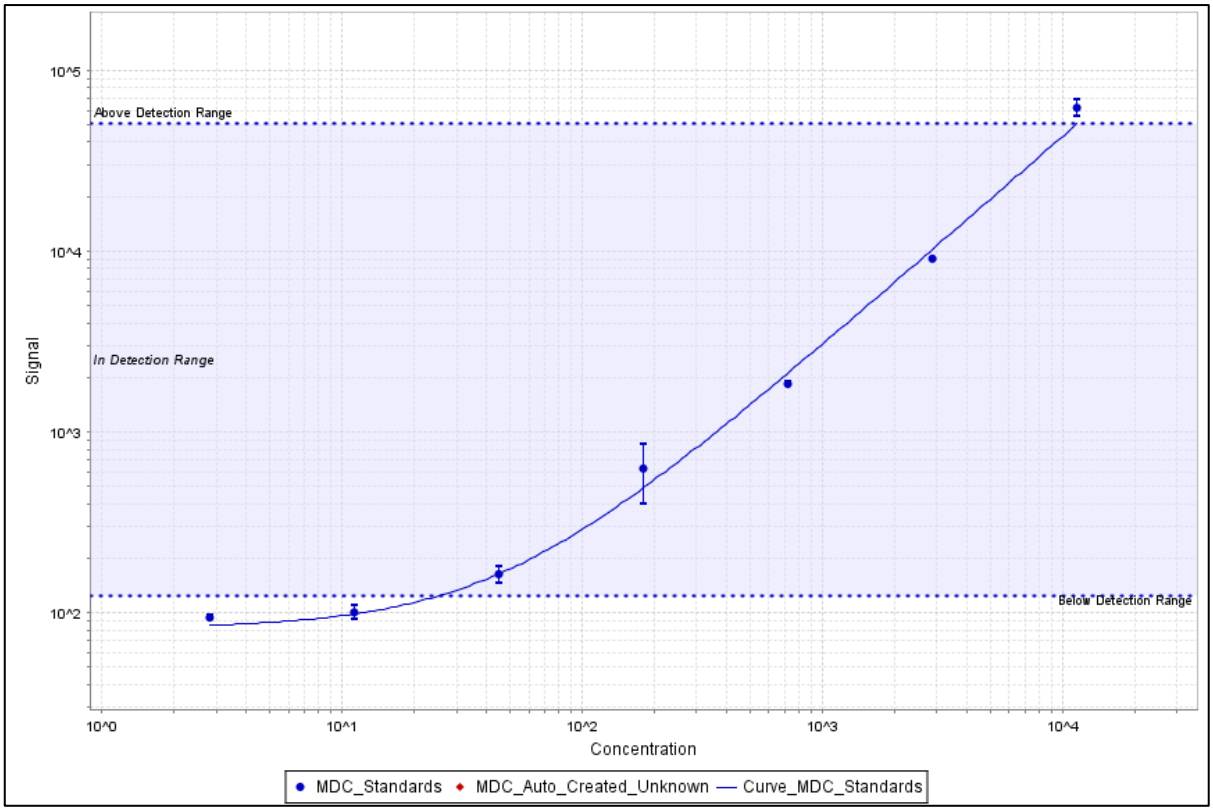

Supplementary Figure 34: MDC standard curve. Generated using the MSD discovery workbench software (Meso Scale Discovery).

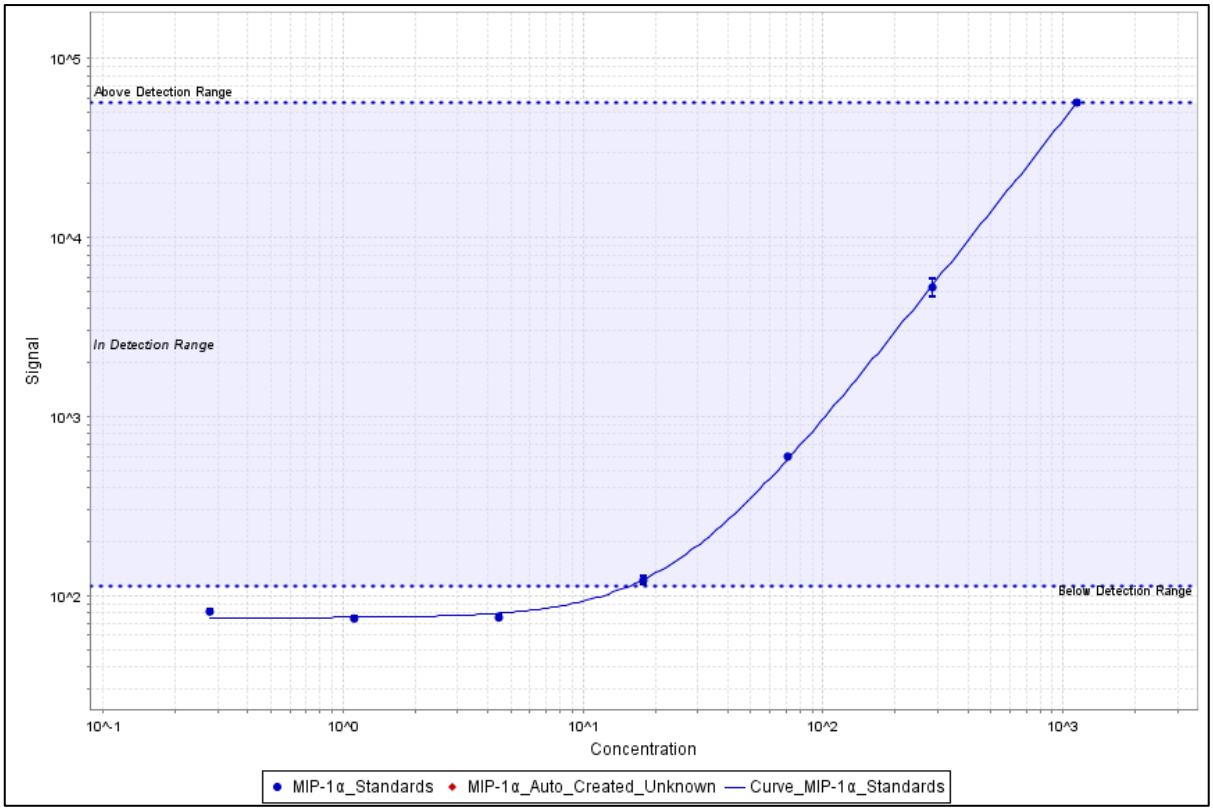

Supplementary Figure 35: MIP-1α standard curve. Generated using the MSD discovery workbench software (Meso Scale Discovery).

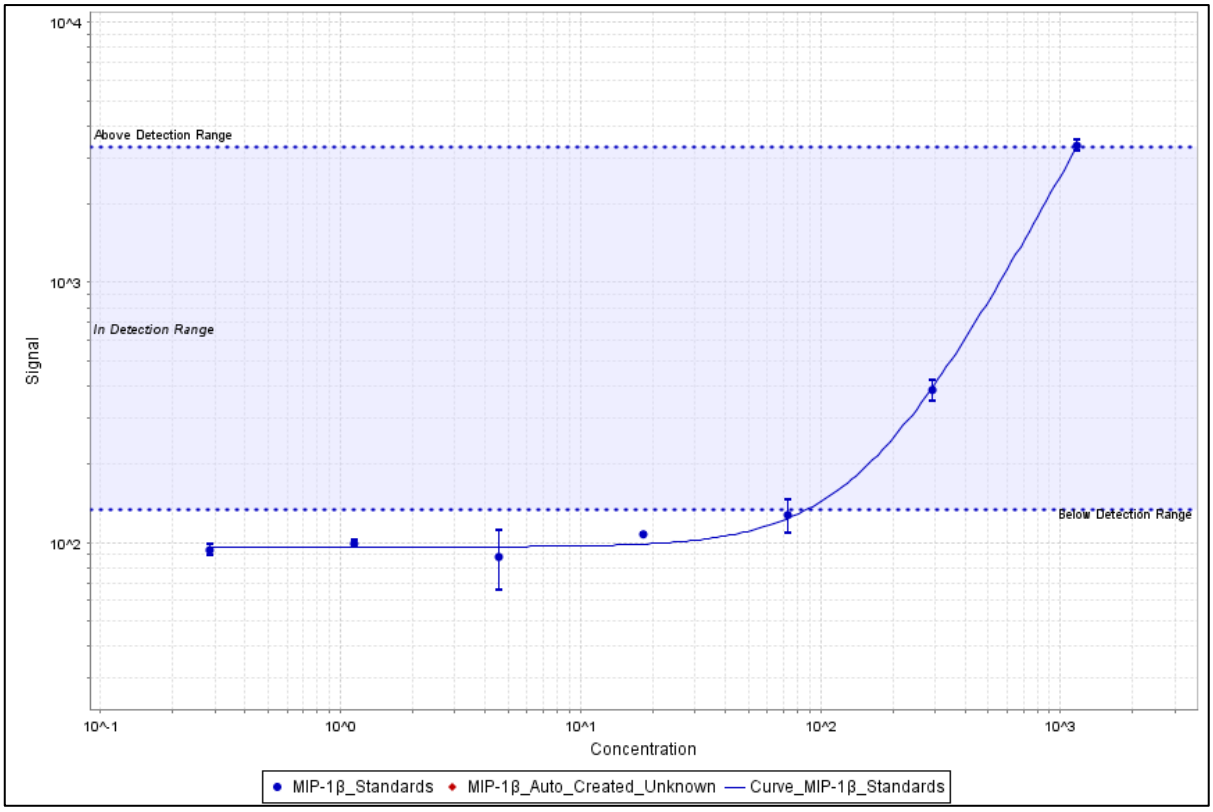

Supplementary Figure 36: MIP-1β standard curve. Generated using the MSD discovery workbench software (Meso Scale Discovery).

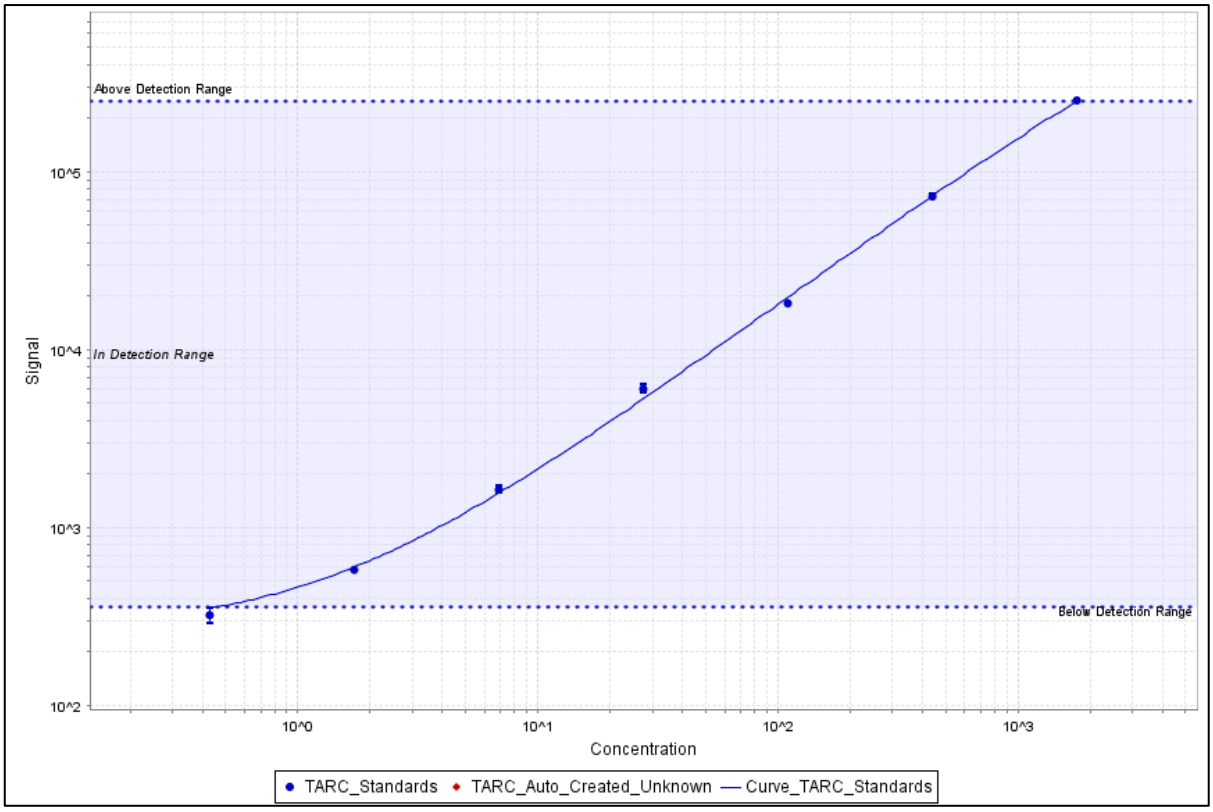

Supplementary Figure 37: TARC standard curve. Generated using the MSD discovery workbench software (Meso Scale Discovery).

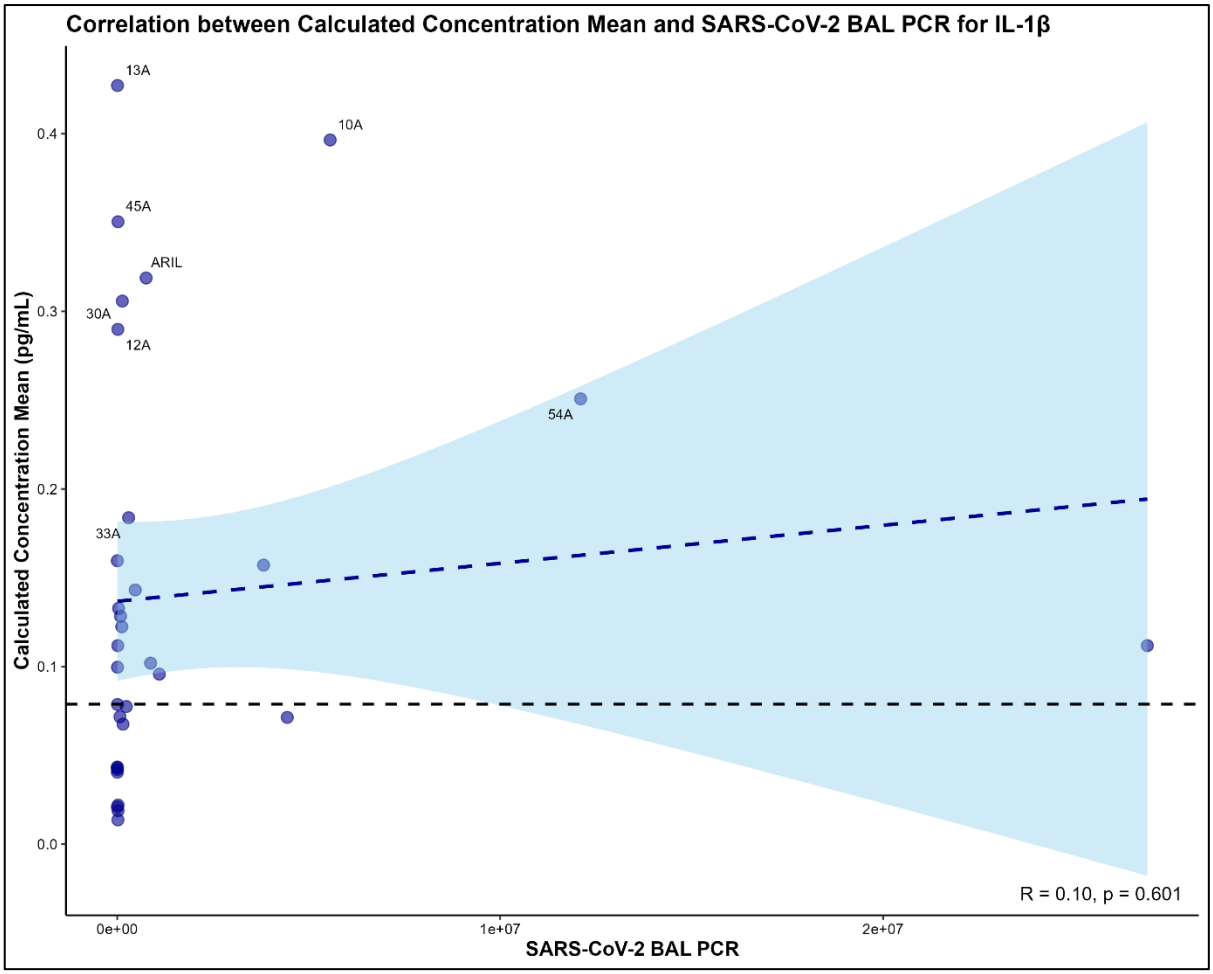

Supplementary Figure 38: IL-1β and SARS-CoV-2 BAL PCR level correlation plot. The dark blue dashed line is the regression line of the correlation between the cytokine concentration (pg/mL) and level of virus detected by BAL PCR (raw values), while the light blue colour represents the range of the associated confidence interval. The black dashed line represents the detection limit of the machine. The samples shown below this level could still be interpolated onto the standard curve. Individual samples are overlaid as blue dots. Samples too low to be interpolated are not shown. Samples in the upper quartile of cytokine concentration are annotated according to NHP ID. The R value is Pearson's correlation coefficient and the p value is calculated using Pearson's correlation test.

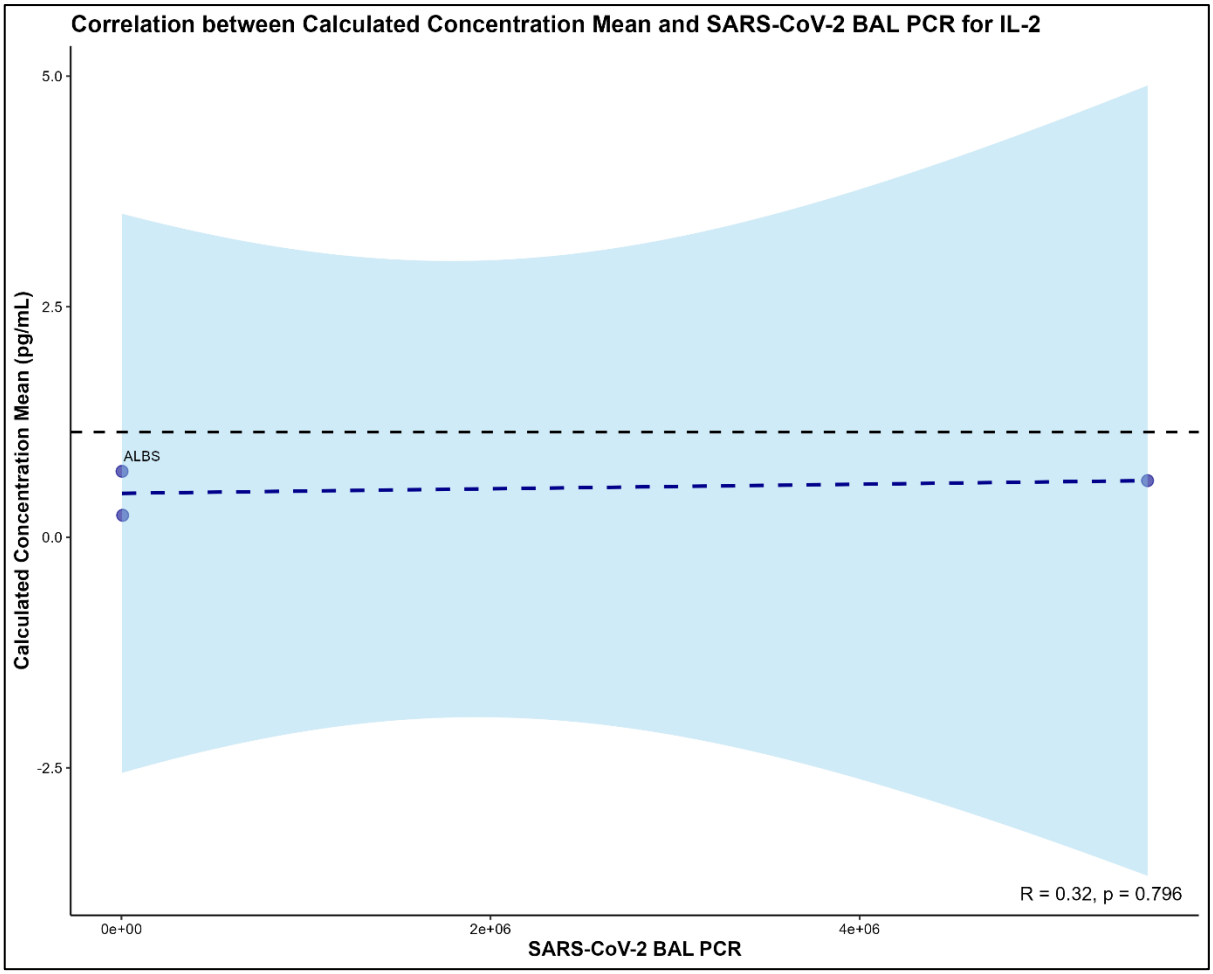

Supplementary Figure 39: IL-2 and SARS-CoV-2 BAL PCR level correlation plot. The dark blue dashed line is the regression line of the correlation between the cytokine concentration (pg/mL) and level of virus detected by BAL PCR (raw values), while the light blue colour represents the range of the associated confidence interval. The black dashed line represents the detection limit of the machine. The samples shown below this level could still be interpolated onto the standard curve. Individual samples are overlaid as blue dots. Samples too low to be interpolated are not shown. Samples in the upper quartile of cytokine concentration are annotated according to NHP ID. The R value is Pearson's correlation coefficient and the p value is calculated using Pearson's correlation test.

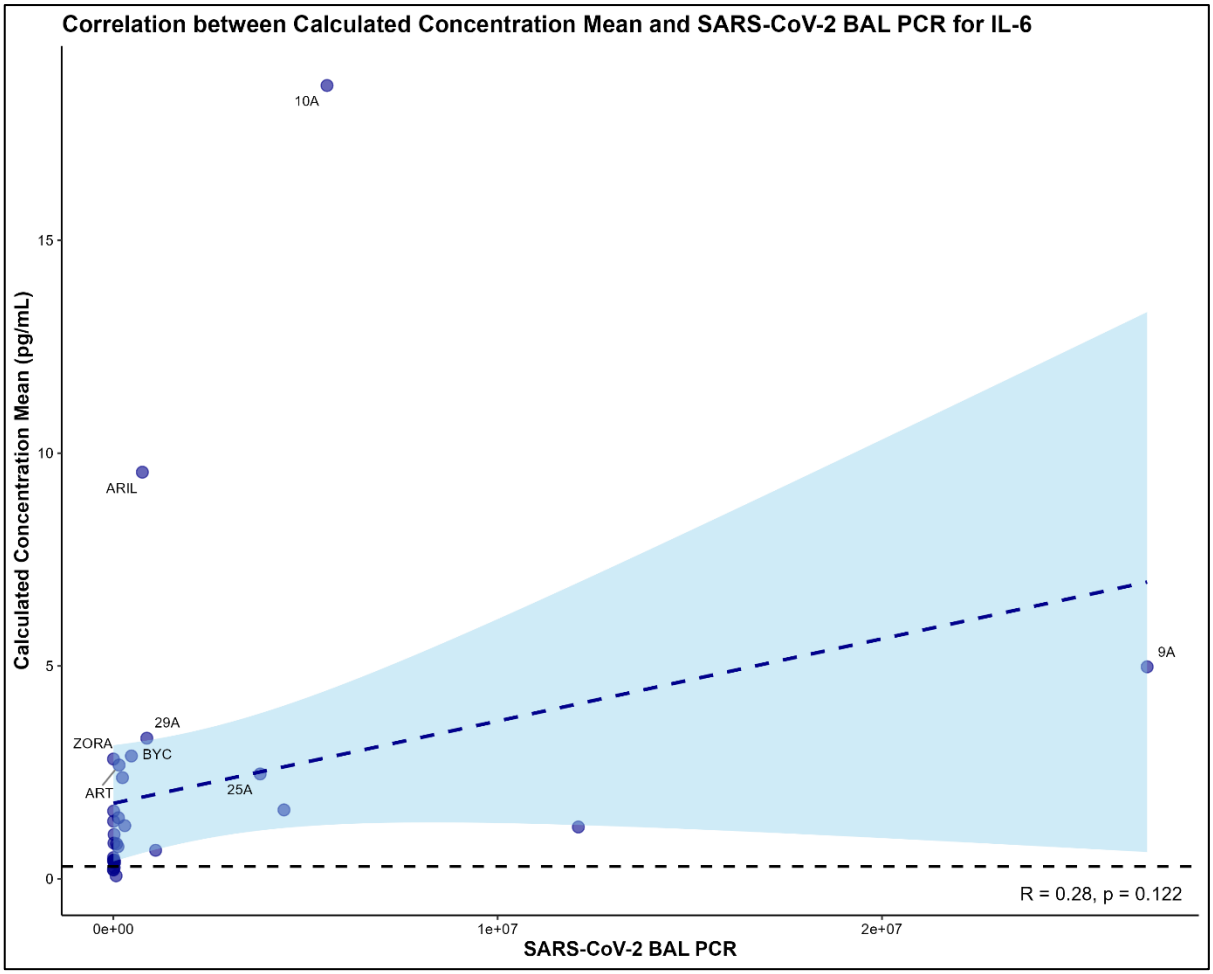

Supplementary Figure 40: IL-6 and SARS-CoV-2 BAL PCR level correlation plot. The dark blue dashed line is the regression line of the correlation between the cytokine concentration (pg/mL) and level of virus detected by BAL PCR (raw values), while the light blue colour represents the range of the associated confidence interval. The black dashed line represents the detection limit of the machine. The samples shown below this level could still be interpolated onto the standard curve. Individual samples are overlaid as blue dots. Samples too low to be interpolated are not shown. Samples in the upper quartile of cytokine concentration are annotated according to NHP ID. The R value is Pearson's correlation coefficient and the p value is calculated using Pearson's correlation test.

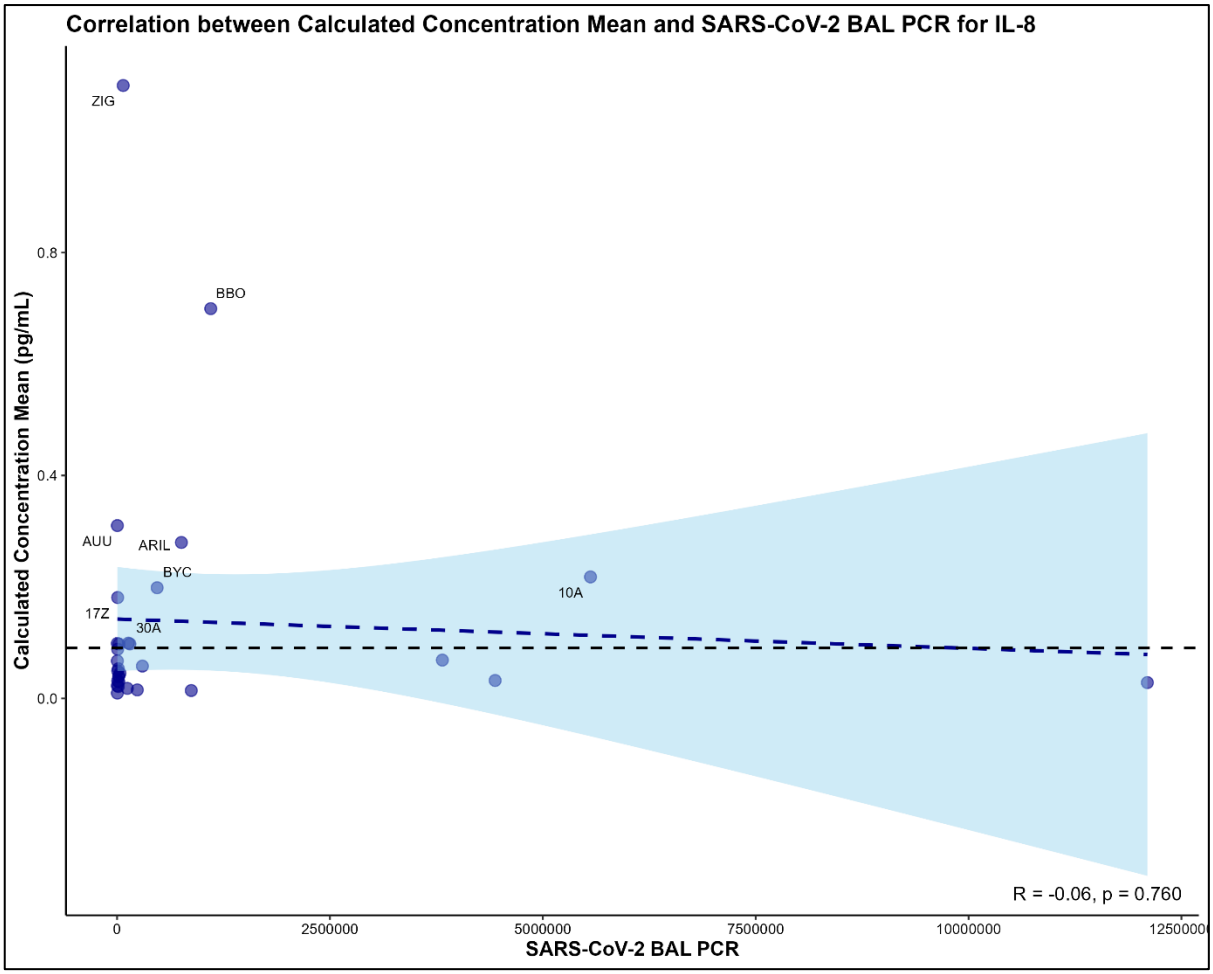

Supplementary Figure 41: IL-8 and SARS-CoV-2 BAL PCR level correlation plot. The dark blue dashed line is the regression line of the correlation between the cytokine concentration (pg/mL) and level of virus detected by BAL PCR (raw values), while the light blue colour represents the range of the associated confidence interval. The black dashed line represents the detection limit of the machine. The samples shown below this level could still be interpolated onto the standard curve. Individual samples are overlaid as blue dots. Samples too low to be interpolated are not shown. Samples in the upper quartile of cytokine concentration are annotated according to NHP ID. The R value is Pearson's correlation coefficient and the p value is calculated using Pearson's correlation test.

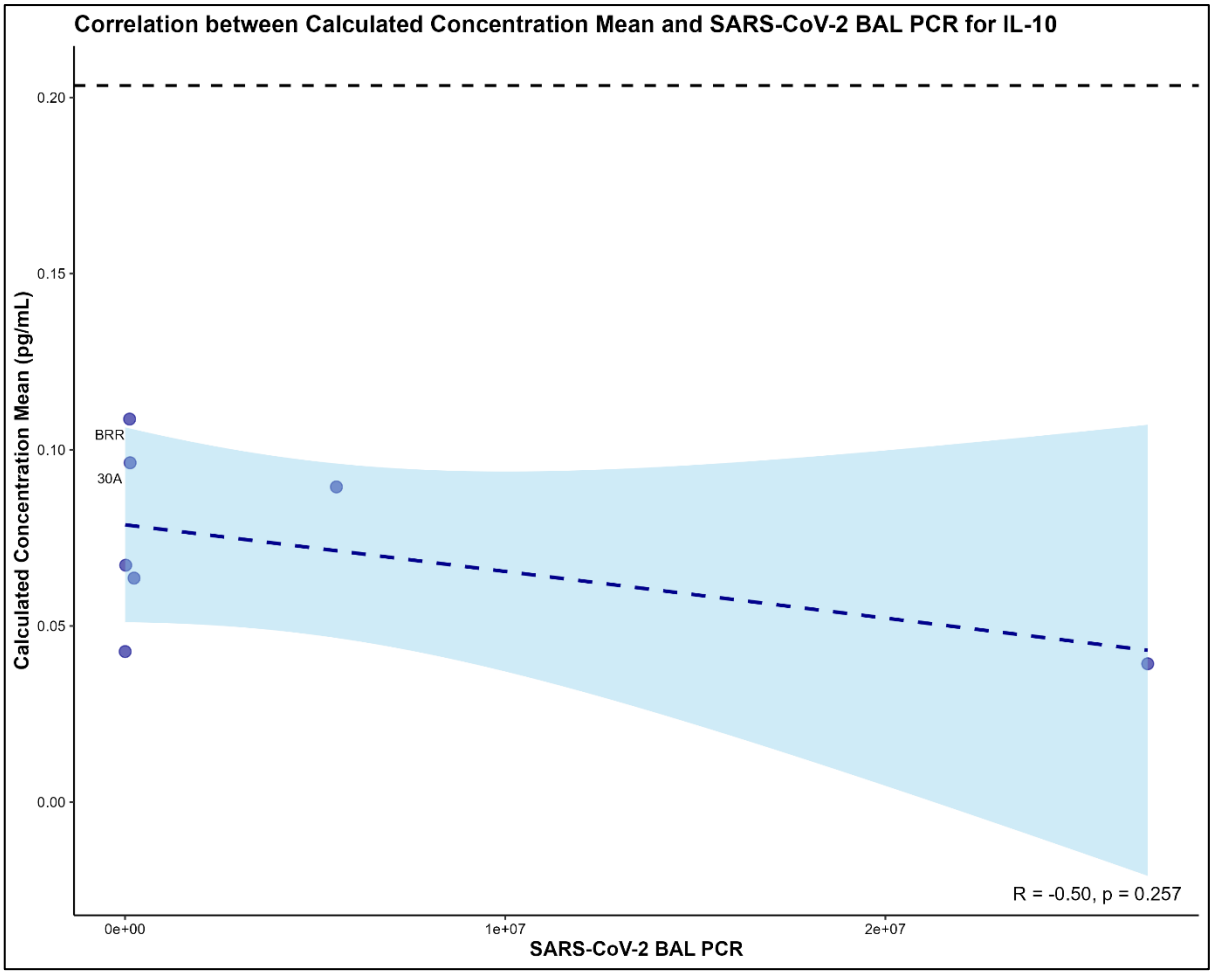

Supplementary Figure 42: IL-10 and SARS-CoV-2 BAL PCR level correlation plot. The dark blue dashed line is the regression line of the correlation between the cytokine concentration (pg/mL) and level of virus detected by BAL PCR (raw values), while the light blue colour represents the range of the associated confidence interval. The black dashed line represents the detection limit of the machine. The samples shown below this level could still be interpolated onto the standard curve. Individual samples are overlaid as blue dots. Samples too low to be interpolated are not shown. Samples in the upper quartile of cytokine concentration are annotated according to NHP ID. The R value is Pearson's correlation coefficient and the p value is calculated using Pearson's correlation test.

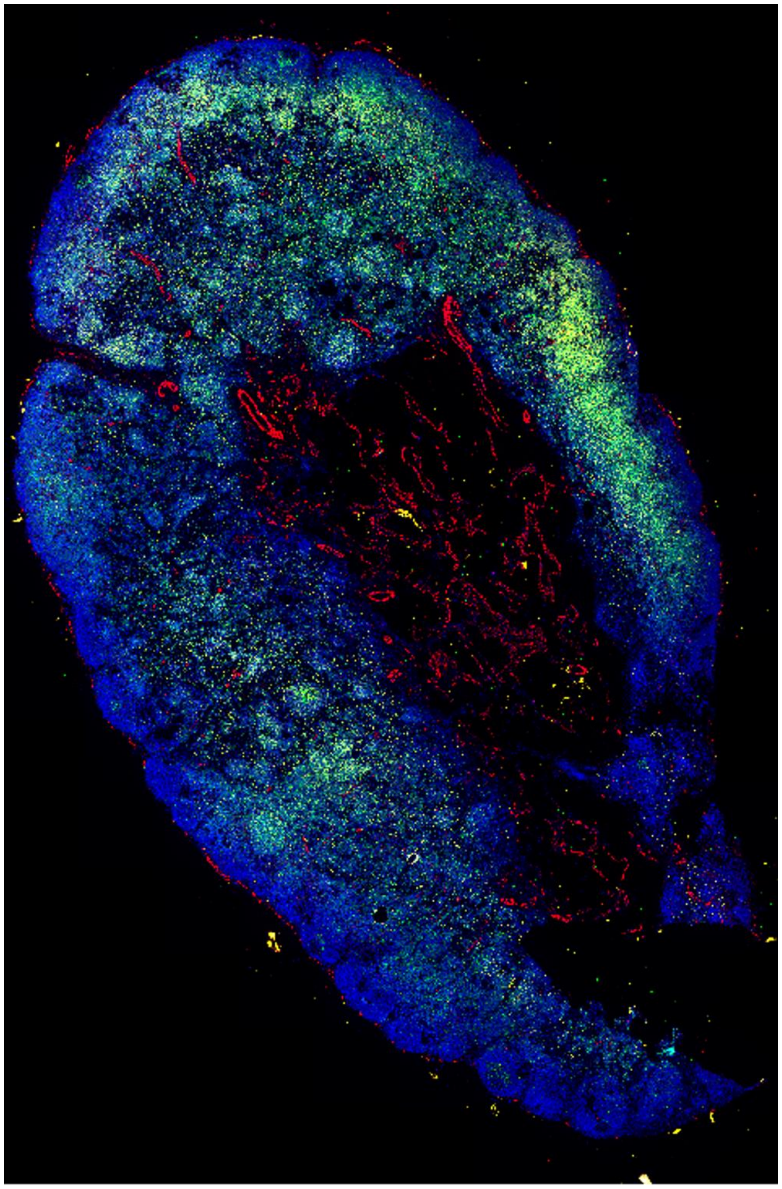

Supplementary Figure 43: Lymph node staining. Stained with CD3 (green), alpha-smooth muscle actin (red) and FOXP3 (yellow).

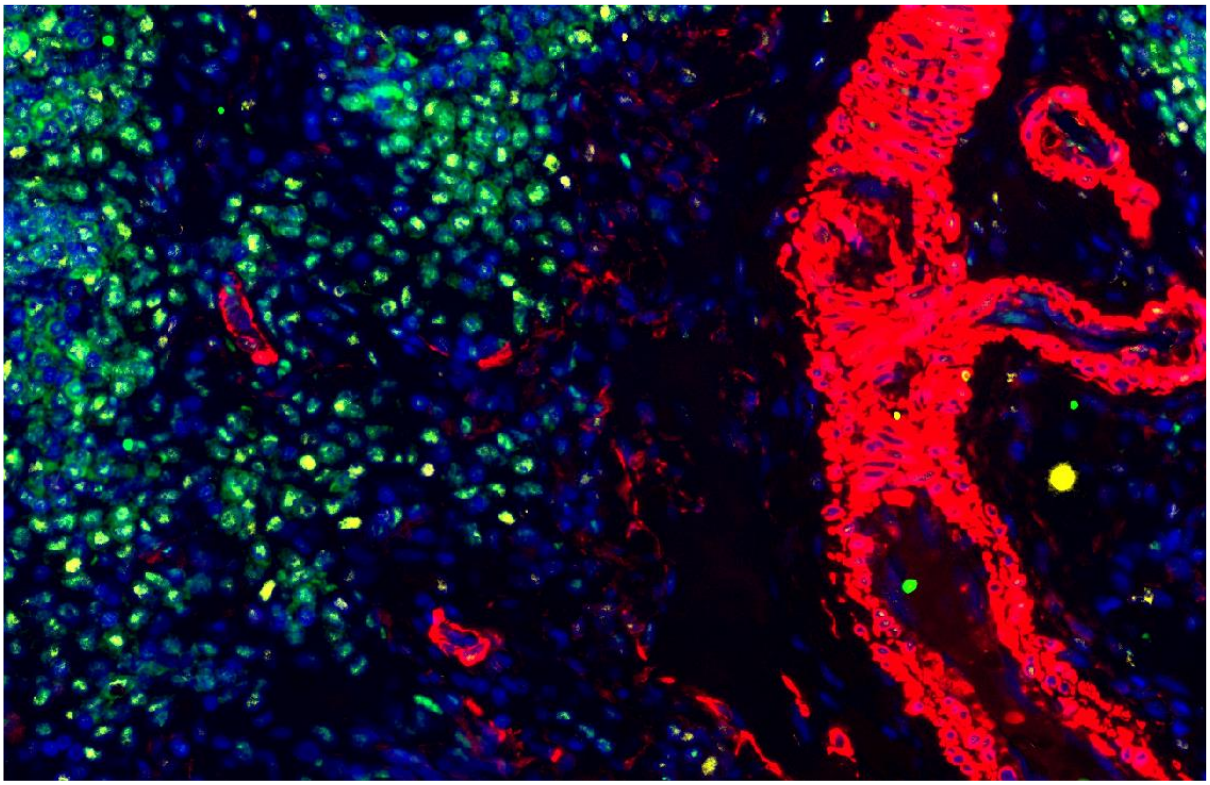

Supplementary Figure 44: Zoomed-in image of lymph node staining. Stained for CD3 (green), alpha-smooth muscle actin (red) and FOXP3 (yellow).

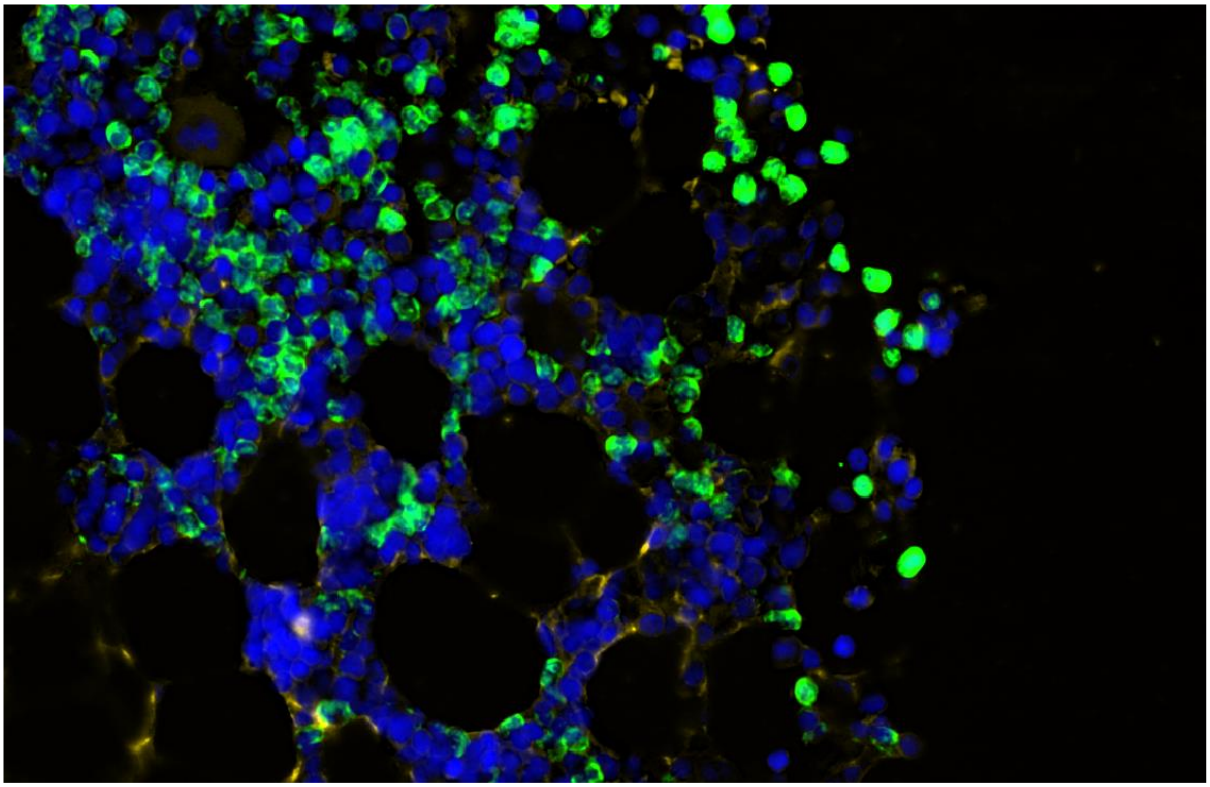

Supplementary Figure 45: Bone marrow staining. Stained for calprotectin (green) and CD10 (yellow).

Macrophage phagocytosis assays

I had originally planned to carry out macrophage phagocytosis assays in order to investigate ADE and AED, similarly to two previously-mentioned papers demonstrating the ability of antibodies from severe COVID-19 patients to initiate inflammatory responses in monocytes and macrophages [109,110]. However, due to the results of our formalin-inactivation experiment (**Chapter 4**) and our focus on in-situ tissue analysis, we decided not to pursue this in detail after some initial work-up.

We derived macrophages from both human and rhesus macaque peripheral blood mononuclear cells (PBMCs). Throughout the differentiation process, the cells were monitored by phase-contrast microscopy and flow cytometry. Once the macrophages were successfully cultured and differentiated, I planned to study how macrophages phagocytose SARS-CoV-2-spike-coated beads (and later live SARS-CoV-2 virus) in the presence or absence of serum from different NHPs at different timepoints and the impact of this on the cytokines produced by the macrophages, for AED context. This could shed light on AED as a potential mechanism of VAED in SARS-CoV-2 vaccination, as presently AED has only been described in unvaccinated severe human cases, as previously mentioned [109,110].

While none of this work ended up in any of my thesis chapters, the images that showed uptake of fluorescent beads by phagocytosis in macrophages were used to explain some findings from Caolann Brady's DPhil thesis, where she hypothesised that bead counts in one of her experiments were being affected by monocytes/macrophages that made it through an NK cell isolation protocol. Phagocytosis assays and additional experiments related to how macrophages respond to SARS-CoV-2 in the presence of sera from vaccinated animals are being continued by another DPhil student in the lab.

Methods

The methods were not fully optimised before we moved on to more in-situ tissue work. We briefly tested: plating concentrations for fresh vs frozen PBMCs, differentiating macrophages, polarising macrophages, flow cytometry and time-lapse fluorescent microscopy. PBMC isolation has been optimised and we have frozen stocks of both human and NHP PBMCs for use in assays.

Results

Below are some images representing some of the work-up.

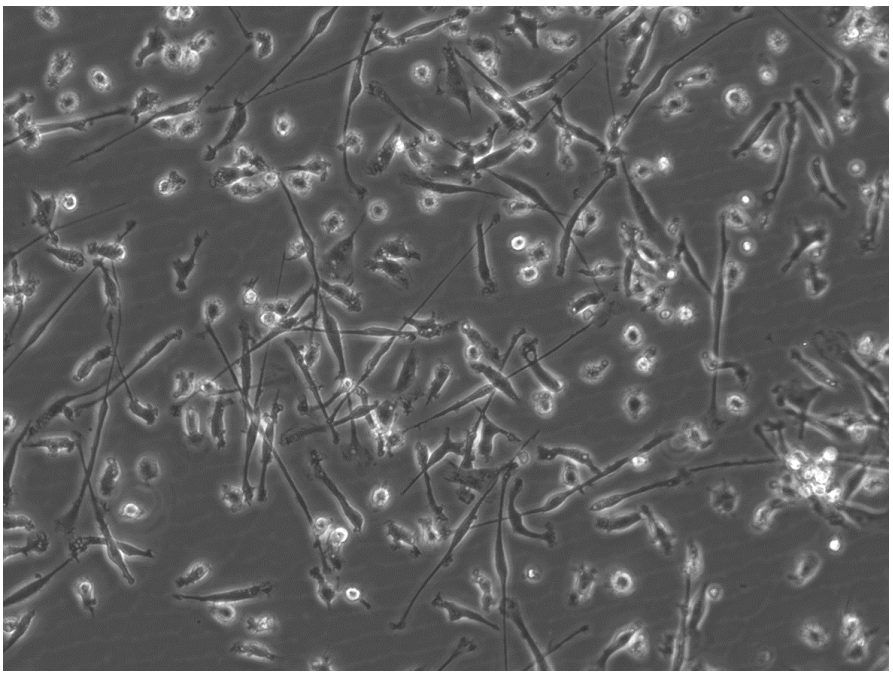

Supplementary Figure 46: Representative image showing differentiation of macrophages. Image taken using EVOS M5000 microscope.

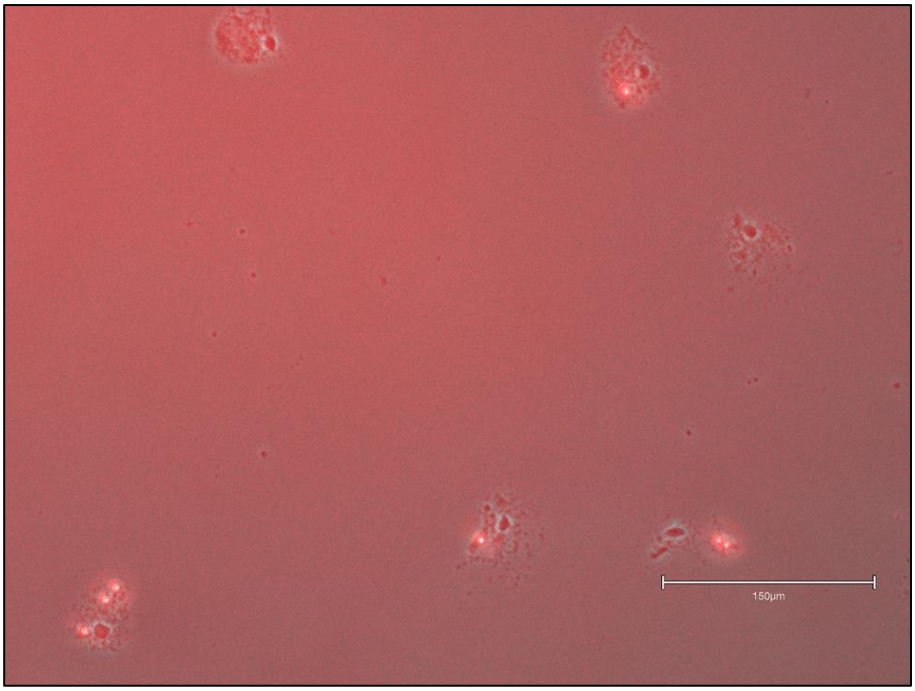

Supplementary Figure 47: Representative image showing uptake of APC-fluorescent spike-coated beads by macrophages. Image taken using EVOS M5000 microscope.